UNIVERSITY OF CALIFORNIA, SAN DIEGO

Development of Composite Renewal Systems for Rapid Rehabilitation and Construction of Bridge Decks

A dissertation submitted in partial satisfaction of the requirements for the degree Doctor of Philosophy

in

Structural Engineering

by

Anna Beth Pridmore

Committee in charge:

Professor Vistasp M. Karbhari, Chair
Professor Gilbert A. Hegemier, Co-Chair
Professor Prabhakar R. Bandaru
Professor Hyonny Kim
Professor Francesco Lanza di Scalea
Professor Vlado A. Lubarda

2009

The dissertation of Anna Beth Pridmore is approved, and it is acceptable in quality and form for publication on microfilm:

_____

_____

_____

_____

_____
Co-Chair

_____
Chair

University of California, San Diego

2009

TABLE OF CONTENTS

LIST OF ABBREVIATIONS

AASHTO	American Association of State Highway and Transportation Officials,
ACI	American Concrete Institute,
AFRP	Aramid Fiber Reinforced Polymer,
ASTM	American Society for Testing and Materials,
CFRP	Carbon Fiber Reinforced Polymer,
CHBDC	Canadian Highway Bridge Design Code,
DSC	Differential Scanning Calorimetry,
DMTA	Dynamic Mechanical Thermal Analysis,
^{o}C	Degrees Celsius,
^{o}F	Degrees Fahrenheit,
ft	Feet,
FRP	Fiber Reinforced Polymer,
GFRP	Glass Fiber Reinforced Polymer,
GPa	Giga-Pascals (10^9 Pascals),
hwy	Highway,
in	Inches,
hwy	Highway,
k	One thousand,
kip	Kilo-pound (10^3 pounds)
ksi	Kilo-pounds per square inch (10^3 pounds per square inch),
kN	Kilo-Newtons (10^3 Newtons),
LC	Lightweight Concrete,
LRFD	Load and Resistance Factor Design,
mil	Million,
mm	Millimeters,
m	Meters,
με	Microstrains,
MPa	Mega-Pascals (10^6 Pascals),
Msi	Mega-pounds per square inch (10^3 pounds per square inch),

N	Newtons,
NC	Normal weight concrete
NSM	Near Surface Mounted,
NSM	Near Surface Mounted Reinforcement,
o.c.	On Center,
pot	Linear Potentiometer
psf	Pounds per Square Foot,
rad.	Radians,
RC	Reinforced Concrete,
SIP	Stay-in-place,
TYP	Typical,
UCSD	University of California, San Diego,
US	United States,

LIST OF SYMBOLS

a	Depth of concrete compression block, assuming a rectangular stress distribution,
A_c	Area of net concrete section,
A_s	Area of tensile steel reinforcement,
A_g	Reduction coefficient that accounts for level of aggregate coverage of the top surface of FRP deck form, recommended by Dieter as addition to ACI shear capacity equation,
b	Section width,
b_w	Width of the concrete slab,
C_E	Environmental reduction factor defined in ACI440.2R Table 8.1,
d	Distance from the extreme compression fiber to tensile reinforcement,
d_f	Distance from the compression fiber to the centroid of the FRP
d_{FRP}	Distance from extreme compression fiber to bottom of FRP panel
δ_f	Deflection at target actuator load, P_f, at the location under consideration,
δ_i	Deflection at minimum threshold actuator load, P_i, at the location under consideration,
δ_o	Deflection at nominal zero actuator load, P_o, at the location under consideration,
Δ_{max_form}	Maximum allowable deflection of stay-in-place formwork,
E_c	Young's modulus of concrete,
E_f	Experimentally determined modulus of elasticity of FRP
E_L	Longitudinal modulus of FRP composites,
E_L^F	Experimental flexural modulus of FRP composites in longitudinal direction,
E_s	Young's modulus of steel,
E_T	Transverse modulus of FRP composites,

ε_{cu}	Maximum usable strain of concrete,
ε_f	Strain level in FRP reinforcement,
ε_{fe}	Effective strain in FRP reinforcement,
ε_{fu}	Design rupture strain in FRP reinforcement,
ε_s	Strain in steel,
ε_s^*	Adjusted steel strains,
$f_c^{'}$	Specified compressive strength of concrete at 28 days,
f_{fe}	Effective stress in the FRP assuming elastic behavior,
f_{fu}	Design ultimate tensile strength of the FRP reinforcement,
f_{fu}^*	Ultimate tensile strength of the FRP as reported by the manufacturer,
f_r	Modulus of rupture of concrete,
f_y	Yield stress of steel,
G_{LH}	In-plane shear modulus of FRP composites,
γ	Density,
Ψ_f	Additional reduction factor from ACI 440.06R (Section 9.6.1),
I_c	Second moment of inertia of net concrete section about its centroid,
I_{cr}	Moment of inertia of cracked section transformed to concrete,
I_e	Effective moment of inertia,
I_g	Gross moment of inertia,
k	Effective length factor for compression members (Equation 3.6),
L	Span length of the deck measured from center-to-center of supports,
L_{span}	Span length of the stay-in-place formwork,
M_{cr}	Cracking moment,
M_n	Moment capacity of the slab,
M_u	Factored moment in the slab at the edge of the outer vertical stem adjacent to the overhang,

n	Modular ratio of steel to concrete,
P_f	Target actuator load of a load cycle based on loading protocol,
P_i	Minimum threshold actuator load of a load cycle,
P_o	Nominal zero actuator load at the start of experimental testing,
φ	Curvature in deck slab (Equation 3.7),
σ_L^F	Longitudinal flexural strength of FRP composites,
σ_T^F	Transverse flexural strength of FRP composites,
σ_L^T	Longitudinal tensile strength of FRP composites,
σ_T^T	Transverse tensile strength of FRP composites,
ϕ	Resistance factor,
ρ	Reinforcement ratio,
$s_{\lim it}$	Maximum spacing limit for FRP,
t	Thickness of deck slab,
t_L	Thickness of the near surface mounted CFRP strips,
τ	Interlaminar strength of FRP composites,
V_c	Shear capacity of the slab,
V_u	Factored shear in the slab at the edge of the outer vertical stem adjacent to the overhang,
$weight_{wall}$	The total load applied to the overhang due to the combined weight of the sound wall and the traffic barrier,
y_t	Distance from the neutral axis to the extreme tensile fiber,

LIST OF FIGURES

LIST OF TABLES

ACKNOWLEDGEMENTS

The author extends her appreciation and admiration to her dissertation advisor, Professor Vistasp Karbhari, for his uncompromising dedication to his students and his passionate enthusiasm for his work. Without his time and efforts, this work would not have been possible.

Partial funding for this research was provided by the California Department of Transportation; Dr. Charles Sikorsky was the fund manager. Sika Corporation donated composite materials and Sika representative, Adriano Bortolin, provided technical assistance for the resin injection repair and near surface mounted composite rehabilitation stages of this research. The author offers appreciation to her dissertation committee members, Structural Engineering Professors Gilbert Hegemier, Francesco Lanza di Scalea, and Hyonny Kim, as well as Mechanical Engineering Professors Vlado Lubarda and Prab Bandaru, for their insightful feedback on this research.

Technical support from the staff at the Powell Structures Laboratory at the University of California, San Deigo, particularly the assistance of Dr. Christopher Latham, Andrew Gunthardt, Bob Parks, Charles Stearns and Edward Stovin is greatly appreciated. Fellow graduate students within Dr. Karbhari's research group and within the structural engineering department, particularly Don Philippi, Griffin Brungraber and SeungDae Kim provided valuable assistance with experiments as well as many insightful conversations.

Lastly, the author wishes to thank her husband and family who have been tremendously supportive during this process.

VITA

2001-2004	Assistant Research Scientist, La Jolla Bioengineering Institute
2004-2006	Research Assistant, Department of Structural Engineering University of California, San Diego
2006	B.S., Structural Engineering University of California, San Diego
2006-2009	Research Assistant, Department of Structural Engineering University of California, San Diego
2007-2008	Teaching Assistant, Department of Structural Engineering University of California, San Diego
2008	M.S., Structural Engineering University of California, San Diego
2009	Instructor, Department of Structural Engineering University of California, San Diego
2009	Ph.D., Structural Engineering University of California, San Diego

ABSTRACT OF THE DISSERTATION

Development of Composite Renewal Systems for Rapid Rehabilitation and Construction of Bridge Decks

by

Anna Beth Pridmore

Doctor of Philosophy in Structural Engineering

University of California, San Diego, 2009

Professor Vistasp M. Karbhari, Chair

Professor Gilbert A. Hegemier, Co-Chair

The deterioration of steel in aging reinforced concrete bridges is a continual problem which could benefit from improved rehabilitation techniques that take advantage of enhanced and more durable materials such as fiber reinforced polymer (FRP) composites. Appropriately designed hybrid material systems benefit from the performance and durability advantages of FRP materials yet remain more cost effective than comparable all-composite systems.

Development of rapid rehabilitation systems for the decks of concrete box girder bridges, which are increasingly common throughout the United States, is presented. One goal of this research is to assess and validate the use of FRP

composite panels for use as both stay-in-place formwork and as the bottom longitudinal and transverse reinforcement in the deck of concrete box girder bridges. Performance assessments for full-scale two-cell box girder bridge specimens through monotonic and extensive cyclic loading provided validation for the FRP panel system bridge deck as a viable rehabilitation solution for box girder bridge decks. The FRP panel system performed comparably to a conventionally reinforced concrete bridge deck in terms of serviceability, deflection profiles, and system level structural interaction and performed superior to the RC bridge deck in terms of residual deflections, and structural response under cyclic loading. Assessment of a damaged FRP panel bridge deck system, which was repaired using a resin injection technique, showed superior performance for the repaired system in terms of integrity of the FRP panel interface and cyclic response.

Rapid rehabilitation techniques for strengthening reinforced concrete box girder bridge deck overhangs using near-surface-mounted (NSM) carbon fiber reinforced polymer (CFRP) were also evaluated. Analytical predictions of load carrying capacity and deflections provided correlation with experimental results, and the developed analysis methods provide an effective design tool for future research. Results from the laboratory testing of a bridge deck overhang strengthened with FRP showed significant increases in load carrying capacity as well as deformation capacity as compared to the as-built specimen without FRP. This research provides enhanced understanding of hybrid structures and indicates significant potential for rehabilitation applications to concrete box girder bridges.

1 INTRODUCTION

1.1 BACKGROUND AND MOTIVATION FOR RESEARCH

Usually designed for a fifty year life span, the average bridge in the United States is now 43 years old [1]. In 2008, the American Association of State Highway and Transportation Officials (AASHTO) estimated that approximately $140 billion would be necessary to repair every currently deficient bridge in the country [2]. The cost to continually eliminate all bridge deficiencies that would occur over the next fifty years was estimated to be $850 billion, however annual government investment in rehabilitation and replacement of bridges falls more than 40% short of the annual investment necessary to achieve this goal [3]. This necessary financial investment creates significant motivation for development of more effective bridge rehabilitation techniques.

The element within a bridge system that usually requires the most maintenance is the bridge deck, which typically lasts half as long as the rest of the bridge, 35 years versus 68 years respectively [4]. Because the bridge deck is directly impacted by traffic loading, it is most susceptible to cyclic loading induced damage and environmental degradation [5]. Nearly 70% of the existing bridge decks in the United States are cast-in-place reinforced concrete [6]. Cracks that form in the concrete allow moisture and deicing salts to penetrate into the deck and corrode the reinforcing steel rebar [7]. The corrosion of steel reinforcement is a significant problem that adversely affects the long term durability of the concrete because the steel rebar expands as it

rusts, causing the surrounding concrete to crack and spall, and further accelerate the deterioration of the bridge deck [8].

Deterioration in steel reinforced concrete bridge decks can be reduced by improving design practices, such as ensuring proper cover for the steel reinforcement, and through the use of higher quality conventional materials. Some techniques for reducing the rate of deterioration include the use of epoxy coated or stainless steel rebar, the application of surface treatments with cathodic protection and sealants to inhibit penetration of salts into the concrete slab, the filling of cracks using a grout or a low viscosity resin, and the use of a wearing surface [9]. These construction methods are typically costly and offer only a temporary barrier to preventing penetration of salts in to the concrete slab. For bridge decks with extensive deterioration, a common technique is the removal of the old deck and construction of a new cast-in-place concrete deck [10]. This costly solution does not address the inherent problems associated with corrosion prone steel reinforcement.

1.2 FRP Rehabilitation of Concrete Bridge Decks

The use of FRP composites is becoming an increasingly popular alternative due to the many performance and potentially enhanced durability benefits of FRPs such as superior resistance to damage from freeze-thaw cycles and deicing chemicals [5, 11]. FRP composites offer high specific strength and stiffness, enhanced fatigue life and corrosion resistance, and highly anisotropic properties that allow for improved tailorability to numerous design applications [5]. While FRP material costs for FRP systems are relatively expensive compared to traditional construction materials such as

concrete and steel, FRP systems provide opportunities for reduced labor and equipment costs as well as accelerated construction schedules [12].

FRPs have been applied to bridge deck applications in the form of all-composite systems [13-28] or as a combination of FRPs with conventional materials such as concrete, known as a hybrid system [29-35]. Further information on applications of FRP composites to bridges can be found in recent reviews presented by Cheng and Karbhari [36], Bank [37], Bakis *et al*. [38], and Keller [39]. While all FRP decks are an attractive option, their cost is still relatively high [40, 41]. A major advantage of hybrid FRP-concrete systems, which include FRP rebar [31, 42-54], grid reinforcement [40, 55-64], and stay-in place (SIP) structural formwork [40, 58, 59, 65-73], is their efficient use of materials. By designing a system where the high performance FRP composites, which are best used in tension, are utilized in tension regions and the economical concrete, which is good in compression, is utilized in compression regions, material usage can be optimized. This judicious material selection creates a more cost-effective system than an all-composite design, while taking full advantage of the excellent tensile strength, tailorability and potential for corrosion resistance provided by FRP materials [5]. Note that FRP rebar generally has a lower modulus than steel and therefore will need to be used either at a great volume fraction than steel, or over shorter spans [38]. Similar constraints exist for grids, although in both cases the potential durability advantages are important for niche applications. Structural stay-in-place FRP formwork however serves as an example of an optimal hybrid – the composite is used as the formwork as well as the bottom layer of tensile reinforcement for the bridge deck, and the concrete is used in compression –

both systems in their best modes of structural response. In addition to potential durability benefits, SIP structural forms can offer economic advantages by reducing labor costs through elimination of the formwork and falsework necessary for construction of a cast-in-place concrete bridge deck. The use of FRP structural panels as both the formwork and tensile reinforcement in the positive moment regions of a reinforced concrete box girder bridge deck is a rehabilitation system that was assessed and validated as part of this research.

1.3 REHABILITATION NEEDS FOR REINFORCED CONCRETE BOX GIRDER BRIDGES

The current research focuses on addressing rehabilitation needs for reinforced concrete box girder bridges. Reinforced concrete box girder bridges are commonly used throughout the United States and comprise 45% of California's bridge inventory, with the majority of these bridges built using cast-in-place concrete [74]. The use of box girder bridges is increasingly common in part due to advantages provided by improved resistance to torsion and the capability for long span lengths. Problems specific to the box girder bridges are that they are more difficult to maintain because of need for access to a confined space and that deck replacement is difficult due to issues of instability in the box.

The first rehabilitation option addressed in this research involves the use of FRP structural formwork panels in conjunction with regular strength concrete to provide an effective design alternative to traditional reinforcement systems for a reinforced concrete box girder bridge. This system can be used as either a method of repair for bridge decks with severe or extensive damage or used for new bridge deck

construction. The design of the system provides significant reserve strengths for the deck panel system and constrains damage within the concrete to a more localized region between stiffeners, thereby allowing damaged concrete to be removed and new concrete to be cast without requiring access to the inside of the box. A resin injection repair technique of the developed FRP panel system was also examined as a further means to accommodate effective rehabilitation of box girders without requiring access to the inside of the box.

Another rehabilitation method examined in this research addresses a problem associated with older box girder bridges, which lack sufficient strength to accommodate the increased dead loads due to the addition of sound walls and traffic barriers onto the overhangs of the bridge decks. The conventional method of increasing the capacity of the overhang region is to remove the overhang and portions of the adjacent bridge deck and stem wall, and then rebuild the section with adequate reinforcement using conventional reinforced concrete. The current research method addresses the use of near surface mounted CFRP strips for flexural strengthening the overhang region of the bridge deck. This method allows the existing overhang to remain intact and significantly reduces construction time over a partial deck rebuild.

1.4 RESEARCH GOALS AND OBJECTIVES

The primary goal for this research is to evaluate rapid rehabilitation methods that employ FRP materials for use in the decks of concrete box girder bridges. The major objectives for achieving this goal include:

1. Assess and validate the use of stay-in-place FRP composite formwork panels for use in the decks of box girder bridges;
2. Characterize the system level behavior of the FRP panel bridge deck system;
3. Provide fundamental performance comparisons between the FRP panel bridge deck system and a conventional reinforced concrete deck system;
4. Determine limit states and develop preliminary design guidelines for the FRP panel bridge deck system;
5. Evaluate the ease and effectiveness of techniques to repair the FRP panel bridge deck system if damage to the bridge deck were to occur;
6. Examine additional rapid rehabilitation techniques such as the use of near surface mounted (NSM) FRP reinforcement for strengthening the negative moment regions of box girder bridge deck overhangs; and
7. Develop analytical performance predictions and design recommendations for rehabilitation of bridge decks using NSM FRP reinforcement.

1.5 SCOPE OF PROJECT

This research is organized into seven chapters. Chapter 1 introduces the problems addressed by this research, the research goals and objectives and the scope and outline for the research. Chapter 2 presents a literature review for the major topics covered in this research.

Chapter 3 presents the development, experimental testing program, and results from an investigation of a full scale two -cell box girder bridge which incorporates the developed hybrid FRP-concrete bridge system, where prefabricated composite panels act as both the formwork and reinforcement for the bridge deck. Chapter 4 addresses the implementation of a epoxy injection technique used to repair the damage caused to the concrete-composite interface of the post-failure FRP panel system deck system. The details of the repair technique and analysis of the test results are presented. Chapter 5 presents the details and test results from an experimental investigation which focuses on the structural response of the FRP panel system under cyclic loading.

Chapter 6 presents the experimental and analytical investigation of the strengthening of a reinforced concrete bridge deck overhang with near surface mounted composite strips. Conclusions and recommendations for future work related to this research are discussed in the final chapter.

2 LITERATURE REVIEW

2.1 OVERVIEW

The first section of this literature review provides information relating to formwork for construction of slab-on-girder bridge decks. Different materials and designs used as formwork for concrete slab-on-girder bridge decks are presented and the relative merits of the different systems are addressed. Particular focus is given to the progression of research relating to FRP stay-in-place structural formwork systems for bridge decks in order to provide context for the current research.

An overview of typical repair methods for reinforced concrete bridge decks given in Section 2.3 offers a background for the epoxy injection repair technique implemented to reinstate load transfer between the FRP panels and concrete on a failed test specimen, which is discussed in Chapter 5.

Next, research related to the use of near surface mounted composites for strengthening concrete structures is provided in Section 2.4. This application of near surface mounted composites provides rapid rehabilitation for bridge decks and often allows repair where conventional mechanisms are too costly or not possible. A comparison between surface mounted and near surface mounted FRP as well as an overview of the different failure modes of NSM, and available specifications are also presented.

2.2 FORMWORK FOR CONSTRUCTION OF SLAB-ON-GIRDER BRIDGE DECKS

The primary purpose of deck formwork is to provide a shape for the concrete deck and to support the dead load from the reinforcement and fresh concrete as well as the live load from construction materials, workers and equipment. The three major objectives considered when designing formwork systems are quality, safety and economy [75]. Quality forms must provide sufficient stiffness to maintain desired tolerances for the cast concrete and must safely support all dead and live loads without system collapse or safety issues. Formwork costs may range from 35 to 60% of the total cost of the concrete structure; therefore, economy of formwork design can provide a significant impact on the overall construction budget for a project [76, 77]. In addition to direct labor costs, the speed of construction is often controlled by formwork operations. In order for work to proceed smoothly and cost effectively, it is necessary to carefully select the bridge deck formwork system to best meet a construction project's job requirements.

2.2.1 Temporary Formwork versus Stay-in-Place Formwork

Removable formwork supports bridge deck construction loads and freshly placed concrete until the deck concrete cures sufficiently to allow removal of the forms. If the deck concrete has not achieved sufficient strength to fully support it own weight without excessive deflections, the deck is reshored with temporary vertical supports until full design strength for the deck is obtained [78]. After the stripped

forms are inspected and any necessary repairs have been completed, the forms may be reused.

Temporary formwork systems are often constructed of wood supports and plywood sheathing, with designs similar to the layout shown in Figure 2.1 [76]. This type of form is usually constructed in place on the job and reuse of form material is limited to the salvaging of individual boards or timbers [75]. Because this type of system is very labor intensive and requires a high-quality labor force, prefabricated reusable forms which can be constructed more quickly with less on-site preparation have become more prevalent. Reusable forms for bridge decks are most commonly made of wood, steel or aluminum, or a combination of these materials, which can be custom fabricated for a specific project or can be part of a proprietary system.

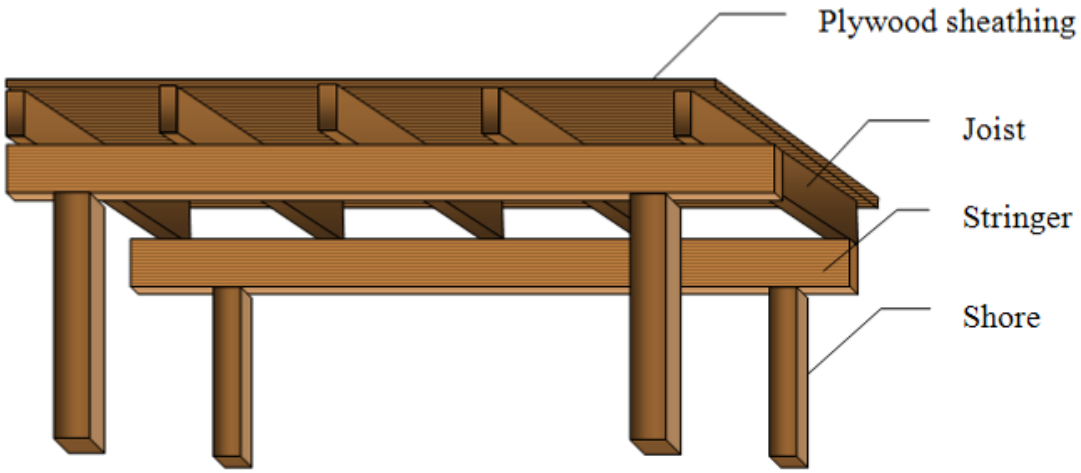

Figure 2.1 Conventional wooden shored formwork layout for deck (after [76])

Formwork systems can also be permanently left in place for the life of the bridge deck. Stay-in-place (SIP) bridge deck forms (also known as lost or permanent

forms) are usually used on short spans where intermediate supports are not required and are made of glass fiber reinforced cement, fiber reinforced polymers, corrugated steel sheets, or precast concrete panels [75]. While temporary formwork systems can reduce material costs by allowing reuse of the forms, potential benefits from the use of stay-in-place forms include simplified construction, reduction in construction time and labor costs, and enhanced safety. By eliminating the need for falsework to support the deck forms and reshoring after forms are removed, construction times and labor costs can be reduced. Safety during the construction process is enhanced, because the stripping of formwork, which is often located in difficult and confined spaces that leave workers vulnerable to falling tools or other objects, is no longer required [79]. The SIP forms also provide a safe working platform at an early stage in the deck construction process, which is a major advantage when the bridge is spanning a river, active roadway, or other hazardous location [80]. The modularity of stay-in-place forms provides the potential for increased standardization and the simple connection details commonly associated with SIP forms can simplify the construction process [69]. SIP forms can also act as structural elements for the bridge deck and help to support service loads, which can allow for reductions in the amount of required steel reinforcement within the deck. However, depending on the type of stay-in-place form used, disadvantages can include trapping of moisture that collects on top of the SIP forms as well as damage and corrosion problems (especially associated with steel SIP forms) due to the trapped moisture [68]. In addition, forms which have smooth surfaces prevent composite action from developing with the concrete deck.

2.2.2 Stay-in-Place Formwork Made from Conventional Construction Materials

Use of precast concrete panel forms has been documented for use in building and bridge construction since before the mid 1930s [75]. Concrete forms can either be plain, reinforced, or prestressed, and can be cast at the job site or in a factory [81]. The forms can act solely as formwork or they can also act compositely with the cast-in-place concrete and become part of the load bearing structure. An early example of a typical structurally participating forms made of precast concrete panels is a Northern Illinois Toll Highway bridge, built in 1956, which uses precast prestressed slabs that spanned between prestressed girders. The panels had a roughened top surface as well as hairpin dowels to improve the bond between the panels and the cast-in-place concrete such that composite action could be ensured. The SIP panel forms provided some of the positive moment deck reinforcement and added to the strength of the full deck through composite action.

Use of precast prestressed concrete SIP forms as part of a concrete bridge deck system without any internal reinforcement, has also been reported [82]. This system is a continuation of the original concept that was developed by Mufti *et al*., which relied on internal arching action of a steel-free cast-in-place concrete or precast concrete deck and used steel straps to provide transverse confinement for the deck [83-85]. The Salmon River Bridge in Nova Scotia, Canada was the first of many steel free bridges to rely on arching action [86], and provisions for designing steel free slabs that rely on arching action have been incorporated into the Canadian Highway Bridge Design Code (CHBDC) [87]. A grid of nominal reinforcement, either made of steel of GFRP is recommended to control unsightly, but not structurally significant, cracks that had

developed on the bottom of the deck slabs [88]. Use of light gage-steel formwork that takes the place of the steel straps to serve as the tension chord has also been presented and design modifications to the CHBDC code were provided by Bakt et al [89].

While the use of corrugated metal SIP forms for bridge decks is prevalent, significant concerns are associated with the difficulty in achieving composite action due to the smooth surface of the forms as well as corrosion problems and freeze/thaw damage of the SIP metal forms due to trapped moisture and chlorides [68]. Therefore, thirteen US states do not allow the use of metal SIP forms due to concerns that the presence of the metal SIP forms may accelerated damage of the bridge deck and cause higher contents of moisture and chlorides to remain within the deck [90]. In addition, AASHTO does not permit concrete decks with metal SIP formwork to be considered as composite slabs for design purposes [91], even though composite slabs are routinely used in building design.

Recent developments of glass fiber reinforced cement SIP forms for bridge decks were presented by Kim *et al.* [92, 93] and Bank *et al*. [94]. Bank *et al*. also provided a model design and construction specification on fiber reinforced non-structural SIP formwork panels, which span narrow gaps of less than 1 m (39.4 in), for use in construction of concrete highway bridge decks [66].

2.2.3 FRP Stay-in-Place Structural Formwork

In the past 20 years, research interest has lead to advances in the development of hybrid systems that combine FRP as stay-in-place structural formwork with concrete. Use of a hybrid system, which involves cast in place concrete, together with

stay-in-place FRP structural formwork allows for the development of a more cost effective system. By appropriate design, that uses concrete which is good in compression and is less expensive than FRP material, in conjunction with FRP material, which are good in tension, materials usage can be optimized. The use of FRP as permanent formwork can also facilitate improved construction schedules, and has the potential for improved bridge deck durability by reducing or eliminating the need for corrosion-prone steel reinforcement.

In 1989, the concept of a pultruded GFRP membrane as the structural formwork for a lightweight concrete bridge deck was proposed by Bakeri [95]. The GFRP membrane design shown in Figure 2.2 was selected from ten different hybrid GFRP-concrete conceptual designs based on ease and cost of manufacturing, as well as analytical calculations predicting mechanical performance of the system. Alternative conceptual designs included light weight concrete filled filament wound GFRP domes, pultruded GFRP vaults, and filament wound doubly-curved membranes as well as pultruded GFRP trusses with light weight concrete overlays. Mechanical performance of the system was analyzed based on quasi-isotropic layups, however no experimental data was available.

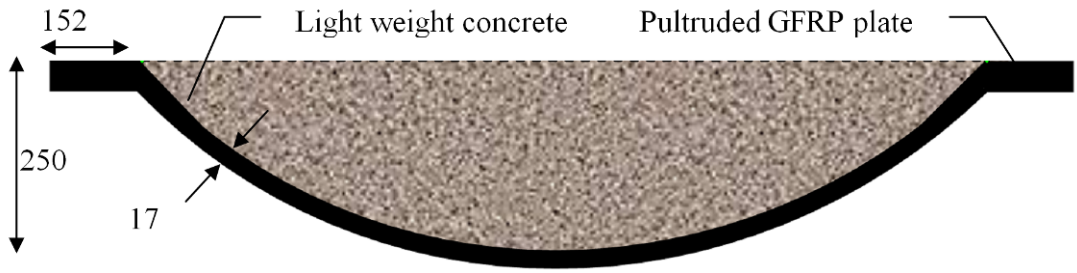

Figure 2.2 Concrete filled membrane deck system (after [95])

2.2.3.1 Composite Slabs Using FRP Panels with T-upstands

In 1990, the concept of a composite slab system constructed using pultruded FRP SIP formwork with concrete fill was proposed by Hillman and Murray as a lightweight floor system for steel framed buildings [96]. The pultruded deck consisted of 76.2 mm (3 in) deep inverted T-beams, which provided the stiffness for the system, that were connected together by plates located approximately 25.4 mm (1 in) from the top flanges. The plates acted as the formwork for a 25.4 mm (1 in) concrete slab placed on top of the flanges, as shown in Figure 2.3. When full composite action between the FRP SIP formwork and the concrete was assumed, Hillman and Murray suggested that a 50-60% weight reduction as compared to the cold-formed steel decking reference slabs could be achieved.

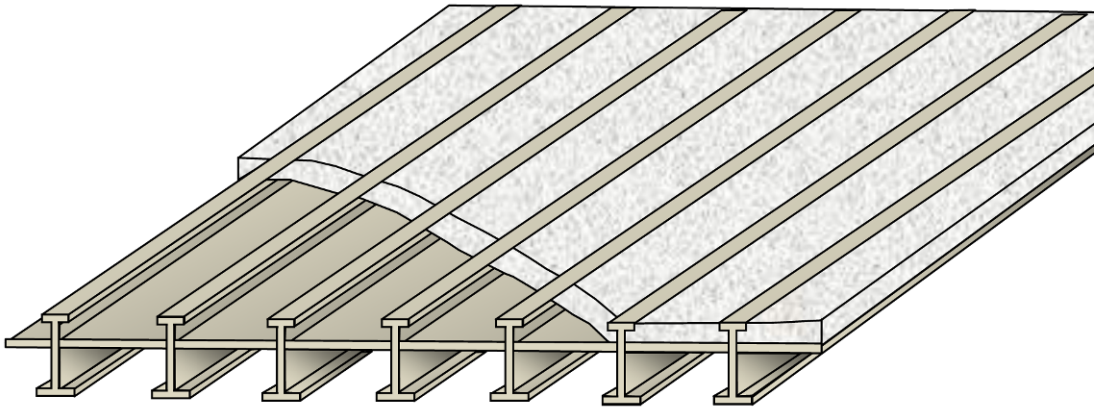

Figure 2.3 Composite slab with structural formwork (after [96])

A feasibility study of the concept proposed by Hillman and Murray was conducted by Hall and Mottram using commercially available pultruded GFRP panels that consisted of two T-upstands with a continuous base [73]. Twelve beams that each

were 120 mm (5 in) wide and had a span of 2 meters (6 ft 10in) were tested to failure using a four point bend test. The beams used different configurations of the pultruded FRP panels and different concrete heights, as shown in Figure 2.4. The system behaved in linear elastic fashion within the serviceability range. However, significant horizontal shear slippage was observed between the concrete and the FRP sections at loads significantly above the serviceability range, which severely reduced the ultimate capacity of the member. In order to enhance the concrete-composite interface, the surfaces of the pultruded panels which came into contact with concrete were coated with an adhesive and the concrete was cast before the adhesive had cured. The beams with adhesive treated FRP-concrete interfaces displayed full composite action and showed significantly improved performance over the beams without adhesive treatment. For the beams which did not fail due to FRP-concrete debonding, the observed failure mode was diagonal tension shear cracking in the concrete. The observed failure mode was attributed to the beam's design, which was over-reinforced in flexure and to the absence of shear reinforcement within the concrete.

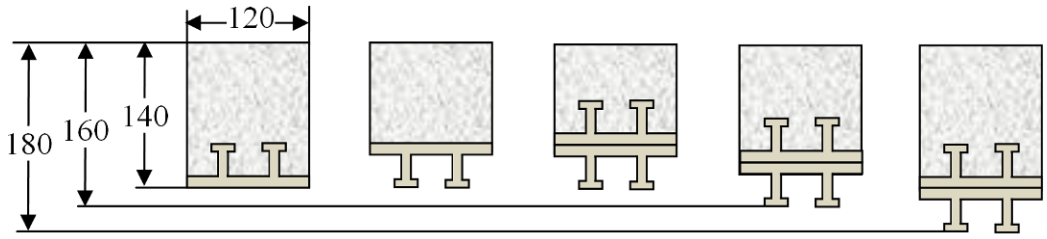

Figure 2.4 Beam specimens with FRP SIP forms (after [73])

Keller *et al*. reported on a further development of FRP panels with T-upstands for use as SIP structural formwork [97-99]. In order to reduce the self weight of the

systems, a sandwich panel was developed that consisted of a pultruded FRP sheet with T-upstands for the tension skin and structural formwork, a lightweight concrete (LC) for the core, and a normal weight concrete (NC) on top for the compression skin, as shown in Figure 2.5 (a). Eight beams, each 400 mm (16 in) wide, 200 mm (8 in) deep and 3.6 meters (12 ft 2 in) long, were tested in flexure using a three-point bending setup with two types of LC and two types of FRP/LC interface: an adhesive bond versus only mechanical interlock between the LC and T-upstands.

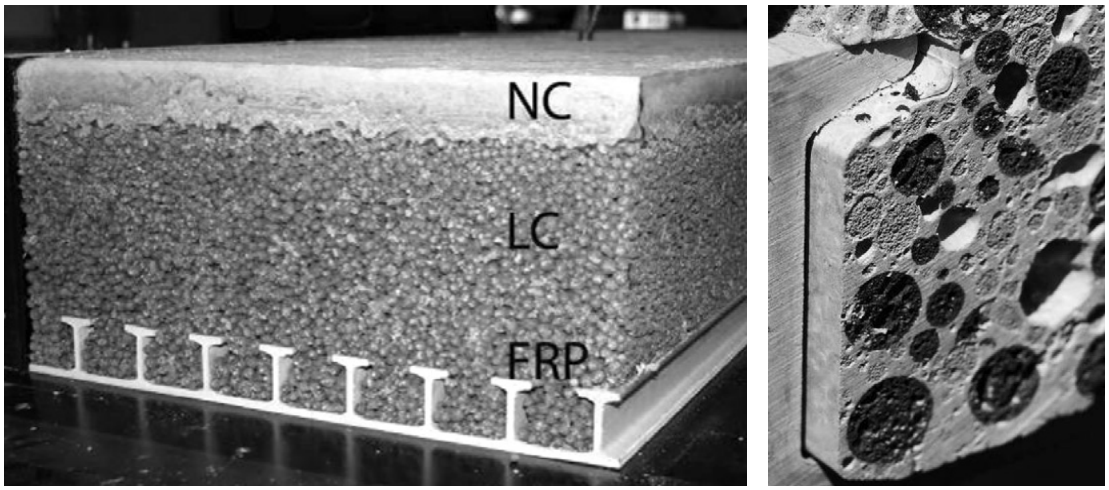

(a) Cross section of sandwich panel
NC = Normal weight concrete
LC = Light-weight concrete

(b) Close-up of failure surface at concrete-FRP interface

Figure 2.5 Sandwich panel with a lightweight concrete core, concrete in compression zone, and FRP panel with T-upstands in tension zone [97, 98]

The beams that relied on mechanical interlock between the LC and FRP panels exhibited significant slippage between the core and the panels, as shown in Figure 2.5 (b), thereby reducing composite action for the section. The adhesive bond between the

LC core and FRP panels provided sufficient interface strength such that full composite action was observed prior to the observed failure mode of horizontal shear within the LC core. Successful serviceability performance and overall results showed the feasibility of the proposed hybrid deck system.

In 2006, Bank *et al*. reported on the experimental testing of commercially available pultruded FRP planks used as formwork and reinforcement for a concrete member [65, 71]. The FRP planks with T-upstands were coated with different types of aggregate that were bonded with epoxy to the FRP planks to increase mechanical interlock and prevent slip between the concrete and the FRP panels. The feasibility of this system was experimentally examined using a total of seven 203 mm wide (8 in) by 178 mm (7 in) deep beams with spans of 1.1 m (3 ft 7 in) and 1.8 meters (6 ft) tested in three-point bending While partial debonding between the FRP plank and the concrete was observed for all the beams, no slip between the concrete and aggregate coated FRP planks was noted. In contrast, the control specimen, which consisted of the same type of FRP plank without any surface treatment, exhibited significant slip and failed at approximately half the failure load exhibited by comparable beams with aggregate coated FRP planks. The aggregate coated FRP plank system compared favorable to a steel reinforced system indicating the system's potential for serving the dual functions of formwork and tensile reinforcement.

Based on the results of this study, the examined FRP plank SIP formwork and reinforcement system was used in the construction of a new bridge in Wisconsin located over Coffee Creek at Black River Falls, as shown in Figure 2.6. This two lane 30 m span bridge was completed in 2008 consists of a reinforcement free concrete

deck (except for guardrail attachments) placed on precast concrete bulb-Tee girders in which aggregate-coated FRP planks are utilized as SIP formwork and secondary reinforcement for the bridge deck.

The same research group also investigated a FRP SIP structural formwork system consisting of a pultruded GFRP plate which is bonded to a GFRP grid formed by I bars that are intersected by periodically spaced GFRP rebar which have been inserted through holes drilled into the I bars [69]. Multiple one span and two span slabs were tested under flexural as well as combined flexural and axial loading. ACI 440 design guidelines were found to accurately predict flexural and flexural-shear capacities and additional capacity prediction techniques were proposed for flexural and flexural-shear under combined loading.

Figure 2.6 Use of commercially available FRP plank as SIP forwork and secondary reinforcement in reinforcement-free deck [66]

2.2.3.2 FRP Box Beams with Concrete in the Compression Zone

In the early 1990's, Deskovic *et al*. tested the short term and long term behavior of GFRP box beams with concrete in the compression zone and CFRP in the tension zone [100-102]. This work built upon previous studies of GFRP box beams from the 1980's [103, 104], which established the following design deficiencies:

1 . failure of the GFRP box beam is usually catastrophic, because composite materials are observed to behave in a linear elastic fashion until failure, without significant plastic deformation as seen in steel or reinforced concrete;

2. the compressive flange is significantly weaker than the tensile flange, due to local buckling phenomena and because a unidirectional of GFRP has a compressive strength of approximately half its tensile strength; and

3. design is usually governed by stiffness, due to the relatively low stiffness of GFRP, which results in a overly costly design due to the required use of additional composite material in order to satisfy stiffness requirements.

In order to mitigate the aforementioned problems, concrete was chosen for use in the compression zone of the section because of concrete's excellent compressive strength and stiffness to cost ratio. The use of concrete in the compression zone allowed for a reduction in the amount of composite material needed, thereby providing significant reductions in material costs for the system. To minimize fabrication costs, the upper flange of the GFRP cross section acted as formwork for casting the concrete as shown in Figure 2.7. A thin layer of unidirectional CFRP was bonded to the section's tensile flange in order to enhance the section's rigidity because CFRP

possesses a higher stiffness than GFRP. In addition, the lower strain-to-failure of CFRP as compared GFRP provided a warning mechanism prior to ultimate collapse of the system (pseudo-ductility).

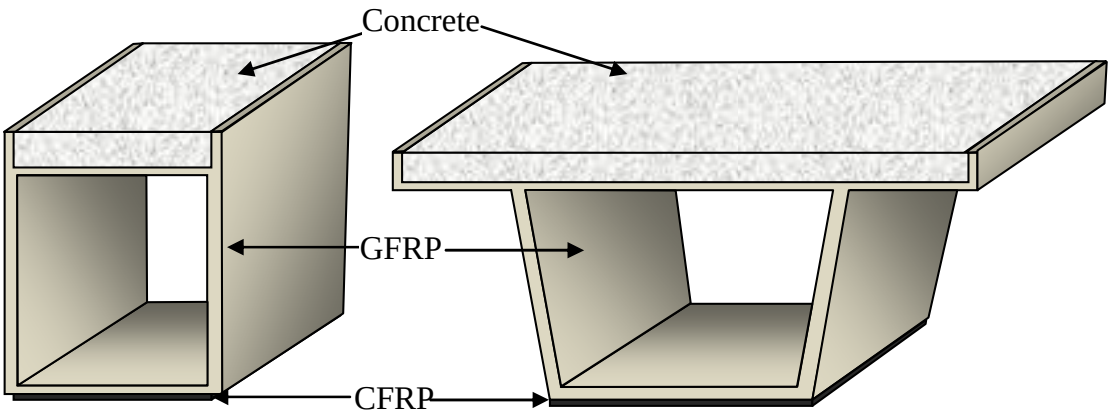

Figure 2.7 FRP box beam with concrete in compression zone (after [100])

A total of seven full sized filament wound GFRP box beams of the type shown in Figure 2.7 with dimensions of 180 mm (7.3 in) by 300 mm (12.2 in) and a span length 3 meters (10 ft) were tested in three point bending, with three beams tested for short term performance and the other four beams tested to establish long term characteristics. The first beam, which had no shear connectors between the concrete and the GFRP beam, failed due to fracture of the CFRP followed by GFRP-concrete interface debonding. An examination of the fractured surfaces suggested the lower bond strength was partially attributed to poor surface preparation in which silane, a component used during the composite manufacturing process, was not properly removed from the surface of the composite. Subsequent beams that used shear connectors to increase the bond strength showed the anticipated pseudo-ductile failure

behavior of CFRP fracture followed by concrete crushing at a higher load [100]. Results of creep and fatigue testing also provided good agreement with analytical predictions.

Further research related to FRP box beams with a thin concrete top layer was reported by Canning *et al*. [105] and Hulatt *et al*. [106]. Canning *et al*. examined the effectiveness of different techniques used to develop shear transfer between the top layer of concrete and the FRP box beam. Experimental results from flexural testing of six beams with 1.5 m (5 ft) spans indicated that the use of an adhesive applied directly prior to concrete casting was the most practical of the techniques outlined that still achieved a high level of composite action. Hulatt *et al*. experimentally tested nine vacuum bagged GFRP box beams with concrete in the compression zone and CFRP in the tension zone under both static and fatigue four-point bending. The beams were stiffened with composite diaphragms adhesively bonded to the inside of the beam as shown in Figure 2.8 in order to prevent buckling of the thin webs.

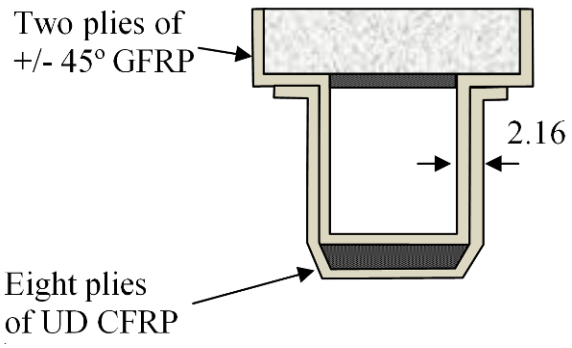

Figure 2.8 FRP box beam with concrete compression flange (after [106])

The beams behaved compositely throughout testing and the primary observed failure mode was concrete crushing. The results showed appreciable resistance to sustained and fatigue loading as well as close agreement between experimental and theoretical work [106].

A further development of the concept proposed by Descovic *et al*. was reported by Kitane *et al* in 2004 [29, 30, 107], which involves three hollow trapezoidal GFRP tubes bonded together and partially filled with concrete in the compression zone, as shown in Figure 2.9. CFRP strips were also bonded to the bottom side of the trapezoidal tubes in order to increase the stiffness of the system. Specimens with spans ranging from 2.31 m (8 ft) to 4.95 m (16 ft 10 in) were tested under multiple loading scenarios including three-point bending, negative bending, eccentric positive flexure and shear dominated loading.

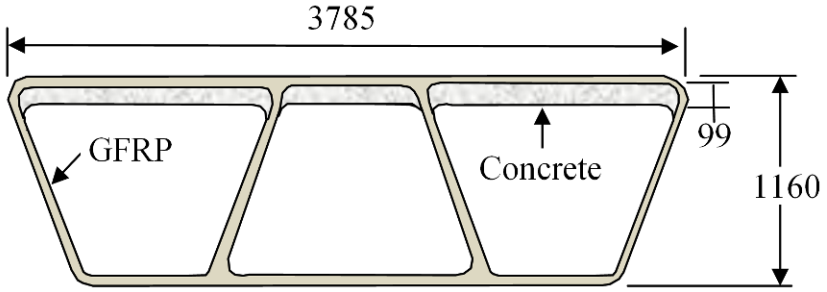

Figure 2.9 Hollow trapezoidal tubes partially filled with concrete (after [108])

The stable structural response of the system under different loading cases showed the feasibility of the system and matched closely with analytical predictions. The researchers had proposed a 6.5 m (22 ft 1 in) long, 4.06 m (13 ft 10 in) wide prototype bridge system which was designed as a simply supported steel girder bridge

with the examined hybrid FRP-concrete deck system. In 2008, Alnahhal *et al*. reported on the structural response of a 3/4 scale version of the FRP-concrete deck on steel girders specimen, which was tested under seven different. loading conditions [109]. The system satisfied the AASHTO live load deflection limits and the hybrid deck and steel girders were observed exhibit a partially composite action under service loading conditions.

In 2008, Honickman experimentally and analytically examined the performance of GFRP box sections made of trapezoidal GFRP plates connected to flat GFRP sheets with concrete poured on top [79]. A total of eight 3.10 m (10 ft 5 in) long specimens were tested in four point bending under either positive or negative flexure and the results were compared to conventional reinforced concrete slabs. The three variables for the treatment of the cavity between the GFRP trapezoidal plate and top GFRP flat sheet were partially filled with concrete such that a void was cast in the tension region of the concrete, completely filled with concrete, or not filled with any concrete as shown in Figure 2.10. All specimens had a thin steel mesh and a 610 mm thick concrete layer cast on top of the concrete upper plate as well as concrete diaphragms in the end regions to allow for loading in negative bending.

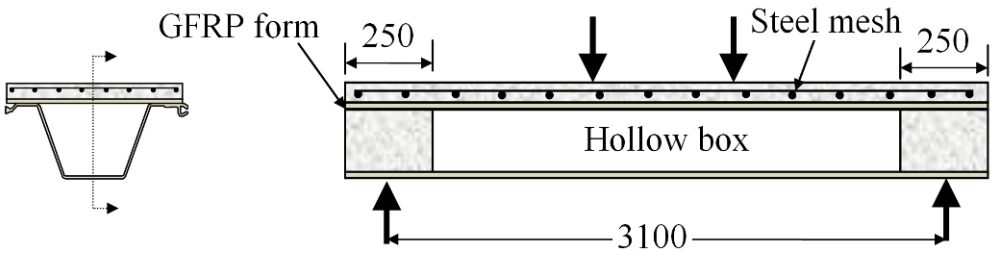

Figure 2.10 Corrugated GFRP SIP formwork acting as reinforcement for a concrete beam (after [79])

The all-GFRP box section with the concrete slab showed the best performance with a significantly higher strength as compared to any other specimen and a reduction in weight of 50% and 65% relative to the partially concrete filled and completely filled specimens, respectively. The flexural strength for the specimens loaded in positive bending was 45% to 90% higher than in negative bending, depending on the cross-sectional configuration. Different bond mechanisms were also examined and the wet adhesive bonding of fresh concrete to the GFRP plate was preferred in terms of structural performance as well as ease and speed of fabrication, however specimens which incorporated headed studs in conjunction with adhesive bonding were able to achieve a mode of flexural failure with concrete crushing rather than the debonding failure observed in the other specimens.

2.2.3.3 FRP Panels with Rectangular Stiffeners

In 2000, pultruded GFRP panels were installed as SIP structural formwork for one and a half spans of the five span Salem Avenue bridge deck replacement project in Dayton, Ohio [110-113]. The three lane, 207 m (704 ft) long, bridge used four different FRP deck systems which were supported on steel girders spaced at 2.64 m (8 ft 8 in) on center. One of the deck systems, shown in Figure 2.11, consisted of a 216 mm (8.5 in) thick layer of concrete cast on top of a mat of GFRP rebar for the top layer of reinforcement and pultruded planks with 76 mm (3 in) high tubular stiffeners as the formwork and lower level of reinforcement for the deck. The other three FRP deck systems were made entirely out of GFRP and were not filled with concrete. The

performance of the deck systems was field tested over a two year period using controlled truck loads as well as modal tests and results were compared to an adjacent companion reinforced concrete bridge. Throughout the monitoring period, the structural formwork system exhibited composite action with the cast-in-place concrete deck and performed better than the other GFRP deck systems in terms of impact factors, thermal effects and system stiffness.

Figure 2.11 Cross section of hybrid FRP panel-concrete bridge deck system with SIP formwork and tubular stiffeners used in the Salem Avenue Bridge [113]

The performance of the FRP structural formwork system used in the Salem Avenue Bridge was also experimentally evaluated by Harik *et al*. using static loading of single and double span deck slabs with different lengths and depths [114, 115]. The single and double span panels satisfied serviceability and strength criteria specified by the Ohio Department of Transportation for consideration in highway bridge construction. A combined flexure-shear failure mode and debonding of the FRP tubular sections from the concrete was observed for the hybrid FRP/concrete bridge deck panels at failure loads between 3.0 and 3.8 times the service loads. Structural performance was also evaluated under fatigue loading of 10 million total cycles per deck at extreme temperatures of -30ºC (-22ºF) and 50°C by Dutta [116] and Lopez-

Anido *et al*. [70]. The hybrid GFRP-concrete system performed favorably in static and fatigue tests as compared to the all-GFRP decks, and exhibited comparable performance to the reinforced concrete bridge deck that was tested for comparison. The exposure of the deck systems to extreme temperatures was observed to cause a larger effect on performance as compared to the number of applied load cycles.

Further experimental investigations of deck systems using the FRP structural formwork panels installed in the Salem Avenue Bridge were presented by Dieter *et al*. in 2002 [59]. The deck system investigated by Dieter *et al*., which is illustrated in Figure 2.12, consists of 203 mm (8 in) thick concrete deck with a pultruded GFRP bi-directional grid for the top reinforcement which was developed by Bank *et al*. in 1992 [117] as well as pultruded FRP panels with tubular stiffeners and gravel bonded to the horizontal surfaces. Eight 0.91 m (36 in) wide beams with span lengths ranging from 2.44 m (8 ft) to 2.59 m (8 ft 6 in) and three 2.74 m (9 ft) wide deck panels with span lengths of 2.44 m (8 ft) and 3.51 m (11 ft 6 in) were tested in either positive or negative flexure under static and fatigue loading.

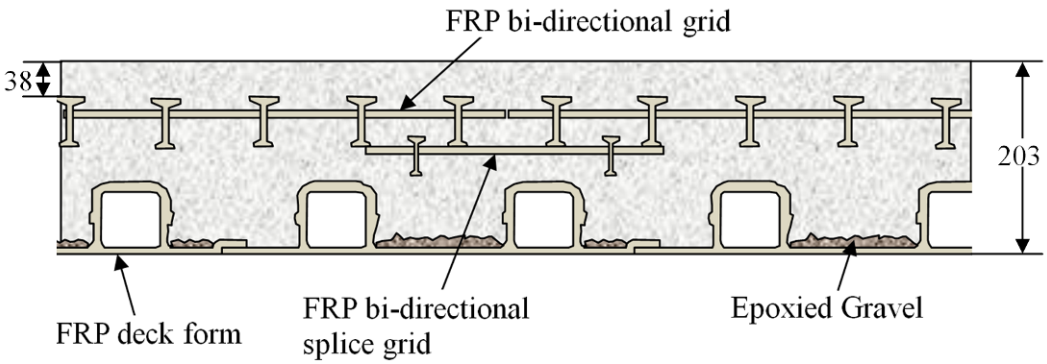

Figure 2.12 Hybrid system used in US-151/ Hwy 26 Bridge consisting of pultruded FRP structural form with aggregate bonded surface and tubular stiffners as well as FRP grid for top layer of reinforcement (after [67])

Detailing modifications were made to later test specimens, based on observations from testing the first three deck panels, in which bidirectional FRP grids were placed above the connections between panels in order to reduce longitudinal cracking above the joints between panels and to improve composite action between the FRP structural formwork panels and the surrounding concrete [58]. Punching shear failure was observed in most of the deck test specimens and Dieter recommended predicting shear capacity using the ACI 318 Equation 11-35 with the addition of a reduction coefficient, A_g, which takes into account the level of aggregate bonded to the top surface of the FRP panel [118]. The recommended modified version of the ACI shear capacity equation is given below:

$$V_c = A_g \cdot 4 \cdot \sqrt{f_c'} \cdot b_o \cdot d \qquad 2.1$$

where

A_g = reduction coefficient accounts for level of aggregate coverage on top surface of FRP deck form
= 0.60 for partial coverage
= 1.0 for aggregate bonded to all horizontal surfaces.

f_c' = specified compressive strength of concrete at 28 days,

b_o = critical perimeter section of the rectangular loaded area,

d = distance from the extreme compression fiber to tensile reinforcement,

In 2003, a new bridge on US Highway 151 in Waupun, Wisconsin was constructed using this bridge deck system. The two-span bridge, with equal spans of 32.7 m (107 ft), was built using the same bridge deck system design examined by Dieter *et al*. supported on five prestressed concrete girders spaced at 2.65 m (8 ft 8 in) on center. Load testing performed on the completed bridge indicated stress levels in the FRP were within allowable limits [40].

Recently, a new stay-in-place structural formwork panel system using rectangular stiffeners was developed by Cheng *et al.* [119]. The structural formwork consists of a bottom plate with foam filled rectangular stiffeners spaced 305 mm (12 in). All surfaces of the panels are treated with a rough sand coating to increase the level of mechanical interaction between the concrete and the FRP panel. Treatment of the entire surface with a sand interface is in contrast with many of the other systems discussed, which provided enhanced bond mechanisms only on the horizontal surfaces of the panels [65, 69, 71, 73, 97-99, 102, 105]. In addition, the presence of interfacial shear ribs between each stiffener spaced at 152 mm (6 in) on center, as shown in Figure 2.13, further improved the mechanical interlock between the cast-in-place concrete and the FRP panel. Parameters such as the composite layup, the position of the shear ribs, and the geometry and spacing of the stiffeners were optimized through experimental and analytical investigations [120].

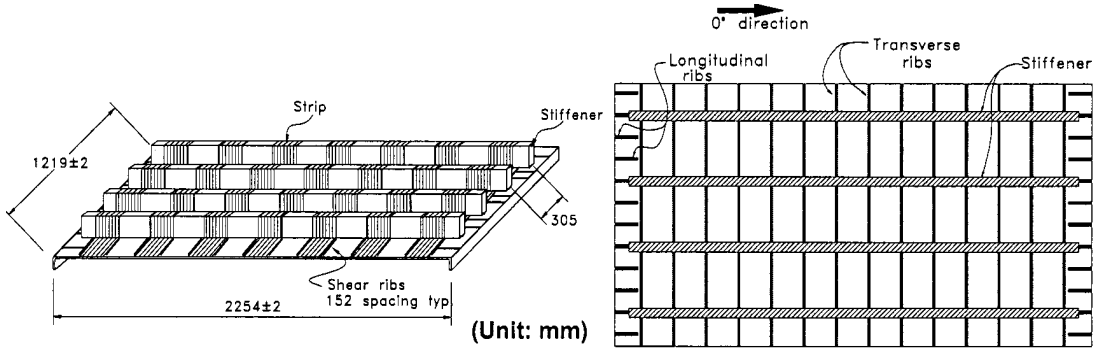

Figure 2.13 Steel-free hybrid FRP-concrete bridge with FRP tubular girders [119]

The structural formwork panels were developed as part of a steel-free hybrid FRP-concrete bridge which consists of a polypropylene fiber concrete mix which is

cast on top of the FRP structural formwork panels. The panels snap into grooves on top of hollow FRP tubular girders and a carbon fiber mesh is place above the negative moment regions, as shown in Figure 2.14. Satisfactory performance was observed for the 12 concrete slab tests that were performed to characterized component and system level flexural, shear, and fatigue response [121]. A simplified design procedure and design guidelines are presented [72].

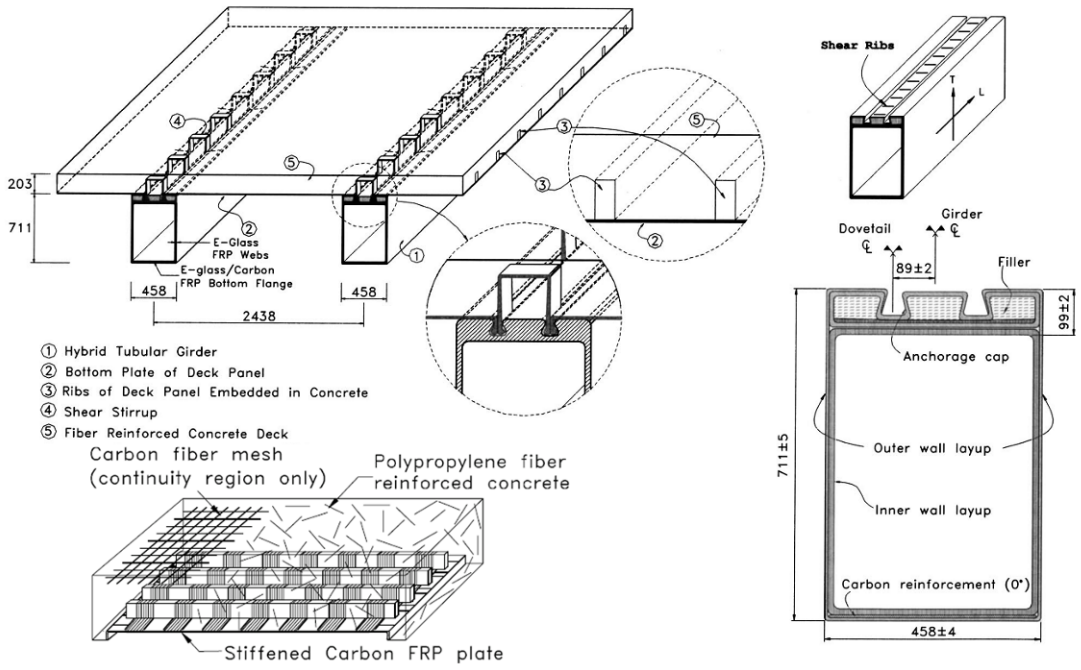

Figure 2.14 Steel-free hybrid FRP-concrete bridge with FRP tubular girders [119]

Bridges that have been constructed with deck systems containing FRP stay-in-place structural formwork for bridge decks are summarized in Table 2.1.

Table 2.1 Representative bridge systems constructed using FRP structural SIP formwork for bridge decks

BRIDGE NAME	YEAR	VENUE	GENERAL DESCRIPTION
Steel-Free Hybrid FRP-Concrete Bridge	2000 [119, 120]	University of California, San Diego	A slab-on-girder system for short span bridges with cast-in-place steel-free polypropylene fiber mixed concrete slab reinforced by CFRP deck panels and FRP box girders spaced at 2.44 m (8 ft 4 in) on center.
Salem Avenue Bridge (MOT- 49)	2001 [110-113]	Dayton, Ohio	A three lane, five- span 207 m (704 ft) long bridge with four different types of FRP decks installed on top of steel girders. One of the FRP deck systems consisted of a mat of GFRP rebar for top reinforcement and pultruded FRP panels with rectangular stiffeners that acted as both the formwork and bottom layer of reinforcement.
US-151/ Hwy 26 Bridge	2003 [59]	Waupun, Wisconsin	A two lane bridge, with two equal spans 34.7 m (107 ft) long, that consists of a FRP bi-directional grid, the same type of FRP SIP structural formwork panels used in the Salem Avenue Bridge, and a 203 mm (8 in) thick concrete slab. The deck system is supported on prestressed concrete girders spaced 2.65 m (8 ft 8 in) o.c.
US Hwy 12 Bridge (Structure B-27-150)	2008 [65, 66]	Black River Falls, Wisconsin	A two lane 30 m (102 ft) span bridge consisting of reinforcement free concrete deck (except for guardrail attachments) with aggregate-coated FRP panel with T-standups as SIP formwork and secondary reinforcement that spans between closely spaced bulb-Tee girders.

2.3 TYPICAL REPAIR METHODS FOR REINFORCED CONCRETE BRIDGE DECKS

Damaged reinforced concrete bridge decks are repaired using different methods depending a variety of factors such as the type of damage which occurred, the availability, cost, structural compatibility and anticipated life of different repair materials, the environmental conditions near the repair site and availability of qualified contractors in the area [10, 122]. Chapter 5 describes the repair and retesting of a test specimen in which damage consisted of cracking of the deck concrete above the FRP panels and separation at the interface between the concrete and composite panels. Therefore, techniques for repairing cracked and damaged concrete are of primary concern.

For relatively small areas of damage which only extend partially through the depth of the slab, surface patching using cement-based materials or resin-based materials can be used [123]. These materials include cement-based mortar or concrete, non-shrink quick-setting mortar, epoxy mortar, cement-based or resin-based polymer concrete, and pneumatically applied mortar [122]. The boundaries of the removal region in the damaged concrete are typically marked by saw cuts and the unsound concrete is removed to an appropriate depth using either jack hammers or water jets. After the reinforcing steel is cleaned to the bare metal and reinforcement with significant deterioration or other forms of damage are replaced, the surface patch is installed and allowed to cure prior to reopening of the bridge. Patching has advantages in terms of cost effectiveness and practicality, however it is generally considered a temporary repair because patching can cause surrounding steel

reinforcement to corrode more quickly due to the differences in chloride ion content between the patch installation and the adjacent concrete [124].

If a concrete deck is still structurally sound but a significant portion of the deck surface has deteriorated from heavy in-service traffic, freeze thaw cycles or other exposures, the deck can be resurfaced with an overlay. A deck overlay provides a uniform layer of repair material over an extensive area or the entire deck and can also serve as a wearing agent and moisture barrier. Common material choices for overlays include low slump high density concrete, latex modified concrete, polymer concrete, and monolithic resinous toppings [125]. The overlay either rely on full composite action with the existing bridge deck, which is known as a bonded overlay, or can be separated from the existing concrete by a flexible interlayer, typically hot-mix asphalt, to create an unbonded overlay. An unbonded overlay can move independently from the existing concrete thereby preventing reflective cracking, which is caused by peaks in strains over cracks from the existing concrete deck. The thickness of the overlay is 25 to 75 mm (1 to 3 in) for a fully bonded overlay and at least 75 mm (3 in) for an unbonded overly, with the thickness of the overlay based in part on the structures ability to tolerate the increased dead weight and slab elevation [125].

For cracks in the concrete caused by overloading from an extreme event in which no further movement is expected, such as those observed in the post-failure test specimen described in Chapter 5, the cracks may be filled in order to bond together the concrete surfaces and restore the structural integrity of the system. Cracks larger than approximately 1mm (0.04 in) can be filled with cement grout, whereas low viscosity liquid polymers can be used for smaller cracks down to a width of approximately 0.1

mm [124]. Cracks filled can be filled by ponding using low viscosity polymer resin systems under gravity, or through the more common technique of applying positive or negative pressure to assist the resin to flow into the crack. The resin is injected into a crack though an injection port which is drilled into the surface of the concrete and the resin spreads out though the concrete [7].

2.4 NSM FRP SYSTEMS FOR FLEXURAL STRENGTHENING

2.4.1 NSM versus Externally Bonded FRP Reinforcement

The use of FRP composites for flexural strengthening of existing concrete structures was developed in Europe and Japan in the 1980s as an alternative to steel plate bonding [126]. Externally bonded FRP systems for flexural strengthening include but are not limited to wet layup processes with installation on site, resin impregnation of fabrics and strips, bonding of pre-cured FRP profiles to a structure, resin infusion of dry fabric after installation of the FRP, and use of prepreg sheets [23, 127]. Application of externally bonded prefabricated strips and externally bonded on site impregnated fabric laminates for the rehabilitation of bridge deck slabs are shown in Figure 2.15 (a) and (b) respectively [128].

FRP reinforcement can also be adhesively bonded into precut grooves made in the cover region of the concrete surface, which is referred to as “embedded reinforcement” or “near-surface mounted reinforcement” [129] rather than bonded to the surface. Near surface mounted FRP systems only have been actively researched during the past decade, although the general use of the strategy can be traced to the use of steel rebar in surface cut grooves in Europe in the 1950’s [130].

a) Pultruded strips b) Wet layup fabric laminates

Figure 2.15 Rehabilitation of bridge deck slabs using externally bonded FRP reinforcement [128]

The use of near-surface-mounted (NSM) FRP reinforcement for rehabilitation has a number of advantages over the more common externally bonded FRP reinforcement. These advantages include the potential for reduced site installation work, since the creation of grooves for the FRP decreases the labor required for surface preparation, the reduced likelihood of debonding failures from the concrete surface, and improved protection from mechanical damage provided by recess of the NSM reinforcement into the concrete surface [129, 131, 132]. Also, prestressing of FRP reinforcement in order to further utilize the capacity of the FRP material has been shown to be more effective in NSM applications than externally bonded systems [133]. The use of near surface mounted FRP rehabilitation techniques provide particular advantages for flexural strengthening of the negative moment region of reinforced concrete slabs and decks [129]. In these applications, the top surface of the deck may be subject to harsh environmental and mechanical conditions, which would require the FRP reinforcement to be surrounded by a protective cover. An appropriate

bond and protection of the FRP reinforcement would be more difficult to achieve using externally bonded strips whereas the near surface mounted reinforcement is already embedded and therefore not exposed to these influences [134].

2.4.2 Types of NSM Reinforcement

FRP reinforcement used for near-surface-mounted applications is typically manufactured using the pultrusion processes and can be manufactured in a wide variety of shapes including round, oval, square and rectangular bars, as well as strips with varying aspect ratios [131].

Carbon fiber reinforced polymer composite NSM reinforcement is the primary type of FRP material used to rehabilitate concrete structures because of the higher tensile strength and tensile elastic modulus of carbon over glass or aramid [135]. Also, the inertness of the carbon fibers reduces the effect of concrete based alkalinity on the FRP itself, however the alkalinity still affects the fiber-matrix bond and the matrix itself. The superior tensile properties of CFRP allow for a smaller cross-sectional area NSM CFRP bar to be used over a GFRP or AFRP bar with the same tensile capacity, which has additional constructability benefits by allowing a shallower groove to be used, thereby reducing the risk of interfering with the internal steel reinforcement [131].

While the initial use of NSM was with circular bars, the transition to rectangular strips was predicated on the desire to achieve better bonding of the reinforcement [131]. It has been shown that all other factors being equal, near surface mounted strips have higher average bond strengths than circular bars because the development of a three-dimensional distribution of bond stresses into the surrounding

concrete [136, 137]. Further, in the case of round bars used as near surface mounted reinforcement, forces due to the radial stresses can induce tensile forces that can force the bar out of the groove, resulting in bond splitting or failure. Also note that since strips have significantly larger ratios of perimeter to cross-sectional area than square or circular rods, bond stresses are lower which allows increased utilization of the capacity of the NSM strips [137]. While the use of NSM reinforcement for flexural strengthening is extremely simple, the use of square bars and circular rods requires larger and deeper grooves than flat strips placed horizontally in order to achieve the same efficiency.

2.4.3 NSM Failure Modes and Design Assumptions

The distinct failure modes observed for experimentally investigated concrete structures flexurally strengthened with NSM reinforcement are concrete crushing, FRP rupture, cover splitting, and bond failure within the concrete adjacent to the adhesive layer, at the interface between the concrete and the adhesive, within the adhesive itself, or at the interface between the adhesive and the FRP [126, 129, 134, 138]. A brief description and explanation of each failure mode as well as relevant design assumptions are provided below.

2.4.3.1 Concrete crushing

Crushing of the concrete in compression is occurs then the compressive strain in the concrete reaches its crushing strain. A system which exhibits this failure mode

during flexural loading is considered to be over-reinforced. For design purposes, crushing of the concrete is assumed to occur at a strain value of $\varepsilon_{cu} = 0.003$.

2.4.3.2 FRP rupture

Rupture of the FRP reinforcement occurs then the tensile forces in the FRP reinforcement exceed the tensile strength of the FRP. Because FRP materials loaded in tension are observed exhibit linear elastic behavior until tensile failure, FRP rupture is usually a catastrophic failure mode for the structural element strengthened with FRP. For design purposes, FRP rupture is assumed to assumed to occur if the tensile strain in the FRP reaches its design rupture strain, $\varepsilon_f = \varepsilon_{fu}$. In order for FRP rupture to occur, the system must have the necessary bond strength to delay debonding failures. While tensile rupture has rarely been observed in NSMR systems which are not prestressed [134], this failure mode is considerably more likely to occur in systems which use NSM strips rather than NSM bars or externally bonded FRP (for systems where all other factors are equal) because the geometry of the NSM strips provides more efficient bonding to the concrete [138].

2.4.3.3 Bond failures

Debonding occurs when loss of composite action is exhibited across an interface. Figure 2.16 illustrates the four different bond failure modes that can occur. Splitting in the concrete adjacent to the concrete-composite interface is a result of the high tensile stresses that are transferred into the concrete. This failure mode is more

common when the adhesive strength is much higher than the concrete strength [139]. A failure at the interface between the concrete and the composite has been reported as critical for pre-cast grooves due to their even surface [140]. Failure within the adhesive, known as cohesive failure, can be avoided through the selection of an appropriate adhesive system. A debond failure between the adhesive and the FRP reinforcement can be critical for reinforcement with smooth or lightly sand-blasted surfaces that provide insufficient surface deformation for mechanical interlock between the reinforcement and the adhesive [137].

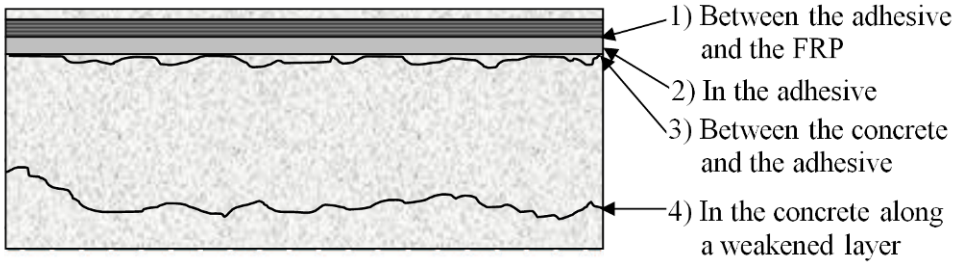

Figure 2.16 Bond failure modes for FRP strips (after [134])

2.4.3.4 Cover Splitting

Splitting of the adhesive cover for the NSMR, which is often accompanied by spalling of the surrounding concrete, is referred to as cover splitting [129]. Cover splitting is more commonly observed for NSM bars than for strips due to the radial distribution of bond stresses that load the concrete cover. Conversely, the stress components for NSM strips act parallels to the concrete surface, so splitting failure is less likely to occur [134]. NSMR close to the edge of a concrete member can cause

edge splitting failure which can be critical, however this failure mode can be avoided by keeping a minimum distance from the edge members close to the edge [136, 137].

2.4.4 Prior Use

While NSM FRP has been used successfully for flexural strengthening of concrete beams [46, 137, 141-144] and the flexural strengthening concrete slabs in the positive moment regions, there is still limited research on NSM FRP applications to increase the flexural capacity of concrete slabs in the negative moment regions. A summary of research on flexural strengthening of reinforced concrete slabs with FRP is presented.

In 1998, Warren reported on the use of NSM FRP bars and strips for increasing the flexural capacity in negative moment regions of a bridge deck slab [145]. NSM FRP bars were applied to both reinforced concrete and prestressed concrete slabs and the NSM FRP bars were used in both the longitudinal and transverse directions on the slabs. In 2002, NSM FRP bars were used to strengthen the negative moment regions of a reinforced concrete parking garage in which the steel reinforcement had corroded [146]. Alkhrdaji et al. reported on the structural response of a decommissioned three span reinforced concrete bridge deck, in which one slab was strengthened in flexure using NSM bars [147]. The NSM strengthened slab failed in FRP rupture, whereas the other slab which was strengthened using externally bonded strips failed by a combination of FRP rupture and debonding of the sheets. The NSM strengthened slab was 27% stronger than the unstrengthened control slab, compared to a 17% strength increase over the control slab for the externally bonded FRP slab.

Field studies and laboratory work have shown that NSM FRP strengthening systems for reinforced concrete structures have significant advantages over externally bonded FRP strengthening systems. These advantages include enhanced ability to utilize the FRP prior to debond, less surface preparation required prior to strengthening, and more efficient and effective material usage. The application of NSM FRP strengthening to negative moment regions of decks has particular advantages in terms of ease of construction and better protection for the FRP reinforcement from the external environment. Research on NSM FRP also clearly documents the advantages of NSM FRP strips over NSM FRP circular or rectangular bars. The smaller grooves necessary to mount a strip placed horizontally reduces concerns about damaging existing reinforcement during groove cutting and accelerates construction time. The enhanced surface area to volume allows for better utilization of the FRP reinforcement, which makes FRP rupture at higher loads more likely than debonding at lower loads. The benefits from NSM FRP strips have been recognized by the research community, as most recent research has shifted away from NSM FRP circular and rectangular bars to examination of NSM FRP strips.

2.4.5 Available Specifications for Flexural Strengthening using NSM FRP

The 2nd edition of Concrete Society Technical Report No. 55 discusses a variety of applications for strengthening with NSM reinforcement in Section 6.4 and recommends that for aspects other than FRP curtailment, design of flexural strengthening with NSM reinforcement (NSMR) should be done using the design methods described for surface mounted reinforcement, with the allowance made to

adjust the location of the reinforcement from the surface of the section to within the section such that the strains in the FRP are lowered appropriately [139]. Approaches for anchorage design are detailed and design suggestions for reducing the likelihood of different common modes of failure for NSMR are described.

The previous edition of the ACI 440.2R code, ACI 440.2R-02, made no specific mention of strengthening using NSMR, however contained extensive information pertaining to surface mounted reinforcement [148]. The most recent edition of the ACI 440.2R code, ACI 440.2R-08, has added sections pertaining to near surface mounted reinforcement. The new guidelines recommend that flexural strengthening with NSM FRP systems be designed using the same equations as externally bonded FRP systems, with different procedures provided for the determination of the strain level at which debonding may occur (Section 10.1.1), calculation of the required bar development length (Section 13.3), and detailing of the bond parameters between the bars and the concrete (Section 13.3) [126].

The 2nd edition of the Canadian Highway Bridge Design Code (CHBDC) for fiber-reinforced structures includes strengthening with NSMR as part of its discussion on flexural and axial rehabilitation (Section 16.11.2) and gives resistance factors for NSMR made from pultruded carbon, glass and aramid (Section 16.5.3) [149]. For structures with a concrete cover less than 20 mm (0.79 in), NSMR is not permitted [150]. This code determines NSMR anchorage lengths for flexure using the same calculation provided for internal FRP bars (Sections 16.11.2.4.4 and 16.8.4.1) and provides only a general description of failure modes for FRP strengthened systems, without mention of NSMR specific modes of failure.

3 USE OF FRP PANELS AS THE STAY-IN-PLACE STRUCTURAL FORMWORK SYSTEM FOR A BOX GIRDER BRIDGE DECK

3.1 INTRODUCTION

This chapter presents the assessment and validation of a hybrid fiber reinforced polymer (FRP)-concrete bridge system, where prefabricated composite panels act as both the formwork and reinforcement for the bridge deck. Experimental results from the full-scale testing of a box girder bridge test specimen with FRP stay-in-place structural formwork panels integrated into the bridge deck are discussed. The system's structural response as well as the interaction between elements under static loading is evaluated and a direct performance comparison is drawn between the hybrid FRP panel-concrete bridge deck system and a conventional steel reinforced concrete system bridge deck system. The structural aspects addressed in this chapter include overall structural response, changes in stiffness for the decks, deflection profiles, load transfer between the panels, strain development, differences in residual deflections, and progression of damage within the decks.

3.2 OVERALL GEOMETRY AND CONSTRUCTION DETAILS

The overall test specimen geometry consisted of a two-cell box girder bridge segment, with a center-to-center distance of 1830 mm (6 ft) between each of the stems and a longitudinal length of 3660 mm (12 ft) as shown in Figure 3.1. The deck slab was 178 mm (7 in) thick and included overhangs which extended 483 mm (19 in) beyond the exterior longitudinal edge girders. The bottom slab was 152 mm (6 in) and

the widths of the outer and center girders were 252 mm (10 in) and 305 mm (12 in) respectively as shown in Figure 3.2.

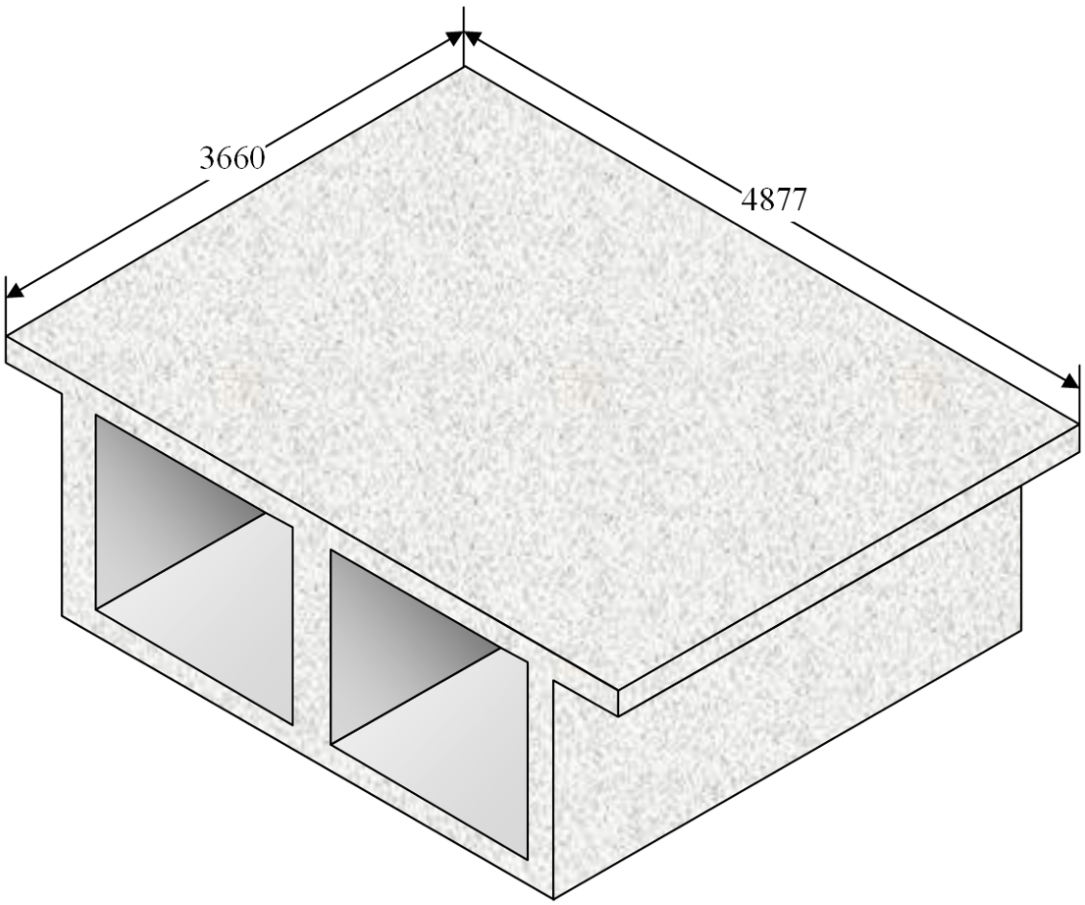

Figure 3.1 Overall representation of test specimen

There was also a continuous layer of top steel reinforcement. Traditional wooden shored formwork and steel reinforcement was used for the remainder of the specimen. This test setup allowed for a side-by-side performance comparison of the reinforced concrete deck to the prefabricated FRP panel strengthened system. All steel reinforcement used within the test specimen was designed in accordance with the AASHTO-LRFD specifications [91] and the construction practices employed

mimicked field techniques. The steel reinforcement in the deck consisted of a top and bottom layer of 15.9 mm diameter (#5) rebar with the transverse rebar spaced at 203 mm (8 in) on center and variable spacing for the longitudinal rebar in order to accommodate the location of the girder stems. The top layer of steel reinforcement was continuous across the test specimen as shown in Figure 3.3, whereas the bottom layer of steel reinforcement was curtailed completely on the composite side in the central region due to the presence of the FRP panels which served as the bottom layer of reinforcement.

The remaining steel reinforcement consisted primarily of 15.9 mm diameter (#5) rebar for the bottom slab and the stem reinforcement, with two 22.2 mm diameter (#7) rebar at the bottom of each girder web and 9.5 mm diameter (#3) rebar used for shrinkage and temperature reinforcement in the longitudinal direction of the girder webs. Grade 60 steel was used for all the steel reinforcing bars and tensile tests were performed on samples of the rebar used for construction of the test specimens. The experimentally determined average tensile strength values of the steel reinforcement are summarized in Table 3.1. Steel reinforcement detailing for the test specimen is shown in Figure 3.3 - Figure 3.5.

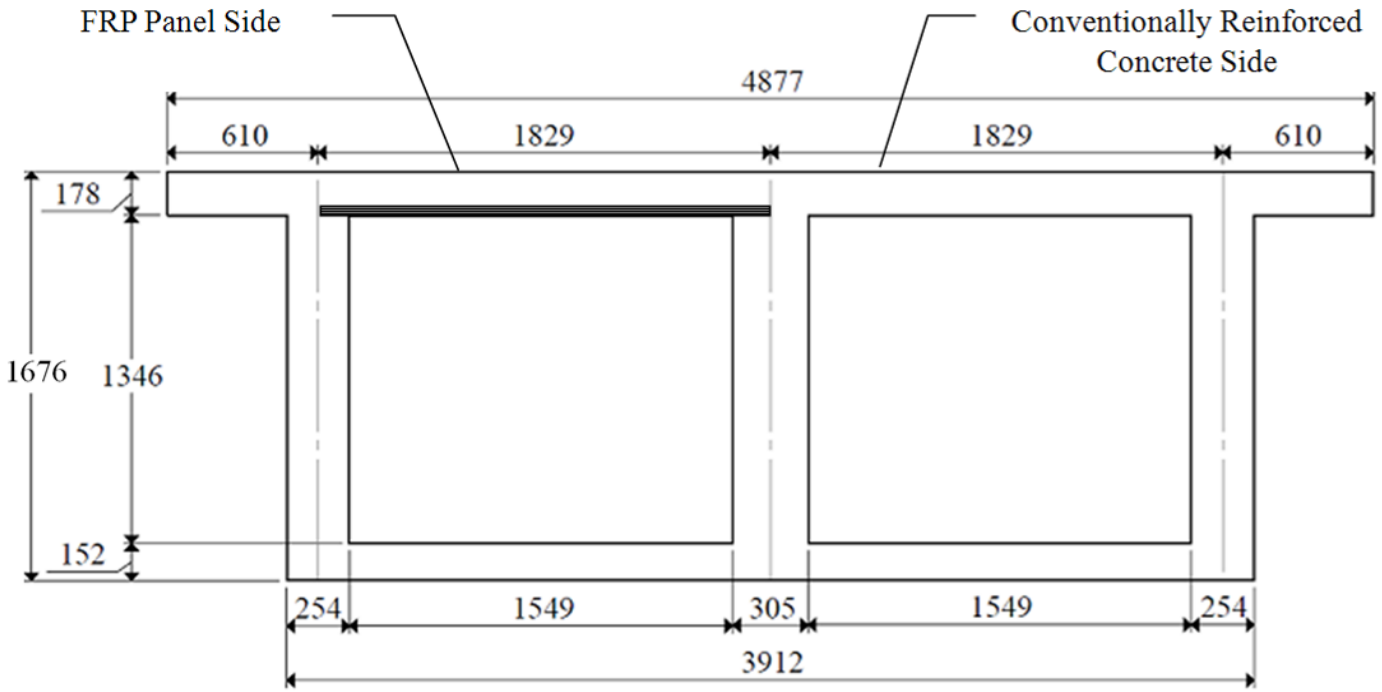

Figure 3.2 Overall test specimen dimensions- front elevation view

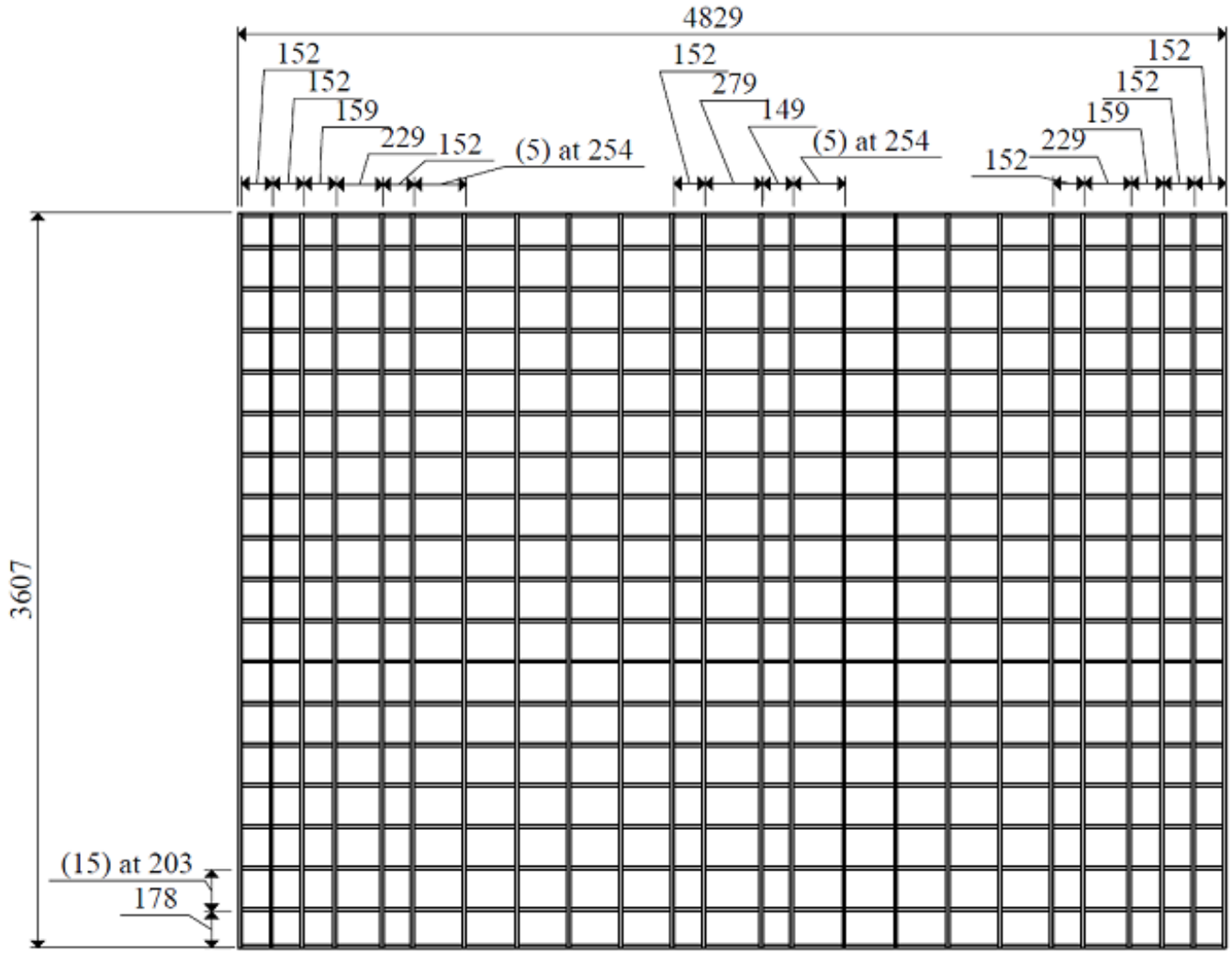

Figure 3.3 Top layer of steel reinforcement for deck slab- plan view

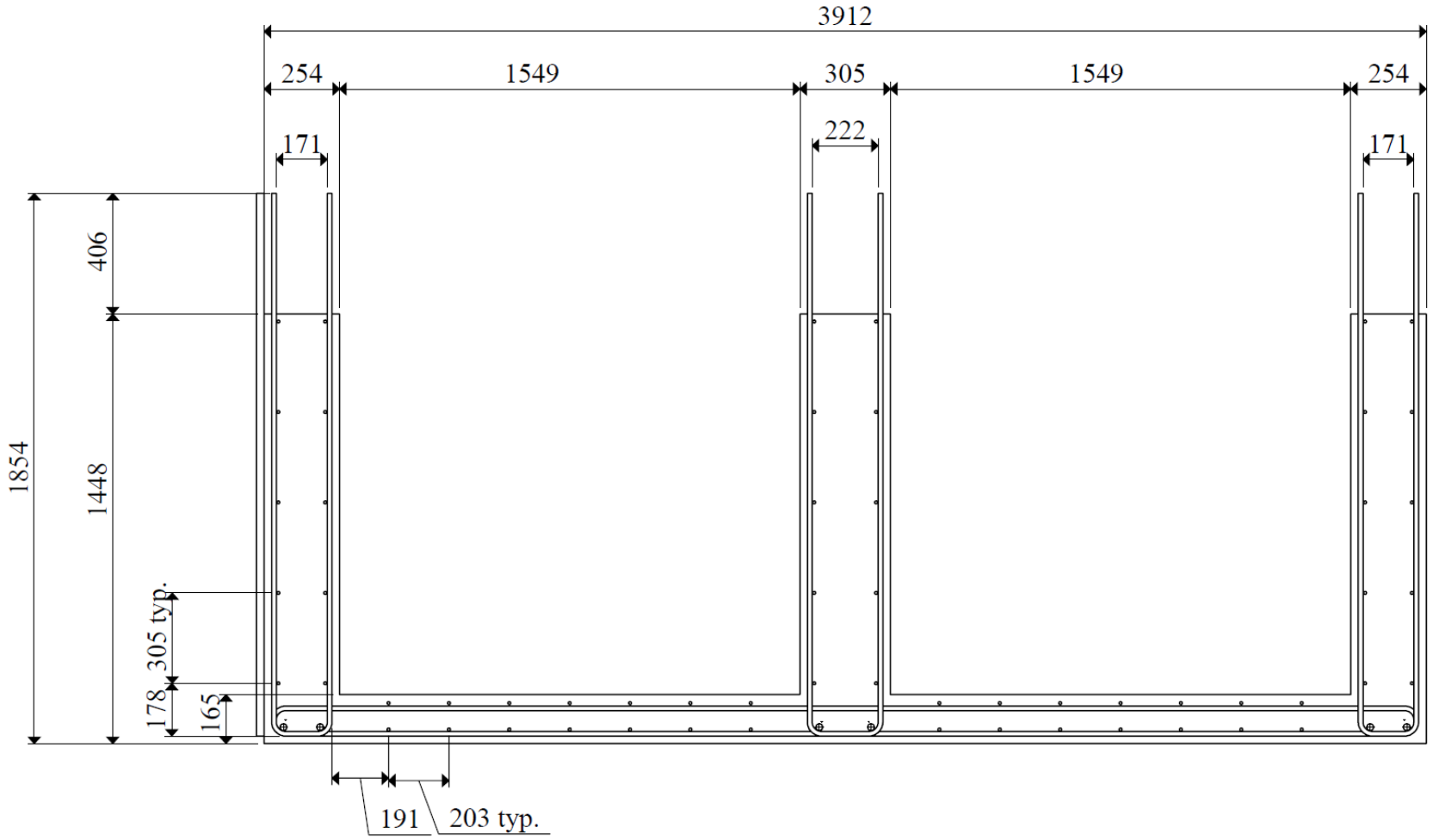

Figure 3.4 Steel reinforcement detailing in lower portion of box girder - front elevation view

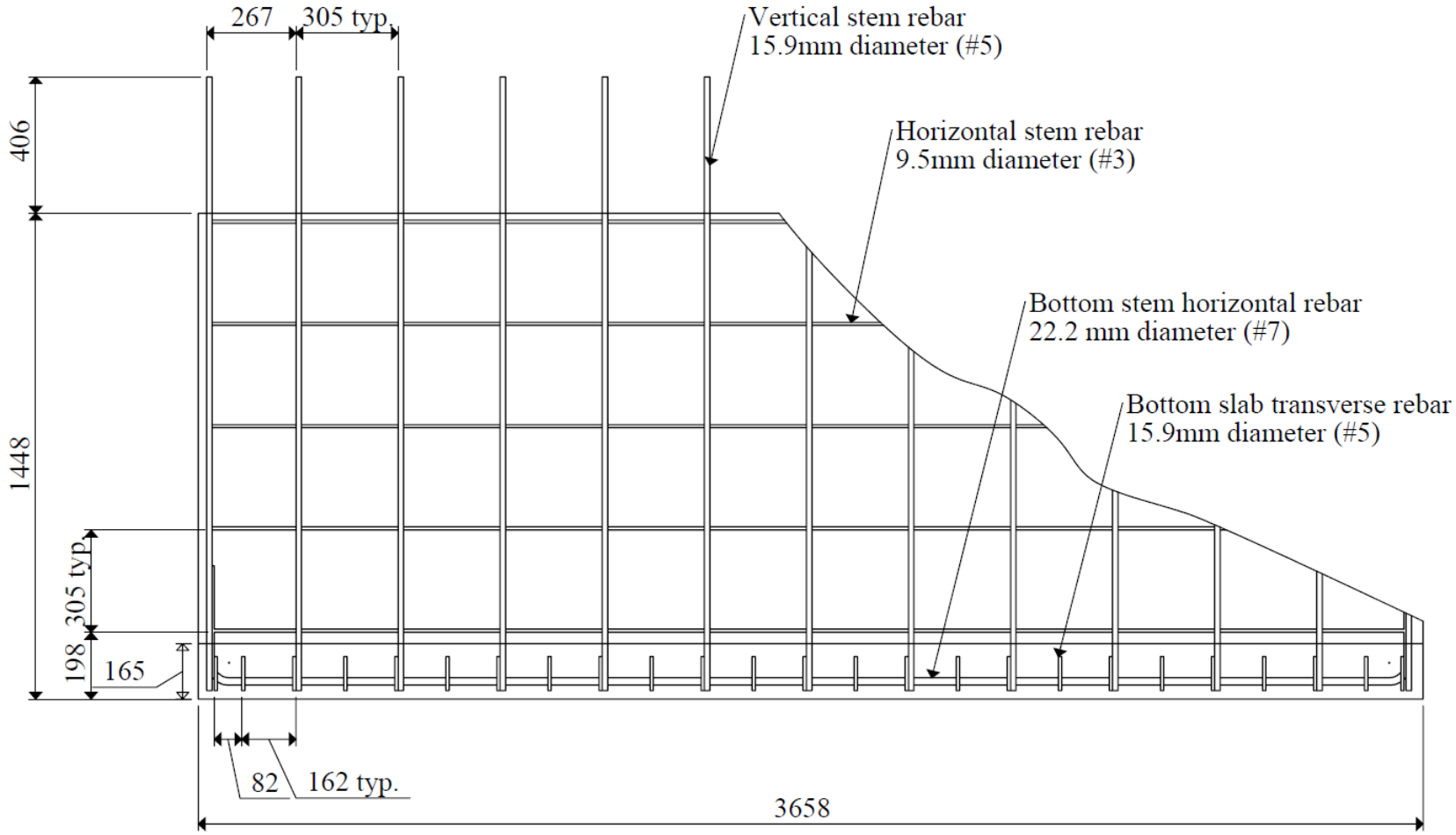

Figure 3.5 Steel reinforcement detailing in lower portion of box girder–side elevation view

The specimen was constructed in two separate concrete pours with the initial pour for the bottom slab and the lower portion of the stems and the second pour for the deck slab and the upper portion of the stems. Wooden formwork was constructed for the bottom slab and stems and the reinforcement was detailed such that a clear cover of 25 mm (1 in) was maintained throughout the specimen. The lower portion of the specimen was cast with a cement-based concrete that had a nominal design compressive strength of $f_c^{'}$ = 34.5 MPa (5 ksi) at 28 days and an average aggregate size of 127 mm (0.5 in). The specimen was cured with a moisture barrier on top of the cast concrete for 7 days prior to formwork removal as shown Figure 3.6.

Table 3.1 Performance characteristics of the Grade 60 reinforcing steel

REBAR SIZE	YIELD STRENGTH, f_y		ULTIMATE STRENGTH, f_u	
	MPa	ksi	MPa	ksi
#3	464.92	67.43	734.00	106.46
#5	429.68	62.32	703.36	102.01
#7	507.64	73.63	662.13	96.03

The strength development plots of all concrete poured for the test specimen, as obtained from periodic testing of cylinders made during construction of the specimen, are presented in Figure 3.7 and Figure 3.8 and the results are summarized in Table 3.2.

Figure 3.6 Lower portion of the box girder bridge before and after casting of concrete

Table 3.2 Performance characteristics of the concrete

DESIGNATION	LOCATION OF CONCRETE POUR	28-DAY STRENGTH		STRENGTH ON DAY OF TEST	
		MPa	ksi	MPa	ksi
1st pour-Truck# 1	Lower portion of stems	32.8	4.75	39.7	5.76
1st pour-Truck# 2	Bottom slab	29.5	4.28	35.9	5.20
2nd pour	Deck slab and upper portion of stems	32.9	4.78	34.8	5.04

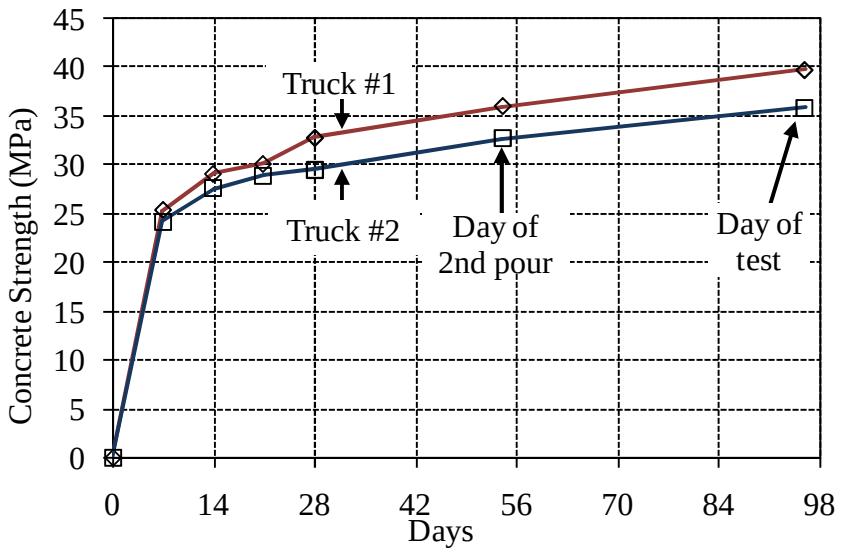

Figure 3.7 Strength development for concrete from 1st pour
(First pour consists of the bottom slab and the lower portion of the stems)

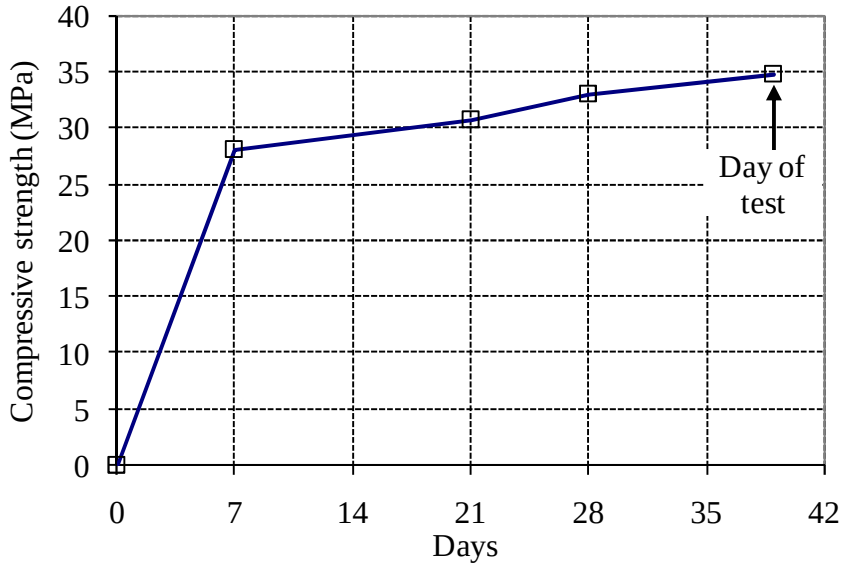

Figure 3.8 Strength development for concrete from 2nd pour (deck)

After the concrete reached 28 days of cure, the test specimen was placed on top of the support blocks used as part of the test setup and the deck was constructed in

place as shown in Figure 3.9 and Figure 3.10. Details on the construction of the deck and the installation of the FRP panels are discussed in Sections 3.3 and 3.4.

Figure 3.9 Construction of test specimen formwork for 2nd pour

Figure 3.10 Pouring of deck concrete and finishing of deck surface

3.3 FRP PANEL FEATURES

The FRP deck panels used for the test specimens were previously characterized by Cheng *et al*. [119, 120] and consist of a bottom plate that serves as the stay-in-place formwork as well as the bottom layer of reinforcement for the deck, rectangular stiffeners that span in the direction transverse to traffic loading, and small shear ribs attached to the bottom plate to increase the shear interlock with the concrete (Figure 3.11) . The bottom plate of the FRP was constructed of hybrid unidirectional carbon fiber fabric, C, and E-glass continuous strand mat, E, with a lay-up of $[C/E/C_2/E/C]_s$. Rectangular stiffeners with non-crushing lightweight foam cores to maintain the desired geometry were reinforced primarily with unidirectional carbon fiber fabric. The foam filler has a density of 0.961 kN/m^3 (0.00347 lb/in^3), a compression strength of 0.785 MPa (0.114 ksi), and Young's modulus in compression of 27.4 MPa (3.98 ksi) [120].

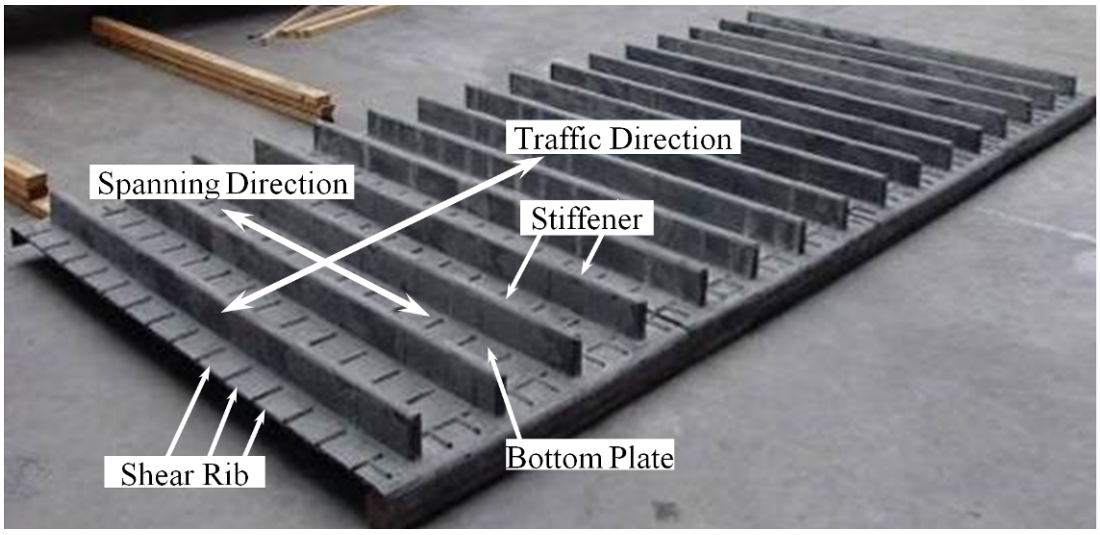

Figure 3.11 FRP deck panel system [119]

The stiffeners were bonded to the bottom plate and reinforced with additional unidirectional carbon fabric which was placed continuously over the panel in the direction perpendicular to the orientation of the stiffeners. The shear ribs were made by bonding sections of sand filled epoxy spaced at 150 mm (6 in) to the bottom panel. A sand coating was applied to the top surface of the panel in order to increase the surface roughness. Details regarding the layup and geometry of the FRP panels are shown in Figure 3.12 and Table 3.3.

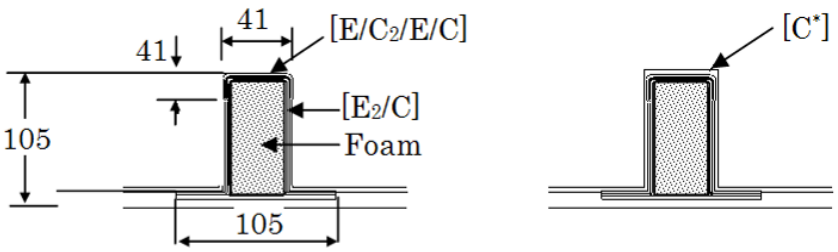

Figure 3.12 Cross-section details of the stiffeners on the deck panel (after [120])

Table 3.3 Lamina information and nomenclature [120]

Ply Name	Material	Total Areal Weight (g/m^2)	Orientation	Composition (%)
C	Carbon	305	0°	100
E	E-Glass	458	Chopped strand mat	100
C*	Carbon	197	0°/90°	50/50

The material properties of the FRP panels were previously characterized by Cheng and these results are summarized below in Table 3.4 and Table 3.5. Table 3.4 provides the experimentally determined properties of the bottom plate (Mark 4) that

were obtained from coupon tests of panel samples that which were tested following the methods prescribed by ASTM Standards [151].

Mark 2: All layers in the top flange and upper web.
Mark 3: All layers comprising the lower web.
Mark 4: All layers in the bottom flange of deck panel.
Mark 6: One layer of the strip.

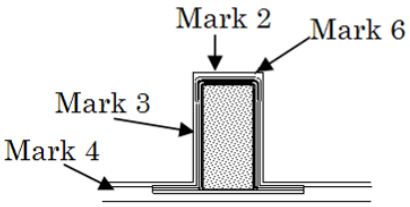

Table 3.4 Experimental mechanical properties of bottom plate (Mark 4) [119]

Direction	Property	Average	Standard Deviation
Tensile Modulus, E^T, MPa [ksi]	Longitudinal, $E_L{}^T$	60391 [8765]	1883 [273]
	Transverse, $E_T{}^T$	6861 [995]	1242 [180]
Flexural Modulus, E^F, MPa [ksi]	Longitudinal, $E_L{}^F$	20464 [2970]	2940 [427]
	Transverse, $E_T{}^F$	6302 [915]	1375 [200]
Tensile Strength, σ^T, MPa [ksi]	Longitudinal, $\sigma_L{}^T$	222.5 [32.3]	11.1 [1.61]
	Transverse, $\sigma_T{}^T$	81.5 [11.8]	25.5 [3.69]
Flexural Strength, σ^F, MPa [ksi]	Longitudinal, $\sigma_L{}^F$	337.0 [48.9]	59.2 [8.59]
	Transverse, $\sigma_T{}^F$	89.7 [13.0]	11.4 [1.65]
Interlaminar Shear Strength, τ, MPa [ksi]	Longitudinal, τ_L	27.7 [4.03]	1.52 [0.221]
	Transverse, τ_T	16.0 [2.32]	1.61 [0.234]
Density, γ, kN/m^3 [lb/in^3]		1472 [91.85]	Not available
Nominal Thickness, mm [in]		7.38 [0.291]	0.649 [0.0256]

The longitudinal direction for the bottom plate was defined as parallel with the orientation of the stiffeners as opposed to direction of traffic, which was defined as the

longitudinal direction for the overall structure. Table 3.5 shows the mechanical properties for the different deck panel components, based off of design data.

Table 3.5 Mechanical properties of deck panel components [120]

Property	Mark 2	Mark 3	Mark 4	Mark 6
Longitudinal Modulus, E_L	46818 MPa [6795 ksi]	10142 MPa [1472 ksi]	61907 MPa [8985 ksi]	116992 MPa [16980 ksi]
Transverse Modulus, E_T	7421 MPa [1077 ksi]	7104 MPa [1031 ksi]	7028 MPa [1020 ksi]	7896 MPa [1146 ksi]
In-Plane Shear Modulus, G_{LH}	2997 MPa [435 ksi]	2928 MPa [425 ksi]	2625 MPa [381 ksi]	3176 MPa [461 ksi]
In-Plane Poisson's Ratio, ν_{LH}	0.23	0.20	0.28	0.29
In-Plane Poisson's Ratio, ν_{HL}	0.04	0.14	0.03	0.02
Density, γ	15.0 kN/m^3 [0.055 lb/in^3]	14.7 kN/m^3 [0.054 lb/in^3]	14.7 kN/m^3 [0.054 lb/in^3]	15.0 kN/m^3 [0.055 lb/in^3]
Longitudinal Coefficient of Thermal Expansion	2.27×10^{-7} /°C [$1.26.\times10^{-7}$ /F]	7.97×10^{-8} /°C [4.43×10^{-8} /F]	9.95×10^{-7} /°C [5.53×10^{-7} /F]	1.68×10^{-7} /°C [9.33×10^{-8} /F]
Transverse Coefficient of Thermal Expansion	1.05×10^{-5} /°C [5.81×10^{-6} /F]	4.75×10^{-6} /°C [2.64×10^{-6} /F]	2.29×10^{-5} /°C [1.27×10^{-5} /F]	2.43×10^{-5} /°C [1.35×10^{-5} /F]
Nominal Thickness	2.41 mm [0.095 in]	1.75 mm [0.069 in]	6.30 mm [0.248 in]	0.25 mm [0.010 in]

Mark 2: All layers in the top flange and upper web.
Mark 3: All layers comprising the lower web.
Mark 4: All layers in the bottom flange of deck panel.
Mark 6: One layer of the strip.

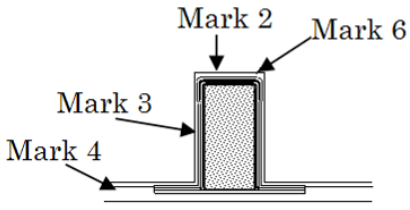

3.4 PANEL PLACEMENT AND CONNECTION DETAILING

The panels were cut to the desired length of 1830 mm (6 ft) and the cut ends were sealed with resin to provide a protective moisture barrier for the composite reinforcement. A central panel with dimensions of 1220 mm (4 ft) wide, 1830 mm (6 ft) long, and 6.3 mm (0.25 in) thick was positioned in the middle of the FRP panel side of the specimen and was bordered on both sides by narrower panels, each 610 mm (2 ft) wide as shown in Figure 3.12. Multiple panels were used side by side to check the effectiveness of load transfer between the panels.

In order to accommodate the steel reinforcement protruding vertically from the girders, the positions of the vertical rebar were measured, and corresponding 25.4 mm (1 in) holes were drilled in the FRP panels. After the FRP panels were lowered into place, the steel reinforcement from the girders was bent, as shown in Figure 3.14 (b), so that the steel reinforcement in the deck could be positioned and tied. Note in Figure 3.14 (a) that wooden shored formwork was installed for the entire deck except for the region in which the FRP panels are placed. Additional holes were drilled in the end regions of the panels so that 12.7 mm (0.5 in) diameter threaded rod could be used to hold the panels in place during the deck concrete pour. The as-built deck prior to the concrete pour is shown in Figure 3.15.

The times required for each step of construction was monitored and construction of the FRP panel bridge deck system was determined to take 60% less time than the construction of the conventional reinforced concrete bridge deck system, with approximately 25 labor hours versus 63 labor hours required for the construction of the FRP panel system and RC bridge deck system respectively.

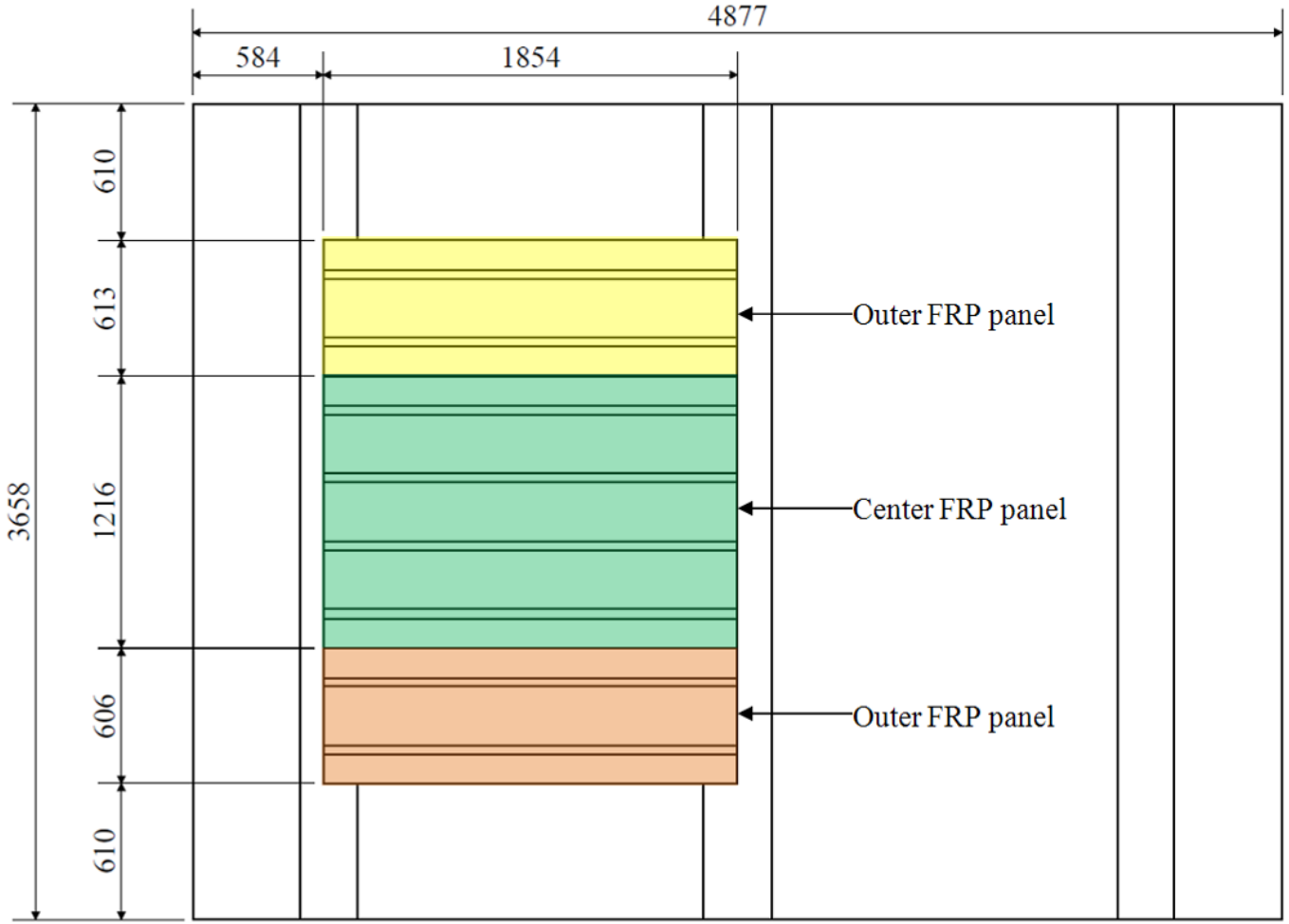

Figure 3.13 Schematic of FRP panel locations

(a) Composite side deck prior to FRP panel installation

(b) Composite side deck after FRP panel installation

Figure 3.14 FRP panel installation details

The installation and removal of the wooden formwork and metal shoring took approximately 24 labor hours, which was one labor hour less than the time required for the construction of the entire FRP panel bridge deck system. This is comparable to other researchers, who reported that the construction of a stay-in-place FRP panel structural formwork deck system was determined to be 57% faster than the construction of a comparable steel reinforced deck system with conventional formwork [67].

Figure 3.15 Plane view looking down on reinforcement system in deck, as built

3.5 SPECIMEN SETUP

The test specimen was supported on six 890 kip (200 kN) capacity load cells, placed directly below the centerline of the three stems and 305 mm (12 in) on-center inwards from the longitudinal edges of the test specimen as shown in Figure 3.16. The purpose of these load cells was to evaluate the percentage of loads on the structure taken by each support and to determine the extent to which the specimen was loaded evenly throughout the testing.

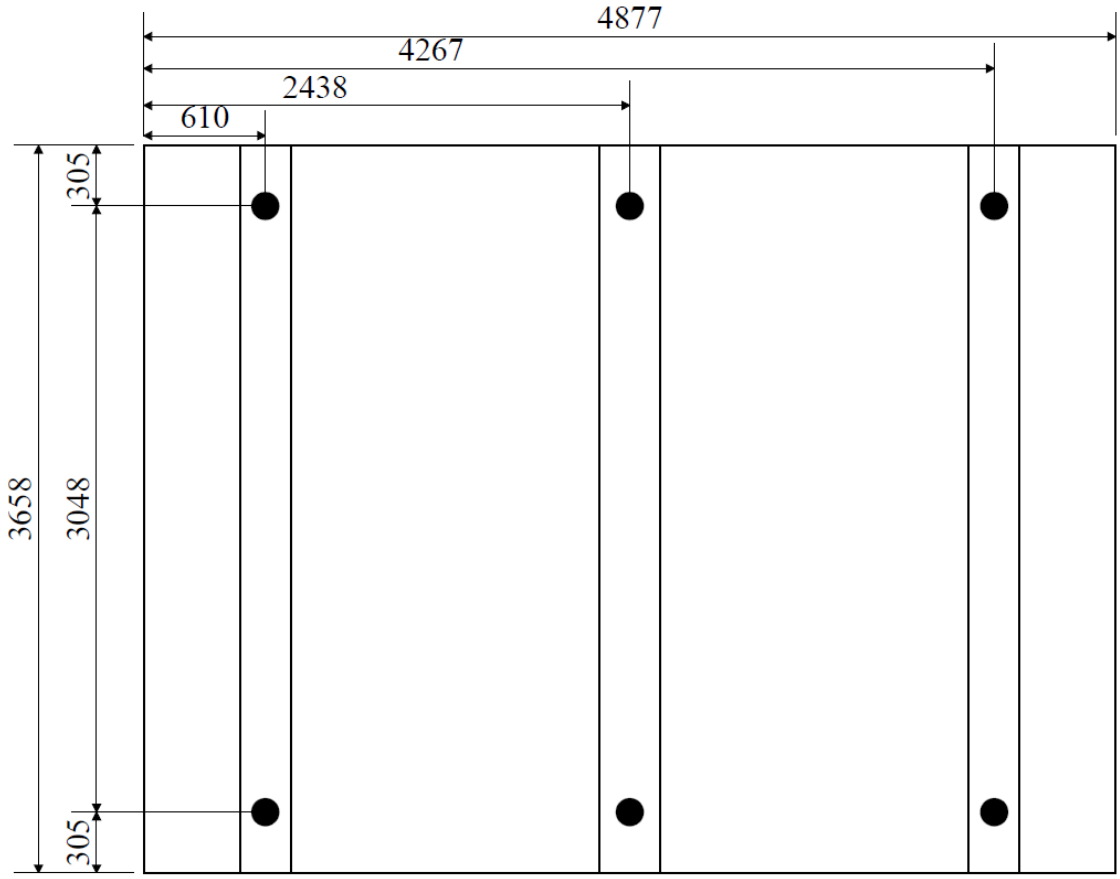

Figure 3.16 Load cell placement below test specimen

Each load cell has a footprint of 254 mm (10 in) by 254 mm (10 in) and consists of a 51 mm (2 in) thick steel plate placed on top of the load measuring device with smooth curved surfaces on both faces such that their interaction can be considered a point contact. The height of the load cells were adjusted in order to allow the test specimen to sit as level as possible and hydrostone was poured to secure the position of the load cells so that the load cells read approximately symmetric load values along both the longitudinal and transverse centerlines when loaded with the self weight of the test specimen. An illustration of load cells used to support the test specimen is shown in Figure 3.17.

Figure 3.17 Detail of load cell used to support test specimen

Two 980 kN (220 kip) capacity double-rod hydraulic actuators were positioned 1830 mm (6ft) apart from each other and in the center of each span to simulate the wheels attached to the axle of an AASHTO specified HS20 truck, which has an unfactored load of 73 kN (16.4 kip) per wheel. In this investigation, all applied load values are reported as the load applied per actuator, which is half of the total load applied to the test specimen. A 76 mm (3in) thick steel reinforced elastomeric bearing pad was placed between the actuators and the specimen and was used to create the 510 mm (10in) by 250 mm (20in) HS20 wheel footprint specified by AASHTO [91].

Figure 3.18 Overall specimen setup

3.6 INSTRUMENTATION

The primary measurements taken during the experimental testing of a structural test specimen are the loads measured by the supports and actuators as well as the deflections and the strains measured throughout the test specimen. The overall load distribution within the test specimen was measured using load cells which supported the structure, deflections were measured with linear potentiometers, strains were measured using electrical resistance strain gages and rotations were determined using inclinometers. Table 3.6 summarizes the total quantity of instrumentation used for this test specimen and the approximate locations in which each instrumentation type was used.

Table 3.6 Summary of instrumentation used for test specimen #1

INSTRUMENTATION TYPE	QUANTITY USED	APPROXIMATE LOCATIONS
Load cells	6	Supporting the test specimen, in line with stems and near both ends of the specimen
Linear potentiometers	47	45 vertically mounted above and below the deck slab 2 mounted horizontally to the outer two stems
Inclinometers	3	On one end of specimen, at the intersection between the mid-plane of deck and the centerlines of the three stems
Strain gages	118	Throughout deck and stems- attached to steel reinforcement and attached to the bottom of the FRP panels

3.6.1 Linear Potentiometers and Inclinometers

Linear potentiometers were used to measure deflected shape of the structure under the applied load. The linear potentiometers were positioned in locations designed to give an accurate representation of the overall structural response. All of the linear potentiometers used were attached to stationary support fixtures mounted to the strong wall and strong floor as shown in Figure 3.18, such that the displacements measured represented the absolute displacements of the structure.

Due to the positioning of the actuators at the center of the two deck slabs, the center deflection of each slab needed to be measured from linear potentiometers mounted below the deck. For consistency, the deflections throughout the deck slabs were also measured from linear potentiometers placed on the underside of the deck as shown in Figure 3.19. Linear potentiometers on the top of the deck were placed along the centerlines of the three stems to measure the combined deflection of the deck and stems. Selected linear potentiometers on the top side of the FRP side deck were also placed in the same position as linear potentiometers located on the underside of the deck in order to evaluate any separation between the concrete and the FRP panels that may occur during loading. Two linear potentiometers were placed on the RC side deck at the same locations as linear potentiometers below the deck in order to establish the appropriate level of precision which could be afforded when determining whether any separation had occurred on the FRP side, based on the linear potentiometer pairs.

The theoretical resolution of the linear potentiometers used in testing was determined based on the analog to digital converter, which has a total of 2^{16} bits, which is equivalent to 56,536 bits. The theoretical resolution was therefore calculated

for a given linear potentiometer as the total stroke of the device divided by 56,536. The noise level within the system has been experimentally determined to be approximately 10 times the theoretical resolution and the calculated linear potentiometer resolutions for the all linear potentiometers used on the test specimen is presented in Table 3.7. Therefore, changes in deflection with magnitudes that are near these resolution limit values were considered to be within the noise threshold for the test setup.

Table 3.7 Resolution attainable by linear potentiometers used on test specimen

Stroke of linear potentiometer		Device resolution, accounting for noise	
mm	in	mm	in
51	2	0.008	0.0003
102	4	0.016	0.0006
152	6	0.023	0.0009

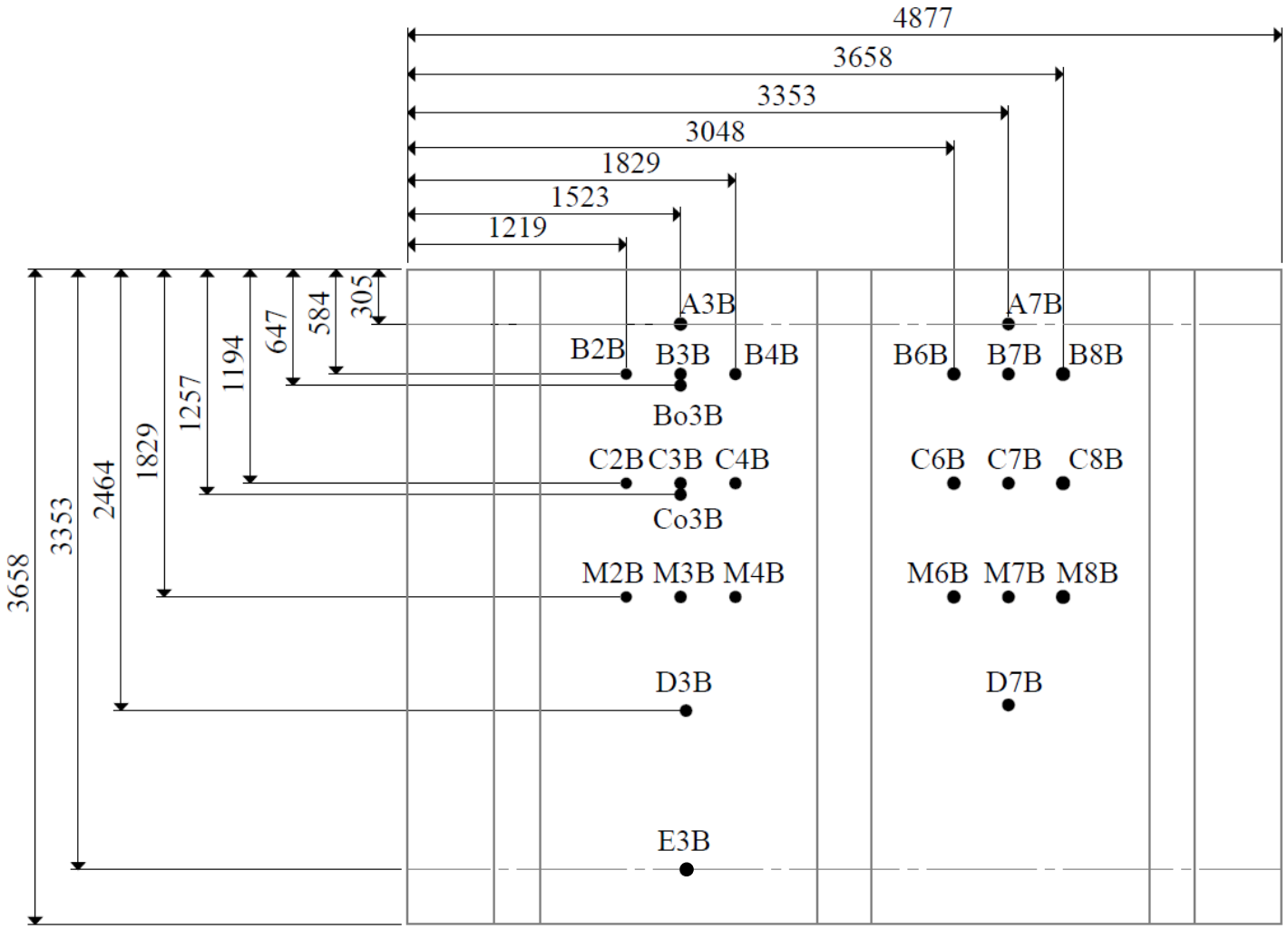

Figure 3.19 Layout of linear potentiometers located on the underside of the deck

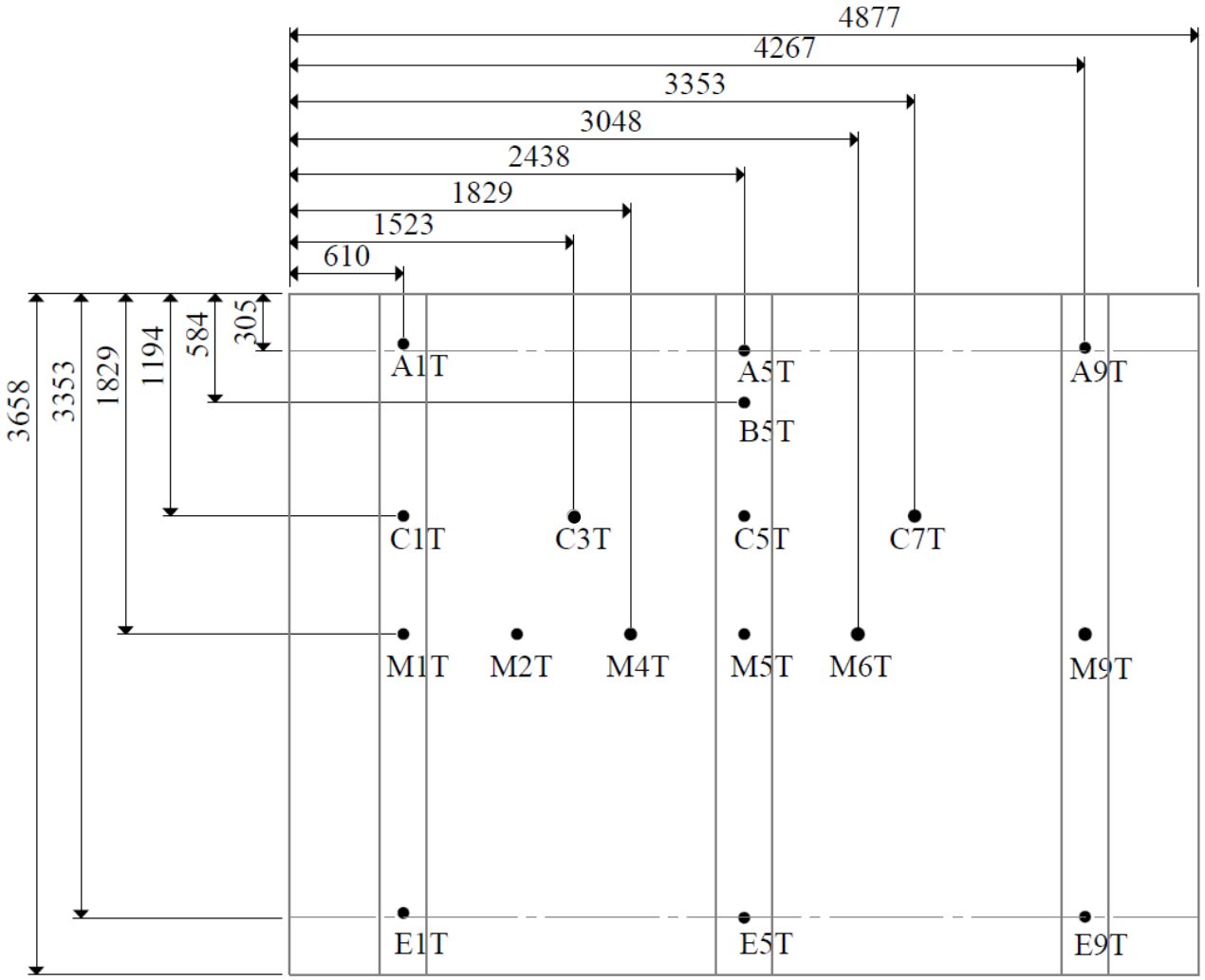

Figure 3.20 Layout of linear potentiometers located on the top of the deck

A detail of the horizontal linear potentiometers and the inclinometers is shown in Figure 3.21 and the layout of instrumentation is shown in Figure 3.22. Two linear potentiometers were mounted horizontally, near the top of the two outer stems, approximately 76 mm (3 in) longitudinally inwards from the edge of the test specimen. The three inclinometers used were attached to the outer edge of the test specimen, with one located at the vertical centerline of each of the three stems and positioned at mid-plane of the concrete deck slab. The purpose of the horizontal linear potentiometers and the inclinometers was to measure any changes in slope within the deck and determine more information regarding the end conditions of the deck slab.

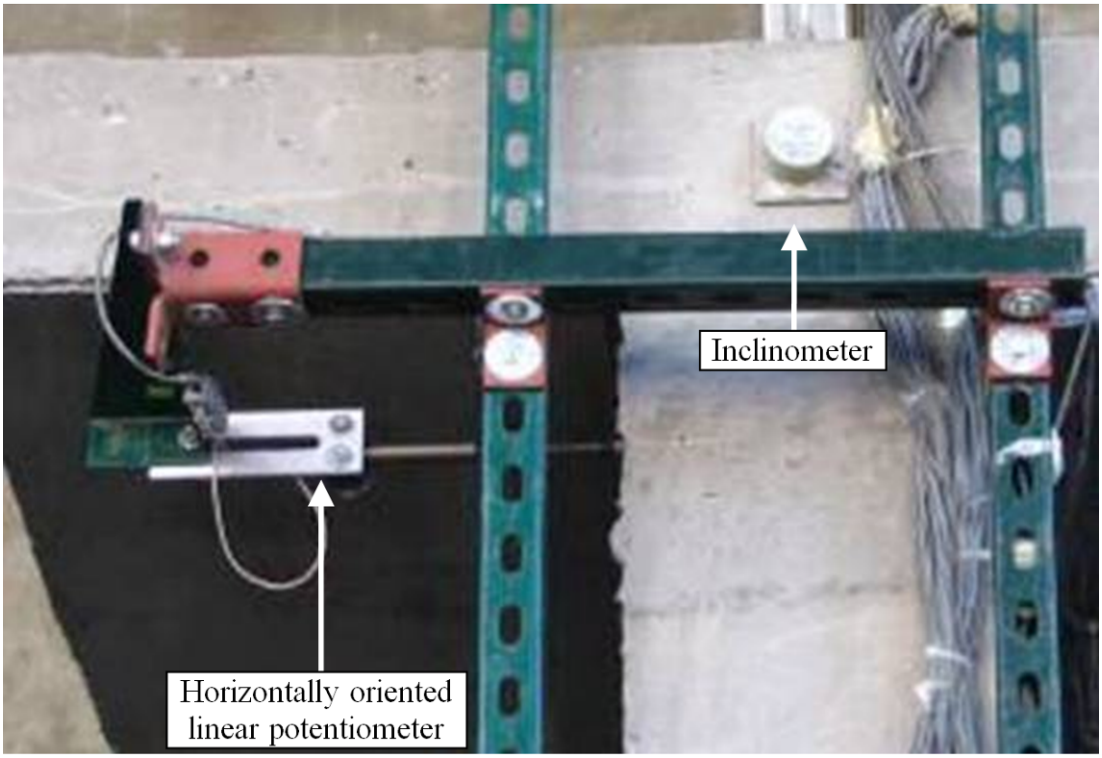

Figure 3.21 Detail of horizontally oriented linear potentiometer and inclinometer

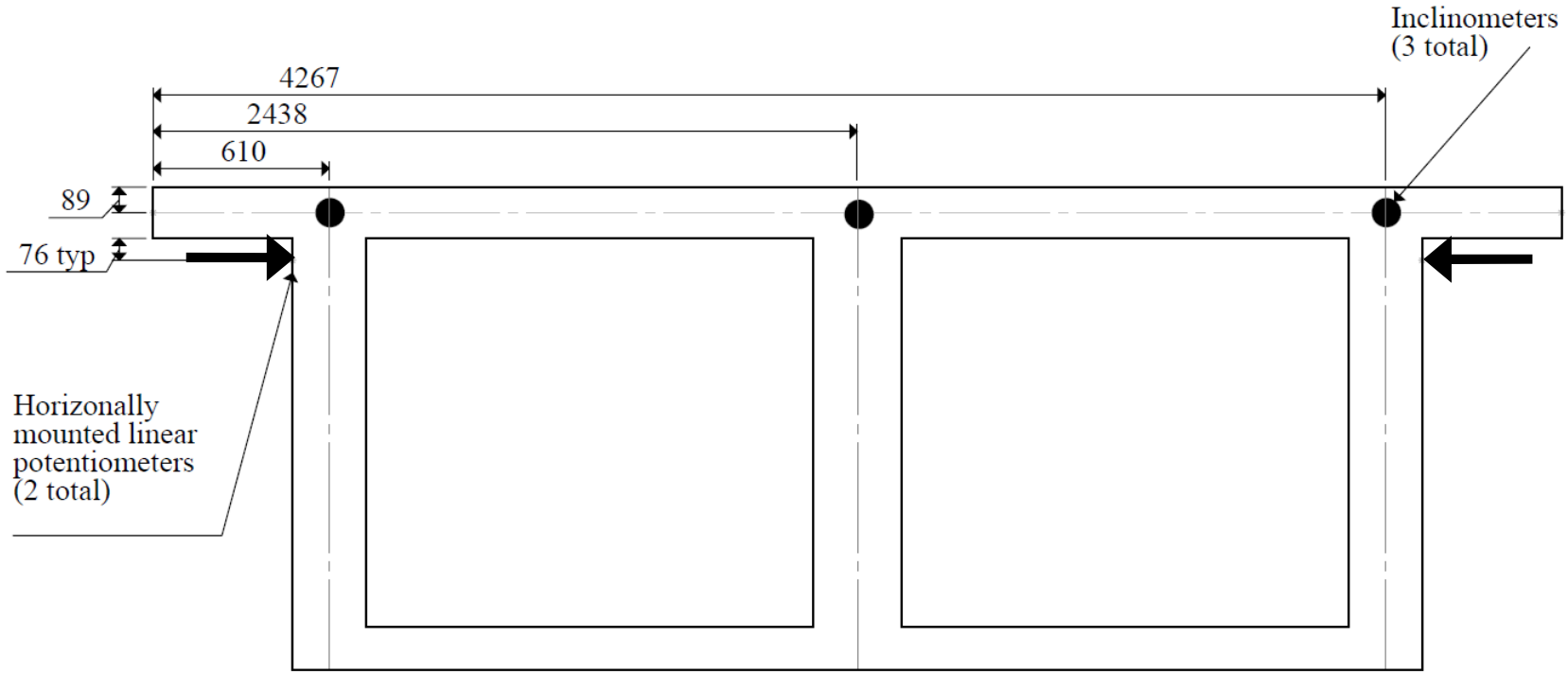

Figure 3.22 Layout of inclinometers and horizontally mounted linear potentiometers
(Inclinometers are attached directly to front surface of test specimen, linear potentiometers are offset inwards 76 mm from edge)

3.6.2 Strain Gages

Strain gages with 5 mm (0.2 in) gage lengths were attached to the steel reinforcement on selected rebar in the top and bottom layers of the deck as well as selected vertical rebar within the stems. Strain gages with 30 mm (1.2 in) gage lengths were attached to the bottom side of the FRP panel. The precise layouts of the strain gages are shown in Figure 3.23 through Figure 3.31.

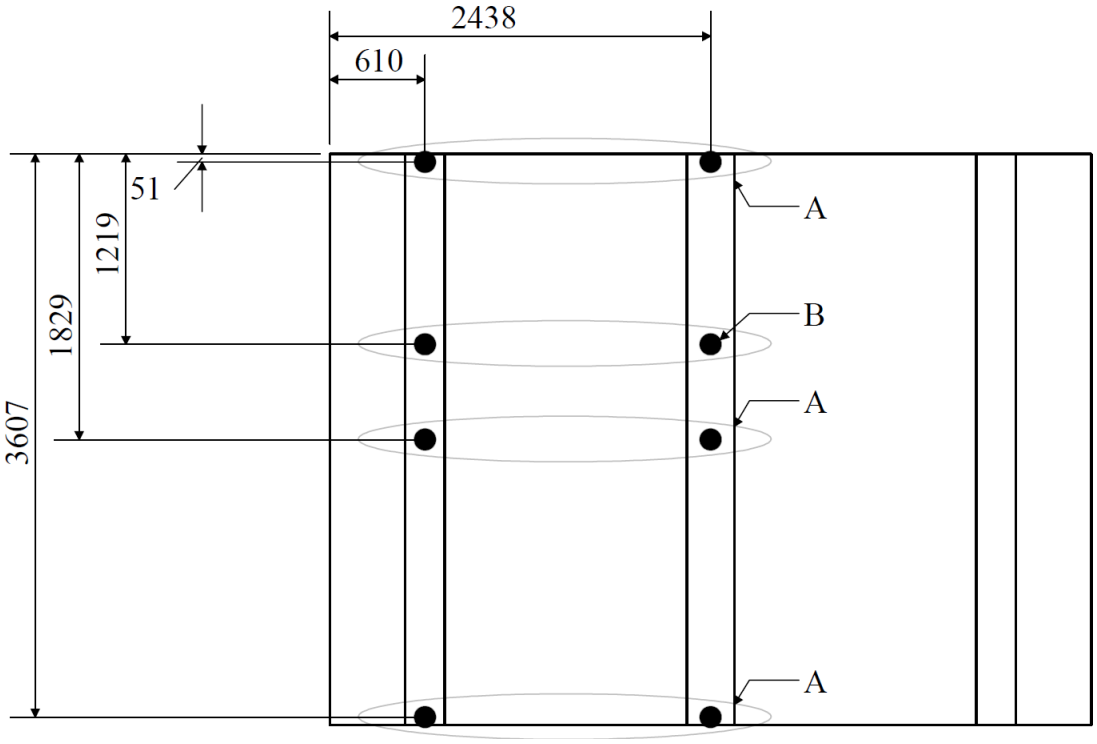

Figure 3.23 Strain gage pattern locations for gages attached to vertical stem rebar

The strain gages attached to the vertical steel reinforcement in the stems are arranged in one of two patterns, termed “A” and “B”, and are located at different positions within the test specimen cross section as designated in Figure 3.23. Strain

gage pattern A contains eight gages, with six attached to the outer stem of the FRP side and two attached to the center stem as shown in Figure 3.24. Strain gage pattern B contains three strain gages total, with one strain gage attached to the outer FRP side stem and two gages attached the center stem as shown in Figure 3.25. There are a total of 27 strain gages attached to the vertical stem rebar.

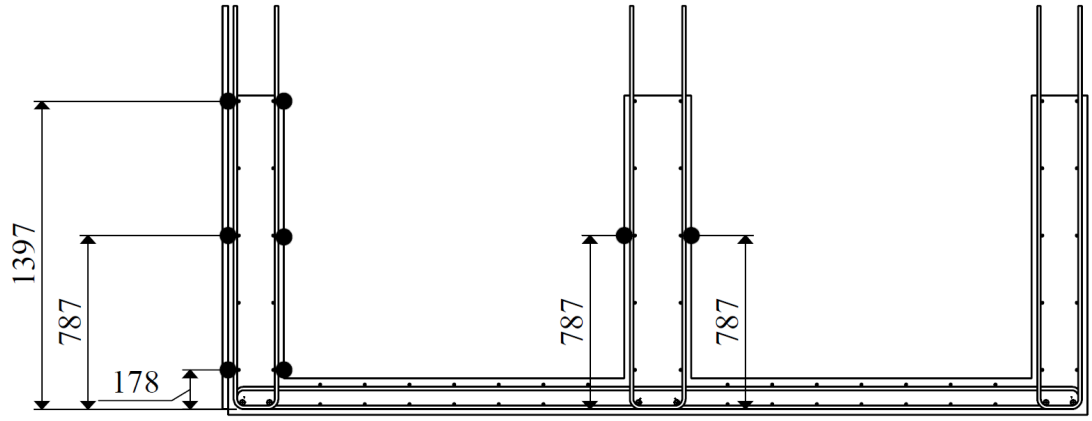

Figure 3.24 Strain gage pattern "A"
(Consists of six strain gages attached to the vertical stem rebar of the FRP side outer stem and two strain gages attached to the vertical stem rebar of the center stem)

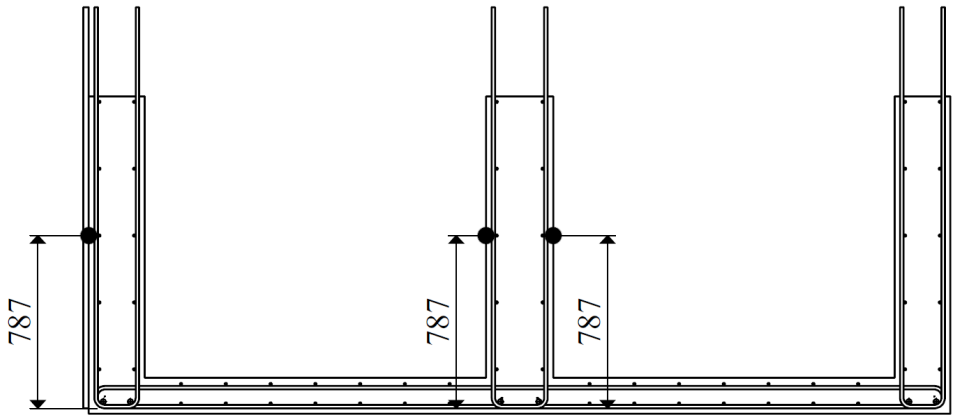

Figure 3.25 Strain gage pattern "B"
(Consists of one strain gage attached to the vertical stem rebar of the FRP side outer stem and two strain gages attached to the vertical stem rebar of the center stem)

The strain gages attached to the bottom side of the FRP panel side deck were oriented in the longitudinal and transverse directions, and the positions of these strain gages are shown in Figure 3.26 and Figure 3.27. The strain gages attached to the bottom of the FRP deck were spaced 305 mm (1 ft) apart from each other in the transverse direction and approximately 610 mm (2 ft) apart from each other in the longitudinal direction. The longitudinally oriented strain gages were primarily positioned in two rows along the FRP deck slab, with one longitudinal row at the midspan of the slab and the other offset from the slab centerline by 305 mm (12 in) in the direction of the outer stem. These longitudinal lines of strain gages serve to assess the progression of strains at different distances away from the applied load.

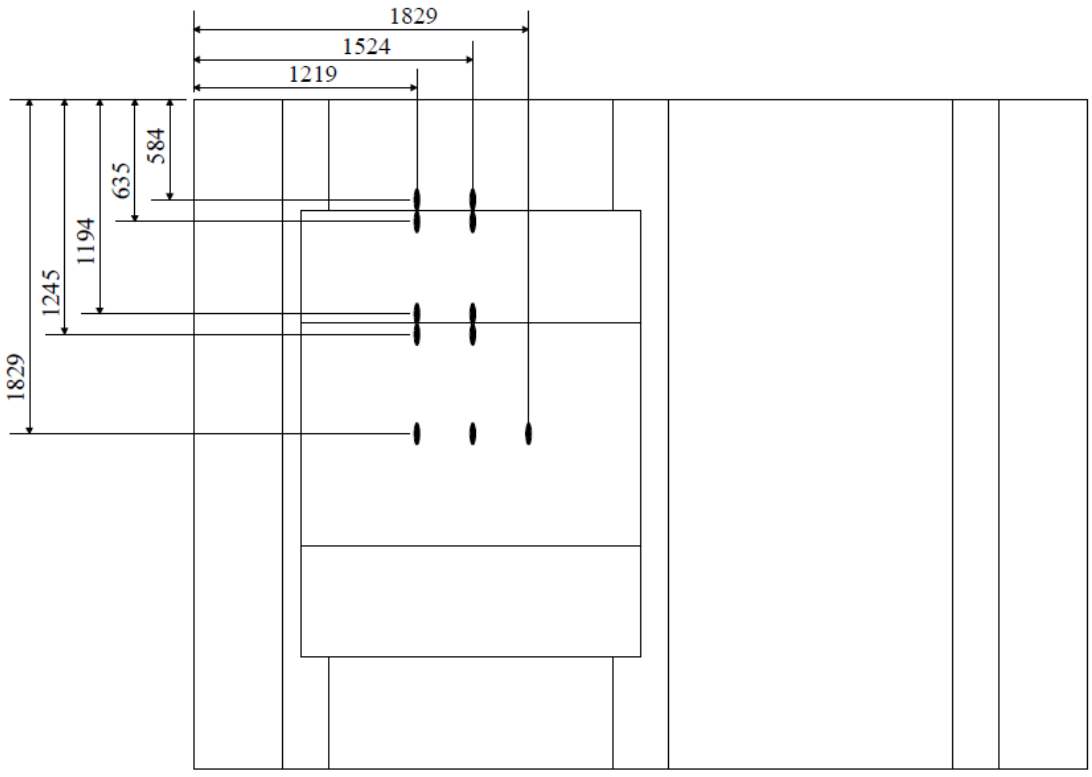

Figure 3.26 Layout of longitudinal strain gages attached to bottom of FRP side deck

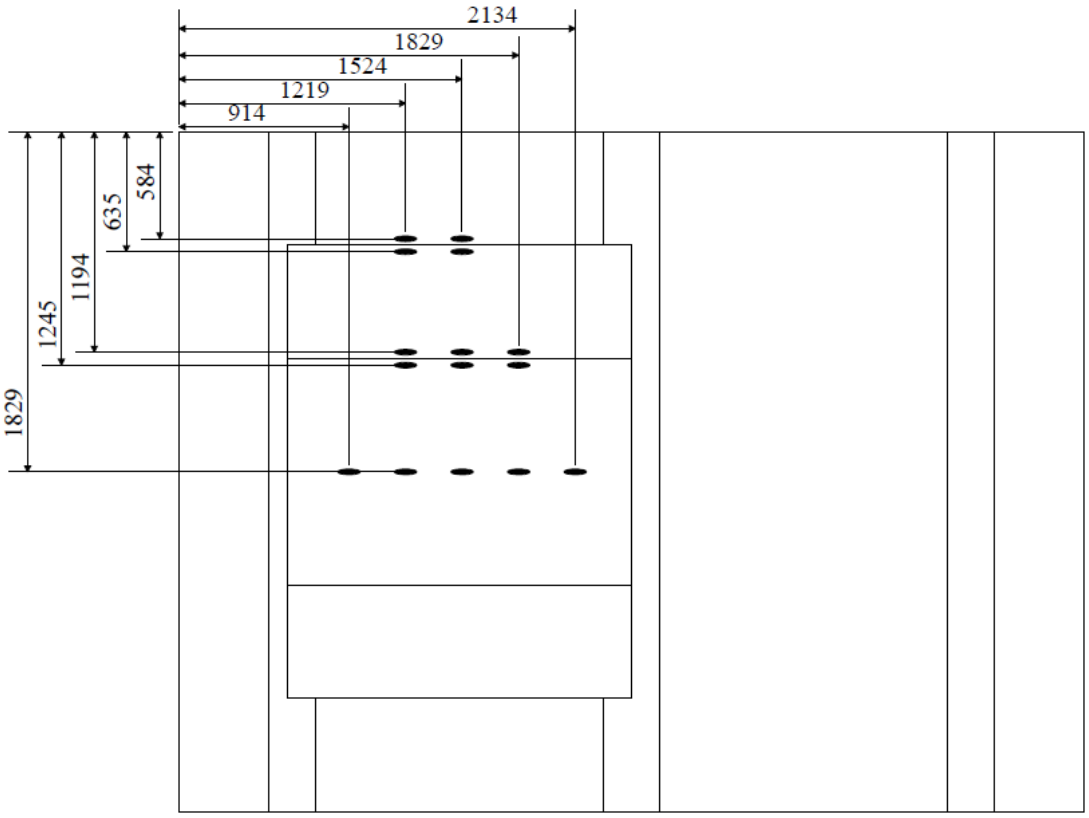

Figure 3.27 Layout of transverse strain gages attached to bottom of FRP side deck

Strain gages were located directly on either side of the intersection between FRP panels and on either side of the intersection between the outer FRP panel and the adjacent concrete in order to evaluate the effectiveness of stress transfer between adjacent panels and between panels and the surrounding concrete. The transversely oriented strain gages attached to the bottom of the FRP side deck consisted of one long row of gages along the test specimen centerline and four smaller rows, located on either side of the intersection between two panels and on either side of the concrete FRP panel intersection as shown in Figure 3.27. There were 15 transversely oriented

strain gages and 11 longitudinal strain gages for a total of 26 gages attached to the bottom of the FRP side deck.

Strain gages were also attached to the top and bottom layer of steel reinforcement in the deck slab and were attached to both longitudinally and transversely oriented rebar. Two rows, consisting of three strain gages each were attached to the top longitudinal rebar that were as close as possible to the centerline of the two deck slabs. The middle strain gage in each row was placed at the centerline of the test specimen and the remaining two gages in each row were spaced at 610 mm (2 ft) increments along the bar as shown in Figure 3.28.

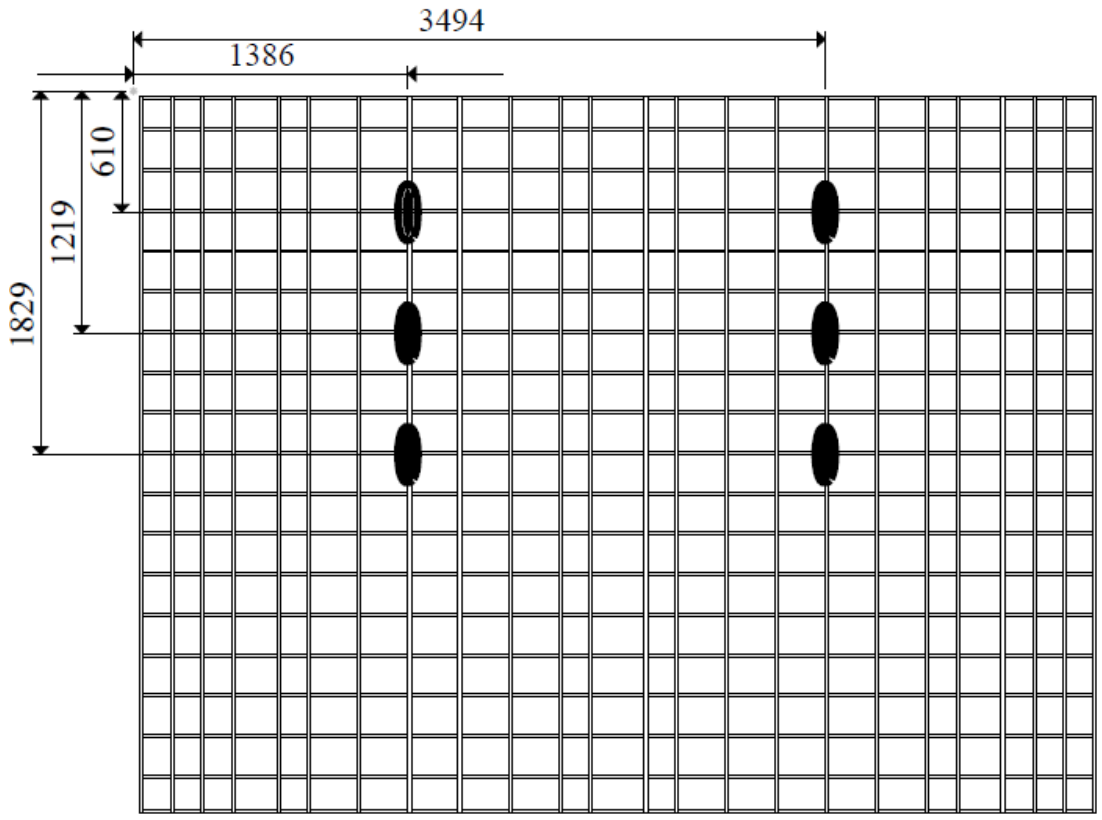

Figure 3.28 Layout of strain gages attached to top longitudinal steel reinforcement

The longitudinal strain gages attached to the bottom layer of steel reinforcement consisted of 12 strain gages which were arranged in two rows of three strain gages each on the RC side and three rows with two strain gages each on the FRP panel side as shown in Figure 3.29. The rows on the RC side were attached to the steel rebar which was closest to the centerline of the RC side actuator and the directly adjacent steel rebar. These gages were spaced using the same pattern as the top longitudinal gages, with one gage at the test specimen centerline and the other two spaced at 610 mm (2ft) increments.

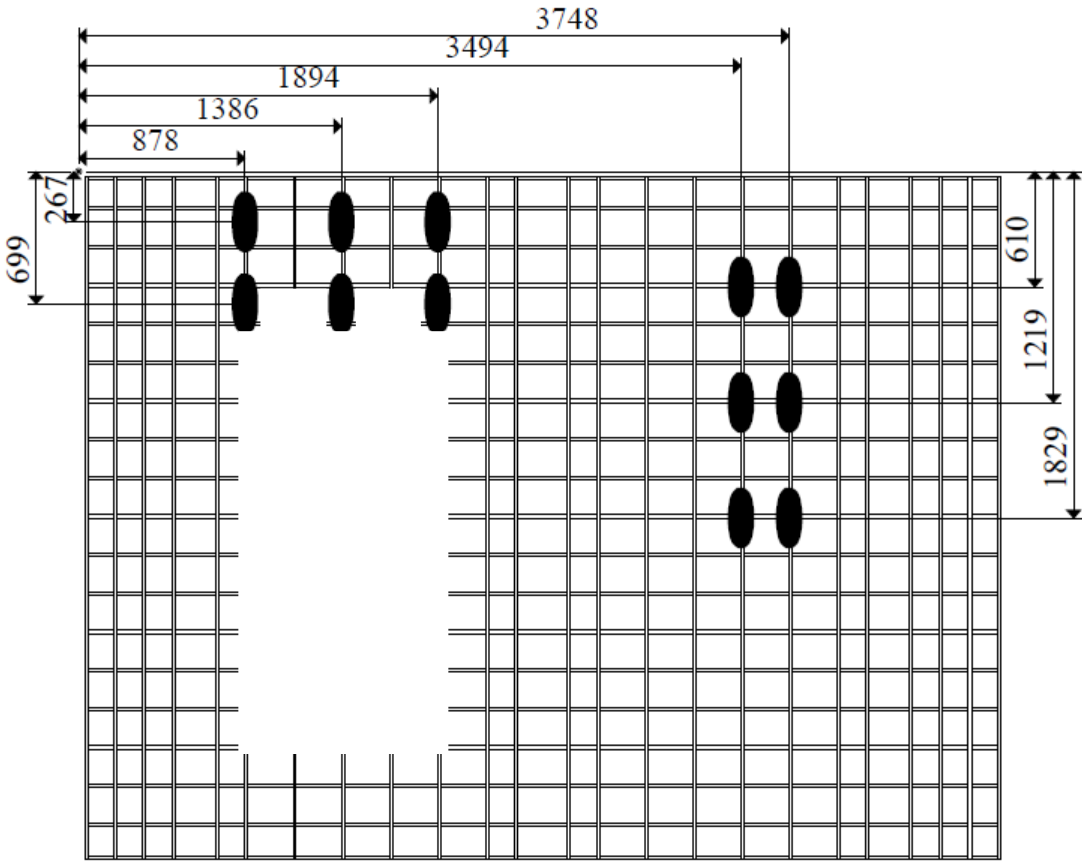

Figure 3.29 Layout of strain gages attached to bottom longitudinal steel reinforcement

There were 16 total strain gages attached to the top transverse reinforcement, which were placed in two rows of eight strain gages each. The strain gages were positioned at 610 mm (2 ft) increments and were attached to the transverse rebar which ran along the centerline of the test specimen as well as the transverse rebar 813 mm (32 in) away from the specimen centerline as shown in Figure 3.30.

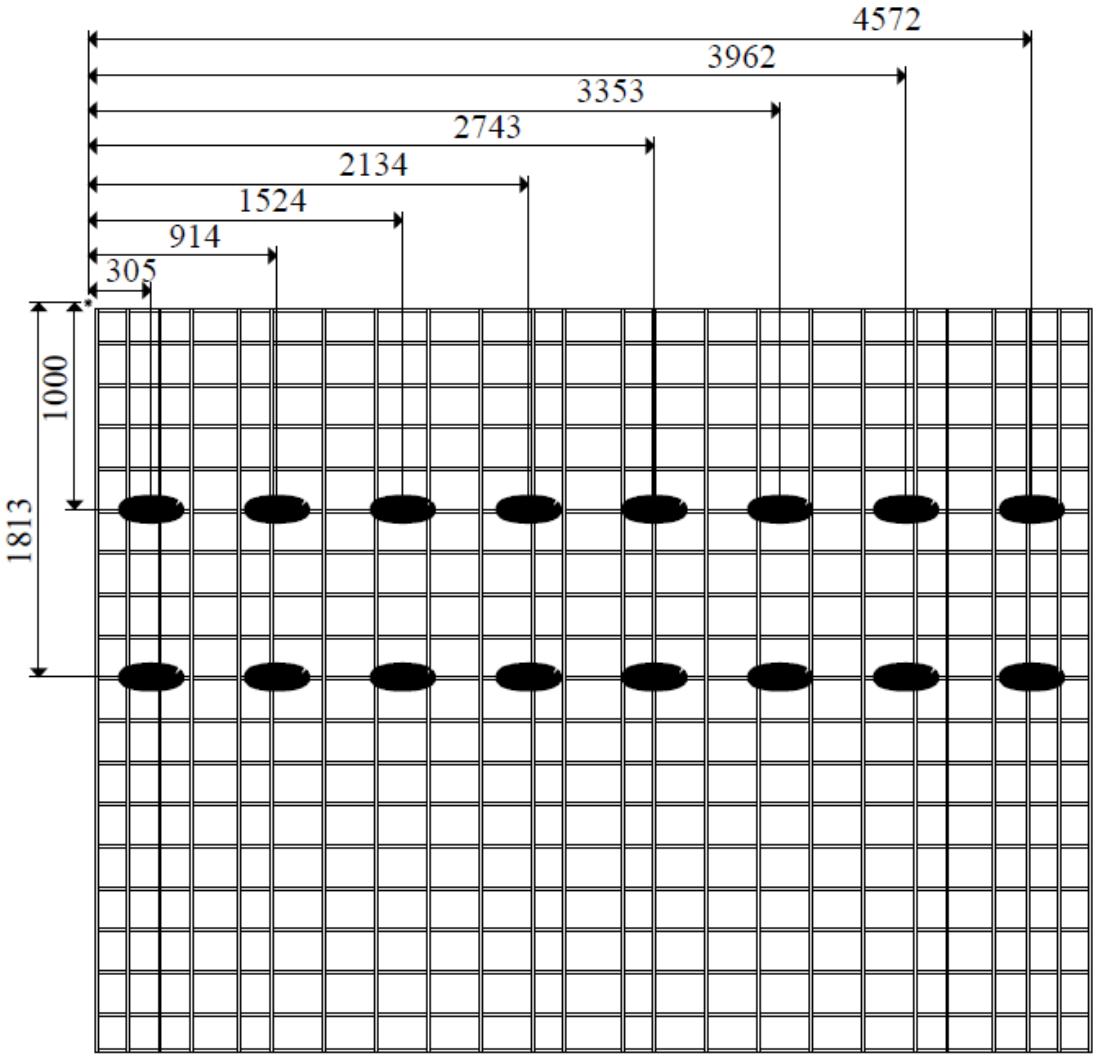

Figure 3.30 Layout of strain gages attached to top transverse steel reinforcement

The strain gages attached to the bottom layer of transverse rebar consisted of six lines of strain gages, which were positioned along the same 610 mm (2ft) spacing pattern used for the top transverse layer of rebar. Six strain gages were used on the rebar that was continuous across the specimen, whereas five strain gages were used for the five rows that contained discontinuous rebar due to the presence of the FRP panels, which took the place of the bottom longitudinal and transverse steel reinforcement. A total of 31 gages were attached to the bottom transverse rebar, bringing the total number of strain gages used to 118.

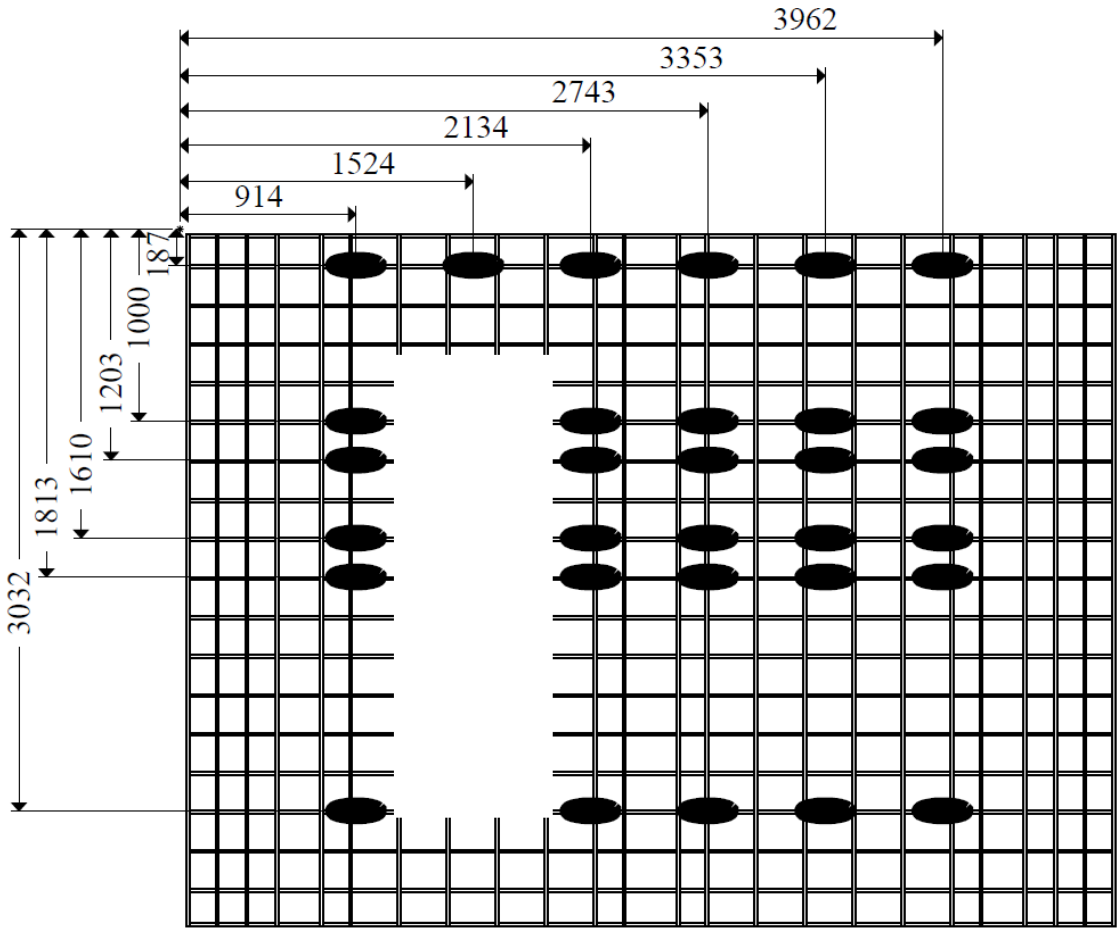

Figure 3.31 Layout of strain gages attached to bottom transverse steel reinforcement

3.7 FORMWORK DEFLECTIONS DURING CASTING OF DECK CONCRETE

Limits on the maximum allowable deflections for stay-in-place formwork caused by the dead load of the forms, reinforcement and the freshly cast concrete, serve to prevent excessive sagging during construction. In order to assess the effectiveness of the two formwork systems, deflection values due to the construction of the deck were obtained for the composite deck panel and for the conventional wooden shored formwork from linear potentiometers (pots) placed directly beneath the center of each cell.

Concrete was placed to create a 178 mm (7 in) thick deck slab, which applied a load per unit area of 4.21 kPa (88 psf). During the pouring of the concrete, the composite deck panel had peak deflections of less than half that of the wooden shored formwork used for the reinforced concrete side, 2.2 mm (0.087 in) versus 5.5 mm (0.217 in), respectively as shown in Figure 3.32.

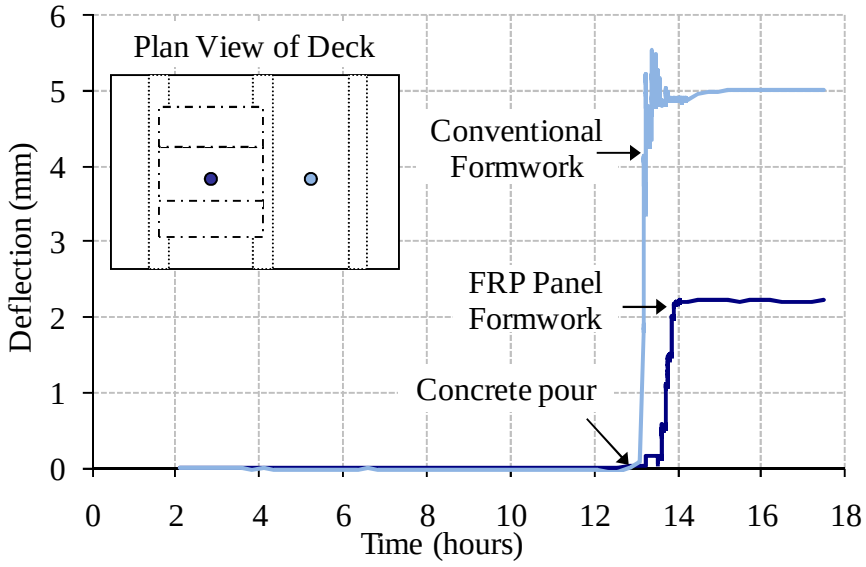

Figure 3.32 Comparison of formwork center deflections under construction loading

Three days after the completion of the concrete pour, the deflections for the composite side's FRP panel formwork versus reinforced concrete side's shored formwork were 2.2 mm (0.087 in) versus 5.0 mm (0.197 in) respectively.

While typical formwork deflection values were not available, due to the numerous variations in wooden shored formwork design, which often depend on material availability and the preferences of the contractors, AASHTO LRFD Bridge Design Specifications provide deflection limits for the formwork under construction loading. For stay-in-place formwork span lengths of less than 3.00 m (10 ft), Section 9.7.4.1 defines the elastic deformation limit under dead load of the forms, plastic concrete and reinforcement as follows [91]:

$$\Delta_{\max\_\,form} = \min\begin{cases} \dfrac{L_{span}}{180} \\ 12.7mm \quad (0.5in) \end{cases}$$

where

$\Delta_{\max\_\,form}$ = Maximum allowable deflection of stay-in-place formwork

L_{span} = Span length of the stay-in-place formwork

The conventional shored formwork and the FRP panel formwork both deflected less than the governing deflection limit of 10.2 mm (0.4 in), which is equivalent to the span length of 1829 mm (6 ft) divided by 180. These deflection results indicate that the FRP panels were able to safely act as formwork, exhibiting minimal deflections under construction loading.

3.8 STATIC LOADING OF TEST SPECIMEN

3.8.1 Loading Protocol

The loading values used in experimental testing were based on the HS20 truck wheel loading described in the AASHTO Bridge Specifications [91], where the vehicle load was the only load effect considered. Two 980 kN (220 kip) capacity double-rod hydraulic actuators were positioned 1830 mm (6ft) apart from each other and in the center of each span to simulate the wheels attached to the axle of the HS20 truck, which has an unfactored load of 73 kN (16.4 kip) per wheel. In this investigation, all load values are reported as the load applied per actuator as opposed to the total load applied to the test specimen. Throughout the testing, two equally loaded actuators were used, therefore the total applied load would simply be twice the load applied per actuator. In order to ensure that the actuators remained in contact with the specimen during testing, a minimum threshold load value of 4.5 kN (1 kip) was applied to the test specimen for the unloaded state during static loading.

For static loading, the service load was defined by the AASHTO SERVICE I level (clause 3.4.1 and Table 3.4.1-1 of the AASHTO specifications) in which the HS20 wheel load of 73 kN (16.4 kip) with an additional AASHTO defined 33% dynamic allowance for the static loading case, or 98 kN (22 kips) was applied [91]. Load levels were also compared with the AASHTO STRENGTH I level, which was computed as the SERVICE I level with an additional 75% live load factor and with the CALTRANS specified Permit truck load of 180 kN (41 kip), which is calculated from a 106 kN (24 kip) wheel load with a 30% dynamic allowance and additional 30% live load factor [152].

The test specimen was loaded statically to failure with single load/unload cycles at increasing load levels up to the ultimate load of 890 kN (200 kips). The first load level applied was the AASHTO service load for static testing of 98 kN (22 kips) as described above. Next, the specimen was loaded to 222.4 kN (50 kips), cycled through the minimum threshold level of 4.5 kN (1 kip) and then loaded in increments of 89 kN (20 kip). Initial signs of punching shear were observed at 823 kN (185 kips), which dictated that the test specimen be loaded more slowly until the ultimate capacity of 890 kN (200 kips) was reached. A summary of the static loading protocol is shown in Table 3.8 .

Table 3.8 Static loading protocol

Target Load		Single Load-Unload Cycle (Yes/ No)	Multiples of Service I load 98 kN (22 kip)	Multiples of Strength I load 169 kN (38 kip)	Multiples of Permit Load 180 kN (41 kip)
kN	kip				
98	22	No	1.0	0.6	0.5
222	50	Yes	2.3	1.3	1.2
311	70	No	3.2	1.8	1.7
400	90	Yes	4.1	2.4	2.2
489	110	No	5.0	2.9	2.7
578	130	Yes	5.9	3.4	3.2
667	150	No	6.8	3.9	3.7
756	170	Yes	7.7	4.5	4.2
845	190	Down to 667 kN (150 kip)	8.6	5.0	4.7
890	200	Ultimate Capacity	9.1	5.3	4.9

3.8.2 Overall Behavior

At each load level in which a single cycle was performed, the target load was held briefly to allow inspection of the test specimen in the loaded state prior to unloading the specimen. This allowed for observation of any cracking or damage which had occurred to the test specimen during a given load level. Indications of partial separation between sections of the FRP panels and the concrete were first observed in the strain and deflection data at the 489 kN (110 kip) load level, which was equivalent to 5 times the AASHTO service load and is discussed in Section 3.8.8, however no cracking or other visible damage was detected during an inspection of the deck surface at this load level. At the 578 kN (130 kip) load level, it was noted that the elastomeric bearing pad below the composite actuator had shifted horizontally by a approximately 5 millimeters (0.2 in) from its original location.

Discontinuous cracking was first observed on the top surface of the deck at the 667 kN (150 kip) load level with the most significant cracks located in the longitudinal direction above the central stem, followed by longitudinal cracking above the RC side stem and only hairline longitudinal cracks above the composite side stem. By the 756 kN (170 kip) load level, discontinuous longitudinal cracks that ran along the length of the specimen above each stem were observed. Some cracking was also noted near the center of the bottom side of the RC side deck in the longitudinal and transverse directions at this load level.

The FRP panel reinforced slab failed in punching shear at a load of 890 kN (200 kip), which is equivalent to 9.1 times AASHTO service load, with initial signs of punching shear observed at a load of 825 kN (186 kip), which is equivalent to 8.4

times AASHTO service load. The midspan deflections at the maximum applied load were 7.09 mm (0.279 in) for the FRP panel reinforced slab and 7.81 mm (0.307 in) for the reinforced concrete slab. The overall load versus midspan displacement response curves for the two slabs are shown in Figure 3.34. In order to better compare the structural response of the two reinforcing schemes, the unloading portion of each curve was removed and the envelope plot of load versus center deflections is shown in Figure 3.33.

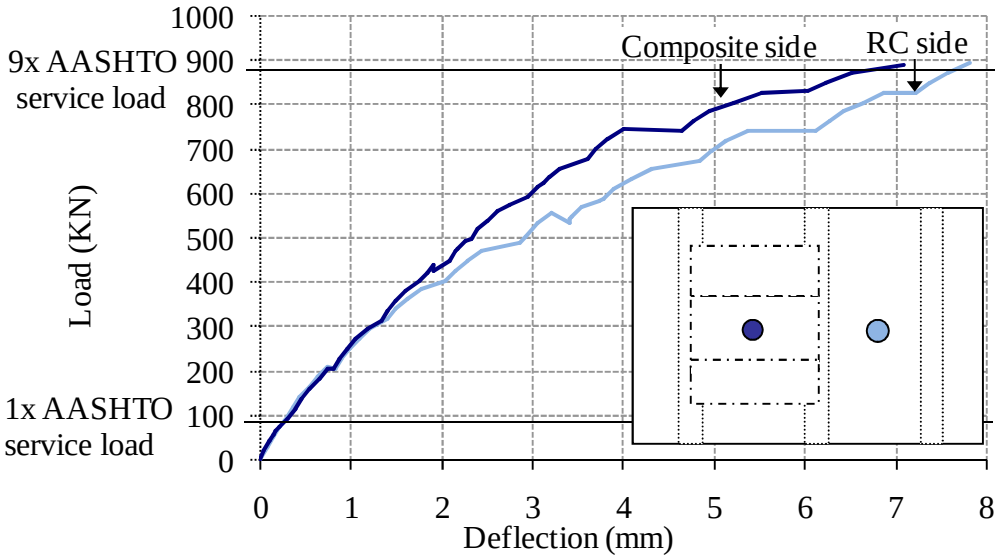

Figure 3.33 Envelope plot of load versus center deflections

At 98 kN (22 kip), equivalent to the AASHTO HS20 wheel load of 73 kN (16.4 kip) with an additional 33% impact factor, the vertical midspan deflection for both slabs was 0.29 mm (0.011 in). The midspan deflections of the two slabs were within 0.1 mm (0.004 in) of each other up to a load level of 338 kN, equivalent to 3.4 times the AASHTO service load.

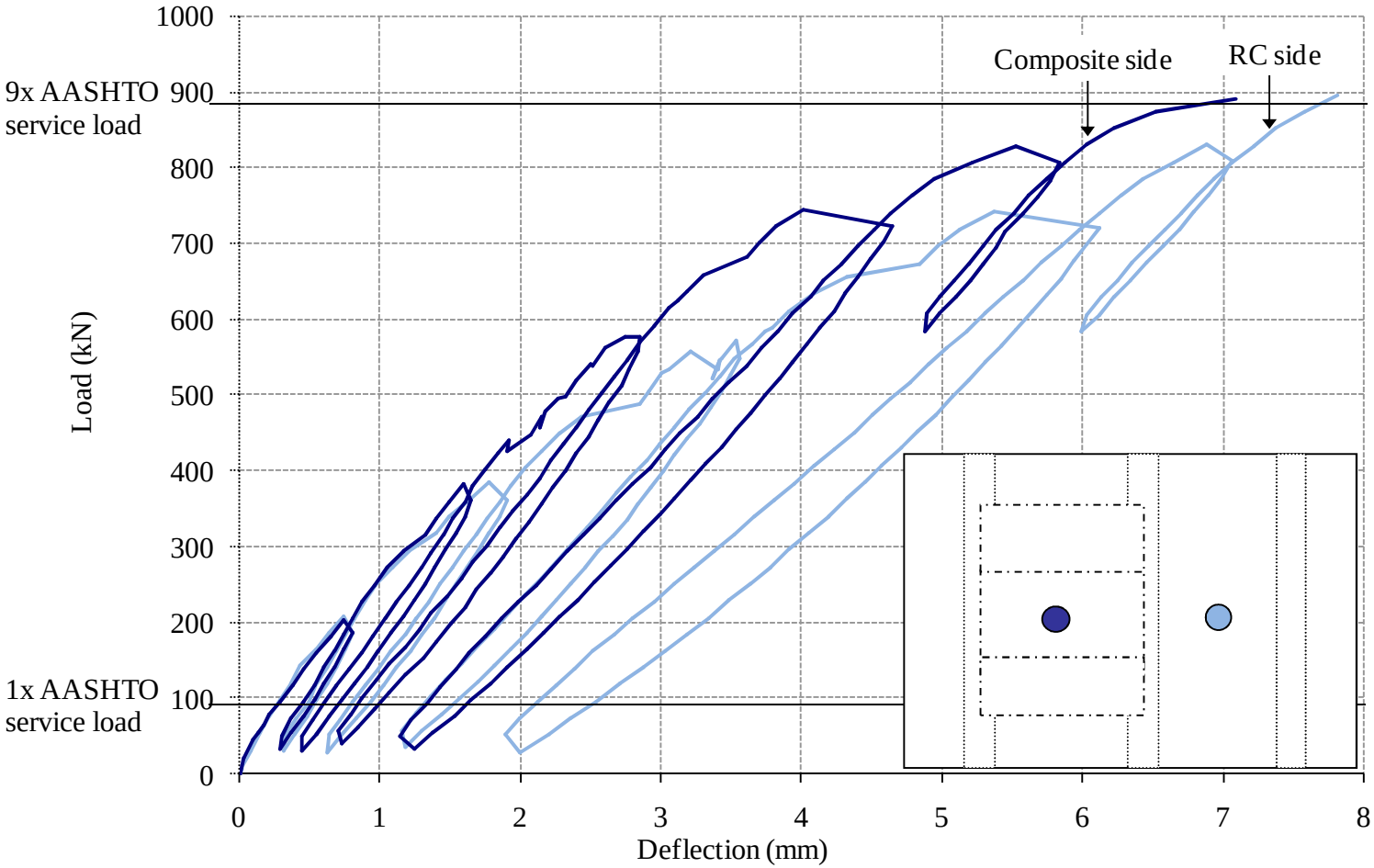

Figure 3.34 Load versus center deflections

For the remainder of the loading, the reinforced concrete side deflected more at the midspan than the composite side, with a maximum difference between the two slabs of 1.5 mm (0.59 in), equivalent to a 31.0% greater RC side deflection, which occurred at a load of 762 kN (171.3 kip). The greatest percentage difference between the two sides, in which the reinforced concrete side deflected 46.6% greater, occurred at a load of 497 kN and corresponded to a 2.32 mm (0.091 in) composite side deflection and a 3.4 mm (0.134 in) reinforced concrete side deflection.

3.8.3 Stiffness Change Throughout the Loading Range

In order to compare the progression in deterioration of performance of the slabs as observed through degradation of the slope of load-deflection response of the slabs over the load cycles, a parameter known as the "effective" stiffness, was defined as follows:

$$\text{Effective Stiffness} = \frac{P_f - P_i}{\delta_f - \delta_i} \qquad 3.1$$

where

P_f = Target actuator load of a load cycle based on loading protocol
P_i = Minimum threshold actuator load of a load cycle
δ_f = Deflection at load P_f, at the location under consideration
δ_i = Deflection at load P_i, at the location under consideration

Note that Equation 3.1 uses the minimum threshold actuator load of approximately 4.5 kN (1 kip) and the corresponding deflection at the start of a load

cycle, P_i and δ_i, in the effective stiffness calculation. Conversely, a standard secant stiffness calculation uses either the origin or the minimum threshold load and deflection value at the start of experimental testing for the lower value. This modification from a standard secant stiffness calculation was chosen in order to evaluate the degradation of the slope of the load-deflection curve independent of the effects of accumulated residual deflections on the stiffness results. The results obtained from the chosen calculation method shown in Equation 3.1 termed the "adaptive secant stiffness method" are compared with results obtained using the standard secant method and a discussion on this topic is found later in this section.

Also note that the effective stiffness obtained from the load-deflection response is different from the actual bending stiffness of the slab because the calculation does not take into account the moment curvature response. The effective stiffness data calculated can be used for comparative evaluation of the relative progression of change in structural response over the load cycles.

In order to examine changes in response, the effective stiffness ratio rather than absolute values of effective stiffness are presented in this section. The effective stiffness ratio was calculated by comparing the effective stiffness at a load level to the effective stiffness at the baseline load as shown in Equation 3.2:

$$\text{Effective Stiffness Ratio} = \frac{\text{Effective stiffness at a load level}}{\text{Effective stiffness at baseline (98 kN)}} \qquad 3.2$$

The load of 98 kN (22 kip), which represented a HS20 truck load of 73 kN (16.4 kip) with an additional AASHTO defined 33% dynamic allowance and was also

the initial load level in the static testing, was chosen as the baseline load. Since the response of the test specimen was in the linear elastic range at this load level, the effective stiffness ratio at this load level is taken to be 1.0.

The effective stiffness ratios shown in Table 3.9 and Table 3.10 highlight a significant difference in the degradation trends of the load deflection slopes for the two reinforcing systems. The degradation trends for the two slabs are most easily observed in Figure 3.35, which plots the effective stiffness values of both slabs for each load level.

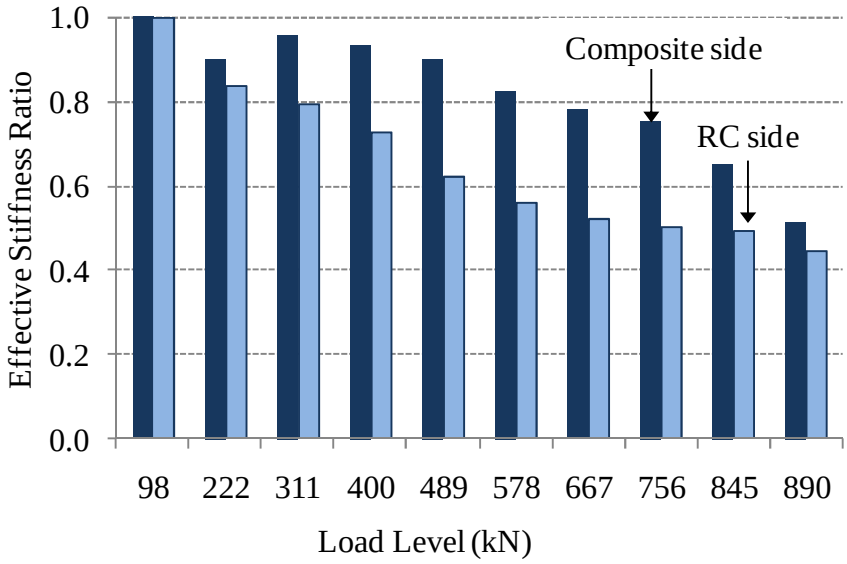

Figure 3.35 Effective stiffness ratios of the two slabs determined from linear potentiometer data

Table 3.9 Effective stiffness ratios of FRP side slab from linear potentiometer data

Target actuator Load		Actual target actuator load, P_f		Actual min. threshold actuator load, P_i		Deflection at target load, δ_f		Deflection at min. threshold load, δ_i		Effective stiffness ratio
kN	kip	kN	kip	kN	kip	mm	in	mm	in	---
98	22	95.9	21.6	22.3	5.0	0.29	0.011	0.03	0.001	1.00
222	50	204.1	45.9	22.3	5.0	0.74	0.029	0.03	0.001	0.90
311	70	316.1	71.1	33.4	7.5	1.33	0.052	0.30	0.012	0.96
400	90	382.5	86.0	33.4	7.5	1.60	0.063	0.30	0.012	0.94
489	110	478.4	107.6	31.7	7.1	2.18	0.086	0.44	0.017	0.90
578	130	576.3	129.6	31.7	7.1	2.75	0.108	0.44	0.017	0.83
667	150	680.9	153.1	40.3	9.1	3.61	0.142	0.73	0.029	0.78
756	170	745.1	167.5	40.3	9.1	4.01	0.158	0.73	0.029	0.75
845	190	828.6	186.3	33.5	7.5	5.52	0.217	1.25	0.049	0.65
890	200	890.5	200.2	33.5	7.5	7.09	0.279	1.25	0.049	0.51

Table 3.10 Effective stiffness ratios of RC side slab from linear potentiometer data

Target actuator Load		Actual target actuator load, P_f		Actual min. threshold actuator load, P_i		Deflection at target load, δ_f		Deflection at min. threshold load, δ_i		Effective stiffness ratio
kN	kip	kN	kip	kN	kip	mm	in	mm	in	---
98	22	99.1	22.3	7.7	1.7	0.29	0.011	0.02	0.001	1.00
222	50	209.1	47.0	7.7	1.7	0.74	0.029	0.02	0.001	0.83
311	70	317.5	71.4	30.6	6.9	1.40	0.055	0.32	0.013	0.79
400	90	384.2	86.4	30.6	6.9	1.78	0.070	0.32	0.013	0.72
489	110	489.3	110.0	29.3	6.6	2.85	0.112	0.62	0.025	0.62
578	130	570.9	128.4	29.3	6.6	3.53	0.139	0.62	0.025	0.56
667	150	673.5	151.4	36.0	8.1	4.84	0.191	1.18	0.047	0.52
756	170	740.8	166.5	36.0	8.1	5.37	0.212	1.18	0.047	0.50
845	190	829.5	186.5	29.1	6.5	6.87	0.271	1.99	0.078	0.49
890	200	895.9	201.4	29.1	6.5	7.81	0.308	1.99	0.078	0.45

The reinforced concrete side slab displayed a 17% degradation of the effective stiffness between the first and second load levels and then continued to decrease in the slope of the load-deflection response for the next four load levels. These first six load levels, which loaded the specimen up to 578 kN (130 kip) (equivalent to 5.9 times the AASHTO service load) accounted for over 85% of the total effective stiffness degradation that occurred in the reinforced concrete side slab during testing and only minor changes in effective stiffness ratio occurred during the remaining four load levels.

The FRP panel reinforced side slab exhibited a significantly higher effective stiffness ratio in comparison to the reinforced concrete slab throughout the loading range and maintained a relatively constant effective stiffness ratio of 0.9 or greater for the first five loading levels. At the 578 kN (130 kip) load level, which is 5.9 times the AASHTO service load, the effective stiffness ratio of the composite side decreased by 8% to 0.83 indicating that additional damage had occurred at this load level. The damage that occurred at this load level however, did not significantly affect the load-deflection slope performance of the system, which decreased an average of 5 % per level during the next two load levels. At the 845 kN (190 kip) load level, equivalent to 8.6 times the AASHTO service load, a 13% decrease in the effective stiffness ratio to a value of 0.65 was observed. Note that initial signs of punching shear were observed on the FRP panel side slab at this load level.

For comparison, the effective stiffness and stiffness ratio values were recalculated with the secant method using the following equation:

$$\text{Effective Stiffness} = \frac{P_f - P_o}{\delta_f - \delta_o} \qquad 3.3$$

where

P_f = Target actuator load of a load cycle based on loading protocol

P_o = Nominal actuator load at the start of experimental testing

δ_f = Deflection at target actuator load, P_f, at the location under consideration

δ_o = Deflection at nominal actuator load, P_o, at the location under consideration

Note that the nominal minimum threshold actuator load of 4.5 kN (1 kip) at the start of experimental testing was used throughout the effective stiffness calculation as opposed to the nominal load and deflection at the start of each load cycle as described previously in Equation 3.1. By using the same lower value for the stiffness calculation, the effect of the residual deflections that occur between load cycles is taken into account, therefore these calculated effective stiffness values are lower than the previously calculated values which ignored residual deflections. The difference between the two calculation methods for the effective stiffness of the bridge decks is illustrated in Figure 3.36.

A comparison between the effective stiffness ratios determined using the two different load-deflection slope calculation methods is given in Table 3.11, in which the effective stiffness results as well as the percent difference between the two methods are tabulated. The first two load level of the effective stiffness ratios are the same for both methods because the same nominal load and deflection value is used in both calculation methods whereas the adaptive secant stiffness method utilizes different nominal load and deflection values for all higher load levels and yields comparatively larger effective stiffness ratios for the remaining load levels.

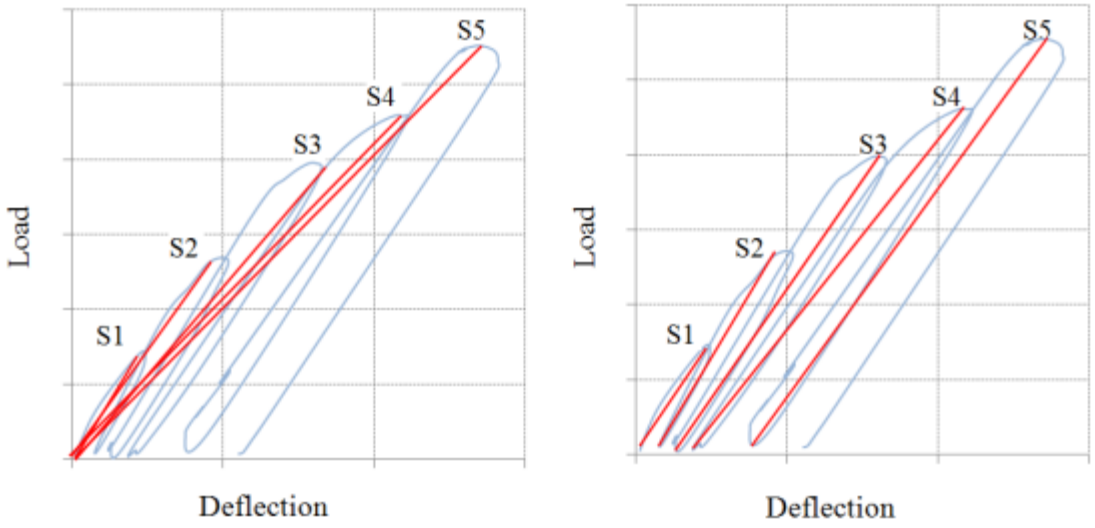

(a) Secant stiffness method (Eqn 3.3) (b) Adaptive secant stiffness method (Eqn 3.1)

Figure 3.36 Illustration showing difference in stiffness calculation methods

Table 3.11 Comparison of effective stiffness ratios found using two different methods of calculating effective stiffness

Target Load Level		Effective stiffness ratio- adaptive secant stiffness method (Equation 3.1)		Effective stiffness ratio- secant stiffness method (Equation 3.3)		% difference in effective stiffness ratios between methods	
kN	kip	Composite side	RC side	Composite side	RC side	Composite side	RC side
98	22	1.00	1.00	1.00	1.00	0.0%	0.0%
222	50	0.90	0.83	0.90	0.83	0.0%	0.0%
311	70	0.96	0.79	0.79	0.67	18.7%	16.9%
400	90	0.94	0.72	0.80	0.64	15.1%	12.5%
489	110	0.90	0.62	0.74	0.51	19.0%	19.5%
578	130	0.83	0.56	0.71	0.48	14.6%	15.0%
667	150	0.78	0.52	0.64	0.41	18.9%	23.3%
756	170	0.75	0.50	0.63	0.41	16.7%	20.6%
845	190	0.65	0.49	0.51	0.36	23.4%	31.1%
890	200	0.51	0.45	0.43	0.34	17.5%	26.6%

In field applications of a bridge deck system, desirable load-deflection slope characteristics of the deck both with and without residual deflections included are very important. Under a given traffic load, the total deflection of the bridge including the accumulated residual deflections determines whether a system can meet the serviceability requirements regarding maximum live load deflections specified by AASHTO. However, the quality of ride for motorists and pedestrians crossing the bridge is established from the effective stiffness calculations which determine the slope of the load deflection curve without including the residual deflections. Figure 3.37 graphically summarizes the data from Table 3.11 to illustrate the difference between the two methods for calculating the effective stiffness.

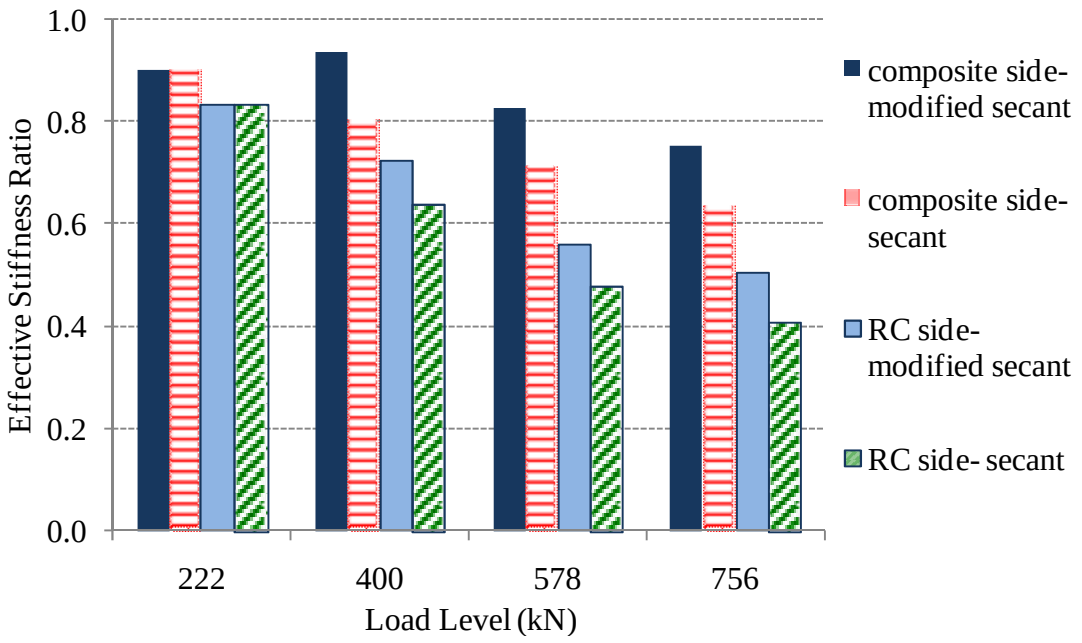

Figure 3.37 Effective stiffness ratios for two methods of calculating stiffness

Based on the effective stiffness ratios calculated using both the secant method described on page 92 and the adaptive secant stiffness method described on page 87, the composite side slab exhibits significantly more desirable load-deflection slope characteristics than the reinforced concrete side slab. The effective stiffness ratios determined using the adaptive secant stiffness method (Equation 3.1) show that for load levels up to the 489 kN (110 kip), which is equivalent to approximately 5 times the AASHTO service load, the slope of the load-deflection curve for the composite side only degraded by 10% overall whereas the reinforced concrete side exhibited a 38% overall decrease in the effective stiffness ratio (Figure 3.35). Additionally, the composite side maintained larger effective stiffness ratio values as compared to the reinforced concrete side for all load levels and degraded at a significantly slower rate. The composite side also retained larger effective stiffness ratios throughout the loading range for the secant stiffness calculations which included the residual deflections of the bridge decks.

3.8.4 Deflection Profiles

In this section, deflection profiles throughout the test specimen for key load levels up to ultimate capacity are presented. The primary purpose for obtaining the displacement profiles was to determine the extent to which the two reinforcement systems were able to distribute the wheel load over a larger area in both the longitudinal and the transverse directions, thus helping to avoid localized punching shear failure. Unless otherwise noted, the deflection profile figures in this section all maintain the same deflection scale, which accommodates the maximum values

observed in the specimen at ultimate capacity, in order provide context for each deflection value in relation to the overall deformation of the structure.

The deflection profiles along the length of the deck above the central and outer stems are presented in Figure 3.38, Figure 3.39 and Figure 3.40. These figures indicate that the deck above each of the three stems deflected evenly along the length of the stems. The uniform deflections observed in deck above the stems indicate that the vertical deformations of the stems do not significantly affect the overall structural response of the test specimen.

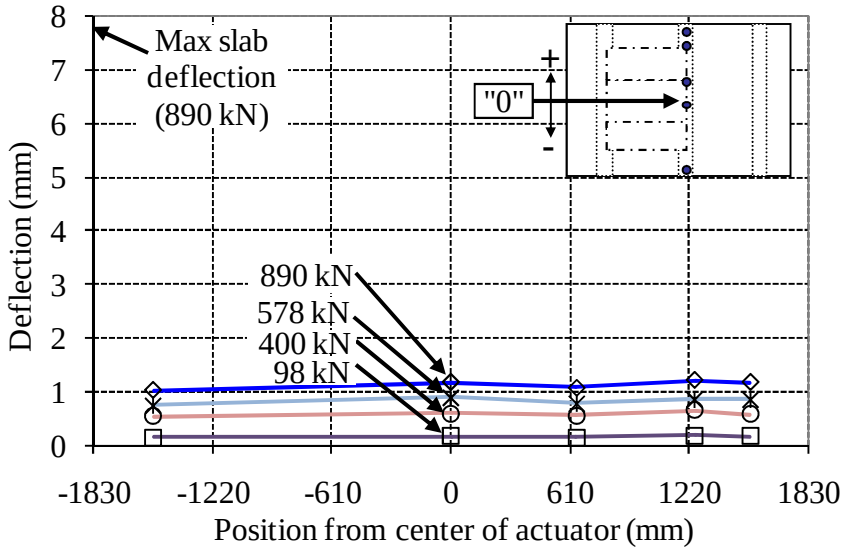

Figure 3.38 Deflection profile along length of deck above central stem

The maximum deflection in the deck above the stems at ultimate capacity was 1.3 mm (0.05 in), which indicates that the actual corresponding maximum deflections at the midpoints of the slabs are approximately 1 mm (0.04 mm) smaller than the values given from the linear potentiometers due to the deflection contribution from

stems. Note that the maximum deflections above the stems at ultimate capacity were approximately 6.2 times smaller than the corresponding midpoint deflection of the reinforced concrete side slab.

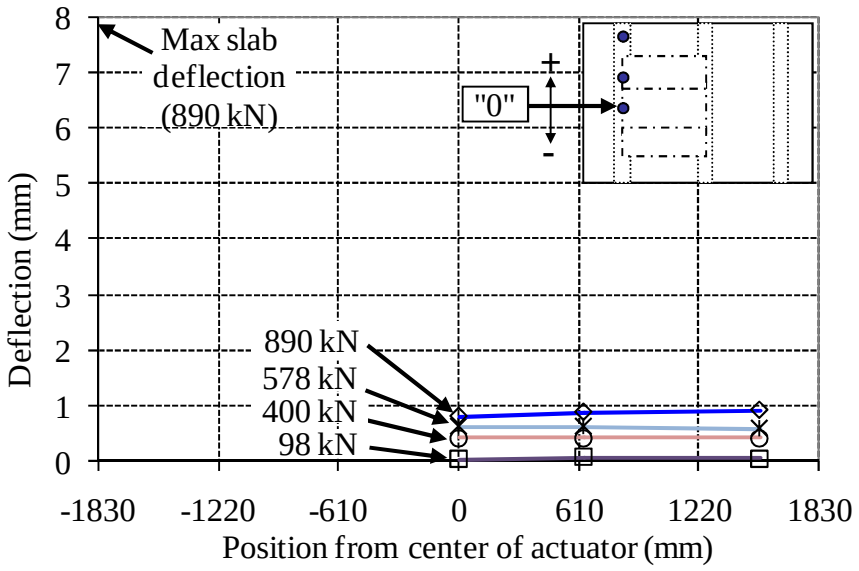

Figure 3.39 Deflection profile along length of deck above composite side stem

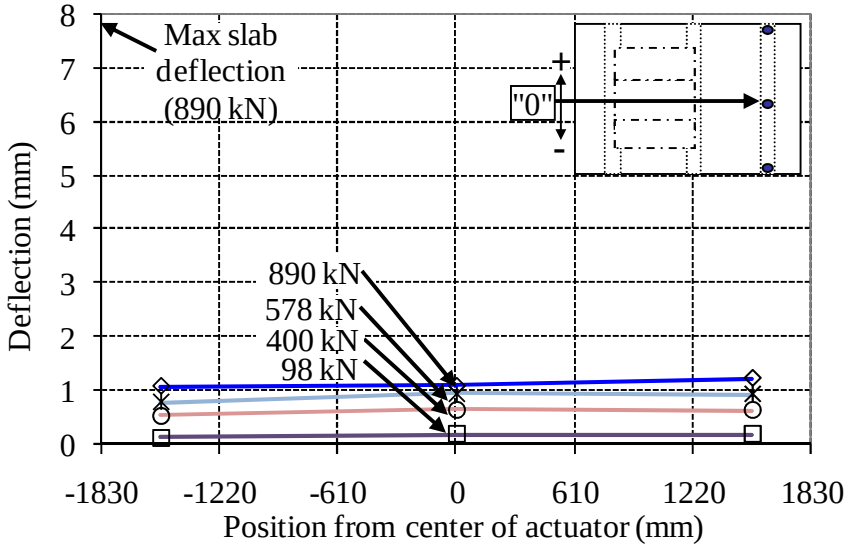

Figure 3.40 Deflection profile along length of deck above RC side stem

The deflection profiles along the centerline of the two slabs are shown in Figure 3.41 and Figure 3.42. Both slabs maintained comparably shaped deflection profiles with larger deflections observed throughout the reinforced concrete side for loadings up to 756 kN (170 kip), equivalent to approximately 7.7 times the AASHTO service load. For the remaining loading up to ultimate capacity, the reinforced concrete side continued to deflect to a greater extent whereas the composite side exhibited a more localized deformation profile at these higher load levels. As expected, the highest deflection values for both slabs were observed from the linear potentiometers below the two hydraulic actuators, with progressively smaller deflections at distances away from these locations. Similarly, because the centerline deflection profiles shown in Figure 3.41 and Figure 3.42 were obtained from locations directly below the actuators, these figures contain higher deflection values as compared to deflection profiles obtained from locations offset from the centerlines, shown in Figure 3.50 - Figure 3.53.

In order to more thoroughly compare the level of localized deformations in the slabs, the superimposed deflection profiles along the centerline of the decks are shown at different load levels. The deflection profiles shown in Figure 3.43 at the load level of 756 kN (170 kip), equivalent to 7.7 times the AASHTO service load, are comparably shaped for the two sides, with larger deflections along the entire length of the reinforced concrete side.

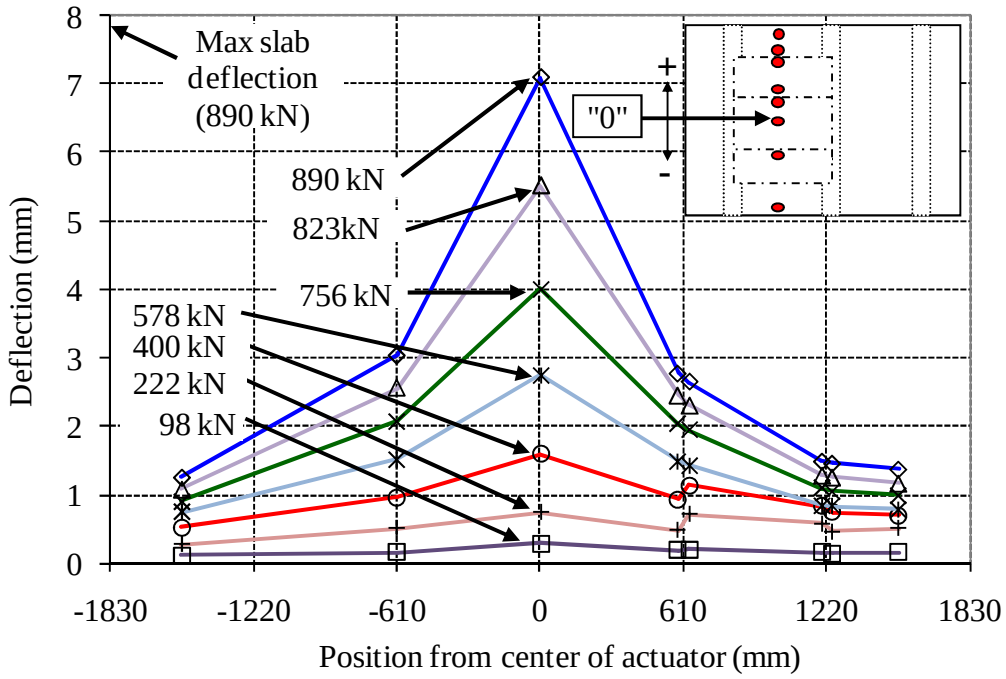

Figure 3.41 Deflection profile along centerline of composite side deck

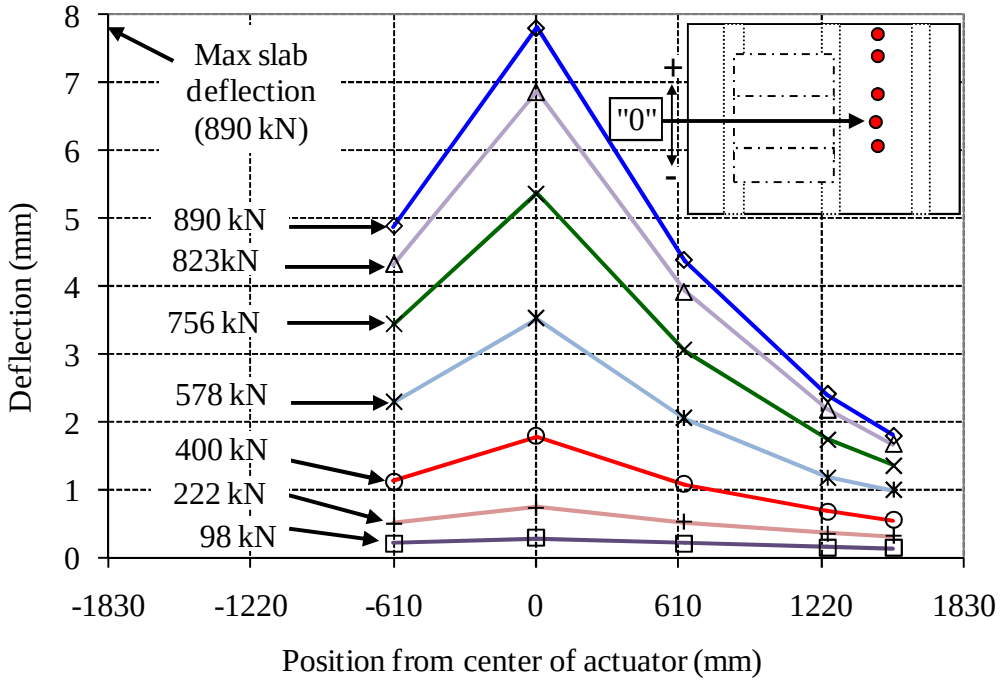

Figure 3.42 Deflection profile along centerline of RC side deck

At the 845 kN (190 kip) load level, which is equivalent to 8.6 times the AASHTO service load and was the load level at which initial signs of punching shear damage were observed, the composite side exhibited more localized deflections in the close proximity to the actuator, however still maintained smaller deflections overall than observed in the reinforced concrete side as shown in Figure 3.44. At ultimate capacity, as shown in Figure 3.45, the localized deflections near the point of load application were significantly more pronounced for the composite side, however, the deflections were still less than the corresponding reinforced concrete values and the load level was equivalent to over nine times the AASHTO service load.

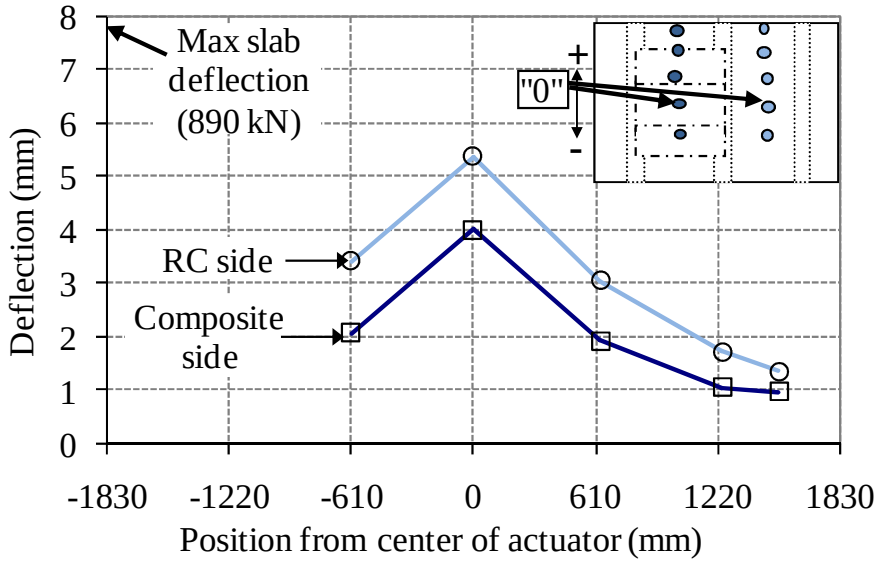

Figure 3.43 Comparison of deflection profiles at a load level of 756 kN

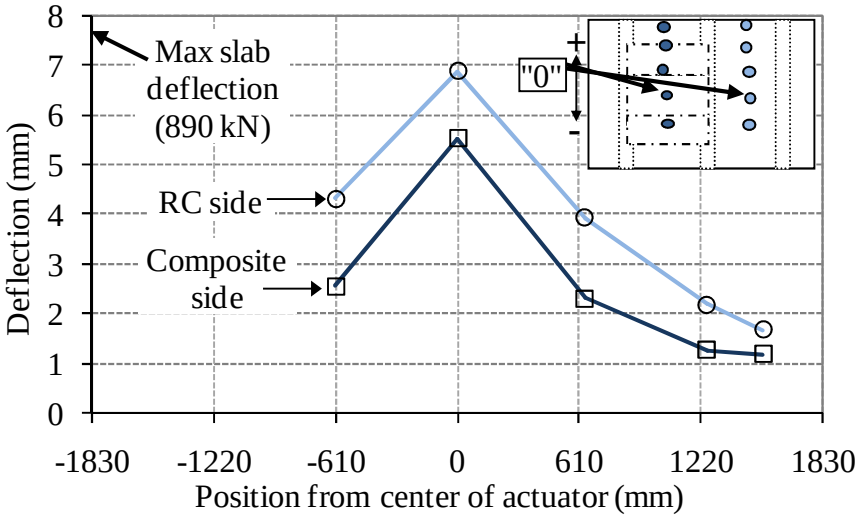

Figure 3.44 Comparison of deflection profiles at a load level of 845 kN

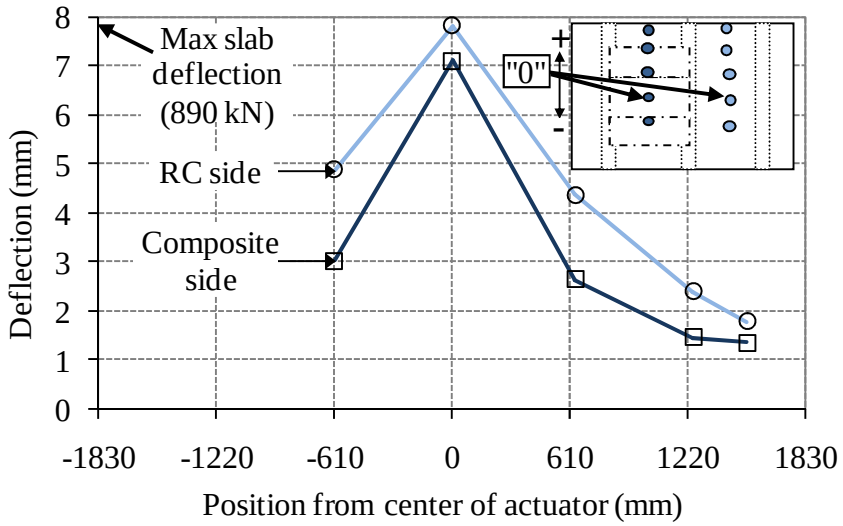

Figure 3.45 Comparison of deflection profiles at ultimate capacity (890 kN)

An alternative comparison of the deflection values along the centerline of the two spans was performed by calculating the percentage change in deflection between a composite side linear potentiometer and a reinforced concrete side linear potentiometer located at the same distance along the centerline of the deck slabs. The percentage change in deflections values were calculated with respect to the composite side and were computed at different load levels. The results for locations 305 mm (2 ft) on either side of the center deflections (Figure 3.47 and Figure 3.48) and 610 mm (4 ft) away from the center deflections (Figure 3.47) all show comparable trends for the different load levels.

The percent change in deflections between the two sides at these locations increases steadily with successive load levels up to a load level of 845 kN (190 kip), which is equivalent to 8.6 times the AASHTO service load, followed by a decrease in values for the ultimate capacity load level of 890 kN (200 kip). This trend illustrates that as the load to which the test specimen is subjected increases, the deflection values on the reinforced concrete side at these locations become increasingly greater than the composite side up until ultimate capacity is reached where the difference between the deflections both sides becomes less pronounced. In contrast, comparison of central deflections shown in Figure 3.49 illustrates a steady increase in values up to a load level of 489 kN (110 kip) followed by relatively constant values for the subsequent four load levels and then a decrease in values for the 845 kN (190 kip) load level and for the ultimate capacity load level.

The difference in the response at the center points as compared to the other locations along the centerlines of the two slabs can be attributed to the more localized

loading of the FRP panel in the longitudinal direction. Note that although the composite side displays a slightly more localized deflection response in the longitudinal direction, the reinforced concrete side deflects significantly more at all locations and at all load levels examined. For instance, at the 489 kN load level, which is equivalent to approximately five times the AASHTO service load, the reinforced concrete side deflected between 23% and 42% greater than the composite side deflections for the linear potentiometers along the longitudinal profile whereas at the 845 kN load level, the reinforced concrete side exhibited between 24% and 73% greater deflections.

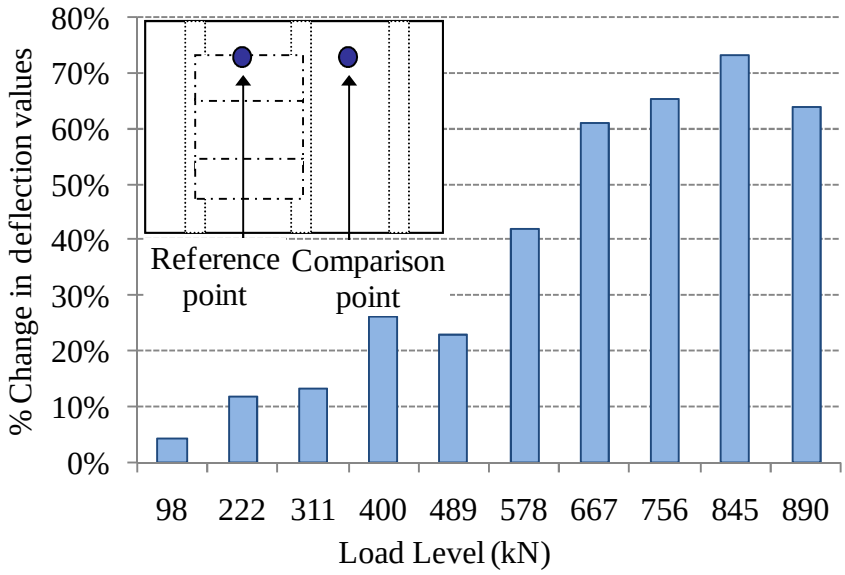

Figure 3.46 Percent change between composite side and RC side deflection values at different load levels- linear potentiometers located at 2/3 span along the centerline of each deck

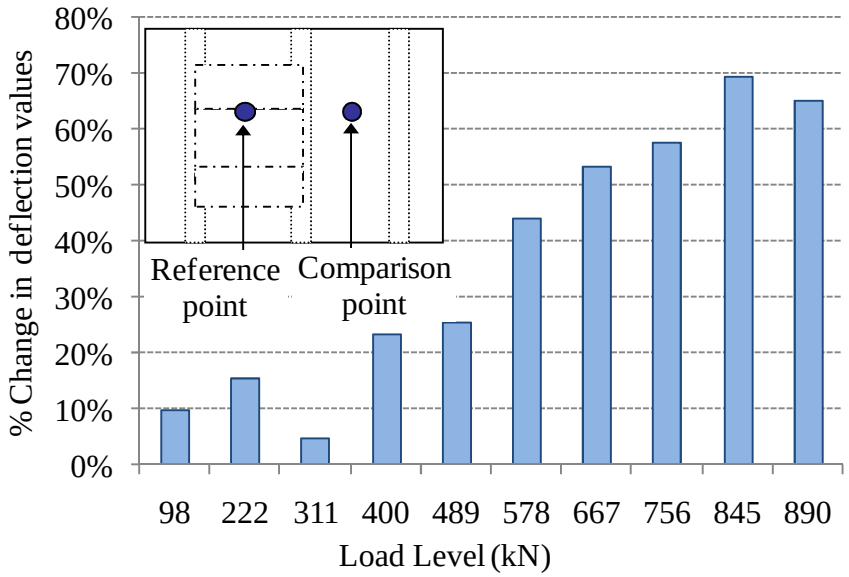

Figure 3.47 Percent change between composite side and RC side deflection values at different load levels- linear potentiometers located at 1/3 span along the centerline of each deck

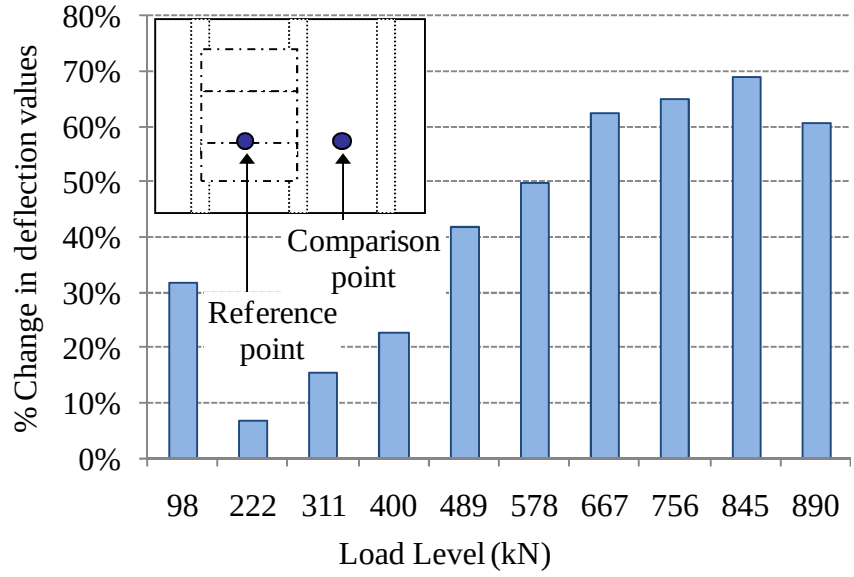

Figure 3.48 Percent change between composite side and reinforced concrete side deflection values at different load levels- linear potentiometers located at 1/3 span along the midspan of each deck

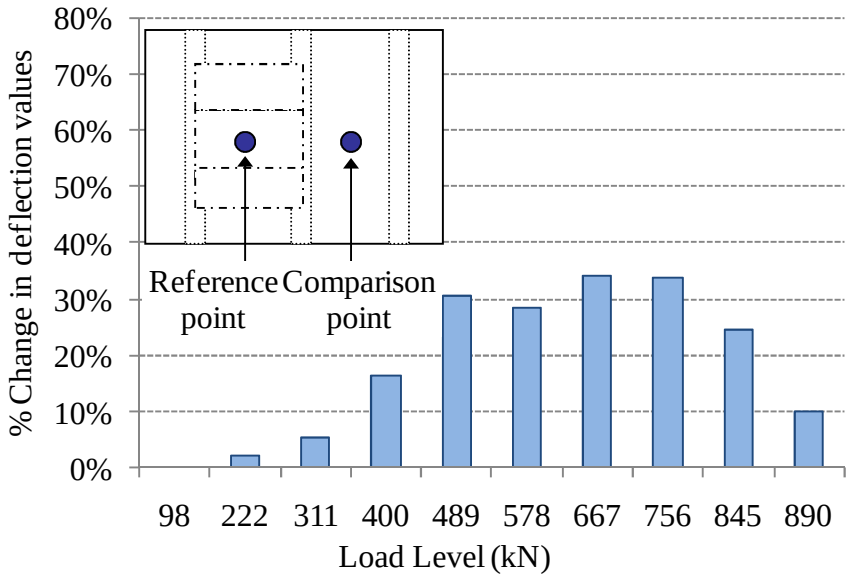

Figure 3.49 Percent change between composite side and RC side deflection values at different load levels- linear potentiometers located at the center of each deck

The deflection profiles along the length of the deck, which are offset from the centerlines of the slabs by 305 mm (12 in), are shown in Figure 3.50 - Figure 3.53 and give useful information regarding the effectiveness of the reinforcement systems to distribute the actuator load to the surrounding regions. For load levels up to 578 kN (130 kip), the deflection profiles in the longitudinal direction near the outer stems (Figure 3.50 and Figure 3.51) as well as the profiles near the central stem (Figure 3.52 and Figure 3.53) illustrate comparable deflections in both slabs, with slightly larger values observed on the reinforced concrete side. For the remaining load levels until ultimate capacity, the composite side clearly exhibits the same localized deformation in close proximity to the actuator that was noted for the centerline deflection profile in Figure 3.41.

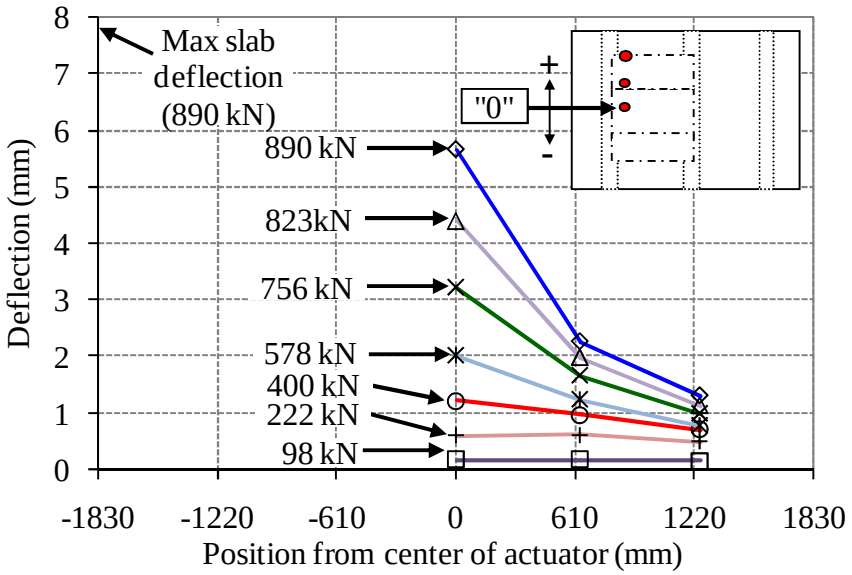

Figure 3.50 Deflection profile along row 2 of linear potentiometers (offset from composite side centerline by 305 mm)

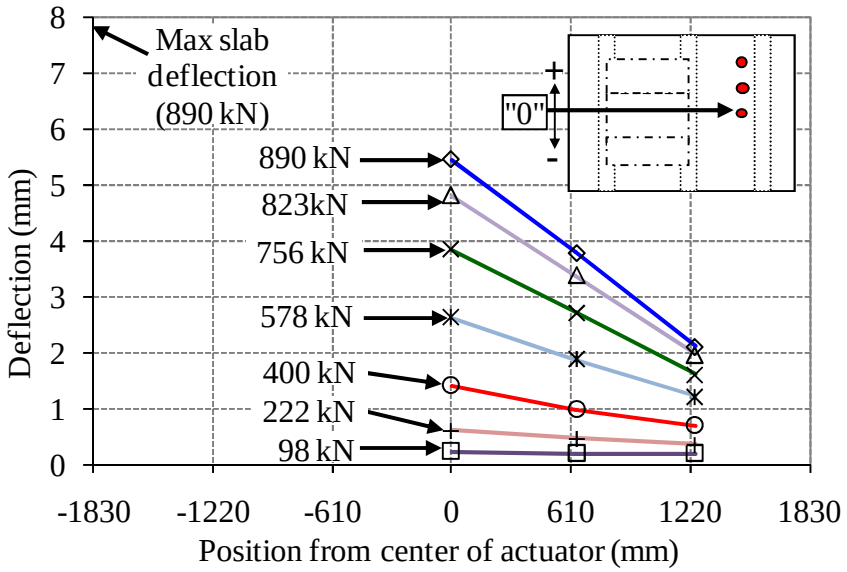

Figure 3.51 Deflection profile along row 8 of linear potentiometers (offset from RC side centerline by 305 mm- see Figure 3.19)

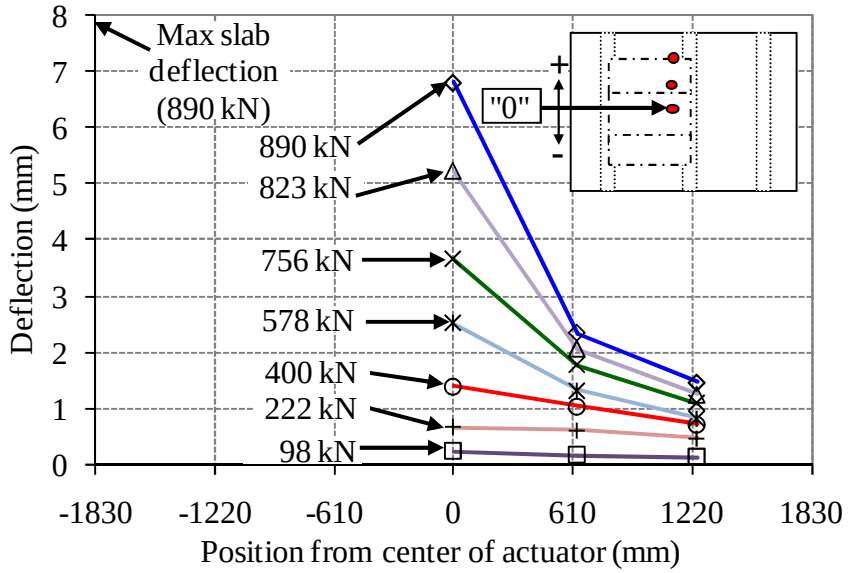

Figure 3.52 Deflection profile along row 4 of linear potentiometers (offset from composite side centerline by 305 mm- see Figure 3.19)

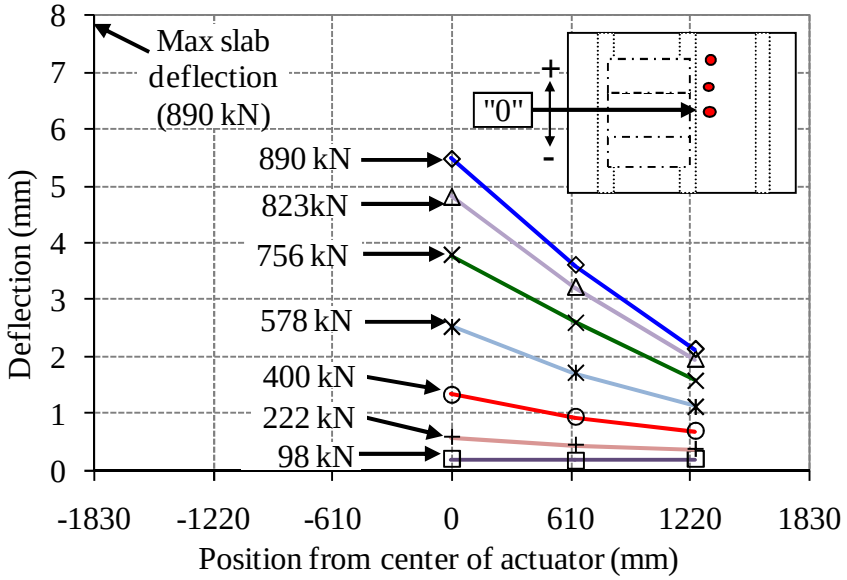

Figure 3.53 Deflection profile along row 6 of linear potentiometers (offset from RC side centerline by 305 mm- see Figure 3.19)

The deflection profile along the transverse centerline of the test specimen is presented in Figure 3.54. The highest deflection values were observed near the actuator locations and minimal deflection values were observed above each of the three stems. Both sides maintained comparable deflection profiles up to the 400 kN (89.9 kip) load level, equivalent to 4.1 times the AASHTO service load. At the higher load levels, the reinforced concrete side exhibited significantly more localized deflections in close proximity to the point of load application as shown in Figure 3.54, which is opposite the trend observed for the longitudinal direction deflection profile where the composite side exhibited more localized deflections at higher load levels. The significantly improved distribution of the localized point load for the composite side slab transverse deflection profile as compared to the longitudinal deflection profile can be attributed to the presence of the stiffeners described in Section 3.3, which are oriented in the transverse direction.

In addition to the centerline profile shown in Figure 3.54, the displacement profiles of three transverse rows of linear potentiometers are presented in Figure 3.55, Figure 3.56 and Figure 3.57, which are offset from the centerline by 1525 mm (60 in), 1245 mm (49 in) and 635 mm (25 in) respectively. The deflections observed on the reinforced concrete side at load levels above 400 kN (89.9 kN) are consistently higher than the composite side deflections.

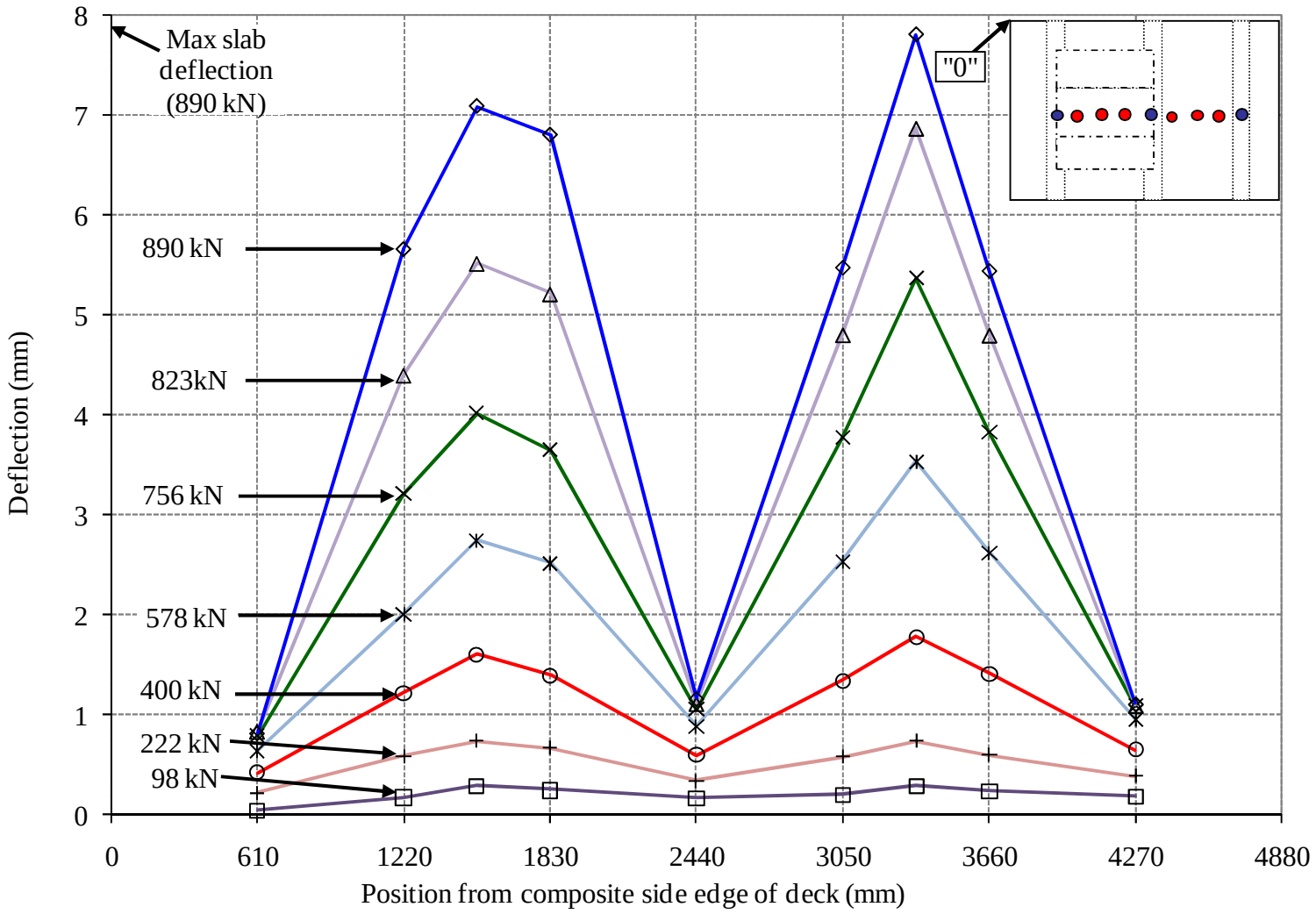

Figure 3.54 Deflection profile along centerline of specimen

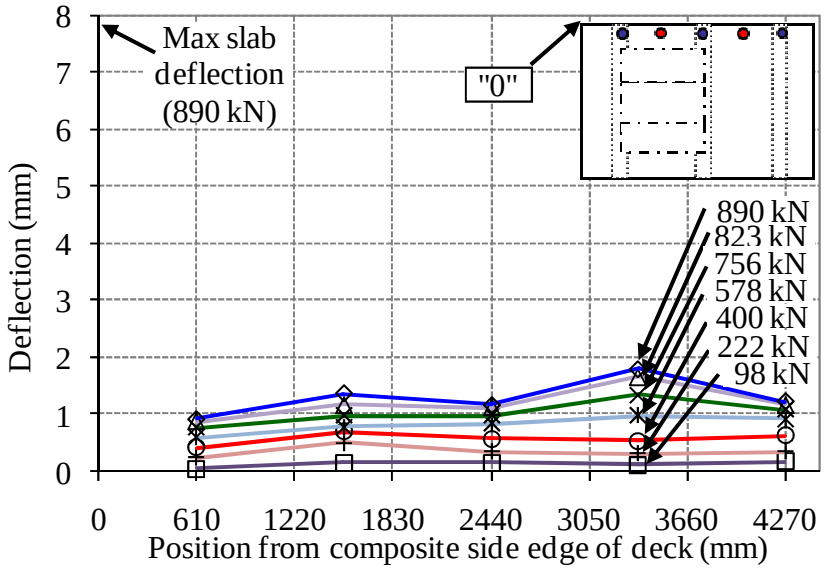

Figure 3.55 Deflection profile along row A of linear potentiometers
(offset from test specimen centerline by 1525 mm- see Figure 3.19 and Figure 3.20)

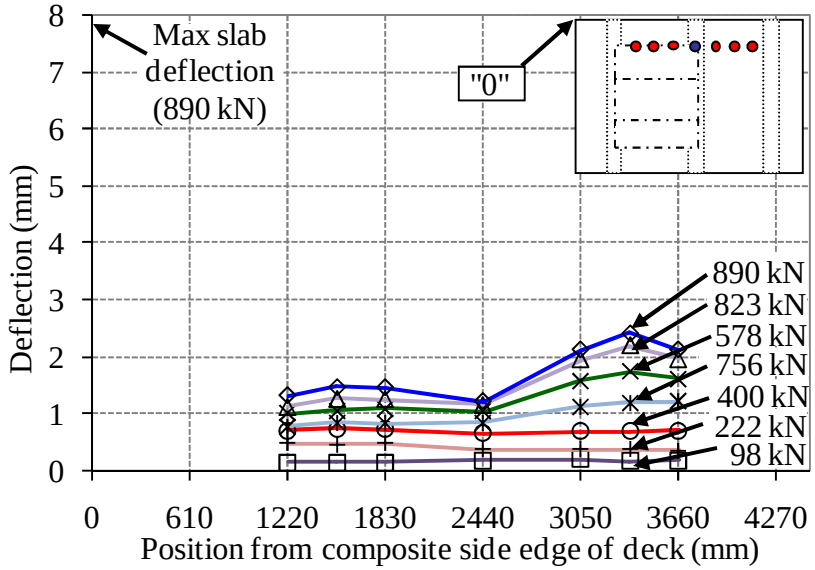

Figure 3.56 Deflection profile along row B of linear potentiometers
(offset from test specimen centerline by 1245 mm- see Figure 3.19 and Figure 3.20)

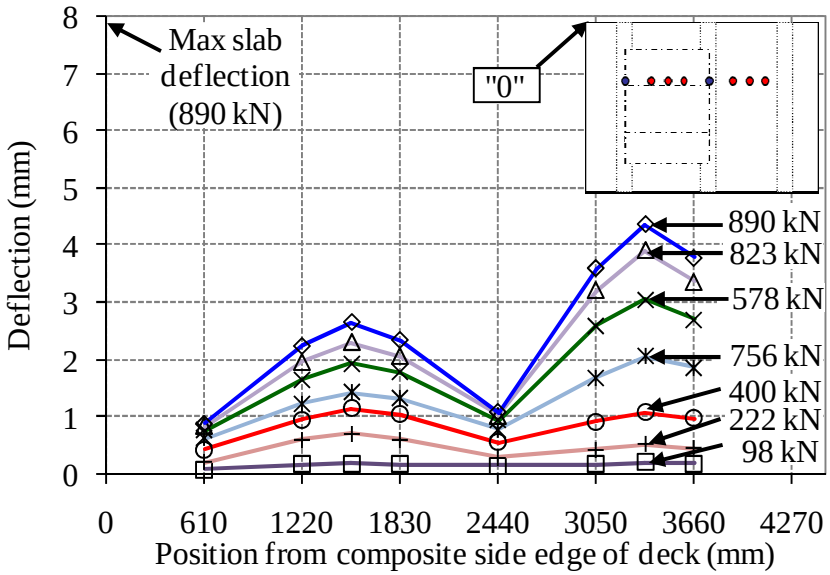

Figure 3.57 Deflection profile along row C of linear potentiometers
(offset from test specimen centerline by 635 mm- see Figure 3.19 and Figure 3.20)

The envelope plots of load versus deflection for linear potentiometers adjacent to the central linear potentiometer locations are shown in Figure 3.58 and Figure 3.59. Figure 3.58 compares the load-deflection plots of the linear potentiometers that are located a distance of 610 mm (2 ft) away from the center of the test specimen along the centerlines of the two slabs. The very similar curves for linear potentiometers the two linear potentiometers on the composite side (C3B and D3B) indicate a very symmetric deflection profile for the composite side deck in the longitudinal direction whereas the reinforced concrete side exhibits slightly unsymmetrical deflections (C7B and D7B). For the composite side, the load-deflection curves remain approximately linear up to the 756 kN (170 kip) load level and displays a more relaxed slope for the remainder of the loading. Conversely, the reinforced concrete side only maintains an

approximately linear slope up to the 311 kN (70 kip) load level and then exhibits a nonlinear response for the remainder of the loading.

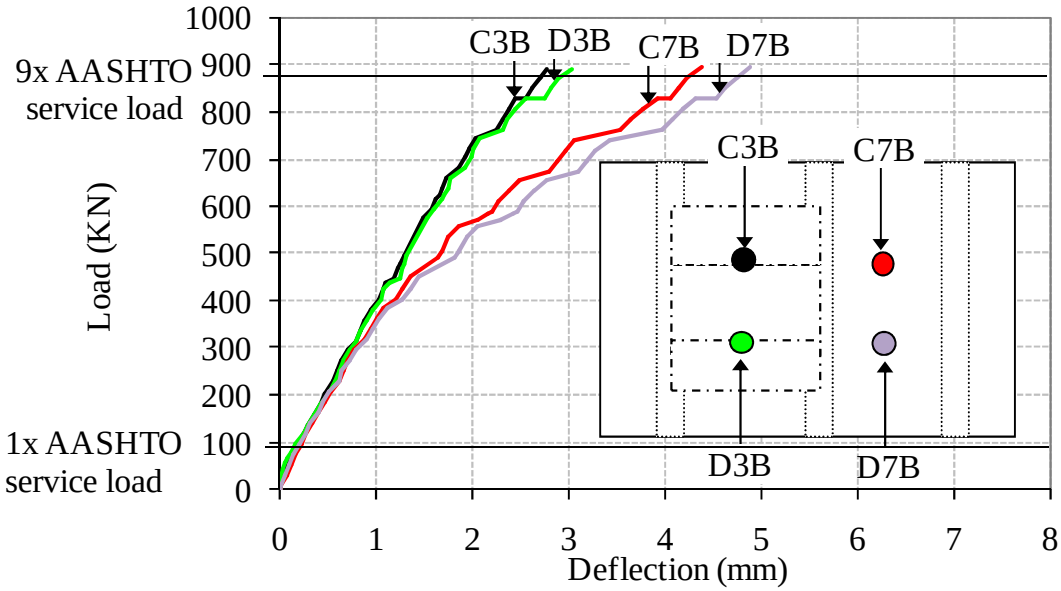

Figure 3.58 Envelope plot of load versus deflections for linear potentiometers along the centerlines of the two slabs
(located 610 mm from the test specimen centerline- see Figure 3.19)

The load versus deflection envelope plots for linear potentiometers which lie along the centerline of the test specimen and are positioned 610 mm (2 ft) on either side of the middle of both deck slabs are shown in Figure 3.59. Note that the linear potentiometers at three of the four locations (M4B, M6B and M8B) display equivalent envelope plots while the fourth linear potentiometer (M2B), located on composite side slab adjacent to the exterior stem, exhibits a higher slope and smaller deflections throughout the loading range. The deflection values for linear potentiometer M2B during experimental testing were an average of 20% smaller than the deflections at the other three locations with a standard deviation of 4%.

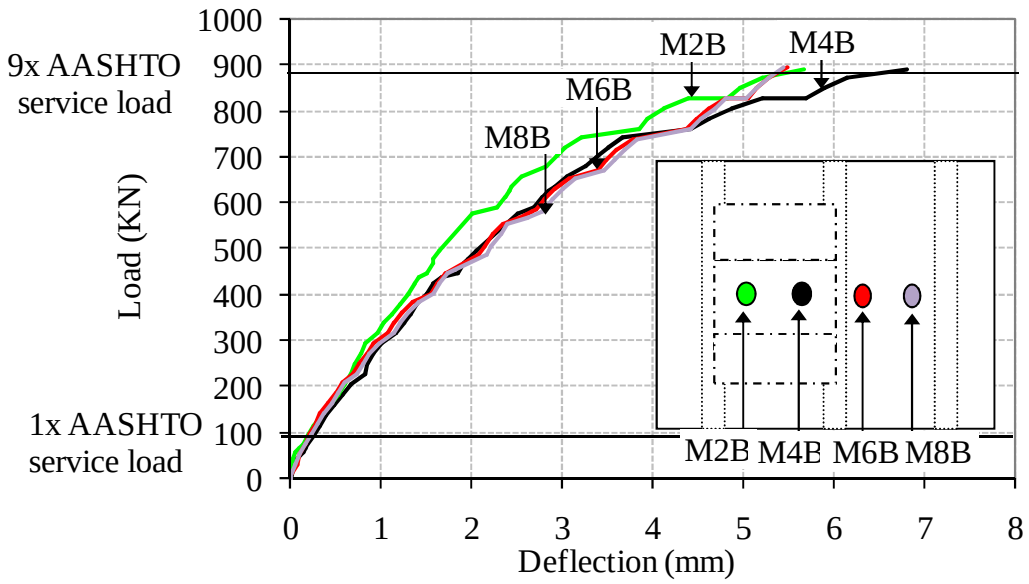

Figure 3.59 Envelope plot of load versus deflections for linear potentiometers along the centerline of the test specimen
(located 610 mm on either side of the deck centerlines- see Figure 3.19)

The maximum deflection values measured in the deck slab were located at the midspan of the two slabs, directly below the two actuators. At the 890 kN (200 kip) load level, equivalent to over nine times AASHTO service load, the composite side displayed a 7.09 mm (0.279 in) center deflection, while the reinforced concrete side displayed a 7.81 mm (0.307 in) center deflection. A detailed discussion of the progression of the center deflections, as they pertain to the effective stiffness of the slabs, is provided in Section 3.8.3, beginning on page 87 for the FRP panel reinforced slab and for the reinforced concrete slab.

One important difference between the deflection profiles in the longitudinal direction versus the transverse direction is the orientation and design of the stiffeners and the layup of the FRP panels. Due to the transverse orientation of the stiffeners, the transverse direction deflection profile is significantly improved due to the

additional stiffening added by the stiffener elements while the longitudinal direction deflection response of the composite side deck slab is not impacted considerably by the presence of the stiffeners. In comparison to the reinforced concrete side, the transverse direction deflection profile for the composite side is significantly more dispersed as observed in Figure 3.54 and the concrete side deflects much more in the localized region surrounding the actuator, especially at high load levels. In the longitudinal direction, in which the stiffeners do not play a large role in the structural response, the two systems exhibit comparable deflection profiles, with the reinforced concrete side deflecting more throughout and the composite side exhibiting a slightly more localized response at high loading levels.

3.8.5 Strain Development

The strain development within the test specimen was observed though the examination of strain gages applied to the steel reinforcement as well as to the FRP panels within the test specimen. The precise location of all strain gages is given in Section 3.6.2. Note that strain values reported as negative indicate compressive strains whereas positive values indicate tensile strains.

As discussed in Section 3.1, the FRP structural formwork panels take the place of the bottom steel reinforcement. Since there is no bottom steel reinforcement for the central section of the composite side deck, the strain measurements for the bottom of the slab are obtained from strain gages attached to the bottom of the FRP panels. Conversely, strain gages attached to the lower level of steel reinforcement in the deck slab are used for the remainder of the test specimen. The difference between the

position within the depth of the deck slab for the strain gages attached to the composite side and reinforced concrete side deck slabs is approximately 41.3 mm (1.63 in) for the bottom transverse strain gages and 57.2 mm (2.25 in) for the bottom longitudinal strain gages as illustrated in Figure 3.60. The total thickness of the deck slab is only 178 mm (7.0 in), therefore a difference in position of 57.2 mm (2.25 in) accounts for over 30% of the total thickness of the slab. As a result, these strain values cannot be directly compared without further data manipulation to account for the difference in positions.

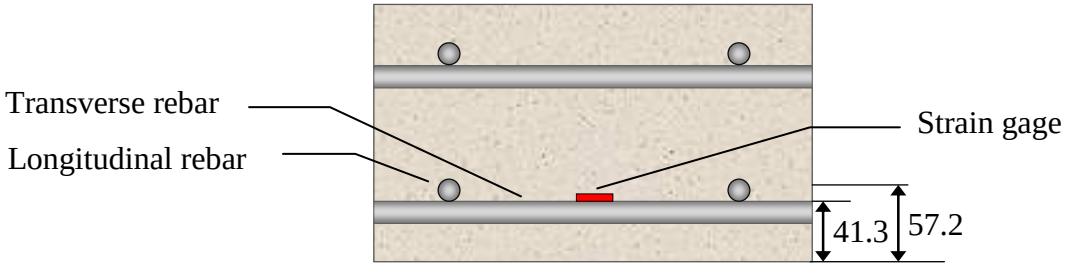

(a) RC side bottom transverse strain gage on top of bottom layer of transverse rebar

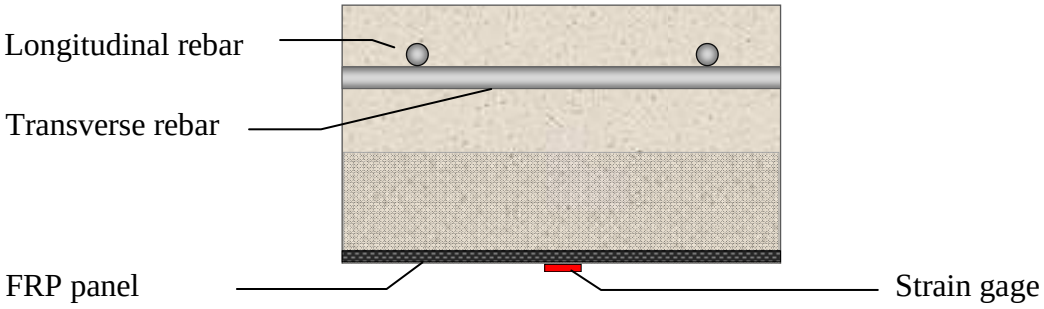

(b) Composite side bottom transverse strain gage on bottom of FRP panel

Figure 3.60 Deck slab cross-section illustrating location of strain gages within depth (measurements, in millimeters, show the difference in depth between strain gages attached to FRP panel and strain gages attached to bottom steel reinforcement)

In order to more easily compare the strains in the FRP panel to the strains in the bottom steel reinforcement, a linear strain distribution as shown in Figure 3.61 was assumed. The modification in strain values is done by adjusting the strains measured in the bottom layer of steel reinforcement on the reinforced concrete side along an assumed linear strain distribution to the equivalent depth within the slab where the FRP panel strain gages were attached on the FRP panel side deck slab. The predicted strains are likely to display larger variations from actual strains for regions of discontinuity within the specimen, however the linear strain distribution and implemented calculations described below have yielded good correlation with experimental results for segments where the FRP panel and bottom steel reinforcement overlap, thereby allowing direct validation of predicted strain values.

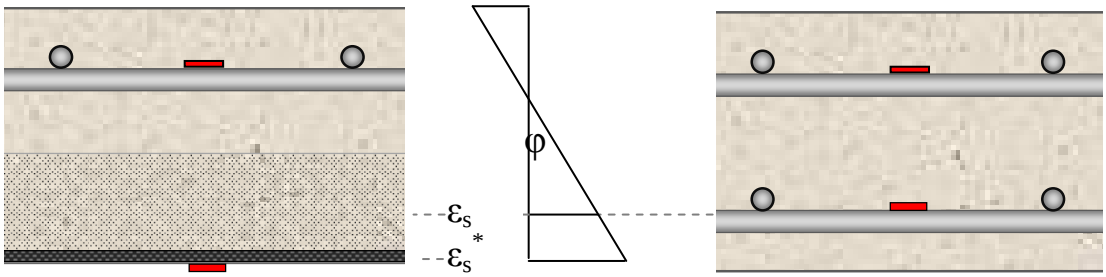

Figure 3.61 Illustration of strain distribution and adjustment of RC side strains

The experimentally determined bottom layer rebar strains, ε_s, were adjusted along the linear strain distribution profile to the same height within the deck slab as the FRP panel strain gages, with the adjusted steel strains labeled as ε_s^*. The curvature, φ, was determined using a straight line theory in which a linear stress

distribution was assumed and transverse effects as well as the top reinforcement were ignored [153]. The strain line theory calculation method uses the reinforcement ratio, ρ, and the modular ratio, n, which are defined in Equations 3.4 and 3.5 respectively.

$$\rho = \frac{A_s}{b \cdot d} \tag{3.4}$$

$$n = \frac{E_s}{E_c} \tag{3.5}$$

where
A_s = Area of tensile steel reinforcement
b = Section width
d = Distance from the extreme compression fiber to tensile reinforcement
E_s = Young's modulus of steel
E_c = Young's modulus of concrete

The values for ρ and n are used to determine the effective length factor for compression members, k, as calculated in Equation 3.6. This term locates the neutral axis at a distance kd down from the extreme compression fiber of the section as shown in Figure 3.62.

$$k = \sqrt{2\rho \cdot n + (\rho \cdot n)^2} - \rho \cdot n \tag{3.6}$$

where
ρ = Reinforcement ratio for the steel reinforcement
n = Modular ratio relating the steel reinforcement to the concrete

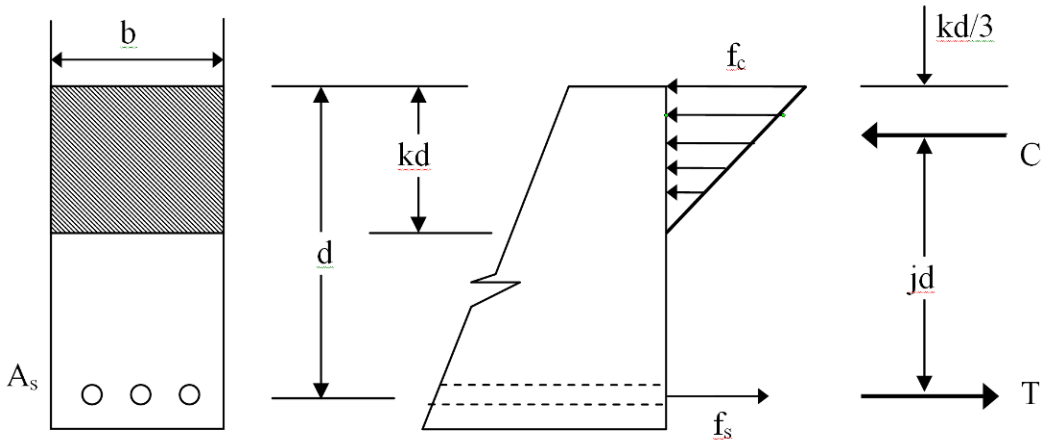

Figure 3.62 Assumed linear stress distribution in straight line theory

The curvature within the slab, φ, is then calculated using Equation 3.7

$$\varphi = \frac{\varepsilon_s}{(d - k \cdot d)} \qquad 3.7$$

where

φ = Curvature in deck slab

ε_s = Strain measured in strain gage on RC side bottom transverse rebar

d = Distance from the extreme compression fiber to tensile reinforcement

k = Effective length factor for compression members (Equation 3.6)

Next, the apparent strain on the RC side, ε_s^*, is found at the same distance along the depth of the deck slab as the strain gages attached to the bottom of the FRP panels using the formula:

$$\varepsilon_s^* = \varepsilon_s + \varphi(d_{FRP} - d_s) \qquad 3.8$$

where

ε_s^* = Apparent strain in the RC side deck adjusted to the same depth as gages attached to FRP panels

ε_s = Strain measured in strain gage on RC side bottom transverse rebar

φ = Curvature in deck slab

d_s = Distance from extreme compression fiber to top of RC side bottom steel reinforcement

d_{FRP} = Distance from extreme compression fiber to bottom of FRP panel

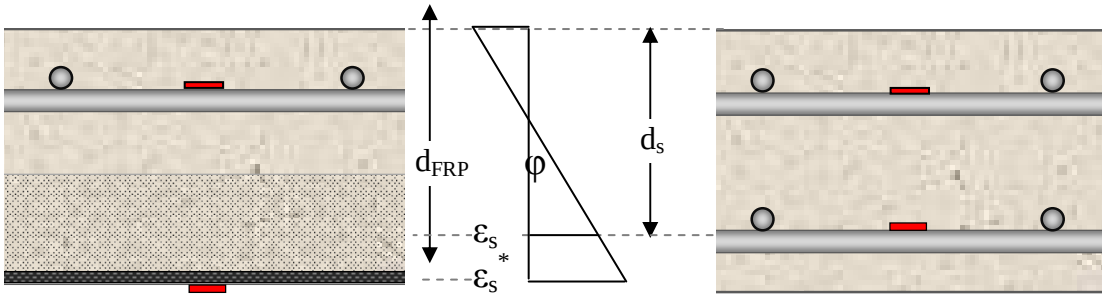

Composite side cross-section Strain distribution RC side cross-section

Figure 3.63 Illustration of strain distribution and adjustment of RC side strains

Note that Equation 3.8 is relevant for calculating apparent strains in either the longitudinal or the transverse direction by simply using a different d_s value. The apparent strain at the bottom of the RC side deck can now be more reasonably compared to the measured strains in the reinforced concrete side.

3.8.5.1 Comparison of Strains in FRP Panel Deck and RC Deck

The load versus strain envelope plot of the bottom longitudinal strain gages located directly below the RC side and composite side actuators is shown in Figure 3.64. The RC side strain values have been adjusted using the method described in Section 3.8.5 in order to determine the apparent strains at the depth within the reinforced concrete side slab that is in line with the FRP panel strain gage.

As observed in Figure 3.64, the two sides maintain comparable strain values up to a load of approximately 200 kN (45 kip), the load at which the reinforced concrete

side load versus strain curve degrades significantly from its original slope due to cracking of the concrete. Note that the composite side strain gage maintains its initial slope up until the 400 kN (90 kip) load level, which is over four times the AASHTO service load. The secondary slope of the load versus strain curve for the composite side remains approximately linear for the remainder of the test specimen loading to ultimate capacity and is shallower than the secondary slope for the reinforced concrete side. The composite side strain values remained lower than the reinforced concrete side strains for loadings up to approximately 500 kN (112 kip) load level, which is approximately 5.1 times the AASHTO service load, because the FRP panel side strain gage reaches a load of nearly double the load taken by the RC side strain gage prior to significant change in the initial load versus strain response.

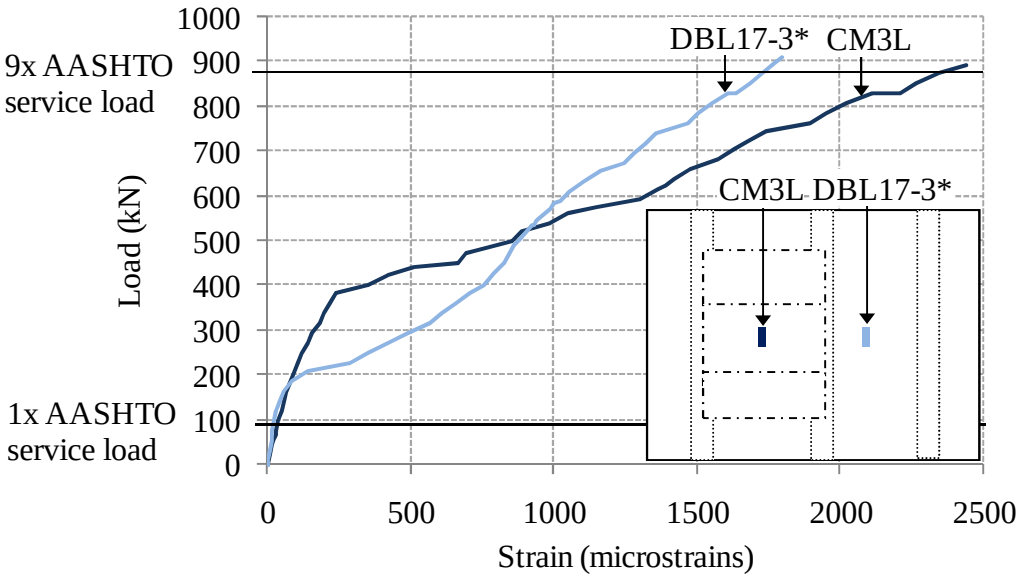

Figure 3.64 Load versus strain for bottom longitudinal strain gages (Gages are located directly below the two actuators. CM3L is on the composite side on the underside of the FRP panel; DBL17-3 is on the RC side bottom longitudinal steel reinforcement and therefore is adjusted using Equations 3.7 and 3.8)

The adjusted strain in the reinforced concrete side bottom longitudinal strain gage at the 489 kN (90 kip) load level, which is approximately 5.0 times the AASHTO service load, was 859.1 microstrains, whereas the strain in the corresponding strain on the FRP panel longitudinal gage was 665.4 microstrains. At the ultimate capacity load of 890 kN (200 kip), the strains in the RC side bottom longitudinal strain gage located directly below the RC side actuator and in the composite longitudinal strain gage located on the bottom side of the FRP panel directly below the composite side actuator were 1119.9 microstrains and 1714.5 microstrains respectively.

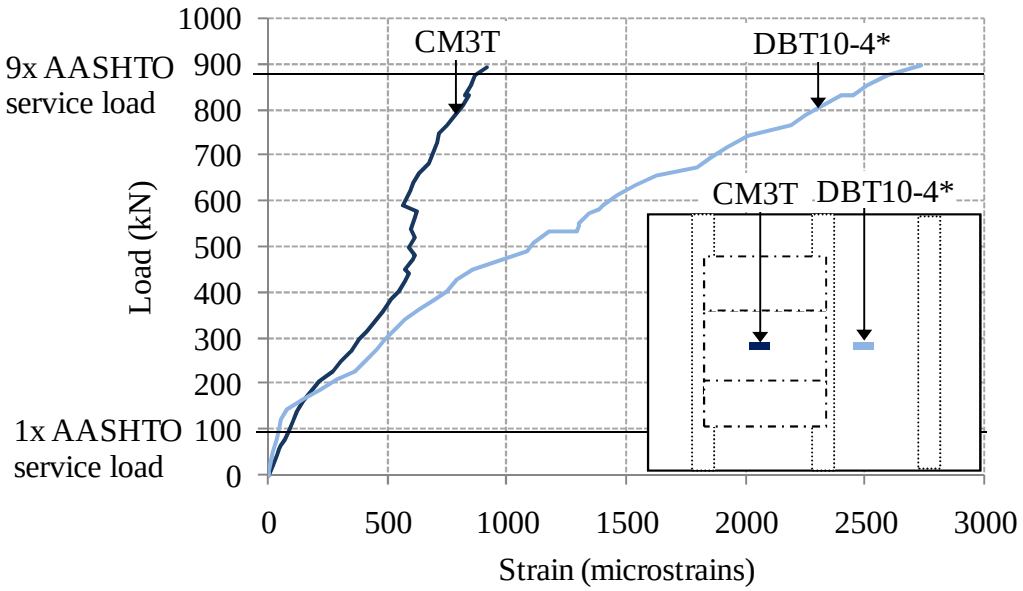

Figure 3.65 Load versus strain for bottom transverse strain gages (Gages are located directly below the two actuators. DBT10-4 is on the RC side bottom transverse steel reinforcement; CM3T is on the composite side underside of the FRP panel and therefore is adjusted using Equations 3.7 and 3.8)

The load versus strain envelope plots for the bottom transverse strain gages are shown in Figure 3.65, where the strain for the reinforced concrete side gage is slightly

less than the FRP panel side gage from initial loading, up to a load of 140 kN (31 kip), which is approximately 1.4 times the AASHTO service load. For higher loadings, the RC side exhibits significantly higher strain values as compared to the composite side. For example, at the 489 kN (110 kip) load level, which is approximately 5.0 times the AASHTO service load, the RC side gage (DBT10-4*) has an adjusted strain of 1079.4 microstrains whereas the composite gage (CM3T) has a strain of 578.3 microstrains, which equates to a 60.5% difference between the two gages.

The strain profile for the top transverse steel reinforcement along the centerline of the specimen is shown in Figure 3.66. As expected for a top rebar under the given loading conditions, the strain gages located at the middle of each deck display compression strains while the gages adjacent to the stems display tensile strains. For each of the displayed load levels, the reinforced concrete side strain gages exhibit comparable or higher values as compared to the corresponding strain gages on the composite side of the test specimen. While Figure 3.66 clearly shows the trend that the reinforced concrete side is experiencing higher strains, especially at higher load levels, the individual comparisons of load versus strain plots for pairs of strain gages are useful in quantifying the difference in response between the two sides.

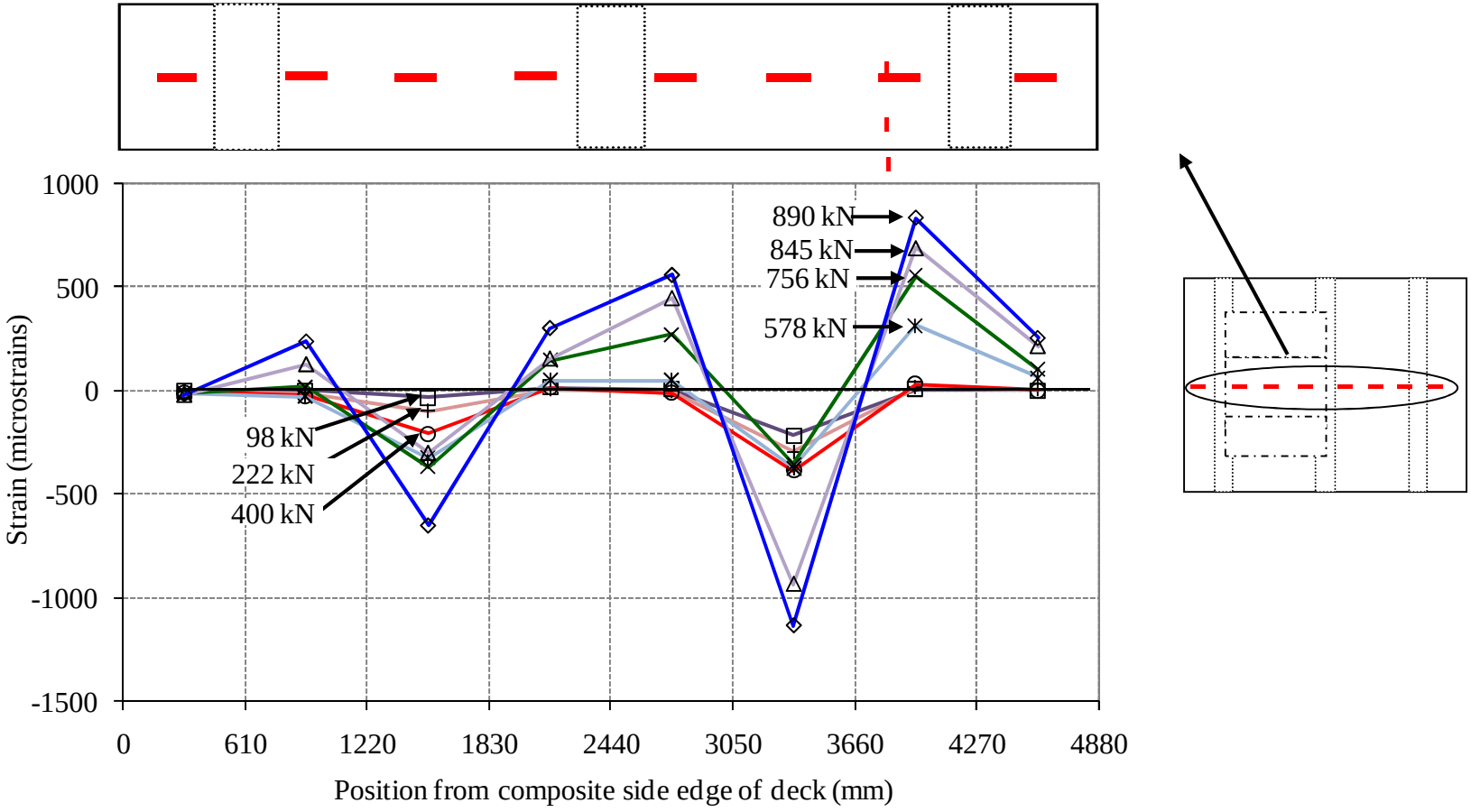

Figure 3.66 Strain profile for top transverse rebar along centerline

The load versus strain responses for the top transverse strain gages located directly below the two actuators (Figure 3.67) illustrates the higher strain values maintained for the top transverse reinforced concrete side strain gage throughout the loading as compared to the composite side strain gage. The reinforced concrete side top transverse strain gage increases nonlinearly up until the 756 kN (170 kip) load level and then it exhibits discontinuities in the remainder of its strain profile. In contrast, the composite side top transverse strain gage displays a far more linear response prior to discontinuities observed at an actuator load of 825 kN (187 kip), which is approximately 8.4 times the AASHTO service load and is the load at which initial signs of punching shear were observed.

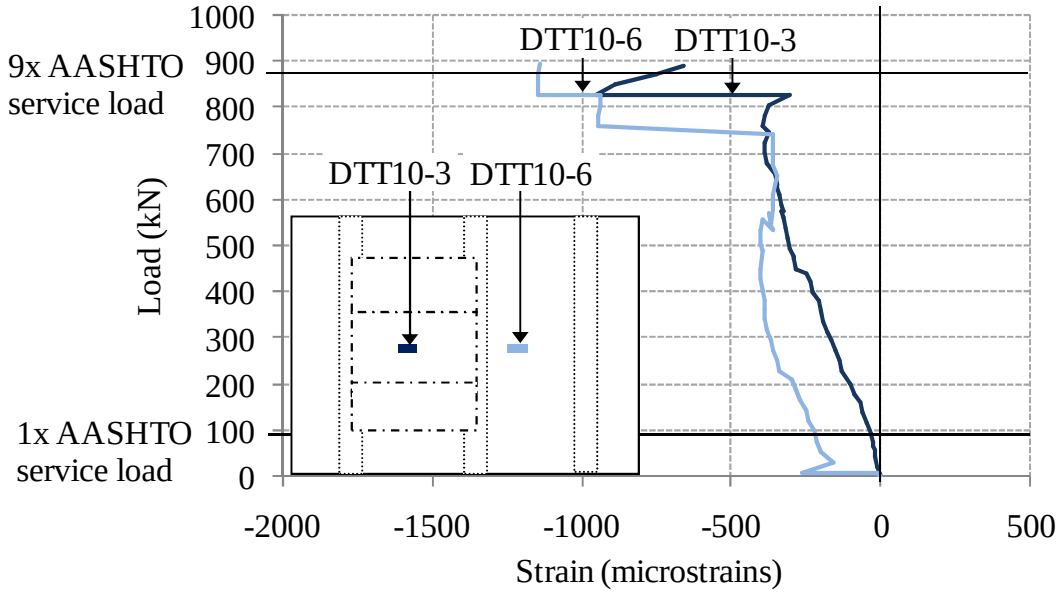

Figure 3.67 Load versus strain for top transverse strain gages
(Both gages are located on the top transverse steel reinforcement directly below the two actuators. DTT10-6 is on the RC side and DTT10-3 is on the composite side)

Figure 3.68 shows the load versus strain envelope plots for the top transverse strain gages which are located 152 mm (6 in) away from either side of the central stem and are 610 mm (2 ft) away from the centerline of the two deck slabs, in the direction of the center stem. The two strain gages showed exhibit equivalent strain values up to a load of 655 kN (155 kip), which is 6.7 times the AASHTO service load. Beyond this load, the reinforced concrete side increased in strain values more quickly such that the strain in the RC side gage (DTT10-5), immediately prior to the discontinuities observed in the load versus strain plots at a load of 829 kN (186 kip) due to the onset of punching shear, was 2.9 times larger than the strain in the composite side strain gage (DTT10-4).

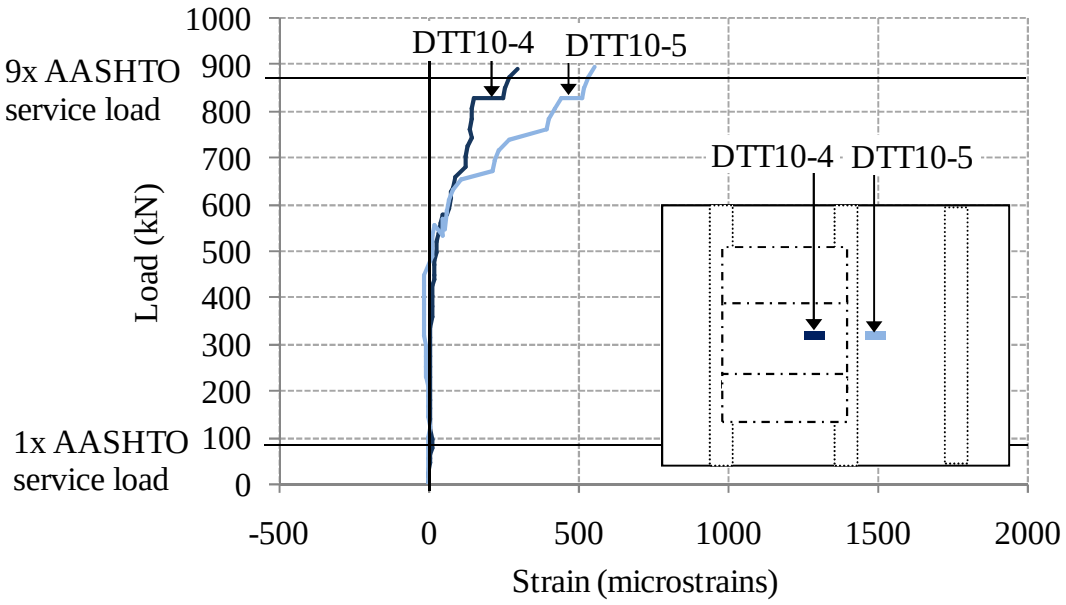

Figure 3.68 Load versus strain for top transverse strain gages near central stem (Both gages are located on the top transverse rebar directly along the test specimen centerline, each a distance of 610 mm away from the midspan of the decks, towards the central stem. DTT10-5 is on the RC side and DTT10-4 is on the composite side)

The load versus strain envelope plots of the top transverse strain gages located 610 mm (2 ft) away (in the direction of the outer stems) from the centerlines of each deck slab and 178 mm (7 in) away from the inside edge of the outer stems are shown in Figure 3.69. For loading of the test specimen up to approximately 400 kN (90 kip), which is approximately 4.1 times the AASHTO service load, the two strain gages both display negligible strain values, with the composite side slightly in compression and the RC side slightly in tension. For loads greater than 400 kN (90 kip), the RC side gage increases in strain values with increasing load significantly more than the composite side gage.

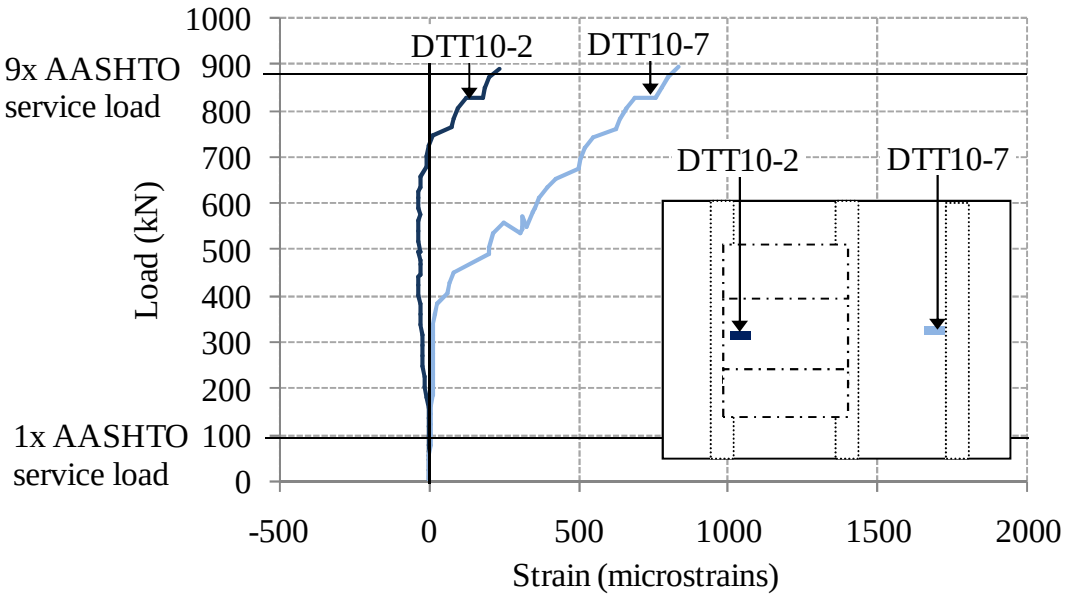

Figure 3.69 Load versus strain for top transverse strain gages near outer stems (Both gages are located on the top transverse rebar directly along the test specimen centerline, each a distance of 610 mm away from the midspan of the decks, towards the outer stems. DTT10-7 is on the RC side and DTT10-2 is on the composite side)

The FRP panel side strain gage remains slightly in compression until a load of approximately 700 kN (157 kip) and then begins to exhibit tensile strains, which increase with load at approximately the same rate as the RC side strain gage. At the ultimate capacity load of 890 kN (200 kip), the composite side strain value is 400.9 microstrains while the RC side strain value is over twice as large at 869.0 microstrains.

3.8.5.2 Strain Profiles along the Longitudinal Direction of the Deck

It is important to determine the degree to which the strains due to live loading distribute along the deck in both directions. The strain profiles along the longitudinal directions for the centerlines of the composite side and reinforced concrete side deck slabs are shown in Figure 3.70 and Figure 3.71 respectively. Note that as discussed in Section 3.8.5, the position of the strain gages within the composite side and RC side deck of the test specimen with respect to the depth of the slab will have an effect on the direct comparability of the absolute magnitude of the strains. Since the FRP side does not have a bottom layer of rebar, the strain gages for the bottom layer on the composite side are attached the underside of the FRP panels, which is located a distance of approximately 57 mm (2.25 in) lower within the deck slab than the gages attached to the bottom longitudinal rebar on the reinforced concrete side.

Regardless of the magnitude of the strain values, the strain profiles of two deck slabs can be compared in terms of profile geometry and loads at which major changes occur. Both sides maintain negligible longitudinal strain values of less than 100

microstrains for the central strain gage up to the load level of 222 kN (50 kips), which is 2.3 times the AASHTO service load. At the 400 kN (70 kip) load level, which is over four times the AASHTO service load, the reinforced concrete side center strain gage exhibits a significantly greater strain while the composite side maintains a low strain value. By the 578 kN (90 kip) load level, which is equivalent to 5.9 times the AASHTO service load, the composite exhibits a significantly higher strain value from its initial strain. For further information on the center longitudinal strains, see page 120 of Section 3.8.5.1, which contains a more detailed discussion.

The composite side and reinforced concrete side deck slabs shown in Figure 3.70 and Figure 3.71 maintain very comparably shaped profiles throughout most of the loading range, which both display large tensile values in the strain gage directly below the actuator, compressive strains in the strain gage approximately 610 mm (2 ft) away from the actuator and smaller compressive strains in the strain gages farthest away from the actuator. The switch in strain values from tension to compression along the strain profile indicates that the point of inflection for both slabs in the longitudinal direction is less than 610 mm (2 ft) longitudinally away from the centroid of the actuators. Since the intersection between the FRP panels is located 610 mm (2 ft) longitudinally away from the centerline of the actuators which is very near the point of inflection for both of the deck slabs it is difficult to reliably determine the effectiveness of stress transfer between the panels from the current experiment. Therefore, it is recommended that the effectiveness of stress transfer between panels be examined in greater detail through future experimental studies.

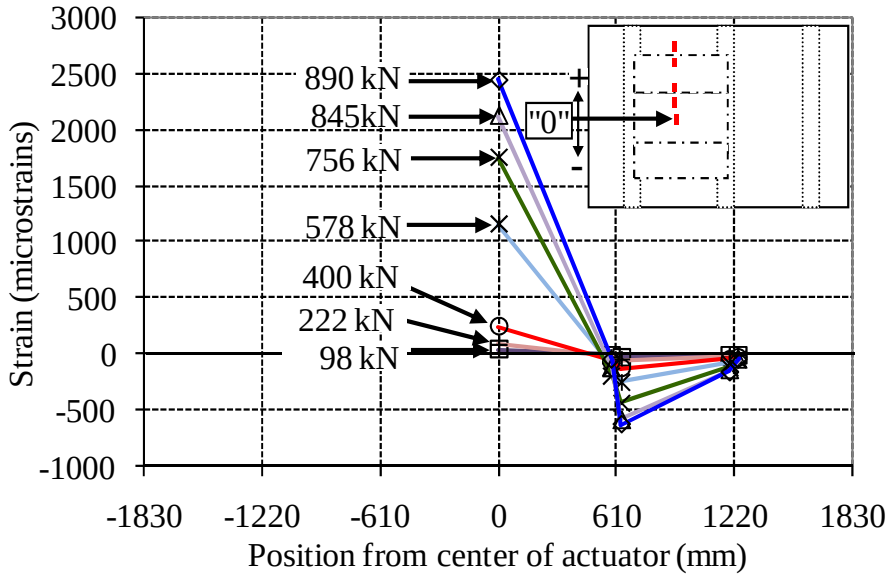

Figure 3.70 Strain profile for gages attached to bottom of FRP panel along line 3
(Line of gages is located directly along the composite side centerline)

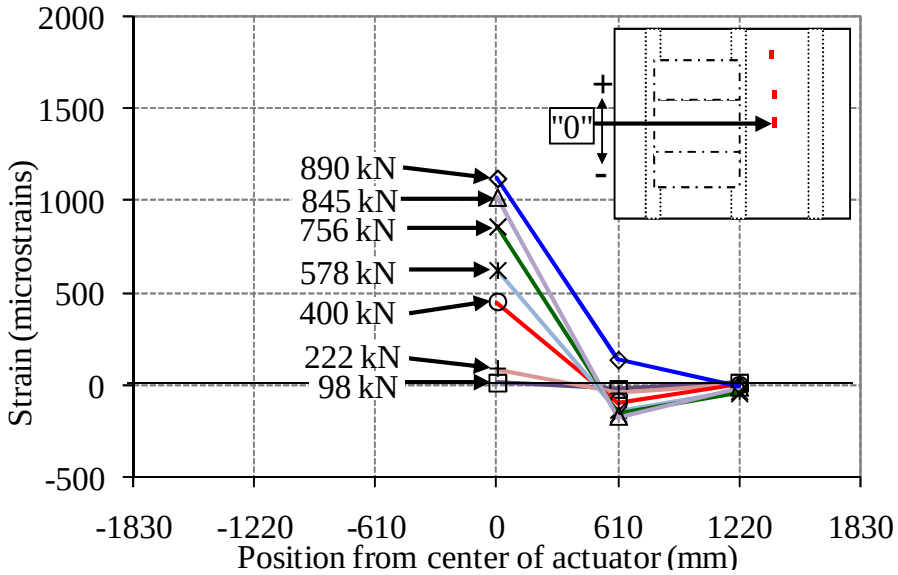

Figure 3.71 Strain profile for bottom longitudinal rebar along line 17
(Rebar is offset from RC side centerline by 140 mm towards the center stem)

The shift from compression to tension values at the 890 kN (200 kip) load level for the bottom longitudinal RC side strain gage shown in Figure 3.71, located

610 mm (2 ft) away from the middle of the specimen, is presumably due to a discontinuity which was observed during the 845 kN (190 kip) loading phase at which the initial signs of punching shear were observed on the FRP panel side deck slab.

The strain profile for gages attached to the top longitudinal steel reinforcement along the centerline of the composite is shown in Figure 3.72. This plot shows the same profile geometry as the bottom longitudinal profiles for both deck slabs, with tensile strains which become appreciable at the 400 kN (70 kip) load level and a point of inflection at a location prior to the strain gage located 610 mm (2 ft) away from the centerline of the test specimen. Note, however, that the top longitudinal strain profile maintains the same signs as the bottom longitudinal strain profile such that the center strain gage is in tension and the two farther away strain gages are in compression, which is indicative of more localized deformations in the region.

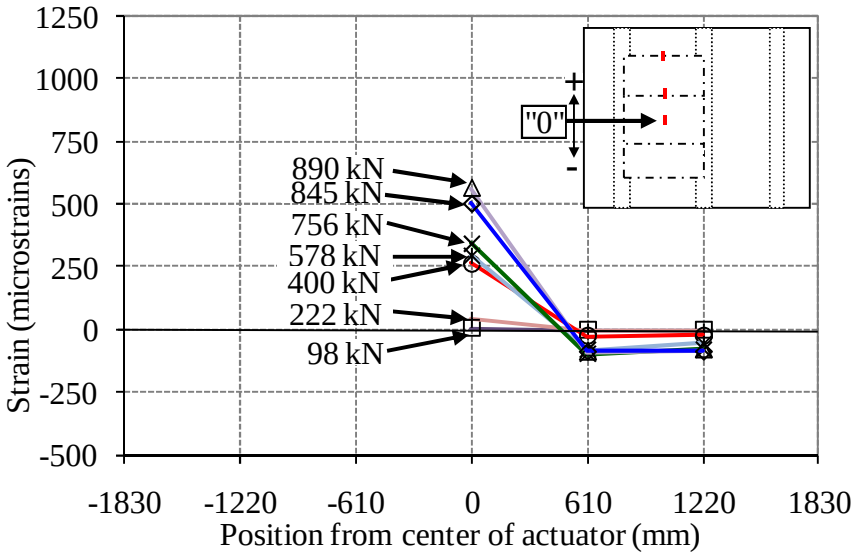

Figure 3.72 Strain profile for top longitudinal rebar along line 8
(Rebar is offset from composite side centerline by 140 mm towards center stem)

3.8.6 Strain Progression and Maximum Strain Levels

At the 1x AASHTO service load of 98 kN (22 kip), all strains in the test specimen were less than 100 microstrains, with the highest strains measured in the strain gages directly below the two actuators. At the 489 kN (110 kip) load level, which is equivalent to approximately five times the AASHTO service load, the highest strain value of 1446.8 microstrains was recorded from the bottom transverse RC side strain gage at midspan located 203 mm (8 in) longitudinally away from the centerline of the RC side actuator. The bottom transverse strain gage directly below the reinforced concrete side and composite side actuators recorded strain values of 762 microstrains and 578 microstrains respectively at this load level. The second highest strain value of -794 microstrains was located on the same bottom transverse bar as the highest recorded strain value at this load level on the segment which extends onto the composite side, at a distance of 152 mm (6 in) away from the edge of the center stem. The bottom longitudinal strain gage readings on the strain gages located directly below the reinforced concrete and composite actuators, were 545 and 665 respectively for this load level.

At the 578 kN (130 kip) load level, equivalent to nearly six times the AASHTO service load, a few of the strain gages in the deck measured sudden shifts in strain values. Most notably, the bottom RC side transverse strain gage which displayed the maximum value during the 489 kN (110 kip) load level measured a sudden jump from 1252 microstrains to a strain value of 1919 microstrains, which was the highest measured strain value in the test specimen at this load level. The other notable strain discontinuity was observed in the composite side transverse strain gage

attached to the bottom of the FRP, located along the test specimen centerline and 152 mm (6 in) from the edge of the center stem. The discontinuities in the strain profile for this strain gage are displayed in Figure 3.78 on page 142.

At the 756 kN (150 kip) load level, equivalent to approximately 7.7 times the AASHTO service load, strain discontinuities occurred throughout the reinforced concrete side, primarily within the strain gages attached to the bottom layer of steel reinforcement. Conversely, the composite side only displayed sudden shifts in strain values in the two transverse strain gages attached to the bottom of the center FRP panel, along the test specimen centerline, located 152 mm (6 in) and 178 mm (7 in) from the edge of the center and outer stems respectively. The maximum strain in the deck slab was 2150 microstrains for the bottom transverse RC side strain gage at midspan located 203 mm (8 in) longitudinally away from the centerline of the RC side actuator. The strains for the bottom transverse RC side and composite side center gages at this load level were 1422 microstrains and 719 microstrains respectively whereas the bottom longitudinal strains on the RC side and composite side were 860 microstrains and 1743 microstrains respectively.

At the 845 kN (190 kN) load level, equivalent to 8.6 times the AASHTO service load, significant strain discontinuities occur throughout the reinforced concrete side deck slab. The most notable strain discontinuities occurred in the RC side bottom transverse rebar strain gages located a distance of 152 mm (6 in) away from the edge of the center stem, with the strain gage located along the centerline of the test specimen abruptly changed from -302 microstrains to -949 microstrains whereas the strain gage located 610 mm (2ft) longitudinally away from the centerline of the

actuators changed from 200 microstrains to 5767 microstrains. Similar abrupt changes in strain were not observed on the composite side.

At ultimate capacity, which occurred at a load of 890 kN (200 kip), equivalent to approximately nine times the AASHTO service load, the highest overall strains in the test specimen were observed in the RC side bottom transverse rebar gages located below the RC side actuator and adjacent to the edges of the center and outer stems, which read 5796 microstrains and 2975 microstrains respectively. The bottom transverse and longitudinal strains measured on the strain gages attached to the bottom of the FRP panel, directly below the composite side actuator were 920 microstrains and 2442 microstrains respectively and the corresponding bottom transverse and longitudinal strains measured on the strain gages attached to the steel reinforcement directly below the RC side actuator were 1930 microstrains and 1120 microstrains respectively. The largest compressive strain in the deck slab of -1676 microstrains was measured in the bottom transverse rebar located along the test specimen centerline and positioned on the composite side a distance of 152 mm (6 in) away from the edge of the center stem.

3.8.7 Unloading Response

3.8.7.1 Loading versus unloading stiffness comparisons

A comparative evaluation of the degradation of the slope of the load-deflection response of the slabs during the unloading portions of the test was obtained using the “effective” stiffness, which was defined earlier in Equation 3.1 on page 87 of Section

3.8.3. The effective stiffness ratio was then computed using the same formulation defined earlier in Equation 3.2 and the equation is repeated here to highlight the use of a different load level for the baseline:

$$\text{Effective Stiffness Ratio} = \frac{\text{Effective stiffness at a load level}}{\text{Effective stiffness at baseline (222 kN)}} \qquad 3.2$$

Note that the baseline for the unloading portions of the test is the 222 kN (49.9 kip) load level rather than the 98 kN load level used for the loading portions of the curve because the 222 kN (50 kip) load level is the first level at which a single unloading cycle is performed. The effective stiffness ratio values for the FRP side slab and the reinforced concrete side slab during unloading sections of the test are presented in Table 3.12 and Table 3.13 respectively.

At each load level, the reinforced concrete side exhibits a lower effective stiffness ratio as compared to the composite side. This indicates that the slope from the unloading portion of the load versus deflection plot for the reinforced concrete side degrades more rapidly than the equivalent values for the composite side. The effective stiffness of the reinforced concrete side also degrades to a greater extent overall, as observed by the 25 % lower effective stiffness ratio of the reinforced concrete side during the final unloading cycle at 756 kN (170 kip) prior to reaching the ultimate capacity of the test specimen.

Table 3.12 Effective stiffness ratio of FRP side slab from linear potentiometer data

Target actuator load		Actual target actuator load, P_f		Actual min threshold actuator load, P_i		Deflection at target load, δ_f		Deflection at min threshold load, δ_i		Effective stiffness ratio
kN	kip	kN	kip	kN	kip	mm	in	mm	in	---
222	50	204.1	45.9	33.4	7.5	0.74	0.029	0.30	0.012	1.00
400	90	382.5	86.0	31.7	7.1	1.60	0.063	0.44	0.017	0.79
578	130	576.8	129.7	40.3	9.1	2.85	0.112	0.73	0.029	0.66
756	170	745.1	167.5	33.5	7.5	4.01	0.158	1.25	0.049	0.67

Table 3.13 Effective stiffness ratio of RC side slab from linear potentiometer data

Target actuator load		Actual target actuator load, P_f		Actual min threshold actuator load, P_i		Deflection at target load, δ_f		Deflection at min threshold load, δ_i		Effective stiffness ratio
kN	kip	kN	kip	kN	kip	mm	in	mm	in	---
222	50	209.1	47.0	30.6	6.9	0.74	0.029	0.32	0.013	1.00
400	90	384.2	86.4	29.3	6.6	1.78	0.070	0.62	0.025	0.72
578	130	548.6	123.3	36.0	8.1	3.56	0.140	1.18	0.047	0.51
756	170	740.8	166.5	29.1	6.5	5.37	0.212	1.99	0.078	0.50

A comparison of the effective stiffness ratios for the loading and unloading portions of the test, shown in Figure 3.73, indicates that the reinforced concrete side exhibits significantly lower effective stiffness ratios as compared to the composite side for both the loading and unloading portions of the curves. Note that the effective stiffness ratios for the loading portions of the test were recalculated using the baseline of 222 kN (50kip) to enable the values to be accurately compared to the effective stiffness ratios for the unloading portions of the test.

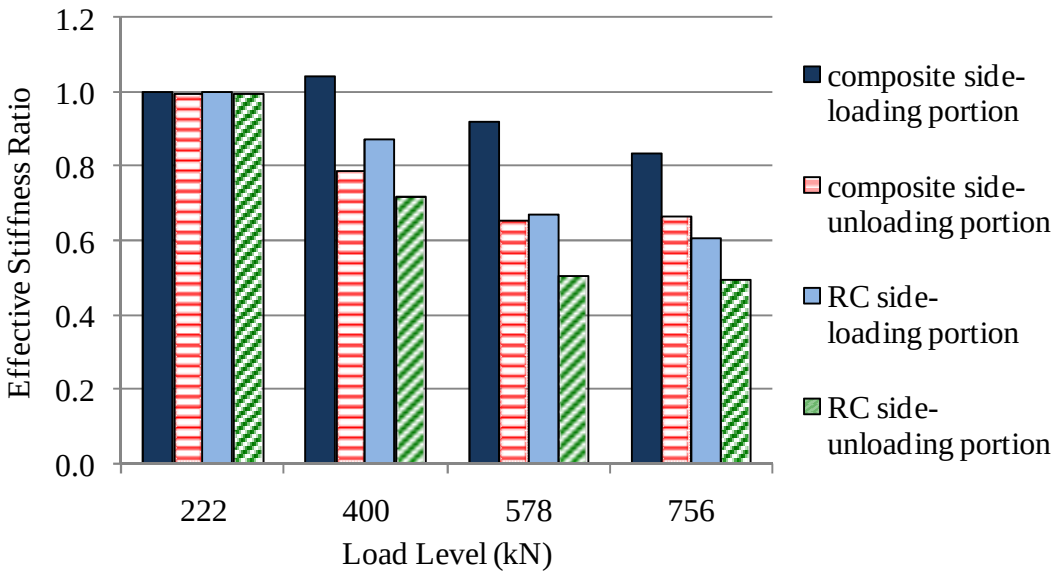

Figure 3.73 Stiffness ratios of the center of the two slabs found from deflection data (loading portion data was recalculated with 222kN instead of 98 kN as the baseline)

3.8.7.2 Residual deflections and strains

The presence of residual deflections and residual strains observed in the test specimen deck slab throughout the loading protocol are an indication of irreversible damage which has occurred. Throughout the loading steps, the residual deflection accumulated for each load level at the midspan of each slab was calculated and the results are displayed in Table 3.14. Note that the reinforced concrete side exhibited higher residual deflection values for each load level as compared to the composite side values. The total residual deflection accumulated with loading up to the 756 kN (170 kip) load level was 1.21 mm (0.048 in) for the composite side as compared to a 62.9% greater total residual deflection for the reinforced concrete side of 1.97 mm (0.078 in).

Table 3.14 Residual deflections of deck slabs (from central linear potentiometers)

Load Level		Composite Side				RC Side			
		Individual residual deflections for the given load level		Accumulated residual deflections up to the given load level		Individual residual deflections for the given load level		Accumulated residual deflections up to the given load level	
kN	kip	mm	in	mm	in	mm	in	mm	in
222	50	0.26	0.010	0.26	0.010	0.30	0.012	0.30	0.012
400	90	0.15	0.006	0.41	0.016	0.30	0.012	0.61	0.024
578	130	0.29	0.011	0.70	0.027	0.56	0.022	1.17	0.046
756	170	0.51	0.020	**1.21**	**0.048**	0.81	0.032	**1.97**	**0.078**
Total residual deflections		**1.21**	**0.048**	**---**	**---**	**1.97**	**0.078**	**---**	**---**

A similar phenomenon is observed in the strain data, in which the reinforced concrete side exhibits significant residual strains for the many of its deck slab gages, while the composite side exhibits significantly smaller and often negligible residual strains for its deck strain gages. For illustration purposes, Figure 3.74 shows a representative load versus strain plot, which includes the unloading portions of the curve. The reinforced concrete side strain gage exhibits significantly greater residual strains than the composite side strain gage and a similar trend is observed throughout the test specimen.

The considerably greater residual deflections and strains observed on the composite side are a good indication of increased damage which has occurred throughout the loading in the examined regions. The smaller residual strains and deflections on the composite side can be partially attributed to the FRP panels, which act mitigate the impact of damage in the deck by catenary action in which the FRP

panels act compositely with the concrete and resists crack development in the concrete.

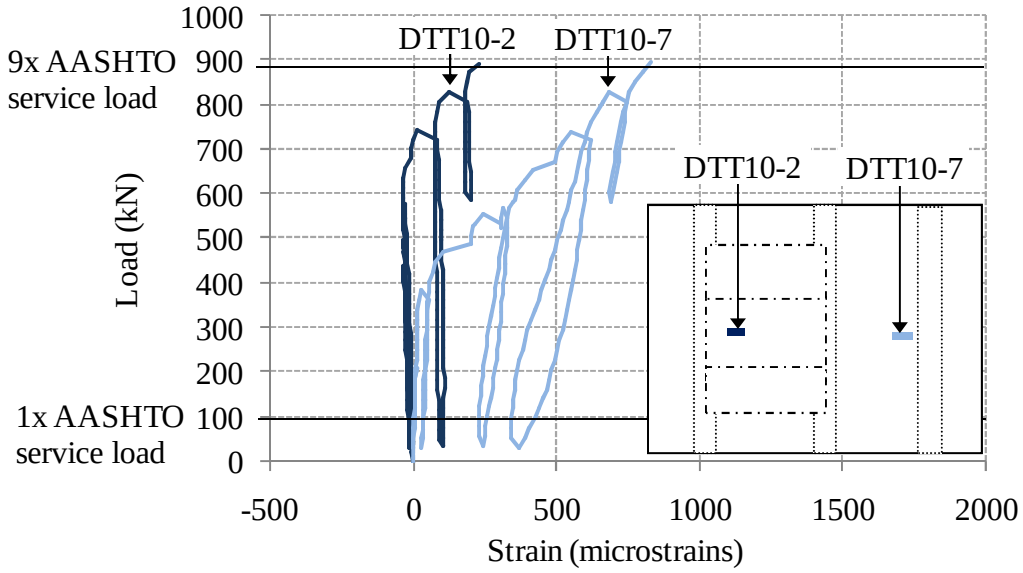

Figure 3.74 Representative load versus strain plot to illustrate difference in residual strains between composite side and RC side strain gages.
(Specific plot shown contains gages on top transverse rebar along centerline, located 178 mm away from of the inner edge of the outer stems and 610 mm away from the centerline of the slabs)

3.8.8 Separation between FRP Panels and Concrete

During the static loading of the test specimen, examination of specific strain and deflection data was used in order to detect the presence of a separation between the FRP panels and the concrete. A select number of linear potentiometers were placed above and below the composite deck in the same location such that their deflections could be compared. The difference in deflection values obtained from pairs of these linear potentiometers was used to obtain information regarding the level of separation that had occurred. A differential between the top and bottom pot

readings indicates that the concrete and composite are no longer acting together as a connected unit and are now deflecting independent of each other.

The load versus deflection envelope plots of the top and bottom pair of linear potentiometers located along the transverse centerline of the test specimen on either side of the actuator on the FRP panel deck are shown in Figure 3.75 and Figure 3.76. Based on the observed fluctuations in measured deflections for top and bottom linear potentiometer pairs on the reinforced concrete side deck, a tolerance level of 0.16 mm (0.006 in) was established as the threshold value for determining that a difference between the top and bottom deflections was significant. For the pair of linear potentiometers located near the outer stem shown in Figure 3.75, a difference of 0.17 mm (0.007 in) between upper and lower deflection values was observed at a load of 673 kN (151 kip), which is approximately 6.9 times AASHTO service load, which increased to 1.09 mm (0.043 in) at ultimate capacity. For the pair of linear potentiometers located near the center stem shown in Figure 3.76, the upper and lower deflection values were separated by 0.17 mm (0.007 in) at a load of 489 kN (109 kip) and the difference increased to 3.12 mm (0.123 in) at ultimate capacity.

Another method for detection of the separation between the concrete and the FRP panels compares strain gauges which are attached to the composite panel, the bottom rebar which protrudes onto the composite panel in order to satisfy the development length required by code, and the top rebar layer which is continuous throughout the specimen. The vertical difference between the strain gauge on the bottom of the FRP plate and the strain gauge on the bottom rebar is approximately 50mm (2 in) and so similar strain values are expected, with the strain gage on the

bottom of the FRP plate reading slightly higher strains than the strain gage on the bottom rebar.

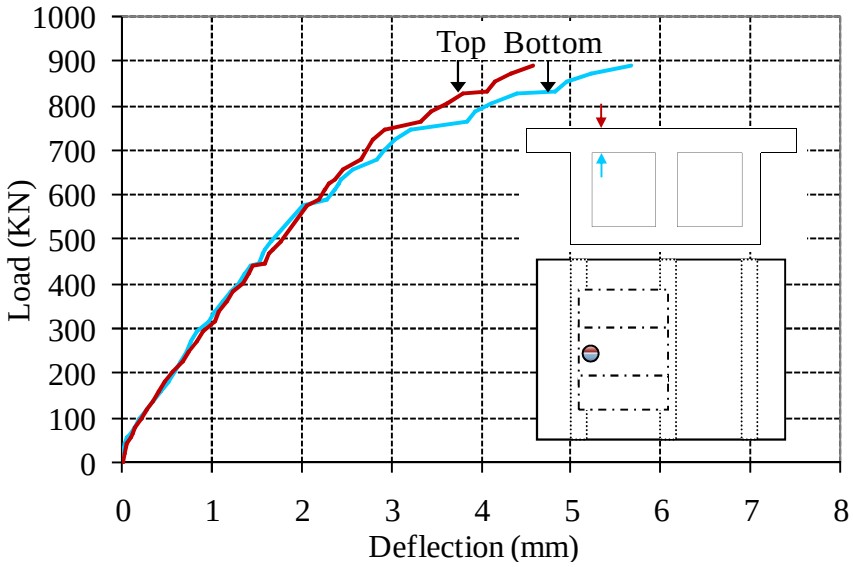

Figure 3.75 Load versus deflection plots for detection of FRP panel separation (located along test specimen centerline and 610 mm away from the composite side centerline, 178 mm from the inner edge of the outer stem)

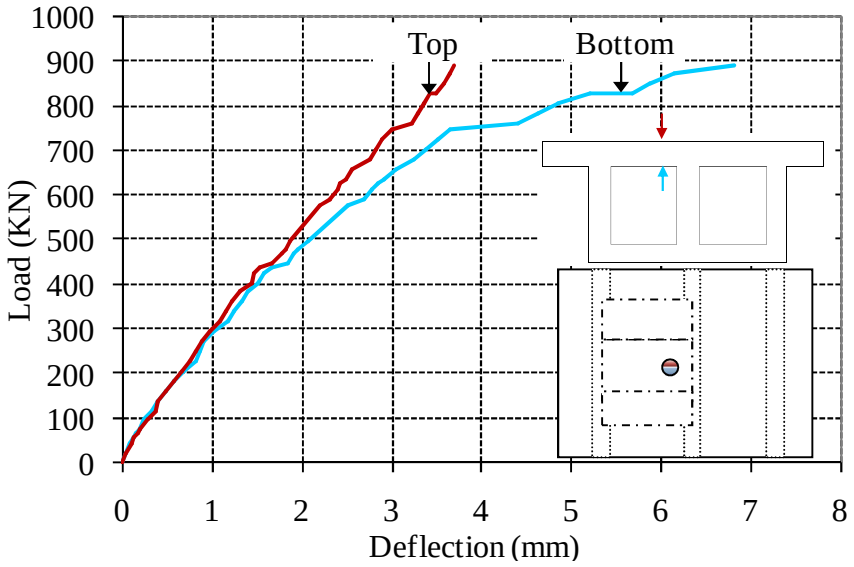

Figure 3.76 Load versus deflection plots for detection of FRP panel separation (located along test specimen centerline and 610 mm away from the composite side centerline, 152 mm from the composite side edge of the center stem)

As shown in Figure 3.77, the strain values for the bottom rebar and the composite panel are very similar until a load of approximately 700 kN (157 kip) then the strains diverge suddenly, whereas Figure 3.78 shows a significant difference in strain values initiating at a load of 500kN (112 kip). The discontinuity in the strain profile between the FRP panel and the bottom rebar indicate that the FRP panel had separated from the concrete. Note that the site of initiation for the debond between the concrete and the composite was adjacent to the support rather than in the center of the FRP panel, due to the high shear present in this region.

Based on the two detection methods described above, sections of the center composite panel exhibited initial signs of separation at approximately the 489 kN (110 kip) load level, which is equivalent to 5.0 times the AASHTO service load. Note that the damage initiation first occurred on the side of the FRP panel adjacent to the center support because the loading in this region was more severe than in the region adjacent to the exterior support. Comparisons based on linear potentiometers and tap tests at different locations throughout the test specimen indicated that the concrete to composite bond for the two outer panels remained fully intact throughout the loading levels.

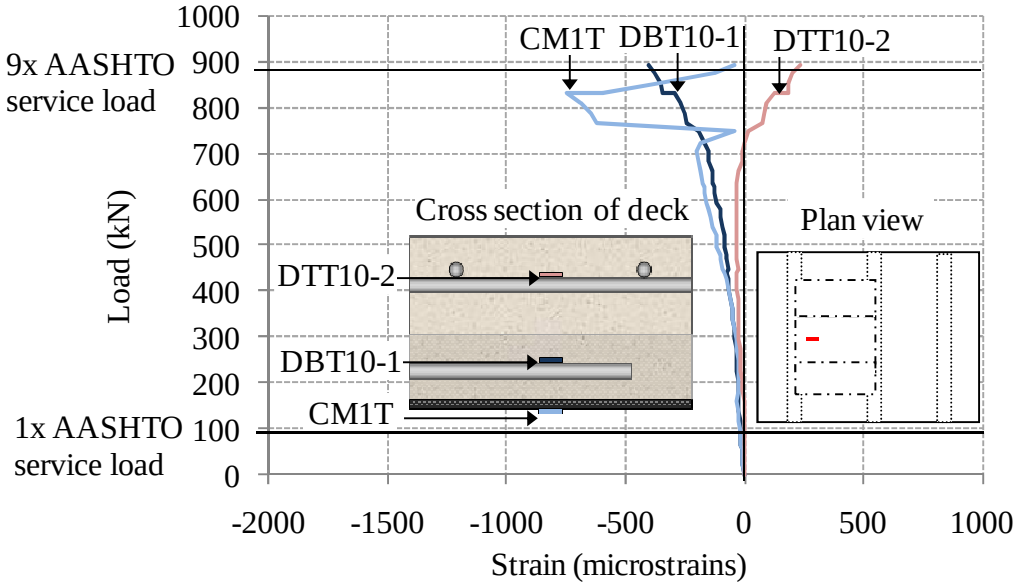

Figure 3.77 Load versus strain comparison of three transverse gages along test specimen centerline at the same location and at different depths within the deck

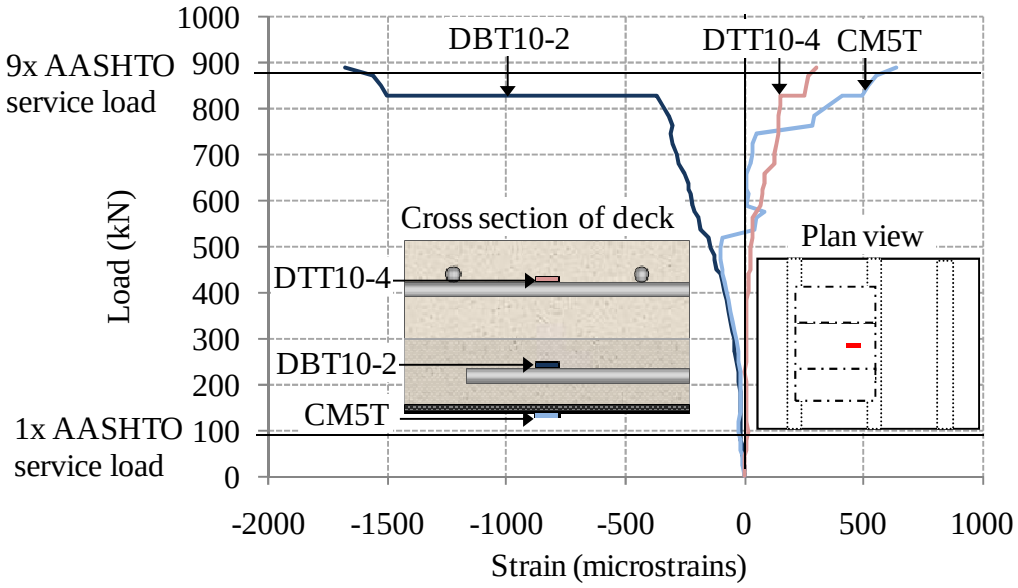

Figure 3.78 Load versus strain comparison of three transverse gages along test specimen centerline at the same location and at different depths within the deck

3.9 LIMIT STATES

In general, a structure must be designed such that the requirements for both serviceability and strength limit states are satisfied. The serviceability limit states relate to the comfort of the occupants in terms of limiting excessive deflections, cracking and vibrations. The strength limit states relate to the structural collapse of all or part of the structure in terms of stability or buckling, rupture of critical parts of the structure, the formation of plastic mechanisms in ductile members [154]. These strength limit states are checked for different loading conditions such as flexure, shear, bond strength and buckling. In addition to serviceability and strength, Section 5.5 of the AASHTO LRFD Bridge Design Manual includes provisions for fatigue and fracture limit states as well as an extreme even limit state [91]. Fatigue and fracture limit states are intended to prevent the failure of a structure through the progression of cracks and other defects. The extreme event limit state is intended to resist structural collapse due to extreme events such as vehicle collisions, floods, or earthquakes. Certain limit states such as deflection and vibration limitations are material independent, whereas of other limit states are different depending on the specific building materials chosen. A brief overview of limit states for reinforced concrete structures and hybrid concrete-FRP structures is included below.

For both steel reinforced concrete structures and hybrid reinforced concrete-FRP structures, limits are placed on the allowable stresses in the steel reinforcement to avoid yielding of the steel reinforcement and inelastic deformations under service loads as described in AASHTO, section 5.7.3.4 [91] and ACI 440, section 9.4 [148]

respectively. At service load, the AASHTO defined the maximum deck deformation due to local dishing at wheel loads using the following criteria:

- L/800 for decks with no pedestrian traffic
- L/1000 for decks with limited pedestrian traffic
- L/1200 for decks with significant pedestrian traffic
-

where

L = Span length of the deck measured from center-to-center of supports

To calculate the immediate deflections due to service loads for concrete or hybrid concrete-FRP, the effective moment of inertia, I_e, as given in ACI 318-05 Section 9.5.2.3 [155], is used:

$$I_e = \left(\frac{M_{cr}}{M_a}\right)^3 I_g + \left[1 - \left(\frac{M_{cr}}{M_a}\right)^3\right] I_{cr} \le I_g \qquad 3.9$$

in which

$$M_{cr} = f_r \frac{I_g}{y_t} \qquad 3.10$$

where

M_{cr} = Cracking moment (ksi)

M_a = Maximum moment in a component at the stage for which deformation is computed (kip-in)

I_{cr} = Moment of inertia of cracked section transformed to concrete (in^4)

I_g = Gross moment of inertia (in^4)

f_r = Modulus of rupture of concrete (ksi)

y_t = Distance from the neutral axis to the extreme tensile fiber (in)

The modulus of rupture for concrete, f_r, is defined by AASHTO as

- $f_r = 0.24\sqrt{f_c'}$ for normal weight concrete
- $f_r = 0.20\sqrt{f_c'}$ for sand-lightweight concrete
- $f_r = 0.17\sqrt{f_c'}$ for all-lightweight concrete

where

f_c' = Specified compressive strength of concrete at 28 days (ksi)

For strength limit states, the factored resistance values are determined through multiplying the calculated nominal resistance values by their corresponding resistance factors, ϕ. Some of the representative resistance factors used for conventionally constructed steel reinforced concrete structures are as follows:

- $\phi = 0.9$ for flexure and tension of reinforced concrete
- $\phi = 0.9$ for shear and torsion of normal weight concrete
- $\phi = 0.7$ for bearing on concrete

In addition to the above resistance factors, FRP-strengthened sections use additional strength reduction factors to account for the effects of different exposure conditions, larger material variability, and potentially lower ductility. For example, the design ultimate tensile strength of the FRP reinforcement, f_{fu}, is defined by ACI 440.2R as:

$$f_{fu} = C_E f_{fu}^* \qquad 3.11$$

where

C_E = Environmental reduction factor defined in ACI440.2R Table 8.1. Values are between 0.50 and 0.95 based on fiber and resin types and exposure conditions

f_{fu}^* = Ultimate tensile strength of the FRP as reported by the manufacturer

A reinforced concrete section in flexure is checked for the strength limit states of crushing of the concrete in compression before yielding of the reinforcing steel as well as yielding of the steel in tension followed by concrete crushing. Additional

failure modes considered for an FRP-strengthened section as described in ACI 440.2R Section 9.2.1 are yielding of the steel in tension followed by rupture of the FRP laminate, shear/tension delamination of the concrete cover and debonding of the FRP from the concrete substrate [148].

3.10 DESIGN THRESHOLDS

While experimental results indicate that the composite panel reinforced bridge deck had an ultimate capacity of over nine times the AASHTO service load and deflected less than the reinforced concrete side deck throughout the loading, it is necessary to determine the loads which the FRP panel system can be safely support without undergoing significant irreversible damage. Since the initial signs of separation between the FRP panels and the concrete occurred at the 489 kN (110 kip) load level, this load will be taken as the maximum threshold for the FRP panel system. This serviceability limit state as well as the experimentally determined strength limit states for punching shear and ultimate capacity of the structure are shown in Table 3.15 in terms of the code defined loads of Service I, Strength I [91], and the Permit Truck [152] load.

Based on the information regarding the observed limit states for the system and the corresponding safety factors for different permit loadings, an acceptable design load for the examined FRP panel system would be 360 kN (82 kip). This would allow for a safety factor of 2.0 for the CALTRANS permit truck and a safety factor of 3.7 and 2.1 for the AASHTO Service I and Strength I load levels respectively. Note that

this design threshold is directly tied to the geometry of the specimen and substantial changes in dimensions could cause significant changes in design threshold values.

Table 3.15 Safety factors for different limit states in terms of permit loadings

Target Load		Level of damage	Safety factor for Service I load 98 kN (22 kip)	Safety factor for Strength I load 169 kN (38 kip)	Safety factor for Permit load 180 kN (41 kip)
kN	kip				
400	90	No visible cracks or observable damage	4.1	2.4	2.2
489	110	Initial signs of separation between FRP panel and concrete	5.0	2.9	2.7
845	190	Initial signs of punching shear	8.6	5.0	4.7
890	200	Ultimate Load	9.1	5.3	4.9

3.11 CYCLIC LOADING OF TEST SPECIMEN

3.11.1 Loading Protocol

After the ultimate capacity of the test specimen was reached, a cyclic phase was implemented. Since the test specimen had already been loaded to ultimate capacity, this loading phase was not an accurate representation of response under actual cyclic loading. Instead, the limited cyclic loading of the test specimen provided useful information regarding further accumulation of damage within the specimen. If an unforeseen event applies loads significantly larger than typical to a bridge structure, it is important to determine whether the structure can still safely support normal traffic

loads. If the system's post failure response to cyclic loading is very stable, the bridge can be left in service while preparations are made to repair the damage caused by the excessive unforeseen loading to the structure.

The test specimen was loaded for 1,000 cycles from the minimum threshold load of 4.5 kN (1 kip) to 1x AASHTO fatigue service load, which is defined as 84 kN (18.9 kip), and cycled to 2x the fatigue service load for another 1,000 cycles as summarized in Table 3.16. For cyclic loading, the fatigue service load of 84 kN (18.9 kip) was defined by the SERVICE I level in which the HS20 wheel load of 73 kN (16.4 kip) with an additional AASHTO defined 15% dynamic allowance for the fatigue limit state was applied.

Table 3.16 Cyclic loading protocol for test specimen #1

PHASE AND CORRESPONDING LOADING LEVEL PER ACTUATOR	LOAD LEVEL		NUMBER OF CYCLES
	kN	kip	
Phase I: cyclic at P	84	18.9	1,000
Phase II: cyclic at 2P	168	37.8	1,000
Cumulative number of cycles:			2,000
Note: P = 1.15 x AASHTO service load Where AASHTO service load is 73 kN (16.4 kip)			

Center deflections were chosen as the primary indicator by which to make comparisons regarding stability and progression of damage. Note that the deflection values were biased using the original bias values from the start of static testing in order to establish the cumulative deflections present in the deck. Since the stability of

the system during the cyclic loading was the focus of this loading phase, changes in deflection and strain values over the course of the cyclic loading rather than their absolute magnitudes are of primary concern.

3.11.2 Changes in Center Deflections during Cyclic Loading

The center deflections during the course of cyclic phases I and II are shown in Table 3.17 and Table 3.18 respectively. As observed in both tables, the changes in center deflections for the FRP panel side were less than the experimentally determined threshold of 0.17 mm (0.007 in) for establishing whether a deflection measurement was statistically significant. Conversely, the reinforced concrete side was slightly less than the deflection threshold for cyclic phase I and was slightly over the deflection threshold for cyclic phase II. So, the changes in the center deflections for the reinforced concrete side of 0.20 mm (0.008 in) over the course of the cyclic loading phase II amounts to a 5.7% increase in deflection values. While this deflection increase is small, it is still considered statistically significant because the values are above the defined threshold of 0.17 mm (0.007 in), unlike the changes in deflection for the FRP panel side throughout both cyclic phases that fall well below the minimum deflection threshold.

Table 3.17 Center deflections during cyclic loading phase I (84 kN target load)

Cycle#	FRP panel side				Reinforced concrete side			
	Deflection at target load		Change in deflection		Deflection at target load		Change in deflection	
---	mm	in	mm	in	mm	in	mm	in
1	4.68	0.184	---	---	2.73	0.108	---	---
500	4.61	0.181	-0.08	-0.003	2.76	0.108	0.02	0.001
1000	4.68	0.184	0.00	0.000	2.85	0.112	0.12	0.005

Table 3.18 Center deflections during cyclic loading phase II (168 kN target load)

Cycle#	FRP panel side				Reinforced concrete side			
	Deflection at target load		Change in deflection		Deflection at target load		Change in deflection	
---	mm	in	mm	in	mm	in	mm	in
1	5.35	0.211	---	---	3.45	0.136	---	---
500	5.43	0.214	0.08	0.003	3.66	0.144	0.21	0.008
1000	5.41	0.213	0.06	0.002	3.64	0.143	0.20	0.008

The effective stiffness ratios for the two decks, shown in Table 3.19 and Table 3.20, were calculated for both cyclic loading phases using the adaptive secant stiffness method described on page 87 in Section 3.8.3. Since the load acting on the system remains constant throughout the cyclic phase, any change in the stiffness ratio is attributed to a change in deflections. During cyclic phase I, the effective stiffness ratios remained constant for both slabs as shown in Table 3.19 and Table 3.20. This is an indication that negligible structural degradation has occurred in either slab during cyclic loading phase I of this test specimen.

Table 3.19 Effective stiffness ratios for FRP panel side during cyclic loading phase I

Cycle #	Actual target actuator load, P_f		Actual min. threshold actuator load, P_i		Deflection at target load, δ_f		Deflection at min threshold load, δ_i		Effective stiffness ratio
---	kN	kip	kN	kip	mm	in	mm	in	---
1	84.5	19.0	4.9	1.1	4.68	0.184	4.28	0.168	1.00
250	84.8	19.1	4.8	1.1	4.66	0.183	4.24	0.167	0.96
500	85.4	19.2	5.2	1.2	4.61	0.181	4.18	0.165	0.96
750	85.3	19.2	5.0	1.1	4.65	0.183	4.23	0.167	0.97
1000	85.4	19.2	5.1	1.2	4.68	0.184	4.26	0.168	0.98

Table 3.20 Effective stiffness ratios for RC side during cyclic loading phase I

Cycle #	Actual target actuator load, P_f		Actual min. threshold actuator load, P_i		Deflection at target load, δ_f		Deflection at min threshold load, δ_i		Effective stiffness ratio
---	kN	kip	kN	kip	mm	in	mm	in	---
1	84.3	18.9	4.7	1.1	2.73	0.108	2.26	0.089	1.00
250	83.9	18.9	5.0	1.1	2.76	0.109	2.30	0.090	0.99
500	86.0	19.3	4.4	1.0	2.76	0.108	2.27	0.089	0.99
750	85.1	19.1	4.4	1.0	2.82	0.111	2.33	0.092	0.99
1000	85.3	19.2	4.6	1.0	2.85	0.112	2.36	0.093	0.97

The progression of the effective stiffness ratios for both sides over the course of cyclic phase II is shown in Figure 3.79. Table 3.21 shows the effective stiffness ratios for the FRP panel side dropped by 12% during the first 250 cycles and dropped by another 5% during the next 750 cycles while Table 3.22 shows the reinforced

concrete side effective stiffness ratios remained constant with only 5% change throughout the loading phase.

Due to the relatively small loads applied to the system during the cyclic phases (the loading at cyclic phase II is less than five times smaller than the loads at the ultimate capacity from the static loading phase) the calculations of effective stiffness are heavily affected by minor changes in deflection values. So, the increase in overall deflections for the composite side of 0.26 mm (0.010 in) from the start to the end of cyclic phase II, which corresponded to a 19% decrease in the effective stiffness ratio, was only 1.5 times the experimentally determined deflection threshold of 0.17 mm (0.007 in).

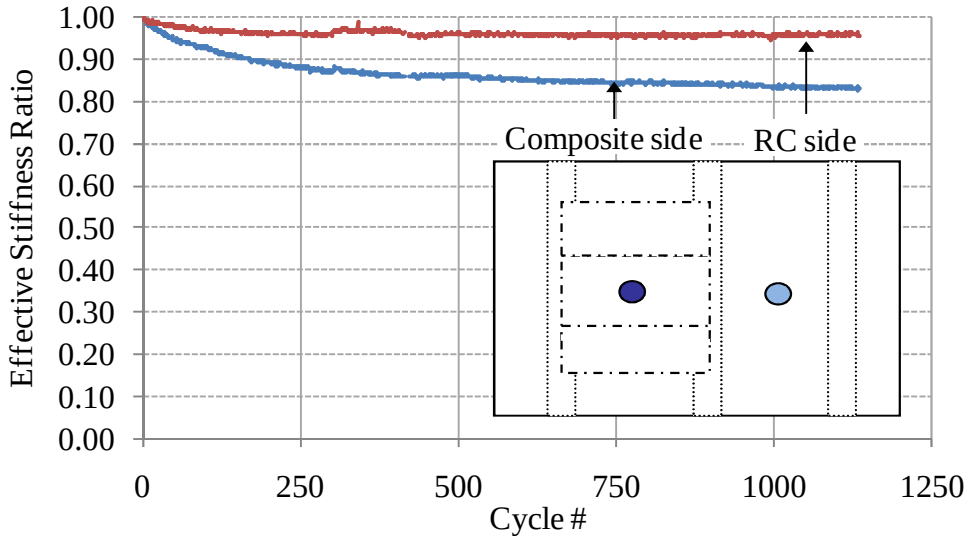

Figure 3.79 Effective stiffness versus cycle number for phase II of cyclic loading

Table 3.21 Effective stiffness ratios for FRP panel side during cyclic loading phase II

Cycle #	Actual target actuator load, P_f		Actual min. threshold actuator load, P_i		Deflection at target load, δ_f		Deflection at min threshold load, δ_i		Effective stiffness ratio
---	kN	kip	kN	kip	mm	in	mm	in	---
1	169.9	38.2	5.2	1.2	5.35	0.211	4.26	0.168	1.00
250	170.1	38.2	5.3	1.2	5.36	0.211	4.11	0.162	0.88
500	170.1	38.2	5.3	1.2	5.43	0.214	4.16	0.164	0.86
750	170.0	38.2	5.2	1.2	5.44	0.214	4.14	0.163	0.84
1000	169.9	38.2	5.1	1.1	5.41	0.213	4.10	0.161	0.83

Table 3.22 Effective stiffness ratios for RC side during cyclic loading phase II

Cycle #	Actual target actuator load, P_f		Actual min. threshold actuator load, P_i		Deflection at target load, δ_f		Deflection at min threshold load, δ_i		Effective stiffness ratio
---	kN	kip	kN	kip	mm	in	mm	in	---
1	169.8	38.2	4.5	1.0	3.45	0.136	2.37	0.093	1.00
250	169.9	38.2	4.5	1.0	3.54	0.139	2.41	0.095	0.96
500	169.8	38.2	4.6	1.0	3.66	0.144	2.53	0.100	0.96
750	169.8	38.2	4.5	1.0	3.68	0.145	2.55	0.100	0.95
1000	169.7	38.1	4.5	1.0	3.64	0.143	2.51	0.099	0.95

3.11.3 Changes in Strains during Cyclic Loading

The progressions of strains during the cyclic loading phases for strain gages located in the deck slab directly below the actuators are presented in Table 3.23 and Table 3.24. Note that all gages were biased using the original strain gage values from

the start of the static testing in order to record the complete history of the strain imposed on each gage due to all previous loading. Also, all data shown in the tables below were taken with the specimen at the full target load for a given cyclic phase. A number of the important strain gages, including the bottom longitudinal gage located directly below the RC side actuator, were permanently damaged when the specimen was loaded to ultimate capacity. However, for most of the strain gages that continued to function properly only minor progressions in strain values during the cyclic loading phases were observed.

For the strain gages located directly below the FRP side actuator which are shown in Table 3.23, the strain values changed by less than 15 microstrains or 7% over the course of the first cyclic phase and changed by less than 20 microstrains or 5% over the course of the second cyclic phase. The top (DTT10-6) and bottom (DBT10-4) transverse RC side strain gages located directly below the RC side actuator, shown in Table 3.24, both exhibit comparable progressions in strain to the corresponding gages on the FRP panel side (DTT10-3 and CM3T) over the course of cyclic loading phase I. However, during the cyclic loading phase II, the top and bottom transverse RC side gages shifted by 50.0 and 38.5 microstrains respectively, whereas the FRP panel gages shifted by only 0.6 and 7.3 microstrains respectively.

Table 3.23 Strain progresssion for composite side gages under target loads- located directly below the composite side actuator (See Section 3.6.2 for detailed information on precise location of each strain gage)

	Strain gage name	CM3T	CM3L	DTT10-3	DTL8-3
Position designations	Location (All on FRP panel side)	Below actuator	Below actuator	Below actuator	Below actuator
	Attached to rebar or FRP	FRP	FRP	Rebar	Rebar
	Near top or bottom of deck	Bottom	Bottom	Top	Top
	Oriented longitudinal or transverse	Transverse	Longitudinal	Transverse	Longitudinal
Cyclic loading phase I	Strain at Cycle # 1 (με)	159.0	671.2	-313.6	311.5
	Strain at Cycle # 250 (με)	153.4	665.4	-308.9	312.7
	Strain at Cycle # 500 (με)	153.4	663.7	-310.1	311.5
	Strain at Cycle # 750 (με)	148.9	661.9	-307.7	312.7
	Strain at Cycle # 1000 (με)	148.3	657.9	-300.6	316.4
	Change in strains (με)	**-10.7**	**-13.3**	**13.0**	**4.9**
	Change in strains (%)	**-6.7%**	**-2.0%**	**-4.1%**	**1.6%**
Cyclic loading phase II	Strain at Cycle # 1 (με)	208.4	825.4	-353.9	337.0
	Strain at Cycle # 250 (με)	205.0	830.0	-355.0	337.6
	Strain at Cycle # 500 (με)	217.4	831.1	-350.3	351.6
	Strain at Cycle # 750 (με)	219.1	831.7	-350.9	353.4
	Strain at Cycle # 1000 (με)	215.7	830.6	-353.3	354.0
	Change in strains (με)	**7.3**	**5.2**	**0.6**	**17.0**
	Change in strains (%)	**3.5%**	**0.6%**	**-0.2%**	**5.0%**

Table 3.24 Strain progresssion for reinforced concrete side gages under target loads- located directly below the RC side actuator (See Section 3.6.2 for detailed information on precise location of each strain gage)

	STRAIN GAGE NAME	DBT10-4	DTT10-6
POSITION DESIGNATIONS	Location (All on FRP panel side)	Below actuator	Below actuator
	Attached to rebar or FRP	Rebar	Rebar
	Near top or bottom of deck	Bottom	Top
	Oriented longitudinal or transverse	Transverse	Transverse
CYCLIC LOADING PHASE I	Strain at Cycle # 1 (με)	484.2	-853.9
	Strain at Cycle # 250 (με)	486.5	-899.1
	Strain at Cycle # 500 (με)	487.1	-909.8
	Strain at Cycle # 750 (με)	488.3	-845.5
	Strain at Cycle # 1000 (με)	497.5	-839.6
	Change in strains (με)	**13.2**	**14.3**
	Change in strains (%)	**2.7%**	**-1.7%**
CYCLIC LOADING PHASE II	Strain at Cycle # 1 (με)	655.0	-634.14
	Strain at Cycle # 250 (με)	665.9	-561.50
	Strain at Cycle # 500 (με)	692.3	-563.89
	Strain at Cycle # 750 (με)	698.1	-579.36
	Strain at Cycle # 1000 (με)	693.5	-584.13
	Change in strains (με)	**38.5**	**50.0**
	Change in strains (%)	**5.9%**	**7.9%**

3.11.4 Progression of Separation between FRP Panel and Concrete

The FRP panel side strain gages located adjacent to the two FRP side stems shown in Table 3.25 are the gages used during static testing as indicators of separation between the concrete and composite panels. Unfortunately, the strain gages attached to the bottom transverse reinforcement at the same locations were both broken and so a complete discussion of strain discontinuities at these locations is not possible. However, because the most severe separation occurred in these regions during the static loading to ultimate capacity, significantly larger progressions in strain over the course of the cyclic loading are observed, as shown in Table 3.25, as compared to the strain gages directly below the actuators. Also note that the strains in the gages adjacent to the center stem are significantly more stable than those located adjacent to the outer stem.

The progression of the separation between the concrete and the composite at the same locations examined in Section 3.8.8 is summarized in Table 3.26. The both pairs of linear potentiometers display relatively constant results during the first cyclic phase. During the second cyclic phase, the linear potentiometers located near the central stem continue to display very similar separation values whereas the linear potentiometer pair near the outer stem exhibits a 0.19 mm (0.008 in) decrease in the overall separation distance between the concrete and the FRP panel.

One possible explanation for the difference in the stability levels of the gages and separation readings for two locations is that the FRP panel had fully separated from the concrete in the region near the center stem and so exhibited a stable response during the cyclic loading.

Table 3.25 Strain progresssion for transverse composite side gages under target loads- located along the centerline, near the stems (See Section 3.6.2 for detailed information on precise location of each strain gage)

	Strain gage name	DTT10-2	CM1T	DTT10-4	CM5T
Position designations	Location (All on FRP panel side)	Along centerline, near outer stem	Along centerline, near outer stem	Along centerline, near center stem	Along centerline, near center stem
	Attached to rebar or FRP	Rebar	FRP	Rebar	FRP
	Near top or bottom of deck	Top	Bottom	Top	Bottom
	Oriented longitudinal or transverse	Transverse	Transverse	Transverse	Transverse
Cyclic loading phase I	Strain at Cycle # 1 (με)	-5791.4	259.8	-33.2	309.1
	Strain at Cycle # 250 (με)	-5772.8	268.8	-41.8	314.6
	Strain at Cycle # 500 (με)	-5771.8	270.0	-40.7	314.1
	Strain at Cycle # 750 (με)	-5801.5	273.3	-64.7	313.5
	Strain at Cycle # 1000 (με)	-5884.1	279.0	-78.5	316.3
	Change in strains (με)	**-92.7**	**19.1**	**-45.3**	**7.2**
	Change in strains (%)	**-1.6%**	**7.4%**	**-136.2%**	**2.3%**
Cyclic loading phase II	Strain at Cycle # 1 (με)	-5878.8	301.5	-71.05	350.9
	Strain at Cycle # 250 (με)	-5923.3	297.0	-75.63	364.1
	Strain at Cycle # 500 (με)	-5955.1	296.4	-76.77	366.9
	Strain at Cycle # 750 (με)	-5970.0	297.0	-77.91	366.9
	Strain at Cycle # 1000 (με)	-6011.8	292.5	-72.18	369.1
	Change in strains (με)	**-133.0**	**-9.0**	**-1.1**	**18.2**
	Change in strains (%)	**-2.3%**	**-3.0%**	**-1.6%**	**5.2%**

Table 3.26 Separation progresssion for linear potentiometers located along the test speciment centerline, near the stems (See Section 3.6.1 for detailed information on precise location of each linear potentiometer)

	Location of linear potentiometers	Along centerline, near outer stem (Linear potentiometers M2T and M2B)					Along centerline, near center stem (Linear potentiometers M4T and M4B)				
	Calculated quantity	Separation		Overall change in separation			Separation		Overall change in separation		
	Units	mm	in	mm	in	%	mm	in	mm	in	%
Cyclic loading phase I	Cycle # 1	3.16	0.125	---	---	---	4.04	0.159	---	---	---
	Cycle # 250	3.10	0.122	-0.07	-0.003	-2.1%	4.07	0.160	0.03	0.001	0.9%
	Cycle # 500	3.08	0.121	-0.08	-0.003	-2.5%	4.04	0.159	0.00	0.000	0.0%
	Cycle # 750	3.14	0.124	-0.02	-0.001	-0.8%	4.13	0.163	0.09	0.003	2.8%
	Cycle # 1000	3.21	0.126	0.05	0.002	1.5%	4.20	0.165	0.16	0.006	5.1%
Cyclic loading phase II	Cycle # 1	3.47	0.137	---	---	---	4.66	0.183	---	---	---
	Cycle # 250	3.39	0.134	-0.08	-0.003	-2.6%	4.67	0.184	0.01	0.000	0.2%
	Cycle # 500	3.35	0.132	-0.12	-0.005	-3.9%	4.69	0.185	0.04	0.001	1.2%
	Cycle # 750	3.35	0.132	-0.13	-0.005	-4.1%	4.70	0.185	0.04	0.002	1.4%
	Cycle # 1000	3.29	0.129	-0.19	-0.007	-6.0%	4.67	0.184	0.02	0.001	0.5%

Conversely, the region of the FRP panel near the outer stem may display a less stable response as the separation between the concrete and the FRP panel propagates during the cyclic loading phases.

3.12 SUMMARY

The system level structural response of the FRP panel structural formwork system integrated within a two cell concrete box girder configuration was characterized through static and limited cyclic testing. Direct performance comparisons between the FRP structural formwork system and a reinforced concrete system were addressed. Aspects of the FRP panel reinforced system's response, including the overall response, the response between the panels, the strain development within the structure, changes in stiffness, and the progression of damage within the system were evaluated and discussed.

As a result of a direct performance comparison to the reinforced concrete deck slab, the FRP panel system was seen to perform either comparable or superior in nearly all aspects examined. The FRP panel side experienced less degradation of the effective stiffness, lower strain values throughout most of the deck slab, less residual deflections and lower center deflections throughout the loading range, especially at higher load levels. Due to the presence of the stiffeners on the FRP panels, the FRP panel system had a significantly more dispersed deflection distribution in the transverse direction and a slightly more localized deflection distribution in the longitudinal direction as compared to the deflection distributions for the reinforced concrete deck slab.

The overall response of the FRP panel system was observed to surpass specified load requirements by a substantial margin, with the system's ultimate load carrying capacity of 890 kN (200 kip) equivalent to 9.1 times the AASHTO service load and 4.9 times the CALTRANS permit truck load [152]. Signs of separation between the concrete and the FRP panels were first observed at the 489 kN (110 kip) load level, which was 5.0 times the AASHTO service load and 2.7 times the CALTRANS permit truck load. By using the load level at which initial signs of separation between the FRP panels and the concrete were observed as the critical state, an appropriate design load was determined for the FRP panel system.

Initial signs of the punching shear failure mode for the FRP panel side were observed at a load of 825 kN (186 kip), which is equivalent to 8.4 times the AASHTO service load. Since the punching shear response occurred at a load substantially above the specified loading requirements, it is unlikely that this potential failure mode would be critical at any point during the service life of the system. The punching shear failure was non-catastrophic and the system's post failure response to applied cyclic loading was very stable. The stability of the response indicates that even after partial loss of composite action between the FRP panels and the concrete ocurred, the bridge could remain open to traffic, albeit with slightly higher deflections during traffic loading. The ability to allow the damaged bridge to remain open to normal vehicular traffic is especially crucial in locations where road closures can cause significant detrimental impact on the surrounding community.

4 REPAIR OF THE FRP PANEL STRUCTURAL FORMWORK SYSTEM

4.1 INTRODUCTION

Following the completion of the cyclic phase for the first test specimen, an epoxy injection technique, which utilized a low viscosity resin, was developed and implemented to repair the damage that was incurred during structural testing. The separation between the concrete and the FRP panels as well as damage due to punching shear were addressed by this repair technique. The repair was analogous to resin injection techniques performed for reinforced concrete bridges as described in Section 2.3. The presence of the FRP structural formwork panels had no significant negative impacts on the ease of the repair and instead provided the added convenience of eliminating the need to provide material below the underside of the deck to catch excess resin that had flowed through the full thickness of the deck.

The goal for this phase of the research was to assess the effectiveness of repair efforts at reinstating proper load transfer and bond between the concrete and the composite panels in terms of field applicability and impact on structural performance. Aspects of the response of the FRP panel reinforced system including the overall response, the response between the panels, changes in stiffness, and the progression of damage within the system were evaluated and discussed. The repaired specimen was loaded statically up to 978kN (220 kip), which was 88 kN (20 kip) beyond the ultimate capacity of the original test specimen and the system did not reach its ultimate capacity. The repaired specimen was then loaded for 500 cycles at 2x the AASHTO fatigue factored service load and then reloaded statically up to the 978kN

(220 kip) load level. Since the primary purpose of testing the repaired specimen was to compare the structural response of the repaired FRP panel side to the original test results, only information relevant to the FRP panel side deck are included in the discussion of experimental results.

4.2 DESIGN AND IMPLEMENTATION OF REPAIR

The extent of the separation between the concrete and the composite was established by performing a tap test on the underside of the composite side deck. The separated region of the composite side deck is mapped in red, as shown in Figure 4.1.

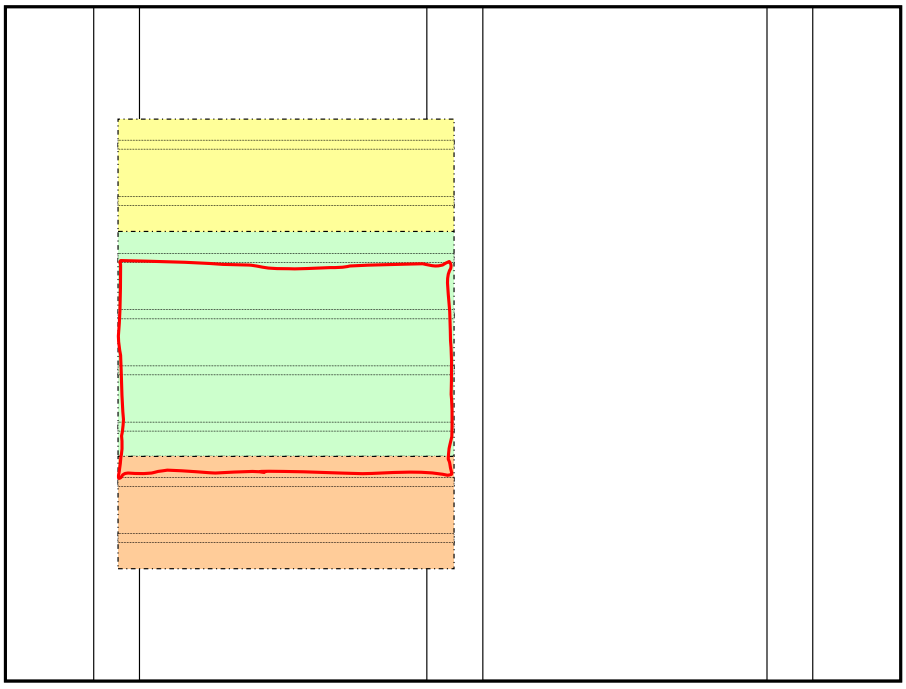

Figure 4.1 Region in which the FRP panels had separated from the concrete

Note that the separation between the concrete and composite is constrained to the region between stiffeners, such that the majority of the center FRP panel has

disconnected from the concrete with the separation arrested at the stiffener walls. The outer FRP panel shown in yellow remained fully intact, whereas the outer FRP panel shown in orange was only separated from the concrete along its length for the 127 mm (5 in) wide section which was adjacent to the center panel. This phenomenon highlights a feature of the FRP structural panel system; the debonded regions are constrained between stiffeners thereby slowing down the progression of damage throughout the system.

The repair technique was implemented by drilling multiple small holes in the top of the composite side deck concrete in a periodic arrangement of 19 mm (.75 in) diameter holes for resin injection ports and 13 mm (0.5 in) diameter holes for vent holes as shown in Figure 4.2 by the blue and red circles respectively. This design allowed the resin to flow within each trough created by the FRP panel stiffeners and act to reinstate load transfer between the concrete and the FRP panels. Note that the grey rectangle shown in Figure 4.2 represents the footprint of the elastomeric bearing pad for the FRP side actuator, which was left in place on the specimen during the repair. Plastic fittings were bonded into each hole using a two part epoxy system and a low viscosity resin system was pumped into the holes using a Masterflex peristaltic pump and the setup shown in Figure 4.3. The resin was pumped into each injection port until the tubing which transported the resin began to swell up with excess resin due to built up backpressure. When this occurred, the tubing was sealed off using a tubing clamp, the tubing was cut and the system was moved to pump resin into the next available injection port.

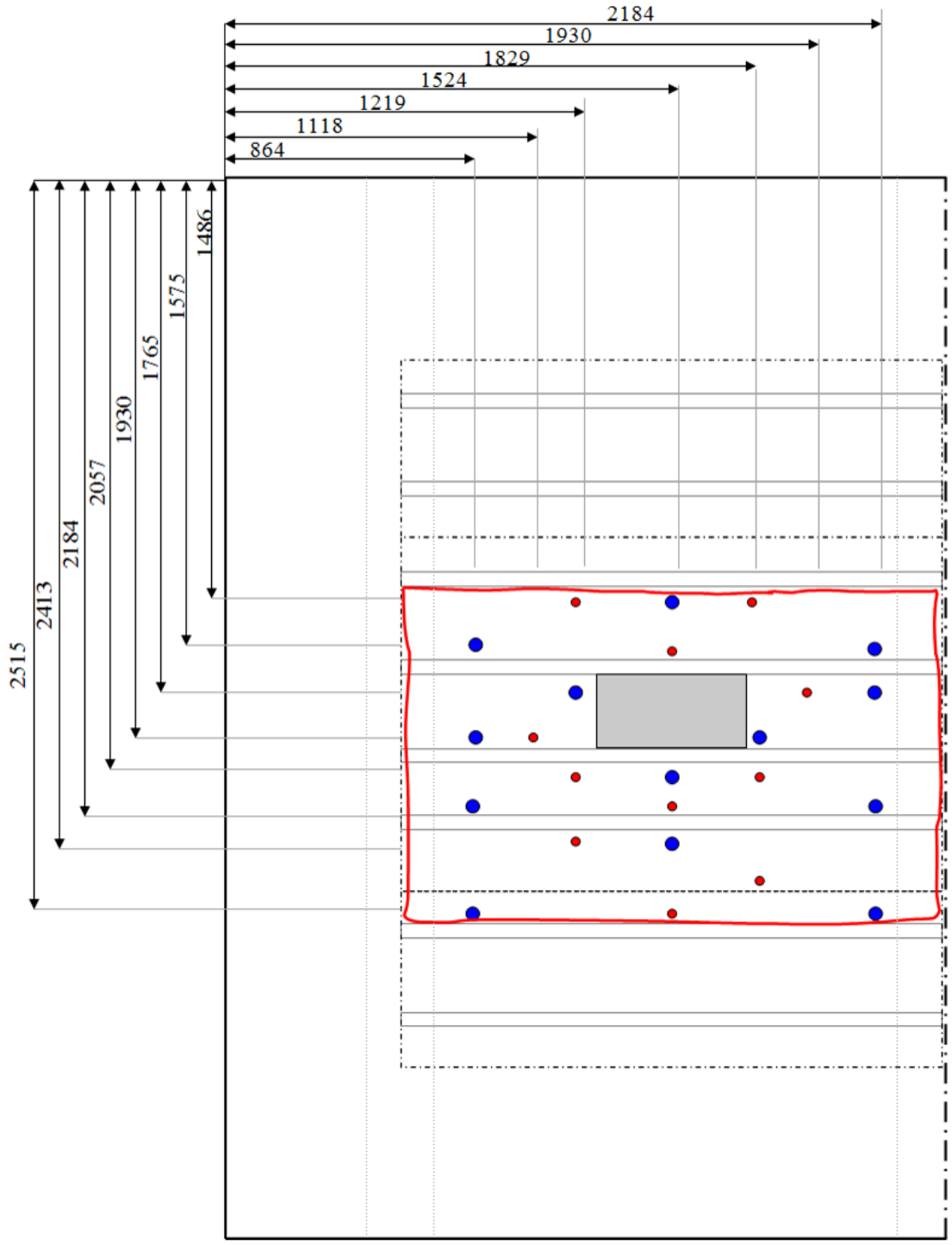

Figure 4.2 Detail of hole pattern arrangement for repair of FRP side deck
(Only the FRP panel side deck and not the RC side deck shown. Region encompassed by red line indicates where separation between FRP panel and conrete has occurred)

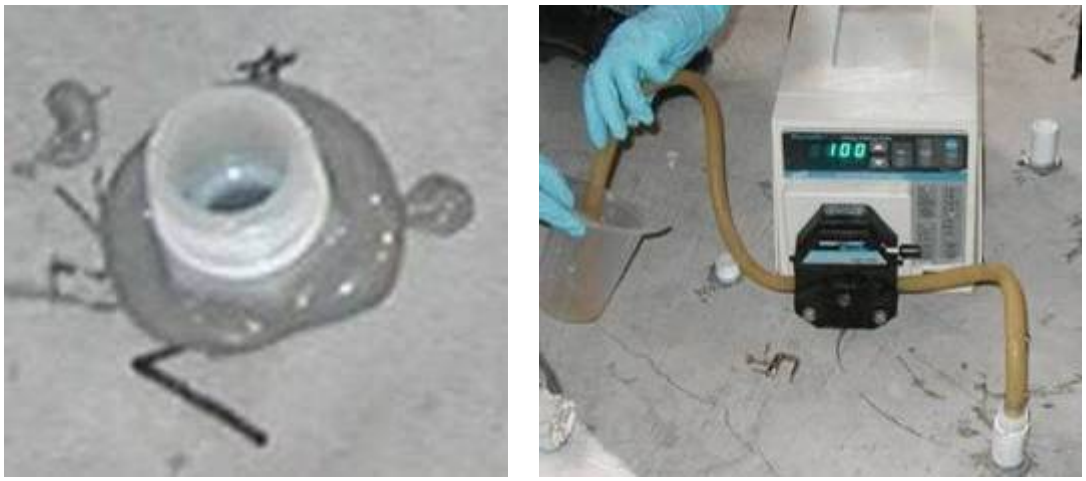

Figure 4.3 Injection port in top of deck and setup used to inject resin into deck

The Sikadur 55 SLV resin system from Sika Corporation used for the resin injection has a viscosity of approximately 105 centipoise and was mixed in a 2:1 ratio by volume of Component 'A' to Component 'B' [156]. The ambient temperature at the time of the repair was 16° C (61° F). Selected manufacturer provided properties for the system are summarized in Table 4.1. The resin system used in the repair of the FRP panel side deck was allowed to cure for 19 days prior to testing.

Table 4.1 Properties of Sikadur 55 SLV resin system [156]

Tensile Strength, 7 Day (ASTM D-638)		Flexural Strength, 7 Day (ASTM D-790)		Shear Strength, 7 Day (ASTM D-732)	
MPa	psi	MPa	psi	MPa	psi
48.9	7,100	58.6	8,500	40.0	5,800

INSTRUMENTATION

All instrumentation was disconnected briefly from the signal conditioning and data acquisition systems so that the instrumentation could be to temporarily moved to allow for unrestricted access to the specimen during the epoxy debond repair. The same instrumentation used for the original test was reconnected for use in the testing of the repaired specimen, however a significant number of strain gages, including the gages used to detect separation between the concrete and composite panels, were broken during the repair.

In order to take into account any residual strains in the gages due to the testing of the original specimen, the strain values from the end of the cyclic loading of the original test specimen taken from the unloaded specimen immediately prior to removing the instrumentation, were used as the initial strain values which were present at the start of testing for the repaired specimen. By biasing the strain gages in this manner, the most accurate representation of the actual strains present within the system, can be maintained.

When the linear potentiometers were reconnected to the specimen, they were rebiased immediately prior to the static loading of the repaired specimen. The use of a new bias value for the repaired deflections facilitated comparisons of load versus deflection data for the original and repaired test specimens however meant that the values for the repaired specimen were relative deflections of the test specimen, rather than absolute values.

4.3 RESULTS FOR STATIC LOADING OF THE REPAIRED SPECIMEN

4.3.1 Loading Protocol

The test specimen was loaded statically and cyclically to evaluate the effectiveness of the repair on performance and integrity. The static portion of testing used the same loading levels used for the original static testing, however the specimen was only cycled through the minimum threshold load value of 4.5 kN (1 kip) at the load levels of 222.4 kN (50 kips) and 578.3 kN (130 kips) instead of at every other load level increase as done in the original static testing of the test specimen. Additionally, the load was increased by 88 kN (20 kip) beyond the ultimate capacity of the original test specimen to a load of 978 kN (220 kips), which was the maximum loading capacity of the hydraulic actuators. The loading steps for the static testing of the repair specimen are summarized in Table 3.8.

Table 4.2 Static loading protocol for testing of repaired specimen

TARGET LOAD		SINGLE LOAD-UNLOAD CYCLE (YES/ NO)	MULTIPLE OF SERVICE I LOAD LEVEL 98 kN (22 kip)	MULTIPLE OF STRENGTH I LOAD LEVEL 169 kN (38 kip)	MULTIPLE OF PERMIT LOAD LEVEL 180 kN (41 kip)
kN	kip				
98	22	No	1.0	0.6	0.5
222	50	Yes	2.3	1.3	1.2
311	70	No	3.2	1.8	1.7
400	90	No	4.1	2.4	2.2
489	110	No	5.0	2.9	2.7
578	130	Yes	5.9	3.4	3.2
667	150	No	6.8	3.9	3.7
756	170	No	7.7	4.5	4.2
845	190	No	8.6	5.0	4.7
890	200	No	9.1	5.3	4.9
934	210	No	9.5	5.5	5.2
978	220	No	10.0	5.8	5.4

4.3.2 Overall Behavior

At each load level, the target load was held briefly to allow inspection of the test specimen in the loaded state. No additional cracking or other visual damage was observed on the test specimen during the static loading phase for the repaired specimen. However, multiple small "popping" noises originating from the composite side deck slab were heard at the 210 kN (934 kip) load level, which was equivalent to 9.5 times the AASHTO service load. The repaired specimen was loaded up to 978 kN (220 kip) per actuator and the ultimate capacity of the specimen was not reached. This load was an 88 kN (20 kip) increase over the ultimate capacity of the original test specimen of 890 kN (200 kip), which is equivalent to 9.1 times the AASHTO service load.

The response of the repaired FRP side under static loading is compared to the response of the original test specimen under static loading and also to the last cycle of the cyclic phase for the original test specimen, which was the last loading experienced by the test specimen prior to the repair. Figure 4.4 shows the overall load versus midspan displacement envelope plots for the FRP side. In order to more easily compare the stiffness of the deck slab before and after the repair, the load-deflection curves for the repaired specimen and the original specimen at the end of cyclic loading were shifted back to the origin by removing the residual deflections, as shown in Figure 4.5.

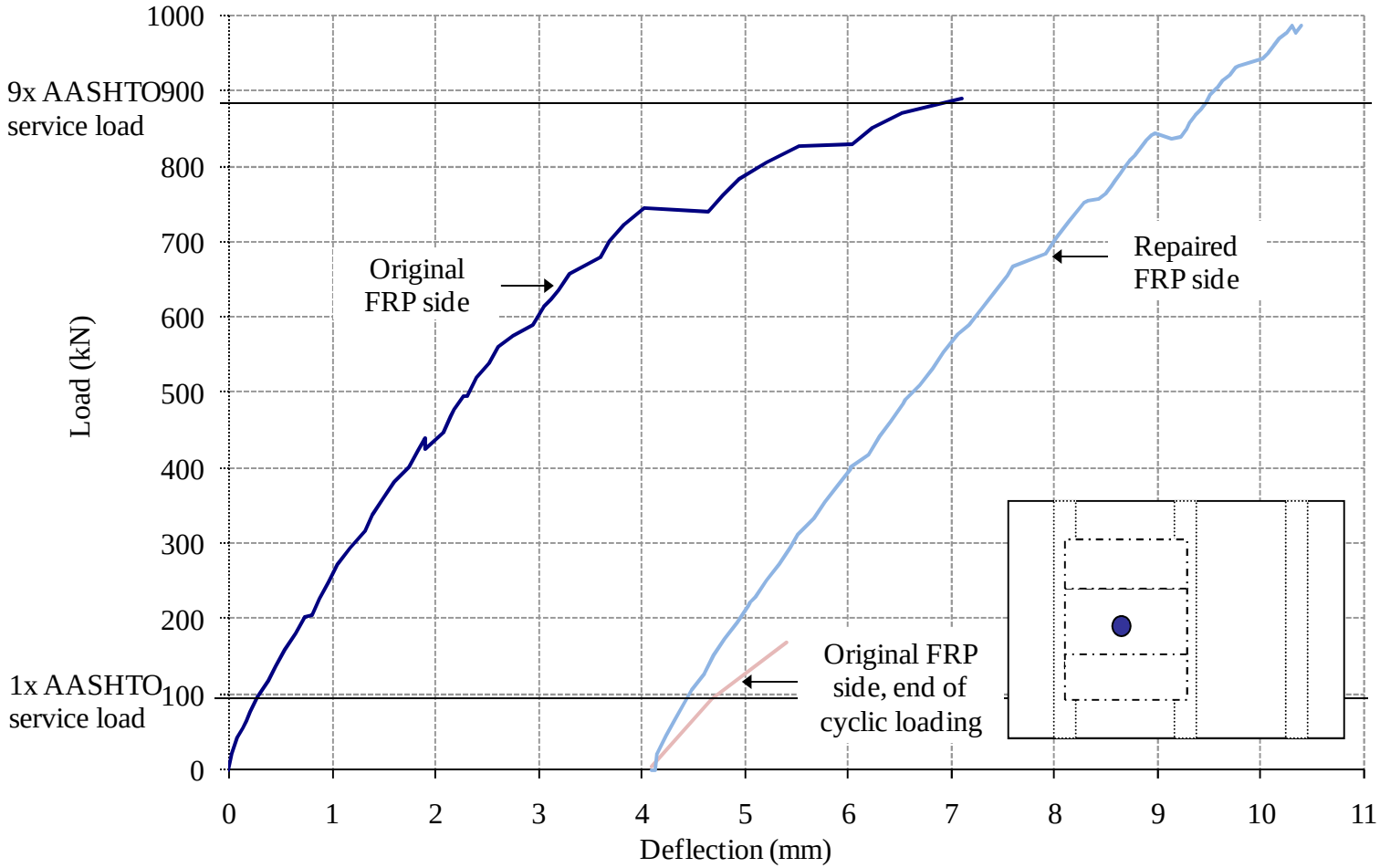

Figure 4.4 Load versus deflection envelope plots of the original and repaired test specimen for both the FRP and RC slabs

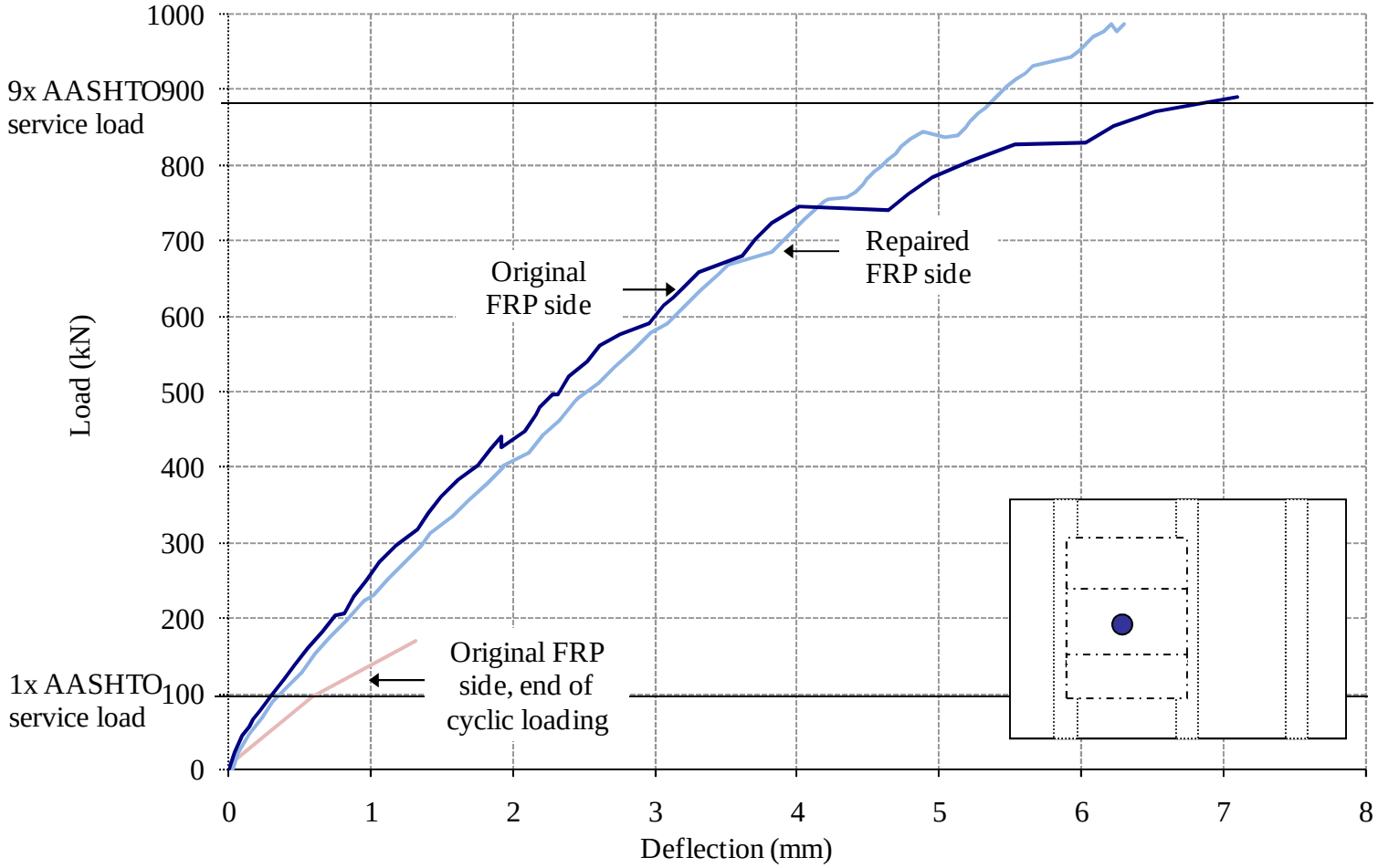

Figure 4.5 Load versus deflection envelope plots of the original and repaired test specimen for both the FRP and RC slabs (Residual deflections removed from data allowing all three load-deflection plots to begin at origin)

As observed in Figure 4.5, the repair of the specimen restores the specimen's stiffness from the significantly degraded response shown for the original specimen at the end of cyclic loading to a structural response comparable to the original static loading of the test specimen. For the majority of the loading range, the slope of the load-deflection curve for the repaired FRP side was slightly lower than the values from the original testing of the FRP side, with the repaired specimen displaying a more linear response throughout the entire load range.

At the 98 kN (22 kip) load level, equivalent to 1x the AASHTO HS20 service load, the vertical midspan deflection was 0.29 mm (0.011 in) for the original FRP side slab and was 0.58 (0.022 in) for the original FRP side at the end of cyclic loading, whereas the deflection for the repaired FRP side slab was 0.39 mm (0.016 in). At an actuator load of 169 kN (38 kip), which was the equivalent to 1x the AASHTO Strength I level, the center FRP side deflection for the original specimen was 0.60 mm (0.024 in), whereas the deflections for the original specimen at the end of cyclic loading and for the repaired specimen were 1.32 mm (0.052 in) and 0.71 mm (0.028 in) respectively. Up till the 756 kN (170 kip) load level, the repaired specimen deflected slightly more than the original specimen, with deflection differences between the two tests of less than 0.3 mm (0.01 in). Beyond the 756 kN (170 kip) load level, the original specimen exhibited greater deflection values for the remainder of the loading levels. The midspan deflection of the FRP panel side of the repaired test specimen at the 890 kN (200 kip) load level decreased by 24% or 1.72 mm (0.068 in) to a deflection value of 5.37 mm (0.211 in) from the 7.09 mm (0.279 in) deflection of the original specimen at the same load level.

4.3.3 Stiffness Change for Repaired FRP Panel Side

The damage progression of the FRP panel side slab for the original and repaired specimen static loadings were determined through examination of the effective stiffness and the effective stiffness ratio, which were defined previously in Section 3.8.3 and are repeated below:

$$\text{Effective stiffness} = \frac{P_f - P_i}{\delta_f - \delta_i} \tag{4.1}$$

where

P_f = Target actuator load of a load cycle based on loading protocol

P_i = Minimum threshold actuator load of a load cycle

δ_f = Deflection at load P_f, at the location under consideration

δ_f = Deflection at load P_i, at the location under consideration

The effective stiffness ratio was calculated by comparing the effective stiffness at a load level to the effective stiffness at the baseline load as shown in Equation 4.2:

$$\text{Effective stiffness ratio} = \frac{\text{Effective stiffness at a load level}}{\text{Effective stiffness at baseline (98 kN)}} \tag{4.2}$$

The load of 98 kN (22 kip), which represented a HS20 truck load of 73 kN (16.4 kip) with an additional AASHTO defined 33% dynamic allowance and was also the initial load level in the static testing, was chosen as the baseline load. The effective stiffness value determined from the loading of the original FRP side up to the 98 kN (22 kip) load level was used as the baseline value in the calculation for determining the effective stiffness ratios for the original FRP specimen at the end of

cyclic loading and for the repaired FRP side. This allowed any change in stiffness between the original and repaired test to be taken into account.

The effective stiffness ratios for the original FRP side deck slab, the original FRP side deck slab after the completion of the cyclic loading phases and repaired FRP side deck slab are shown in Table 4.3, Table 4.4 and Table 4.5 respectively. The degradation trends for the slabs are most easily observed in Figure 4.6, which plots the effective stiffness values of the slabs versus load level.

The effective stiffness ratios for the original FRP side deck slab at the end of cyclic loading, shown in Table 4.4, of only 0.63 at the 98 kN (22kip) load level and 0.52 at the 169 kN (38 kip) load level indicate the significant damage which had occurred to the system. Note that the cyclic loading phase was performed on the post failure specimen to show the structural stability of the system after exposed to extreme event loading levels therefore the level of damage observed was expected. The repaired specimen shows effective stiffness values far closer to original test specimen, which indicates the repair was effective at restoring original capacity.

Throughout the entire loading range, the repaired FRP side effective stiffness ratio gradually decreased following an approximately linear decay, with less than 5% variation from a linear profile. Conversely, the original FRP side effective stiffness ratio decreased by less than 10% during the first five loading cycles and then decreased progressively greater quantities during the final five load levels. The repaired FRP side exhibited an effective stiffness ratio which was initially 11% lower than the corresponding value for the original FRP side.

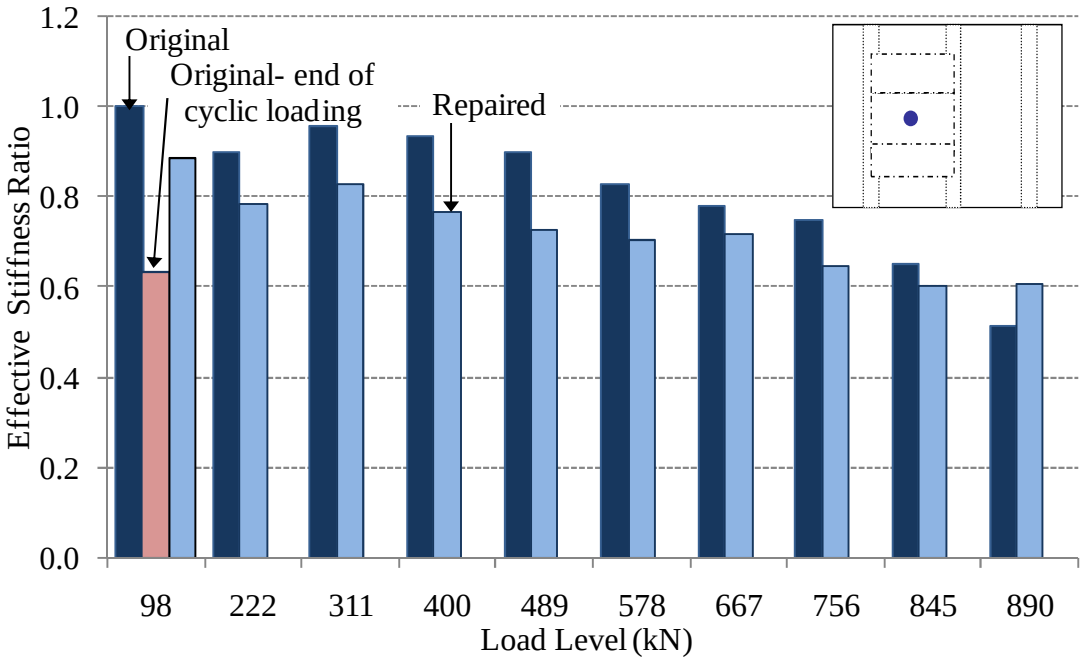

Figure 4.6 Stiffness ratios of the FRP side slab at different loading phases

Table 4.3 Effective stiffness ratios of original FRP panel side slab

Target actuator load		Actual target actuator load, P_f		Actual min. threshold actuator load, P_i		Deflection at target load, δ_f		Deflection at min. threshold load, δ_i		Effective stiffness ratio
kN	Kip	kN	kip	kN	kip	mm	in	mm	in	---
98	22	95.9	21.6	22.3	5.0	0.29	0.011	0.03	0.001	1.00
222	50	204.1	45.9	22.3	5.0	0.74	0.029	0.03	0.001	0.90
311	70	316.1	71.1	33.4	7.5	1.33	0.052	0.30	0.012	0.96
400	90	382.5	86.0	33.4	7.5	1.60	0.063	0.30	0.012	0.94
489	110	478.4	107.6	31.7	7.1	2.18	0.086	0.44	0.017	0.90
578	130	576.3	129.6	31.7	7.1	2.75	0.108	0.44	0.017	0.83
667	150	680.9	153.1	40.3	9.1	3.61	0.142	0.73	0.029	0.78
756	170	745.1	167.5	40.3	9.1	4.01	0.158	0.73	0.029	0.75
845	190	828.6	186.3	33.5	7.5	5.52	0.217	1.25	0.049	0.65
890	200	890.5	200.2	33.5	7.5	7.09	0.279	1.25	0.049	0.51

Table 4.4 Effective stiffness ratios of original FRP panel side slab, end of cyclic phase

Target actuator load		Actual target actuator load, P_f		Actual min. threshold actuator load, P_i		Deflection at target load, δ_f		Deflection at min. threshold load, δ_i		Effective stiffness ratio
kN	kip	kN	kip	kN	kip	mm	in	mm	in	---
98	22	99.9	22.5	12.4	2.8	0.51	0.020	0.03	0.001	0.63
169	38	169.0	38.0	12.4	2.8	1.09	0.043	0.03	0.001	0.52

Table 4.5 Effective stiffness ratios of repaired FRP panel side slab

Target actuator load		Actual target actuator load, P_f		Actual min. threshold actuator load, P_i		Deflection at target load, δ_f		Deflection at min. threshold load, δ_i		Effective stiffness ratio
kN	kip	kN	kip	kN	kip	mm	in	mm	in	---
98	22	106.8	24.0	22.4	5.0	0.39	0.015	0.06	0.002	0.89
222	50	222.8	50.1	22.4	5.0	0.95	0.038	0.06	0.002	0.78
311	70	311.9	70.1	3.8	0.9	1.42	0.056	0.12	0.005	0.83
400	90	400.6	90.1	3.8	0.9	1.93	0.076	0.12	0.005	0.76
489	110	490.1	110.2	3.8	0.9	2.46	0.097	0.12	0.005	0.73
578	130	577.0	129.7	3.8	0.9	2.96	0.117	0.12	0.005	0.70
667	150	667.6	150.1	3.7	0.8	3.51	0.138	0.28	0.011	0.72
756	170	756.1	170.0	3.7	0.8	4.34	0.171	0.28	0.011	0.65
845	190	849.1	190.9	3.7	0.8	5.18	0.204	0.28	0.011	0.60
890	200	894.0	201.0	3.7	0.8	5.42	0.213	0.28	0.011	0.61

Over the next three load levels, the difference between the original and repaired FRP side effective stiffness values gradually increased to a maximum of 19% greater effective stiffness ratio for the original FRP side at the 400 kN (90 kip) load level, then decreased steadily for the remainder of the loading. At the 890 kN (200 kip) load level, the effective stiffness ratio of the repaired FRP side was 19% larger than the effective stiffness ratio for the original FRP side.

4.3.4 Deflection Profiles

In this section, deflection profiles throughout the test specimen for key load levels up to the 890 kN (200 kip) load level are presented. The deflection profiles for the repaired specimen are directly compared to the profiles from the original specimen in order to determine the any changes in structural response between the two systems. Unless otherwise noted, the deflection profile figures in this section all maintain the same deflection scale, which accommodates the maximum deflection values observed in the FRP side deck slab at the ultimate capacity of the original test specimen, in order provide context for each deflection value in relation to the overall deformation of the structure.

The deflection profile of the repaired specimen along the length of the deck above the central stem presented in Figure 4.7 shows uniform deflections in the longitudinal direction at all load levels. Similar uniform deflection profiles are also observed above the two outer stems and these results indicate that the vertical deformations of the stems do not significantly affect the overall structural response of the test specimen. The maximum deflection in the deck above the stems at the 890 kN

(200 kip) load level was 0.87 mm (0.03 in), which indicates that the actual corresponding deflections at the midpoints of the slabs are approximately 0.9 mm (0.03 in) smaller than the values given from the linear potentiometers due to the deflection contribution from stems. Note that the maximum deflections above the stems at maximum loading were approximately 7.7 times smaller than the corresponding midpoint deflection of the reinforced concrete side slab.

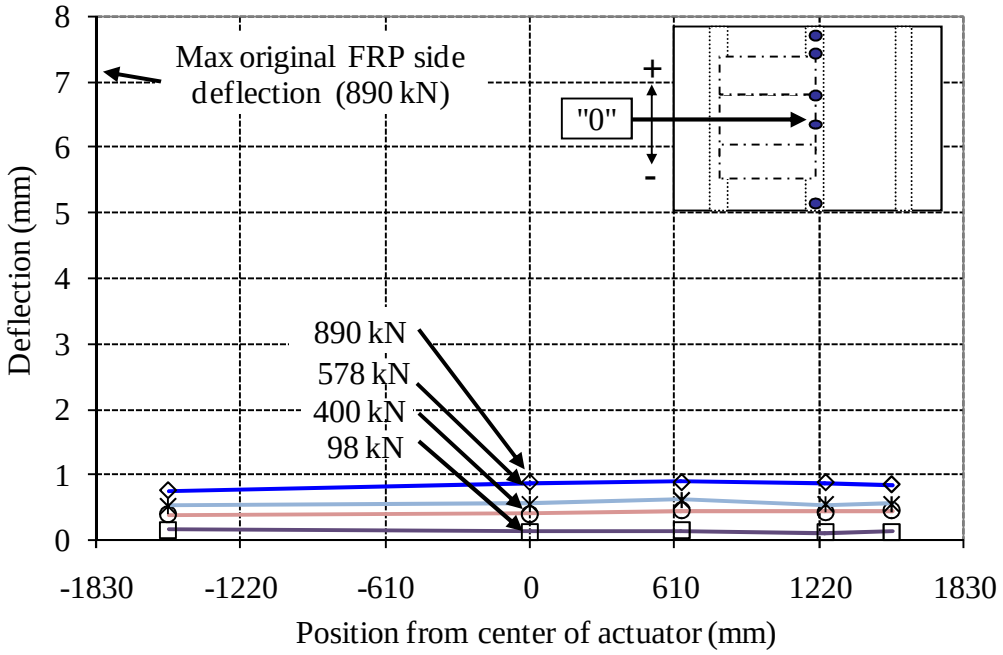

Figure 4.7 Deflection profile of repaired specimen on the deck above the central stem

The deflection profiles along the centerline of the original and repaired FRP slab are shown in Figure 4.8 and Figure 4.9. As expected, the highest deflection values for both the original and repaired FRP side were observed for the linear potentiometer directly below the FRP side hydraulic actuator, with progressively smaller deflections at distances away from this location.

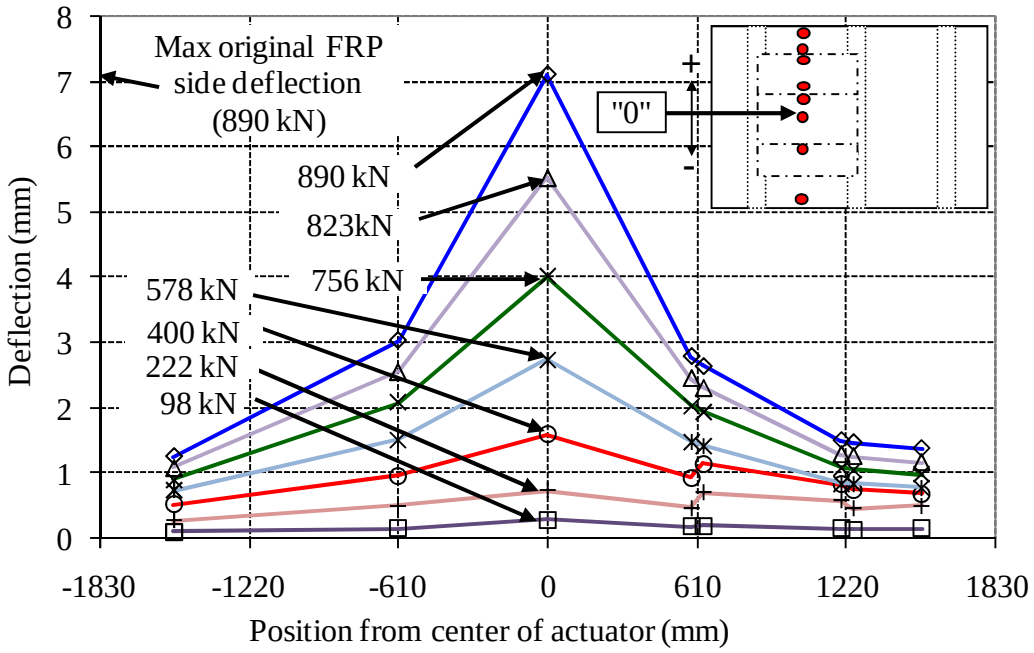

Figure 4.8 Deflection profile along centerline of original FRP side deck

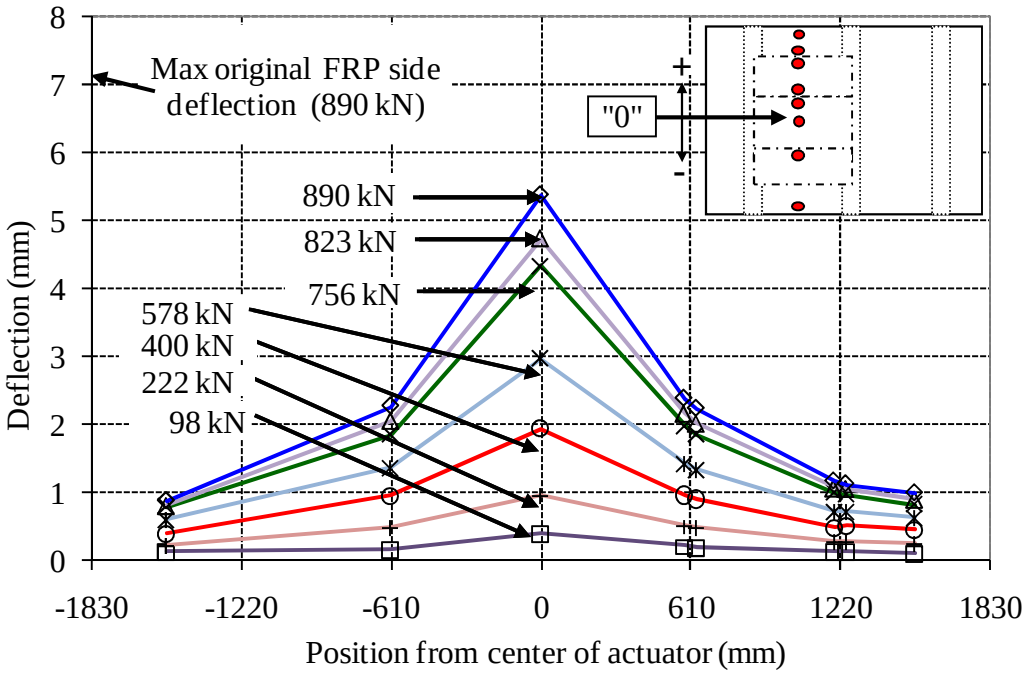

Figure 4.9 Deflection profile along centerline of repaired FRP side deck

Both tests maintain nearly symmetric deflection profiles along the length of the specimen and differ primarily in the magnitude of the center deflection values displayed at different load levels.

In order to more thoroughly compare the level of localized deformations in the original FRP slab and the repaired FRP slab, the superimposed deflection profiles along the centerline of the decks at different load levels are shown in Figure 4.10, Figure 4.11, and Figure 4.12. For loadings up to the 756 kN (170 kip) load level, which is equivalent to 7.7 times the AASHTO service load, the repaired FRP side displayed a slightly more localized deflection profile as compared to the original FRP side, with a higher center deflection and lower deflections away from the actuator, as shown in Figure 4.10 and Figure 4.11.

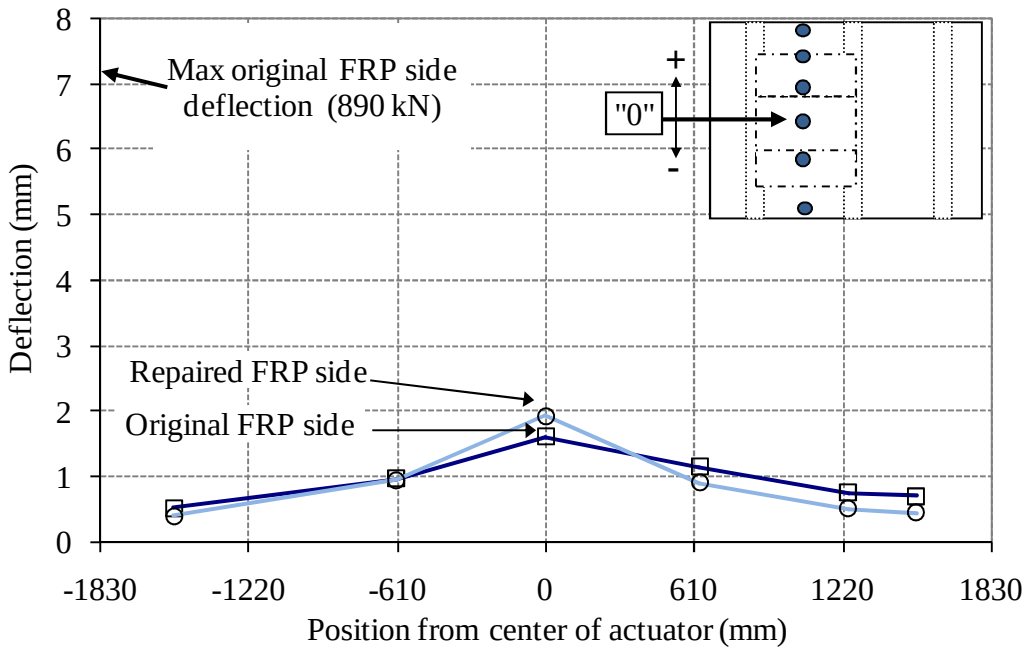

Figure 4.10 Original and repaired FRP side deflection profiles at 400 kN load level

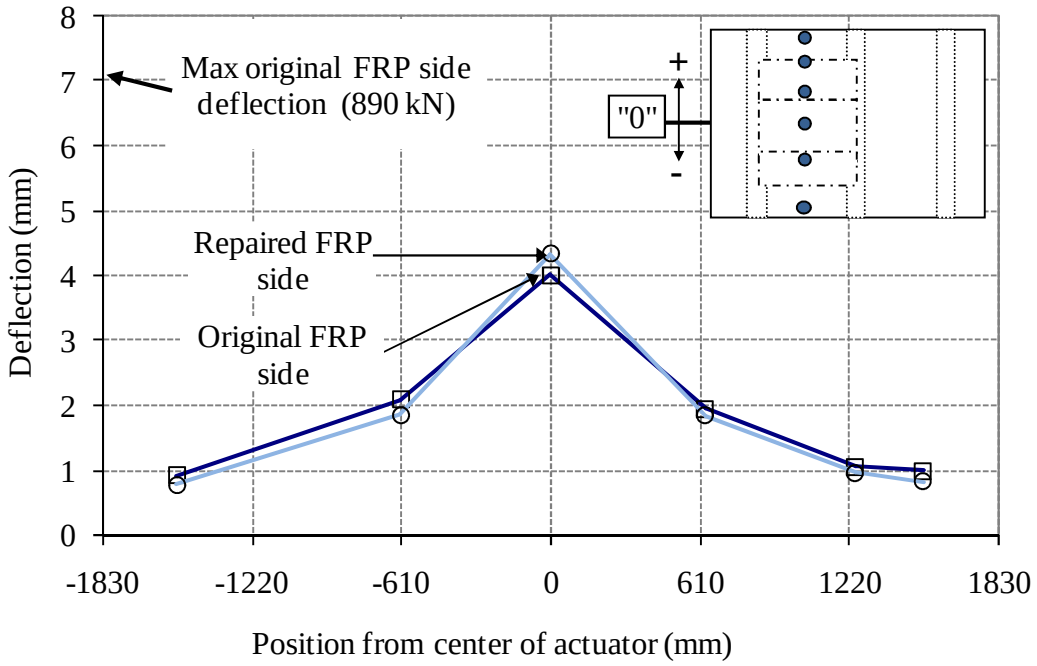

Figure 4.11 Original and repaired FRP side deflection profiles at 756 kN load level

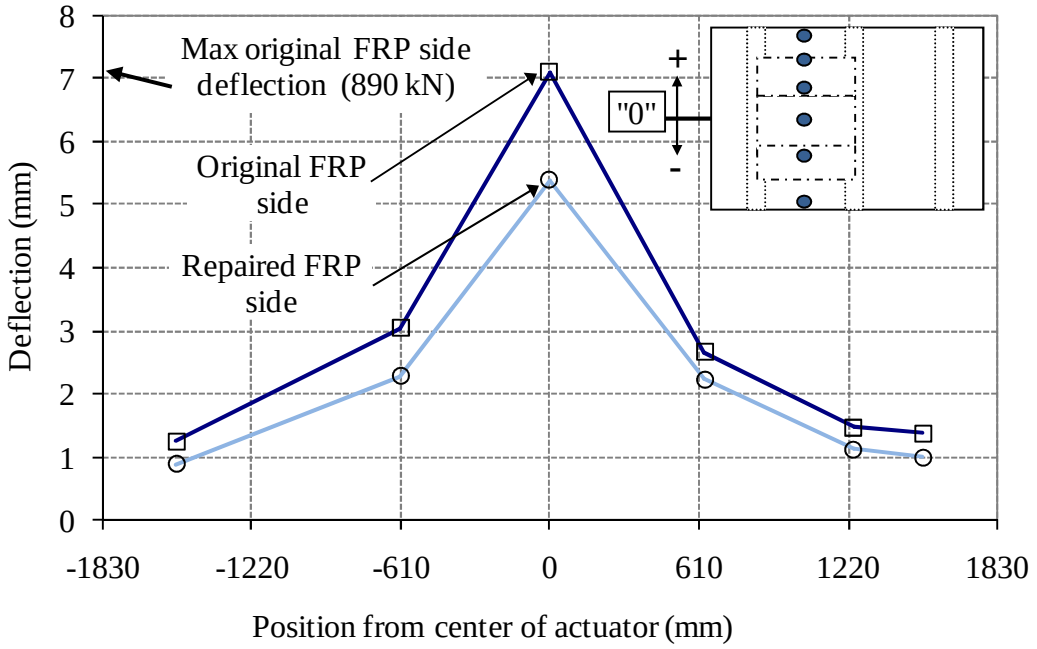

Figure 4.12 Original and repaired FRP side deflection profiles at 890 kN load level

For the load levels between 222 kN (50 kip) and 756 kN (170 kip), the difference in center deflections between the two tests remained within the range of 0.21 mm (0.008 in) to 0.33 mm (0.013 in). This greater center deflection value for the repaired FRP side affected the deflection profile more significantly at lower loading levels such as the profiles shown in Figure 4.10 for the 400 kN (90 kip) load level and was of negligible impact at higher loads as shown in Figure 4.11, which displays the comparably shaped original and repaired FRP side deflection profiles for the 756 kN (170 kip) load level.

At the ultimate capacity of the original test specimen, which occurred at the 890 kN (200 kip) load level (equivalent to 9.1 times the AASHTO service load), the center deflections as well as the overall deflections at locations away from the point of load application were significantly greater for the original FRP side as compared to the repaired FRP side as shown in Figure 4.12. The higher deflection values for the original FRP side were likely due to the punching shear damage that was first observed at the 845 kN (190 kN) load level. The repaired specimen showed no signs of punching shear damage during its loading.

The FRP side deflection profiles along the transverse centerline of the test specimen are presented for the original FRP side and repaired FRP side in Figure 4.13 and Figure 4.14 respectively. The highest deflection values were observed near the actuator locations and minimal deflection values were observed above either stem. Both tests exhibited asymmetric deflection profiles which deflected more on the side adjacent to the central stem.

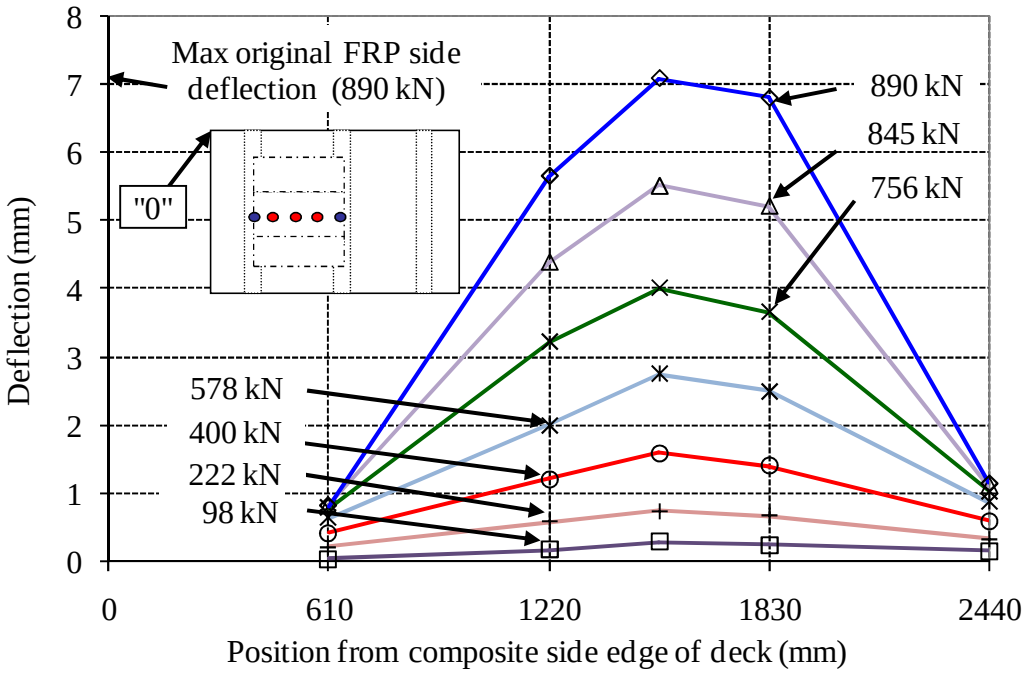

Figure 4.13 Transverse deflection profile for original composite side slab

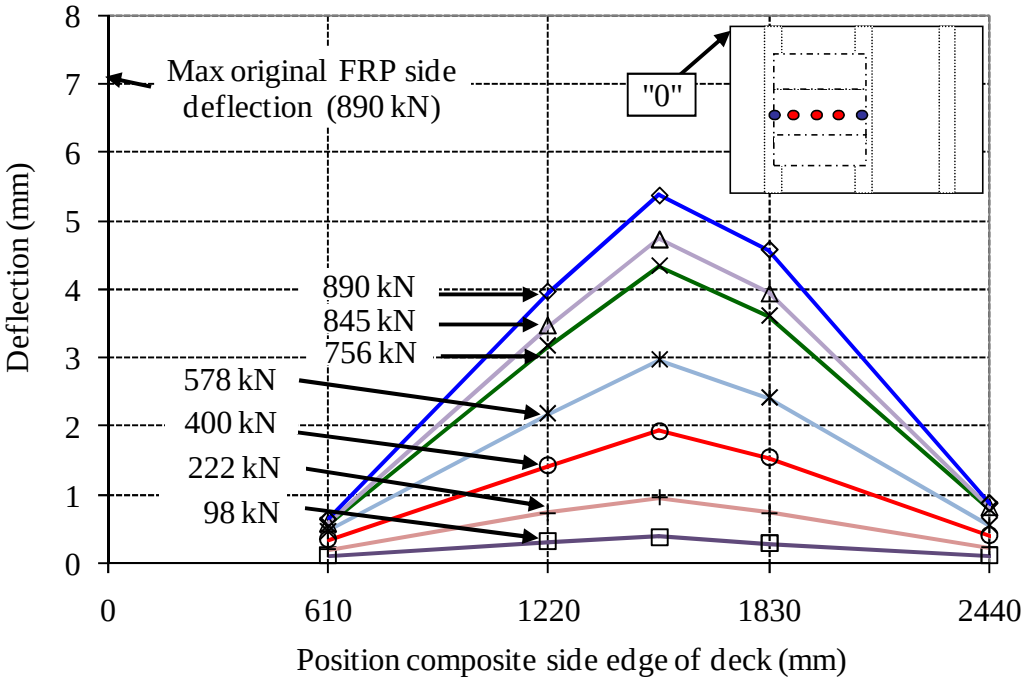

Figure 4.14 Transverse deflection profile for repaired composite side slab

The superimposed transverse deflection profiles were examined at different loads and the profiles for the 756 kN (170 kip) load level and 890 kN (200 kip) load level are shown in Figure 4.15 and Figure 4.16 respectively. Both tests maintained comparable transverse deflection profiles up to the 756 kN (170 kip) load level, equivalent to 7.7 times the AASHTO service load, with the repaired FRP side displaying slightly more localized deflection profiles as shown in Figure 4.15. At loads above the 756 kN (170 kip) load level, the original FRP side deflected significantly more than the repaired FRP side as shown in Figure 4.16.

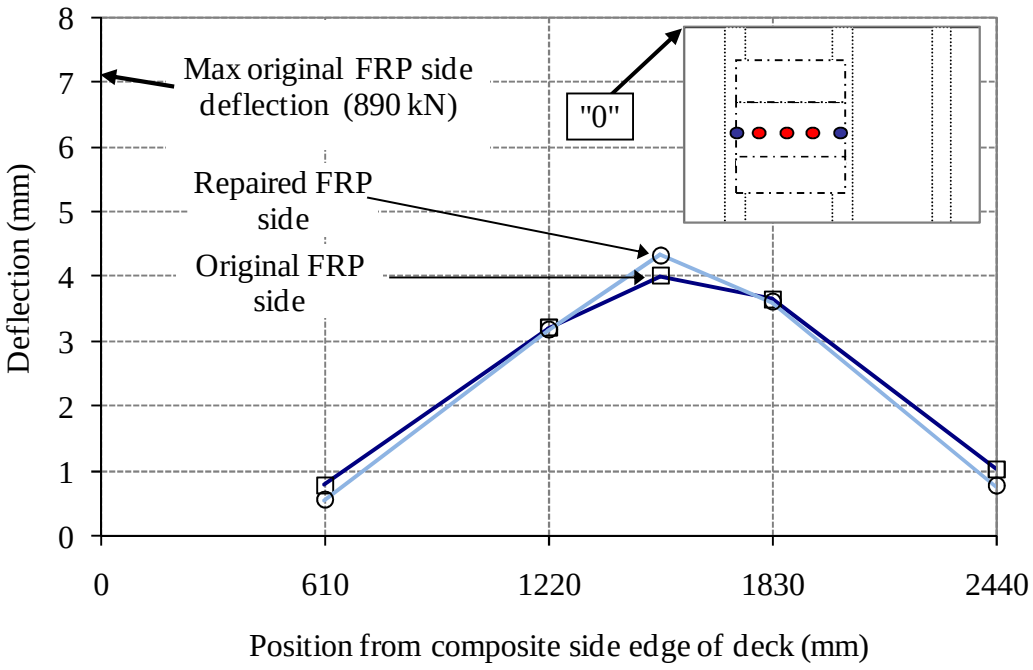

Figure 4.15 Original and repaired FRP side deflection profiles at 756 kN load level

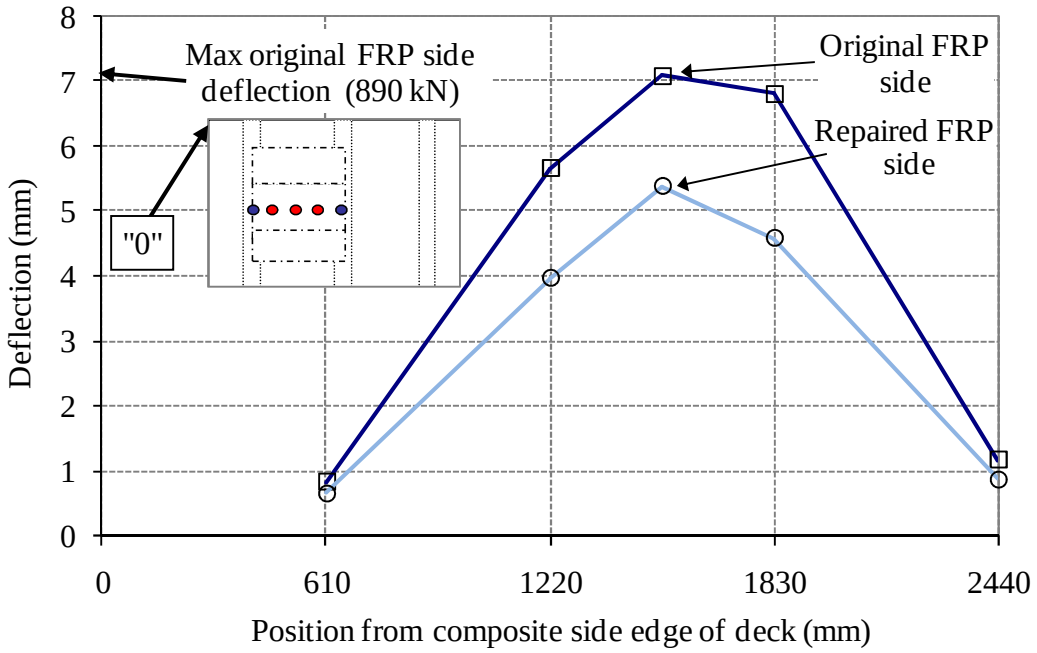

Figure 4.16 Original and repaired FRP side deflection profiles at 890 kN load level

The envelope plots of load versus deflection for linear potentiometers adjacent to the central linear potentiometer locations are shown in Figure 4.17 and Figure 4.18. Figure 4.17 compares the load-deflection plots of the linear potentiometers that are located a distance of 610 mm (2 ft) away from the center of the test specimen along the centerline of the FRP side slab. The very similar curves for all four linear potentiometers indicate a very symmetric deflection profile for the composite side deck in the longitudinal direction (comparison of C3B and D3B) and also indicate that the original and repaired FRP side deck slab exhibit very comparable responses at distances away from the point of load application in the longitudinal direction.

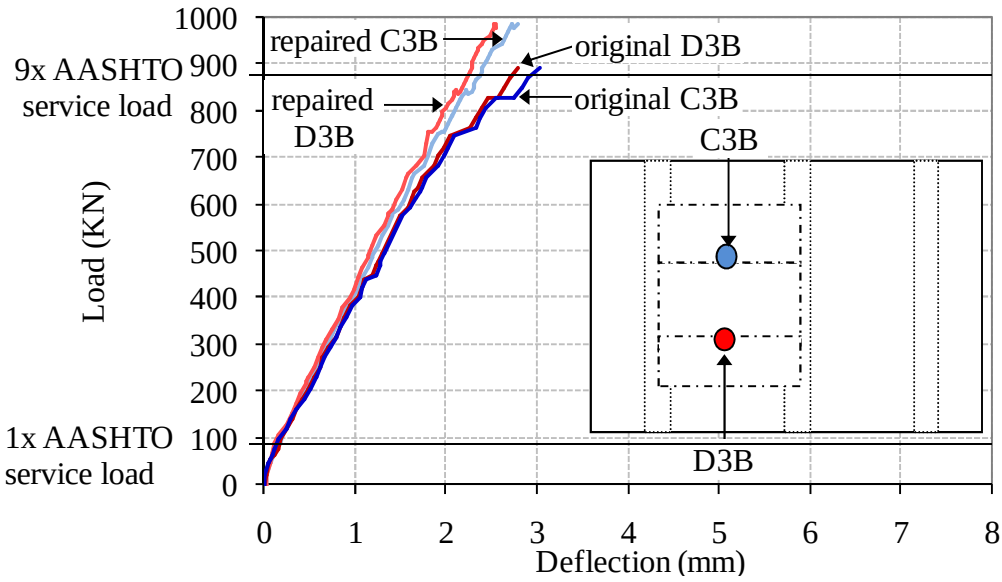

Figure 4.17 Envelope plot for linear potentiometers along the centerlines of the original and repaired FRP slab
(Located 610 mm away in the longitudinal direction from the test specimen midspan)

The load versus deflection envelope plots for linear potentiometers which along the centerline of the test specimen and are positioned 610 mm (2 ft) on either side of the center of the FRP side actuator are shown in Figure 4.18. For the repaired specimen, the two linear potentiometers remained comparable to within the tolerance of the linear potentiometers until approximately the 578 kN (130 kip) load level was achieved. For the remainder of the repaired specimen loading, the linear potentiometer located adjacent to the exterior stem, M2B, displayed an average of 13% lower deflection values, with a standard deviation of 1%, as compared to the linear potentiometer located adjacent the central stem, M4B. Conversely, the deflection values for linear potentiometer M2B throughout the entire loading range of the original experimental testing were an average of 16% smaller than the deflections of M4B during the original test, with a standard deviation of 3%. At higher loading

levels, the repaired specimen deflections for both M2B and M4B were significantly smaller than the corresponding deflections observed during the original testing, indicating that the implemented repair was effective.

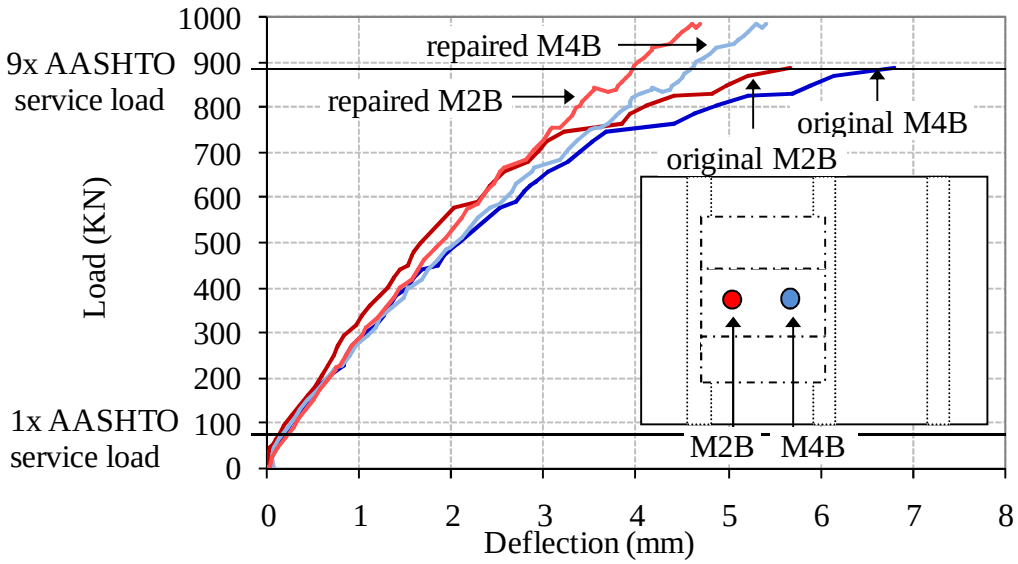

Figure 4.18 Envelope plot for linear potentiometers on original and repaired FRP side along the centerline of the test specimen
(Located 610 mm away in the transverse direction from the FRP side centerline)

The deflections of the original and repaired FRP slabs were compared both near and away from the point of load application and in terms of longitudinal and transverse deflection profiles. The maximum deflection values measured in the both the original and repaired FRP deck slabs were located at the midspan of the slabs, directly below the FRP side actuator. For the majority of the loading range, the center deflection values for the repaired FRP side slab were slightly higher than the original FRP slab center deflections and the deflections away from the point of load application in both the longitudinal and transverse direction were comparable for both tests. At higher loads, the repaired FRP slab deflected less both in terms of center

deflections as well as deflections at points away from the point of load application. At the 890 kN (200 kip) load level, equivalent to over nine times AASHTO service load, the original FRP side displayed a 7.09 mm (0.279 in) center deflection, while the repaired FRP side displayed a 5.42 mm (0.213 in) center deflection. A detailed discussion of the progression of the center deflections for both the original and repaired FRP slabs, as they pertain to the effective stiffness of the slabs, is provided in Section 3.8.3, beginning on page 87. The stable linear deflection response displayed by the repaired FRP slab is an indication that the repair of the FRP side deck slab was successful.

4.3.5 Strain Development

The strain development within the test specimen was observed though the examination of strain gages applied to the steel and composite reinforcement within the test specimen. The precise location of all strain gages is given in Section 3.6.2. Note that strain values reported as negative indicate compressive strains whereas positive values indicate tensile strains. Since the structural performance of the FRP panel side slab is the focus for testing of the repaired specimen, only strains from the FRP panel side slab and non from the RC side are shown. Performance comparisons are made between the repaired specimen strain values and the strains from the original testing of the FRP deck slab.

As discussed previously in Section 0, the repaired specimen strain gages were biased using strain values from the end of the cyclic loading of the original test specimen. This allowed for any residual strains in the gages due to the testing of the

original specimen to be taken into account by presenting absolute strain values rather than relative strain values, which gives a more accurate picture of the actual strains present within the structure. For the discussion of strain progressions, the changes in the strain values for different load levels were presented for the repaired specimen in terms of relative strains rather than absolute strains, which were biased from the start of the repaired specimen testing, in order to allow for easier comparisons with the data from the original test specimen at different load levels.

4.3.5.1 Strain Progression for Gages at Center of Composite Side Deck

At the 1x AASHTO service load of 98 kN (22 kip), all composite side deck relative strains in the original test specimen were less than 100 microstrains and were less than 130 microstrains for the repaired specimen, with the highest strains measured in the strain gages directly below the two actuators. At the 400 kN (90 kip) load level, which is equivalent to approximately four times the AASHTO service load, the highest FRP deck side strain value of 516 microstrains was recorded for the bottom transverse FRP side strain gage at midspan from original test specimen whereas the equivalent relative strain value for the repaired test specimen was 577 microstrains. The bottom longitudinal relative strain gage readings on the strain gage located directly below the composite actuator, was 241 for the original test specimen and 531 for the repaired test specimen for this load level.

At ultimate capacity for the original test specimen, which occurred at load of 890 kN (200 kip), equivalent to approximately nine times the AASHTO service load,

the highest overall strains in the FRP panel side deck slab of the original test specimen and repaired test specimen were observed in the bottom strain gages directly below the composite actuator. The bottom transverse and longitudinal strains measured on the strain gages attached to the bottom of the FRP panel, directly below the composite side actuator were 920 microstrains and 2442 microstrains respectively for the original test specimen and were 1193 microstrains and 1566 microstrains respectively for the repaired test specimen. The strains measured in the bottom transverse rebar located along the test specimen centerline and positioned on the composite side a distance of 152 mm (6 in) away from the edge of the center stem displayed were -1676 microstrains for the original test specimen and 1728 microstrains for the repaired test specimen.

Load versus strain envelope plots, which include both the original and repaired test specimen strain values, are presented for the FRP side strain gages located directly below the actuator. Tabulated values at each load level are also shown for these strain gages. The values for the repaired specimen are reported in the tables both as calculated using the biasing method described in Section 0, which takes into account the residual strains present in the specimen due to the original testing, and as calculated using the start of the repaired specimen testing as the bias value, which does not take into account any previous deformations and thus provides relative strain values. The first method of biasing the repaired specimen strains gives a more accurate picture of the actual strains within the specimen, whereas the second biasing method provides the ability for more direct comparisons between the original and

repaired test specimen of relative changes in strain values over the course of the static loadings.

The load versus strain envelope plot of the bottom longitudinal strain gage located directly below the composite side actuator (CM3L) is shown in Figure 4.19 for the original and repaired test specimen as well as the original specimen at the end of the cyclic loading phase. As observed in Figure 4.19 and Table 4.6, which shows the strain values at each load level, the initial slope of the load versus strain plot for the original test specimen was approximately twice as steep as the slope for the repaired specimen original specimen.

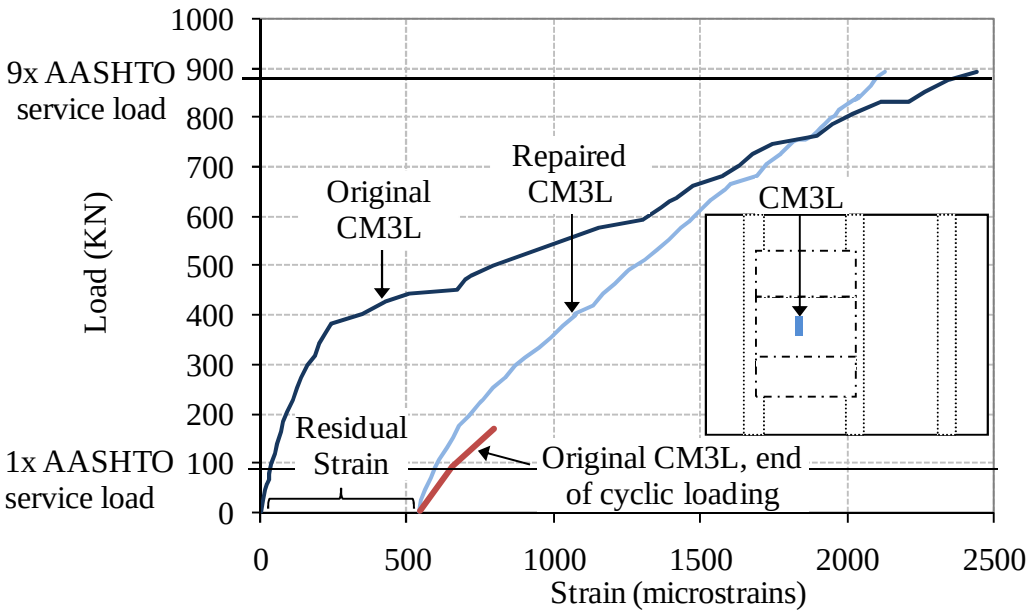

Figure 4.19 Original and repaired test specimen load versus strain plots for the bottom longitudinal FRP side strain gage, CM3L

Table 4.6 Strain values for CM3L at different load levels

Load Level		Original CM3L	Original CM3L, End of Cyclic Loading		Repaired CM3L	
		Strain biased at start of current testing phase	Biased to include residual strain	Strain biased at start of current testing phase	Biased to include residual strain	Strain biased at start of current testing phase
kN	kip	με	με	με	με	με
0	0	0.0	543.5	0.0	543.5	0.0
98	22	37.5	649.2	105.7	611.4	67.9
169	38	90.5	794.2	250.6	749.0	205.4
400	90	240.5			1074.3	530.7
578	130	1149.6			1435.6	892.0
756	170	1743.1			1857.7	1314.1
845	190	2113.7			1991.6	1448.0
890	200	2441.2			2109.3	1565.8

This relationship was maintained up until a load of approximately 400 kN (90 kip), which is over four times the AASHTO service load, after which the original specimen displayed a significantly more relaxed slope. The repaired specimen maintained a nearly linear response for the CM3L gage, especially for loadings beyond the 222 kN (50 kip) load level. While the repaired specimen increased in strain at a significantly slower rate for all loads above 400 kN (90 kip), the repaired specimen maintained higher strain values until a load of 762 kN (171 kip) was reached due to the residual strain of 543 microstrains present within the strain gage from previous testing. The total change in strain values from initial loading to ultimate capacity for the repaired specimen is 36% less than equivalent value for the original specimen at 1565.8 microstrains for the repaired specimen versus 2441.2 microstrains for the original specimen.

The load versus strain envelope plots for the original and repaired specimens' bottom transverse strain gage attached to the center of the FRP panel are shown in Figure 4.20 and tabulated in Table 4.7 which shows the strain values at each load level. The slope of the curves for both tests remain similar up to the 400 kN (90 kip) load level, which is approximately four times AASHTO service load, with less than 6% difference between the strain values for the two tests at this load level. For higher loadings, the original specimen exhibits a more nonlinear response, which is likely related to the onset of the separation between the FRP panels and the concrete that was detected at approximately the 489 kN (110 kip) load level, equivalent to 5.0 times the AASHTO service load. The more linear response observed during the loading of the repaired specimen is an indicator of that the FRP panel repair was successful in improving the structural response of the FRP side deck slab.

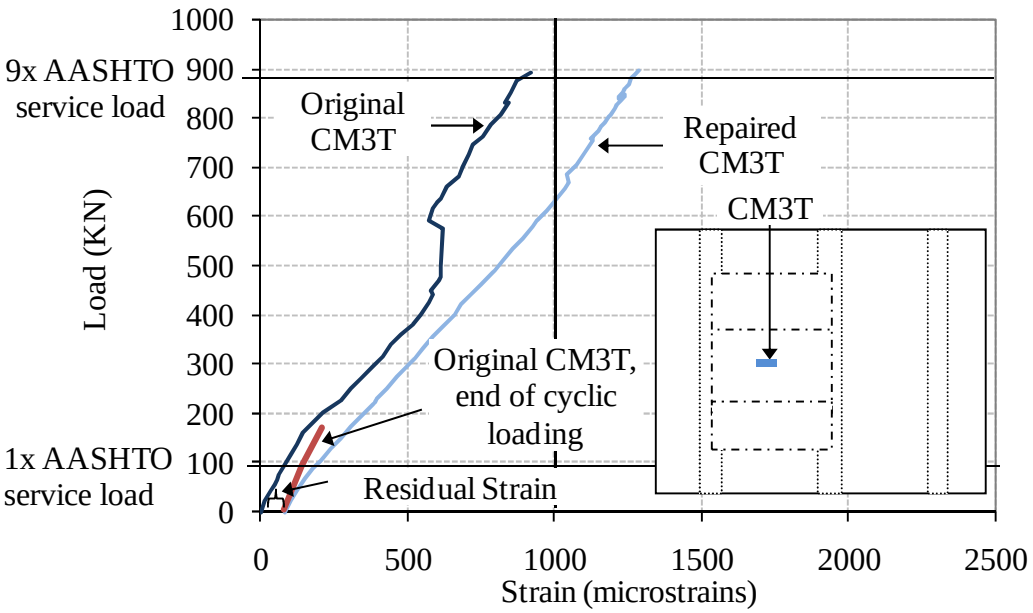

Figure 4.20 Original and repaired test specimen load versus strain plots for the bottom transverse FRP side strain gage, CM3T

Table 4.7 Strain values for CM3T at different load levels

Load Level		Original CM3T	Original CM3T, End of Cyclic Loading		Repaired CM3T	
		Strain biased at start of current testing phase	Biased to include residual strain	Strain biased at start of current testing phase	Biased to include residual strain	Strain biased at start of current testing phase
kN	kip	με	με	με	με	με
0	0	0.0	81.4	0.0	82.0	0.0
98	22	80.3	139.3	57.9	204.5	122.5
169	38	211.8	206.2	124.7	387.5	305.5
400	90	515.9			659.0	577.0
578	130	622.2			929.0	847.0
756	170	719.5			1125.7	1043.7
845	190	848.3			1216.0	1134.0
890	200	920.3			1275.5	1193.4

The loads versus strain envelope plots for the original and repaired test specimens' top longitudinal strain gage are shown in Figure 4.21 and the strain values at each load level are shown in Table 4.8. The positive sign of the data on gage DTL8-3 for both the original and repaired specimen is indicative of more localized deformations in the region directly below the FRP side actuator, where strain gage DTL8-3 is located. A residual strain of 276 microstrains was present on the repaired strain gage due to the previous tests. As stated previously, the more linear response observed during the loading for the repaired specimen as compared to the original specimen is a positive indicator for the performance of the FRP panel repair.

The load versus strain responses for the two tests' top transverse strain gage located directly below the FRP panel side actuator (Figure 4.22) illustrates a significantly different strain response by the DTT10-3 strain gage for the repaired

specimen as compared to the original specimen. While the strain in DTT10-3 for the original specimen increased in compression with increasing load levels and exhibited a discontinuity in strain response at the 845 kN (200 kip) load level, the repaired specimen increases slightly in compression values up to approximately the 222 kN (50 kip) load level, then gains positive, or tensile, strain values for the remainder of the loading. Since the top longitudinal strain gage, DTL8-3, displayed tensile values thereby indicating the presence of localized deformations, it is a reasonable extrapolation that the transverse direction strain response changes due to an increase in the level of localized deformations in the region directly below the actuator.

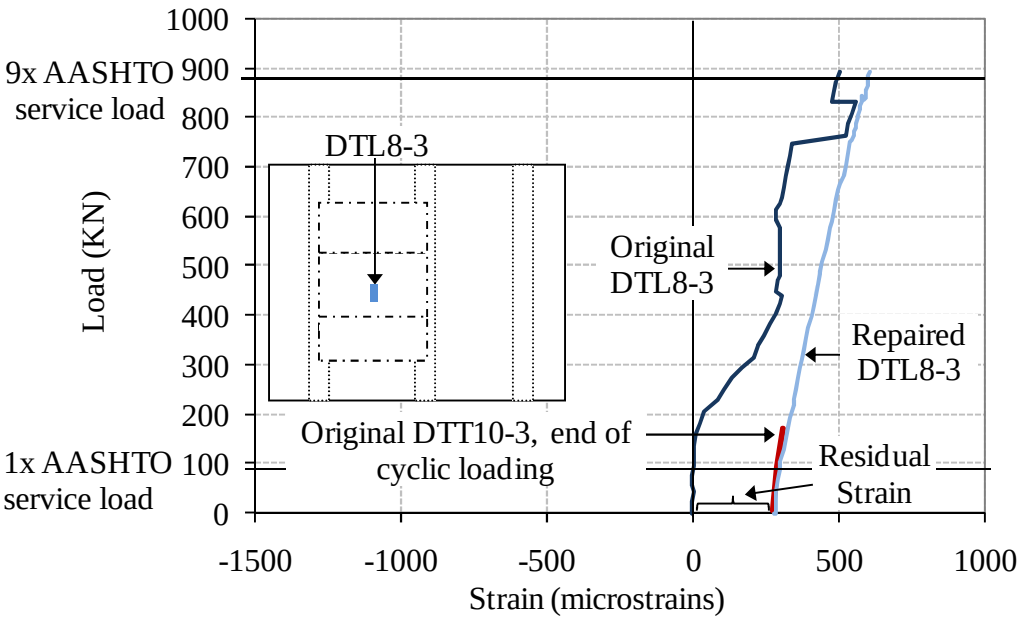

Figure 4.21 Original and repaired test specimen load versus strain plots for the top longitudinal FRP side strain gage, DTL8-3

Table 4.8 Strain values for DTL8-3 at different load levels

Load Level		Original DTL8-3	Original DTL8-3, End of Cyclic Loading		Repaired DTL8-3	
		Strain biased at start of current testing phase	Biased to include residual strain	Strain biased at start of current testing phase	Biased to include residual strain	Strain biased at start of current testing phase
kN	kip	με	με	με	με	με
0	0	0.0	276.3	0.0	276.3	0.0
98	22	3.6	287.2	10.9	299.8	23.5
169	38	39.5	307.9	31.6	342.6	66.4
400	90	265.3			404.8	128.5
578	130	296.9			468.7	192.4
756	170	342.5			546.6	270.3
845	190	561.8			573.7	297.5
890	200	503.5			603.3	327.0

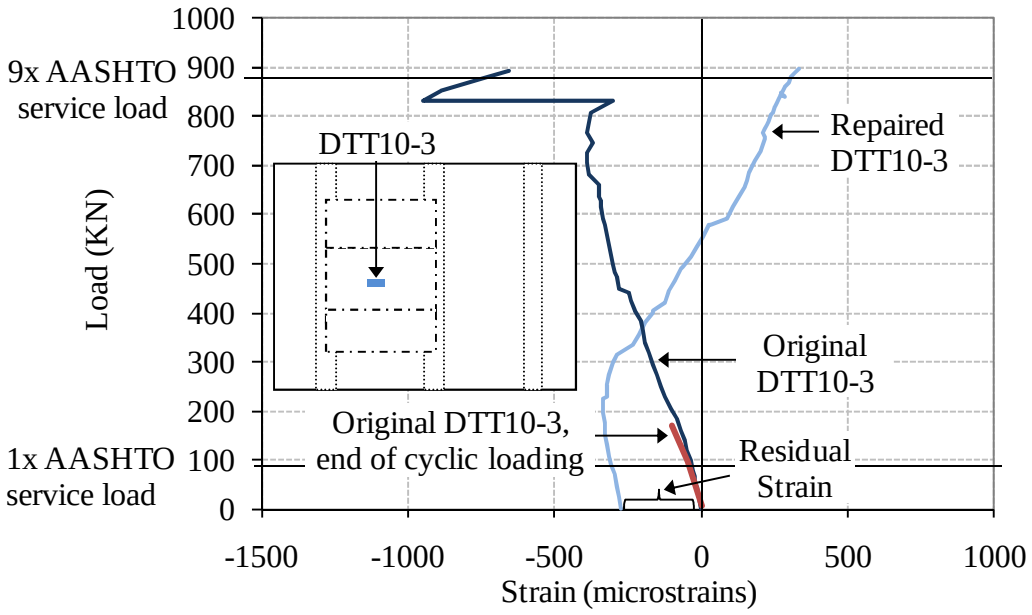

Figure 4.22 Original and repaired test specimen load versus strain plots for the top transverse FRP side strain gage, DTT10-3

Table 4.9 Strain values for DTT10-3 at different load levels

Load Level		Original DTT10-3	Original DTT10-3, End of Cyclic Loading		Repaired DTT10-3	
		Strain biased at start of current testing phase	Biased to include residual strain	Strain biased at start of current testing phase	Biased to include residual strain	Strain biased at start of current testing phase
kN	kip	με	με	με	με	με
0	0	0.0	-277.0	0.0	-274.6	0.0
98	22	-33.7	-323.7	-46.7	-314.5	-39.9
169	38	-99.4	-379.3	-102.3	-335.6	-61.0
400	90	-207.1			-163.1	111.5
578	130	-327.8			30.0	304.6
756	170	-369.2			215.5	490.1
845	190	-302.4			257.2	531.8
890	200	-655.5			321.2	595.8

4.3.5.2 Strain Profiles along the Longitudinal Direction of the Deck

It is important to determine the degree to which the strains due to live loading distribute along the deck in both directions. The strain profiles along the longitudinal directions for the centerlines of the composite side deck slab are shown for the original and repaired tests in Figure 4.23 and Figure 4.24 respectively. Both sides maintained similarly shaped strain profiles with the point of inflection, where the strain values change from tension to compression strains, positioned in approximately the same location. The primary difference between the two tests stems from the degree of spread in the strain values for gage DTL8-3, which is located directly below the FRP side actuator.

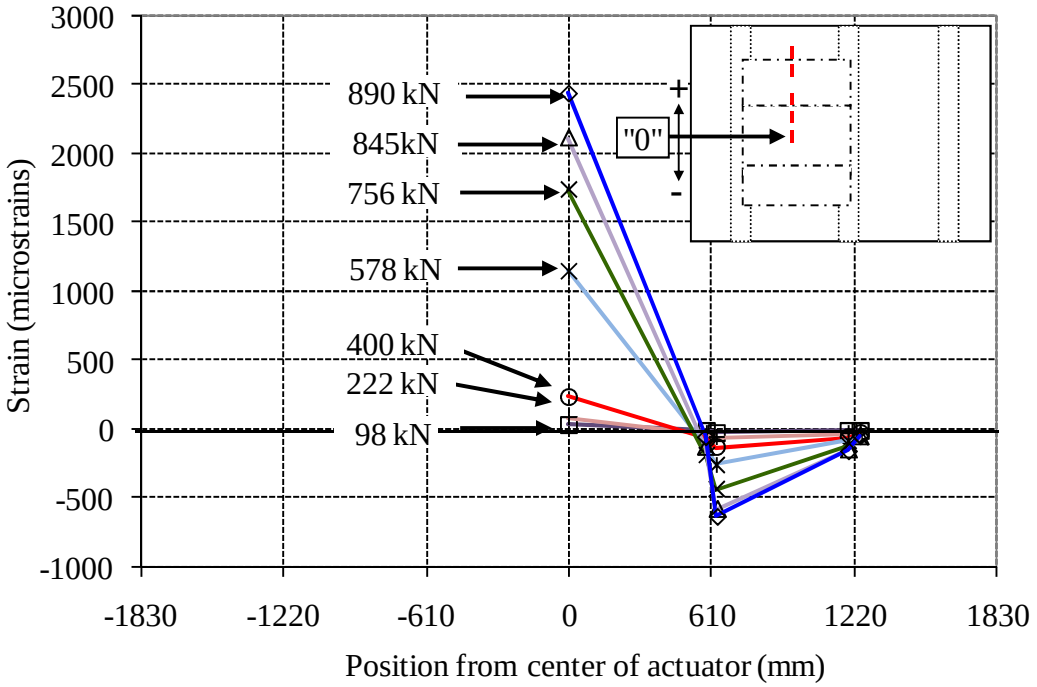

Figure 4.23 Original specimen strain profile for gages attached to bottom of FRP panel along line 3
(Located directly along the FRP side centerline)

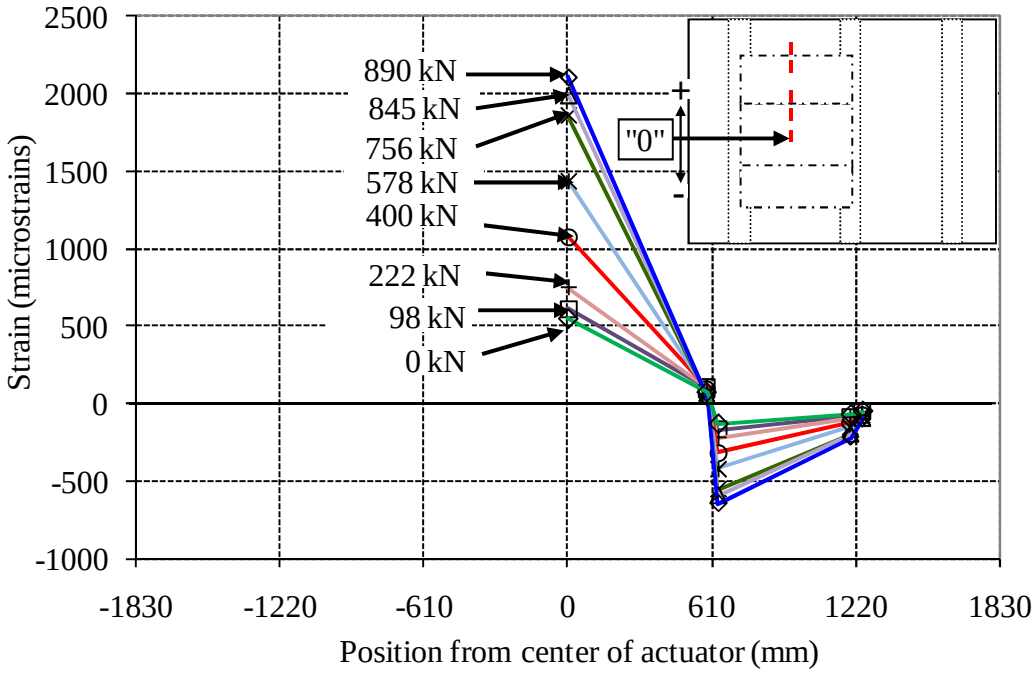

Figure 4.24 Repaired specimen strain profile for gages attached to bottom of FRP panel along line 3
(Located directly along the FRP side centerline)

The repaired specimen started out with approximately 550 με residual strains, however it exhibited an overall change in strain of over 35% less than the original specimen values over the course of the static loading. The progression of these central longitudinal strain gages were discussed in detail in Section 4.3.5.1, which can be referenced for further information.

The strain profiles for gages attached to the top longitudinal steel reinforcement along the centerline of the composite are shown in Figure 4.25 and Figure 4.26. The plot for the original test shows a similar profile shape to the bottom longitudinal profiles for the FRP side deck slab, with tensile strains at the point of load application and a point of inflection at a position prior to the strain gage located 610 mm (2 ft) away from the centerline of the test specimen. The repaired specimen has a modified shape, with the outermost strain gage reading tensile values of approximately 150 to 200 microstrains rather than nearly zero strain values as shown for the original test specimen. This change in profile shape is due the residual strain of 206 microstrains which was present on the strain gage from the start of the repaired specimen testing. Note, however, that the top longitudinal strain profile maintains the same signs as the bottom longitudinal strain profile such that the center strain gage is in tension and the two farther away strain gages are in compression, which is indicative of more localized deformations in the region. This phenomenon will be addressed further in the analysis sections.

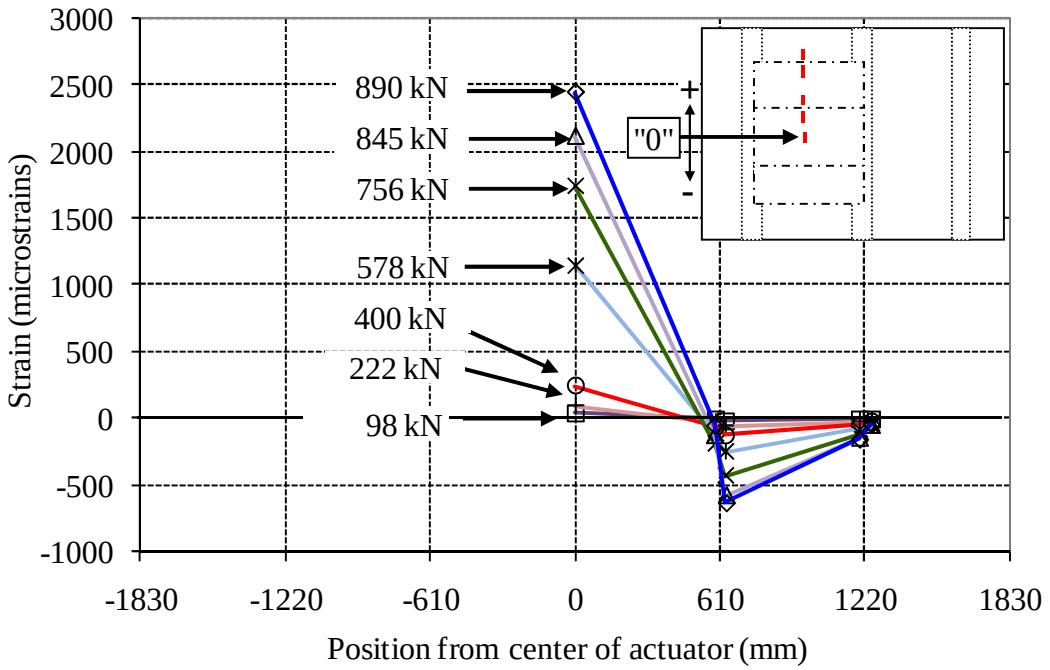

Figure 4.25 Strain profile for original specimen's top longitudinal rebar along line 8 (Rebar is offset from composite side centerline by 140 mm towards center stem)

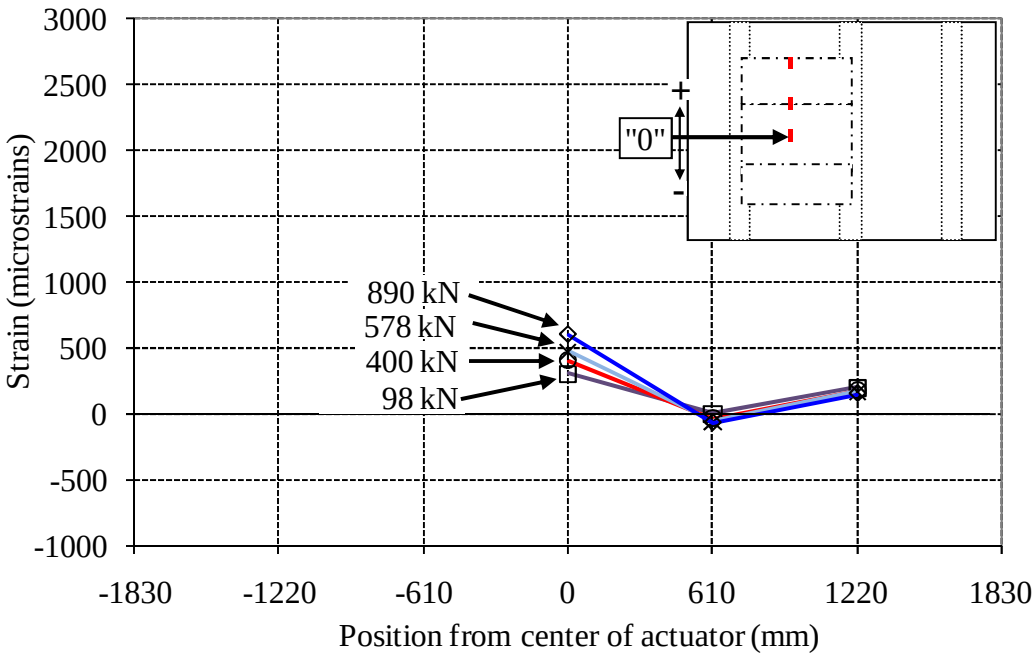

Figure 4.26 Strain profile for repaired specimen's top longitudinal rebar along line 8 (Rebar is offset from composite side centerline by 140 mm towards center stem)

4.3.6 Separation between FRP Panels and Concrete

The occurrence and extent of any separation between the FRP panels and the concrete which was poured on top of the panels was evaluated through the examination deflection data from instrumentation on the FRP side deck slab. Unfortunately, the strain gages necessary for determining the separation between the FRP panel and concrete from strain data were broken during the implementation of the repair and so the discussion of panel separation is limited to deflection information. Differences in deflection values obtained from pairs of linear potentiometers located above and below the FRP panel side deck slab, were used to obtain information regarding the level of separation, if any that had occurred. A differential between the top and bottom pot readings indicated that the concrete and composite were no longer acting in unison and were now deflecting independent of each other.

The load versus deflection envelope plots of the top and bottom pair of linear potentiometers located along the transverse centerline of the test specimen on either side of the actuator on the FRP panel deck are shown in Figure 4.27 and Figure 4.28. Based on the observed fluctuations in measured deflections for top and bottom linear potentiometer pairs on the reinforced concrete side deck during the testing of the original specimen, a tolerance level of 0.16 mm (0.006 in) was established as the threshold value for determining that a difference between the top and bottom deflections was significant.

For the pair of linear potentiometers located near the outer stem shown in Figure 4.27, a difference of 0.17 mm (0.007 in) between upper and lower deflection values was observed at a load of 835 kN (188 kip), which is approximately 8.5 times

the AASHTO service load. At the 890 kN (200 kip) load level, which was the ultimate capacity of the original test specimen, the difference between the linear potentiometers shown in Figure 4.27 increased to 0.22 mm (0.009 in) and at 980 kN (220 kip), the maximum capacity of the actuators, the difference increased to 0.42 mm (0.017 in). This separation was significantly less than the corresponding values measured during the original test, which had a separation at ultimate capacity of 1.09 mm (0.043 in). In addition, the first detectable separation was recorded for the original test at a load of 673 kN (151 kip), which was 162 kN (36 kip) lower than the corresponding load for the repaired specimen.

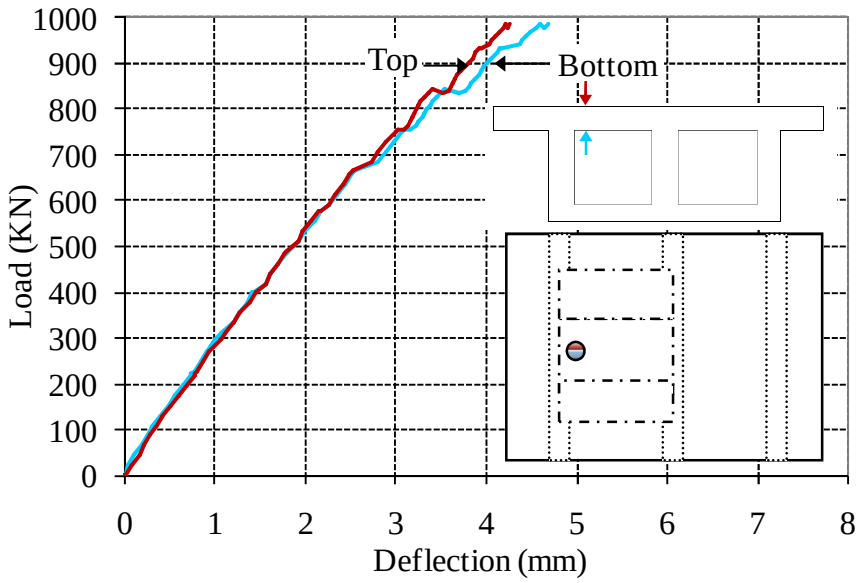

Figure 4.27 Load versus deflection plots for linear potentiometers on top and bottom of repaired FRP side deck
(Located along test specimen centerline and 610 mm away from the composite side centerline, 178 mm from the inner edge of the outer stem)

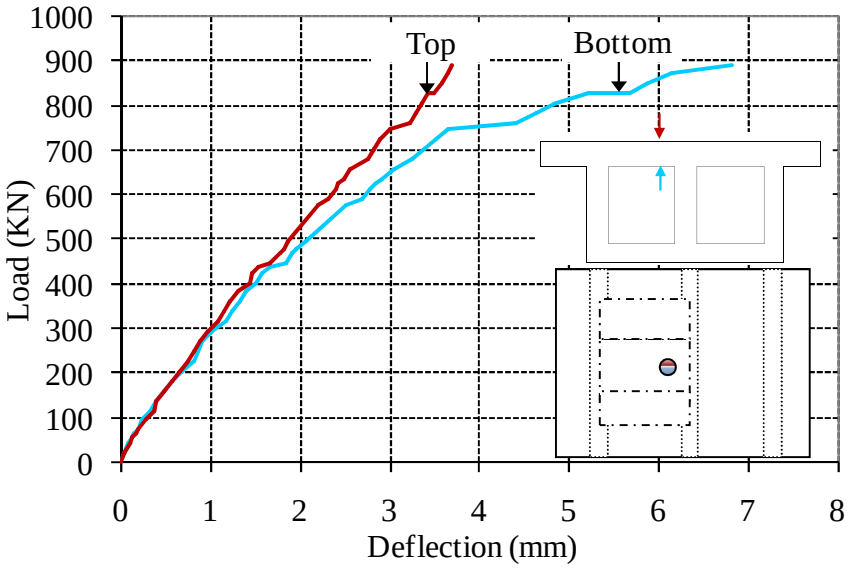

Figure 4.28 Load versus deflection plots for linear potentiometers on top and bottom of repaired FRP side deck
(Located along test specimen centerline and 610 mm away from the composite side centerline, 152 mm from the FRP side edge of the center stem)

The upper and lower deflection values for the pair of linear potentiometers located near the center stem shown in Figure 4.28 were separated by 0.17 mm (0.007 in) at a load of 356 kN (80 kip), which is equivalent to 3.6 times the AASHTO service load. The difference between the upper and lower linear potentiometers for the repaired FRP test increased to 1.13 mm (0.044 in) at 890 kN (200 kip) and 1.47 mm (0.058 in) at the ultimate capacity of the actuators. For the original test specimen, the corresponding upper and lower linear potentiometers were separated by 0.17 mm (0.007 in) at a load of 489 kN (109 kip) and the difference increased to 3.12 mm (0.123 in) at ultimate capacity. While the onset of detectable separation for the repaired specimen occurred at a load which was 133 kN (30 kip) lower than that for the original specimen, the separation for the repaired specimen remained over 2.75

times smaller than for the original specimen. This indicates that the epoxy repair was effective at reinstating the bond between the FRP panels and the adjacent concrete and perhaps creates a better bond that under original conditions. This also indicates that surface treatment during original construction to create a better bond between the concrete and the FRP panels may be desirable.

4.4 RESULTS FOR CYCLIC LOADING OF THE REPAIRED SPECIMEN

4.4.1 Loading Protocol

The cyclic testing of the repaired specimen consisted of 500 cycles at 168 kN (37.8 kip), which is equivalent to 2x the AASHTO service load of 73 kN (16.4 kip) with the additional 15% fatigue with an additional AASHTO defined 15% dynamic allowance for the fatigue limit state [91]. After the cyclic loading was completed, the specimen was loaded with a single cycle static loading to 978 kN (220 kips) in order to compare system structural response from before and after the cyclic loading.

Table 4.10 Cyclic loading protocol for repaired specimen

PHASE AND CORRESPONDING LOADING LEVEL PER ACTUATOR	LOAD LEVEL		NUMBER OF CYCLES
	kN	kip	
Phase I: cyclic at 2P	168	37.8	500
Phase II: static up to 978 kN	978	220	1
Cumulative number of cycles:			501
Note: P = 1.15 x AASHTO service load Where AASHTO service load is 73 kN (16.4 kip)			

The current cyclic loading protocol was different from the cyclic loading of the original test specimen, which consisted of 1,000 cycles at 1x AASHTO service load followed by 1,000 cycles at 2x AASHTO service load. The cyclic loading of the original specimen at 1x service load caused no noticeable change in structural response to the system and over 80% of the changes in stiffness for the FRP panel side deck occurred in the first 500 cycles of the 2x service load phase. Therefore, it is reasonable to directly compare the FRP panel side deck performance during the 2x AASHTO service cyclic loading from the repaired specimen with the first 500 cycles of the 2x AASHTO service loading of the original test specimen.

In order to determine the overall response of the structure, the data from the cyclic testing was biased using the original bias scan from the start of static testing of the repaired specimen, enabling the cumulative deflections throughout the loading of the repaired test specimen to be established. Therefore, a comparison of stiffness values would be more accurate than a comparison of the absolute magnitude of deflection values.

4.4.2 Changes in Center Deflections during Cyclic Loading

The effective stiffness ratios for the original FRP panel side deck during the first half of cyclic phase II and the repaired FRP panel side deck during the cyclic loading were calculated using the adaptive secant stiffness method described on page 87 in Section 3.8.3 and are shown in Table 3.21 and Table 3.22 respectively. Since the load acting on the system remains constant throughout the cyclic phase, any change in the stiffness ratio is attributed to a change in deflections. The progression of

the effective stiffness ratios for both sides over the course of 500 cycles of 2x AASHTO service load is shown in Figure 3.79.

The effective stiffness ratios for the original FRP panel side, shown in Table 3.21, dropped by 12% during the first 250 cycles and displayed a total decrease in effective stiffness of 14% during the first 500 cycles of cyclic phase II for the original test specimen. Conversely, the cyclic phase for the repaired specimen had no measurable impact on the specimen, which maintained its full effective stiffness throughout the loading, with less than 2% variation throughout the loading phase.

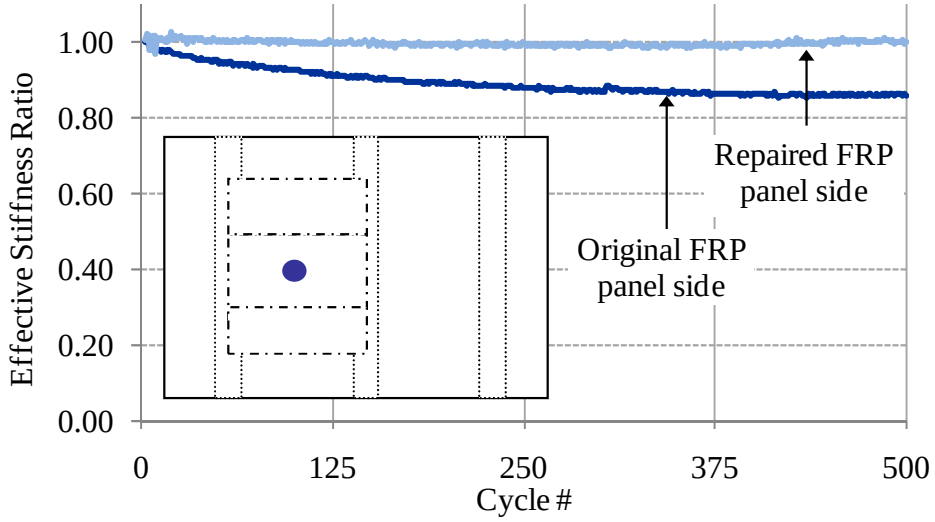

Figure 4.29 Effective stiffness versus cycle # for original and repaired FRP side deck

Table 4.11 Effective stiffness ratios for FRP panel side of original test specimen during the 1st 500 cycles of cyclic loading phase II (2x AASHTO service load)

Cycle #	Actual target actuator load, P_f		Actual min. threshold actuator load, P_i		Deflection at target load, δ_f		Deflection at min threshold load, δ_i		Effective stiffness ratio
---	kN	kip	kN	kip	mm	in	mm	in	---
1	169.9	38.2	5.2	1.2	5.35	0.211	4.26	0.168	1.00
125	170.2	38.3	5.1	1.1	5.38	0.212	4.18	0.165	0.91
250	170.1	38.2	5.3	1.2	5.36	0.211	4.11	0.162	0.88
375	169.9	38.2	5.1	1.2	5.39	0.212	4.13	0.163	0.86
500	170.1	38.2	5.3	1.2	5.43	0.214	4.16	0.164	0.86

Table 4.12 Effective stiffness ratios for FRP panel side of repaired test specimen during cyclic loading (2x AASHTO service load)

Cycle #	Actual target actuator load, P_f		Actual min. threshold actuator load, P_i		Deflection at target load, δ_f		Deflection at min threshold load, δ_i		Effective stiffness ratio
---	kN	kip	kN	kip	mm	in	mm	in	---
1	165.8	37.3	3.8	0.9	1.24	0.049	0.52	0.020	1.00
125	169.9	38.2	3.5	0.8	1.23	0.049	0.49	0.019	1.00
250	169.7	38.2	3.5	0.8	1.24	0.049	0.49	0.019	0.99
375	169.2	38.0	3.5	0.8	1.24	0.049	0.49	0.019	0.98
500	169.6	38.1	3.4	0.8	1.26	0.050	0.52	0.020	1.00

4.4.3 Changes in Strains during Cyclic Loading

The progression of strains during the cyclic loading phases for important strain gages in the deck slab is presented in Table 3.23. Note that all gages were biased using the original strain gage values from the start of the static testing in order to record the complete history of the strain imposed on each gage due to all previous loading. Also, all data shown in the tables below were taken with the specimen at the full target load for a given cyclic phase.

Throughout the cyclic loading of the repaired specimen, only minor progressions in strain values were observed for the FRP side deck strain gages. For the strain gages located directly below the FRP side actuator which are shown in Table 3.23, the strain values for the repaired specimen changed by less than 15 microstrains or 4% over the course of the cyclic phase and changed by less than 20 microstrains or 5% for the original specimen over the course of the first 500 cycles of cyclic phase II. The consistent strain values observed for the FRP panel side during the cyclic loading phases, both for the original specimen and for the repaired specimen, are an indication that the FRP panel system exhibits a very stable response under cyclic loading.

Table 4.13 Strain progresssion for composite side gages under target loads- located directly below the composite side actuator (See Section 5.2.2 for detailed information on precise location of each strain gage)

Position designations	Strain gage name	CM3T	CM3L	DTT10-3	DTL8-3
	Location (All on FRP panel side)	Below actuator	Below actuator	Below actuator	Below actuator
	Attached to rebar or FRP	FRP	FRP	Rebar	Rebar
	Near top or bottom of deck	Bottom	Bottom	Top	Top
	Oriented longitudinal or transverse	Transverse	Longitudinal	Transverse	Longitudinal
Original FRP panel side cyclic loading phase II	Strain at Cycle # 1 (με)	207.85	823.64	-354.46	336.40
	Strain at Cycle # 125 (με)	202.80	832.30	-353.87	337.01
	Strain at Cycle # 250 (με)	205.04	828.84	-354.46	337.62
	Strain at Cycle # 375 (με)	204.48	832.30	-367.47	316.96
	Strain at Cycle # 500 (με)	217.40	831.15	-350.32	351.59
	Change in strains (με)	**9.6**	**7.5**	**4.1**	**15.2**
	Change in strains (%)	**4.6%**	**0.9%**	**-1.2%**	**4.5%**
Repaired FRP panel side cyclic loading phase I	Strain at Cycle # 1 (με)	339.35	533.77	-225.32	326.94
	Strain at Cycle # 125 (με)	336.56	539.52	-241.16	335.38
	Strain at Cycle # 250 (με)	336.00	541.25	-235.88	335.99
	Strain at Cycle # 375 (με)	334.32	542.97	-230.60	338.40
	Strain at Cycle # 500 (με)	333.20	542.97	-217.69	339.00
	Change in strains (με)	**-6.2**	**9.2**	**7.6**	**12.1**
	Change in strains (%)	**-1.8%**	**1.7%**	**-3.4%**	**3.7%**

4.4.4 Changes in Separation between the FRP Panel and the Concrete

The progression of the separation between the concrete and the composite at the same locations examined in Section 4.3.6 is summarized in Table 3.26. During the first 500 cycles of cyclic phase II for the original specimen, the pair of linear potentiometers located near the central stem continued to display very similar separation values whereas the linear potentiometer pair near the outer stem exhibited a minor change of 0.19 mm (0.008 in) in the overall separation distance between the concrete and the FRP panel. Both pairs of linear potentiometers for the repaired specimen show no change in separation values over the course of the cyclic loading phase.

Table 4.14 Separation progression for linear potentiometers located along the test speciment centerline, near the stems (See Section 5.2.2 for detailed information on precise location of each linear potentiometer)

	Location of linear potentiometers	Along centerline, near outer stem (Linear potentiometers M2T and M2B)				Along centerline, near center stem (Linear potentiometers M4T and M4B)			
	Calculated quantity	Separation		Overall change in separation		Separation		Overall change in separation	
	Units	mm	in	mm	in	mm	in	mm	in
Original FRP panel cyclic loading phase II	Cycle # 1	3.47	0.137	---	---	4.66	0.183	---	---
	Cycle # 125	3.42	0.135	-0.06	-0.002	4.67	0.184	0.01	0.000
	Cycle # 250	3.39	0.134	-0.08	-0.003	4.67	0.184	0.01	0.000
	Cycle # 375	3.31	0.130	-0.16	-0.006	4.60	0.181	-0.06	-0.002
	Cycle # 500	3.35	0.132	-0.12	-0.005	4.69	0.185	0.04	0.001
Repaired FRP panel cyclic loading phase II	Cycle # 1	0.03	0.001	---	---	0.28	0.011	---	---
	Cycle # 125	0.06	0.002	0.02	0.001	0.28	0.011	0.00	0.000
	Cycle # 250	0.02	0.001	-0.01	0.000	0.27	0.010	-0.01	-0.001
	Cycle # 375	0.06	0.002	0.02	0.001	0.28	0.011	0.00	0.000
	Cycle # 500	0.02	0.001	-0.01	-0.001	0.27	0.010	-0.01	-0.001

4.4.5 Static Loading Following the Repaired Specimen Cyclic Phase

Apart from a minor increase in residual deflection, the structural response of the repaired FRP panel side deck was equivalent before and after the cyclic loading phase, as shown in Figure 4.30. This indicates that minimal damage was accrued due to the cyclic loading phase of the repaired FRP side deck.

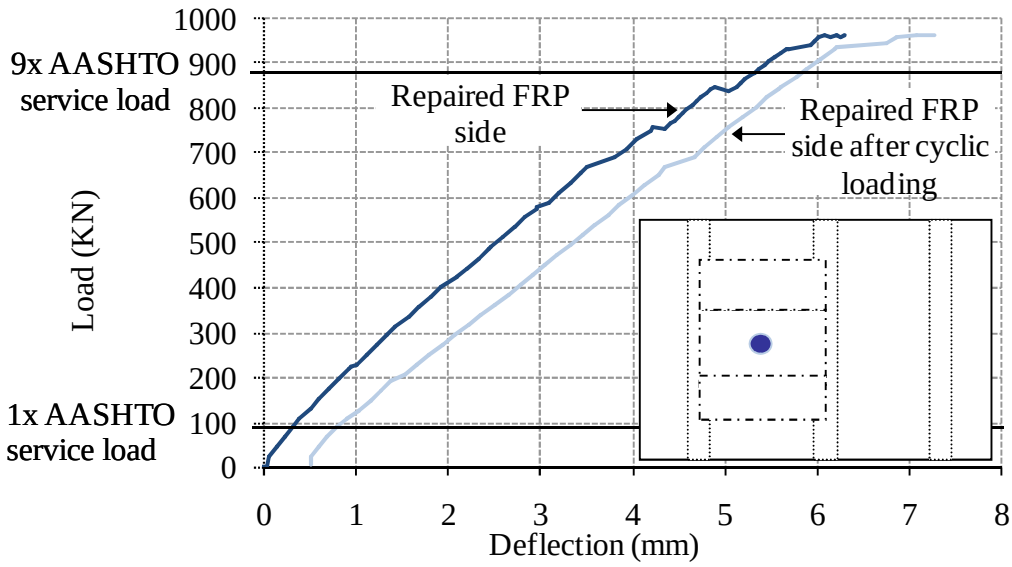

Figure 4.30 Envelope plot of load versus deflections of repaired FRP side before and after cyclic loading phase

4.5 SUMMARY

After the deck was loaded to ultimate capacity, a field applicable epoxy injection repair technique was implemented to reinstate load transfer between the FRP panels and the concrete, which had displayed initial signs of separation during the quasi static loading of the test specimen at a load of approximately five times the

AASHTO service. The repaired specimen was retested both statically and cyclically and its structural response was shown to be very comparable to the structural response of the original test specimen. Since only the FRP panel side was repaired, performance comparisons between the original testing of the FRP structural formwork system and the repaired FRP structural formwork system were addressed. Aspects of the response of the FRP panel reinforced system including the overall response, the response between the panels, changes in stiffness, and the progression of damage within the system were evaluated and discussed.

The repaired specimen displayed slightly larger center deflection values at lower load levels, however exhibited less change in its effective stiffness as compared to the original test specimen. The overall load carrying capacity of the specimen was increased beyond the original specimen's 890 kN (200 kip) ultimate capacity and the system still had reserve strength at the maximum applied load of 978 kN (220 kip). Initial signs of separation between the concrete and the FRP panels were observed at load levels similar to the original test specimen, however significantly smaller separation values were recorded for the repaired specimen and no deterioration of performance was observed due to the onset of initial separation. The repaired specimen showed no change in performance during or after the application of cyclic loading. The very linear response of the repaired specimen throughout the loading levels and the stable response during the cyclic phase indicated that the implemented repair was performed as desired.

Since the composite panel was not damaged during loading, an efficient repair system could be utilized. The efficacy of the system is that that the composite fails at

a much higher load than the damage of the concrete, thereby allowing for a relatively inexpensive repair of the concrete to take place rather than requiring a more costly replacement of damaged reinforcement. The overdesign of FRP panel system allows for robust design that exhibits a stable even after ultimate capacity is reached and displays a readily observable failure mode.

5 CYCLIC RESPONSE OF THE FRP PANEL STAY-IN-PLACE STRUCTURAL FORMWORK SYSTEM

5.1 INTRODUCTION

This chapter discusses the testing of a second box girder bridge specimen with the hybrid fiber reinforced polymer (FRP)-concrete bridge deck system. The testing of this test specimen focuses on the behavior of the system under repeated cyclic loading. A test specimen with the same external geometry and setup of prefabricated composite panels that act as both the formwork and the lower level of reinforcement for the bridge deck as the two cell box girder specimen described in Chapters 3 and 4 is utilized. In the same manner as the first test specimen, a direct performance comparison is drawn between the FRP panel strengthened concrete system and a traditional steel reinforced concrete system.

5.2 OVERALL GEOMETRY AND CONSTRUCTION DETAILS

The overall geometry of the second specimen was the same as the first test specimen, which consisted of a two-cell box girder bridge segment with a center-to-center distance of 1830 mm (6 ft) between each of the stems and a longitudinal length of 3660 mm (12 ft) as shown in Figure 3.2. For further details on overall specimen design and construction, refer to pages 43-52 in Section 3.2. The differences between the first and second test specimens, as summarized in Table 5.1, relate to the detailing used to connect the FRP panels to the surrounding bridge system and the manner in

which the specimen is tested. The loading protocols for the static and cyclic phases are discussed in Sections 5.6.1 and 5.7.1 respectively.

The bottom slab and lower portion of the stems for the first and second test specimens were poured at the same time, therefore the properties for the steel reinforcement and 1st concrete pour can be found in Table 3.1 and Table 3.2 respectively. The concrete for the deck slab and upper portion of the stems had a 28-day compressive strength of 33.5 MPa (4.86 ksi) and a compressive strength on the day of test of 33.9MPa (4.92 ksi). The strength development of the deck concrete is shown in Figure 5.1 below.

Table 5.1 Comparison of 1st and 2nd test specimens

	SPECIMEN #1	SPECIMEN #2
OVERALL GEOMETRY	Same for both specimens	
STEEL REINFORCEMENT	Same for both specimens	
LOCATION OF FRP PANELS	Same for both specimens	
CONNECTION DETAILING BETWEEN FRP PANELS AND STEMS	Representative of new deck construction	Representative of rehabilitated deck construction
STATIC LOADING PROTOCOL	Single cycles to ultimate capacity	Single cycles to 70% of punching shear load
CYCLIC LOADING PROTOCOL	2,000 total cycles, split equally between 1x and 2x AASHTO service load	32,000 total cycles at various loads up to 5x AASHTO service load

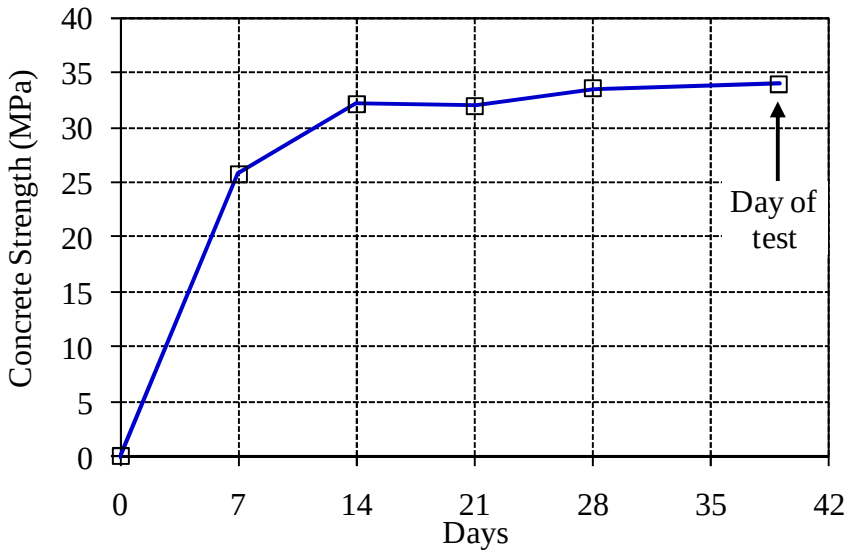

Figure 5.1 Strength development for deck slab concrete in test specimen #2

Figure 5.2 Construction of test specimen formwork for 2nd pour

5.3 PANEL PLACEMENT AND CONNECTION DETAILING

Using the same configuration as Test Specimen #1, three FRP panels were used side by side in the composite side deck of Test Specimen #2 to check the effectiveness of load transfer between the panels. The central FRP panel with dimensions of 1220 mm (4 ft) wide, 1830 mm (6 ft) long, and 6.3 mm (0.25 in) thick was positioned in the middle of the FRP strengthened side of the specimen and was bordered on both sides by narrower panels, each 610 mm (2 ft) wide as shown in Figure 5.3.

The connection detailing used in this second test more closely modeled field repair construction methods and aimed to better accommodate protruding stem rebar. The presence of bent stem rebar is encountered in repair of preexisting bridges where only the deck surface is replaced and existing stem rebar must be integrated into the new deck to enable proper load transfer. The location of the protruding stem rebar was measured and grooves with dimensions 139.7 mm (5.5 in) long by 25.4 mm (1 in) wide were cut into the panel to accommodate the stem rebar. These grooves were located at an average spacing of 305 mm (12 in) on center, which corresponds to the spacing of the vertical stem rebar. The ends of each groove were rounded by terminating each groove cut with a drilled hole in order to reduce stress concentrations in the FRP panel. End connection details for the first and second test specimen are shown in Figure 5.4, parts a) and b) respectively.

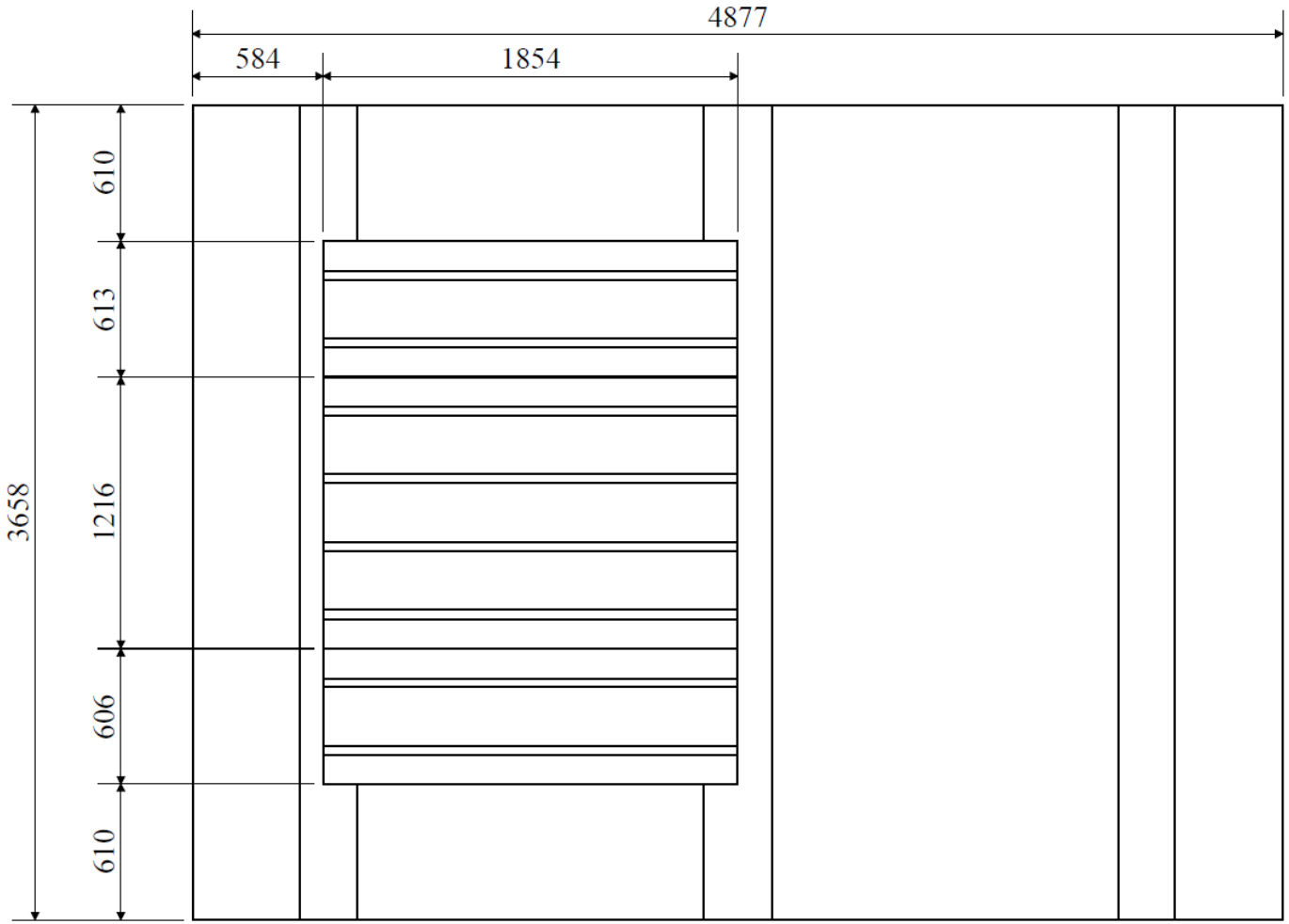

Figure 5.3 Schematic of FRP panel locations (same overall locations for both 1st and 2nd test specimens)

(a) End condition detail from Test Specimen #1.

(b) End condition detail from Test Specimen #2

Figure 5.4 End connection detailing of FRP panels

Additional holes were drilled in the end regions of the panels so that 12.7 mm (0.5 in) diameter threaded rods could be used to secure the panels to the girders prior to the pouring of the deck concrete. The holes in the FRP panels were used as templates for ensuring proper alignment of the corresponding holes drilled into the stem concrete as shown in Figure 5.5. After all holes were drilled into the concrete, any loose concrete pieces were vacuumed up and each threaded rod was attached to the stem concrete using a two–component 1:1 ratio epoxy-based adhesive called Simpson Epoxy-Tie Set 22. This adhesive system is designed for use as a high strength, non-shrink anchor grouting material and its properties are summarized in Table 5.2 [157]. The threaded rods were held to the panels by wrench tightened nuts and washers installed on both sides of the panels as shown in part (b) of Figure 5.4.

Figure 5.5 Drilling of stem concrete using FRP panels for alignment of holes

Table 5.2 Properties of Simpson Epoxy-Tie adhesive system [157]

PROPERTY	TEST METHOD	RESULTS
CONSISTENCY	ASTM C 881	Non-Sag/Thixotropic Paste
HEAT DEFLECTION	ASTM D 648	136° F (58° C)
BOND STRENGTH (MOIST CURE)	ASTM C 882	3,218 psi (2 days) 3,366 psi (14 days)
WATER ABSORPTION	ASTM D 570	0.110% (24 hrs)
COMPRESSIVE YIELD STRENGTH	ASTM D 695	5,065 psi (24 hours) 12,650 psi (7 days)
COMPRESSIVE MODULUS	ASTM D 695	695 439,000 psi (7 days)
GEL TIME (75° F)	ASTM C 881	30 min - 60 gram mass 60 min - thin film

Placement of the threaded rod anchors in relation to the stem concrete was determined by maximizing the load capacity of the anchors with respect to the breakout strength of the concrete in shear, the shear pullout strength of the FRP panel and the tensile pullout of the threaded rod from the stem concrete.

The necessary embedment depth to ensure that the threaded rods would yield prior to a tensile pullout from the stem concrete due to failure of the epoxy was calculated as:

$$L_{embed} = \frac{F}{(\pi \cdot d) \cdot \sigma_{adhesive}} \qquad 5.1$$

where

L_{embed} = Minimum embedment depth required to yield rod prior to epoxy failure

F = Force required to yield rod = $\sigma_y \cdot \pi \cdot \left(\frac{d}{2}\right)^2$

σ_y = Yield strength of rod

d = Diameter of rod

$\sigma_{adhesive}$ = Bond strength of adhesive

The value for the minimum required embedment length calculated from Equation 5.1 was 57 mm (2.23 in), which was smaller than the manufacturer recommended value of 108 mm (4.25 in) [157], therefore the manufacturer recommended embedment depth was used. The position of the threaded rod anchor in relation to the FRP panel and the concrete stem is illustrated in Figure 5.6 below.

As shown in Figure 5.6, the threaded rods were placed such that a clear distance of 60 mm (2.38 in) from the edge of the FRP panel, labeled as distance "L", and a clear distance of 76 mm (3 in) between the threaded rod and the edge of the stem concrete, labeled as distance "c_{a1}", was achieved. The distances L and c_{a1} were determined by calculating the optimal distance for the anchor to be placed away from the edge of the FRP panel in order to maximize the concrete breakout strength in shear for a single anchor in cracked concrete and the maximum shear force that can be applied to the FRP panel prior to inducing a pullout failure in the FRP.

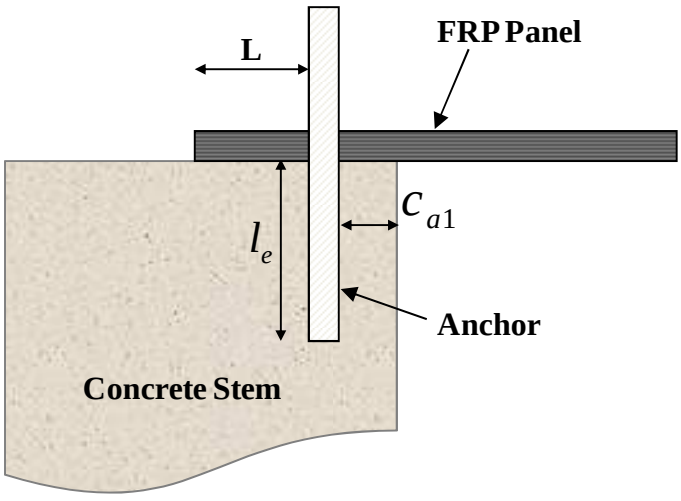

Figure 5.6 Detail of anchor position with respect to concrete stem and FRP panel

The concrete breakout strength in shear of a single anchor in cracked concrete was calculated using Equation D-24 from the ACI SCM-31 [158]:

$$V_b = 7\left(\frac{l_e}{d_o}\right)^{0.2}\sqrt{d_o}\sqrt{f_c'}(c_{a1})^{1.5} \qquad 5.2$$

where
V_b = Concrete breakout strength (psi)
l_e = Load bearing length of anchor in shear (in)
d_o = Diameter of anchor (in)
f_c' = Concrete strength (psi)
c_{a1} = Distance to edge of concrete (in)

The maximum shear force that can be applied prior to pullout failure in the FRP panel was calculated as:

$$V = A\tau_{12} \qquad 5.3$$

where
V = Concrete breakout strength
A = Area in shear, $A = 2tL$
t = Thickness of composite
L = Distance from hole to edge of the FRP panel
τ_{12} = Shear strength of composite

After the FRP panels were lowered into place, as shown in Figure 5.7, the steel reinforcement in the deck was positioned and tied. Figure 5.8 shows the as built deck just prior to the concrete pour. Note that wooden shored formwork was installed for the entire deck except for the region in which the FRP panels are placed.

Figure 5.7 Composite side deck after FRP panel installation

Figure 5.8 Reinforcement system in deck, as built

5.4 SPECIMEN SETUP AND INSTRUMENTATION

The current test specimen setup was the same as the test setup for the first test specimen, with the specimen supported on six load cells and tested using two actuators spaced 1830 mm (6ft) apart from each other and in the center of the two deck slabs. Figure 5.9 shows the as-built test specimen with instrumentation, prior to the installation of the actuators. Information regarding the specimen setup can be found in Section 3.5.

Figure 5.9 Test specimen with instrumentation, prior to installation of actuators

The instrumentation used on this test specimen is similar to what was used on the first specimen. The position of some strain gages and linear potentiometers were moved in order to better characterize the structural response of the system. Table 3.6 summarizes the total quantity of instrumentation used for this test specimen and the approximate locations in which each instrumentation type was used.

Table 5.3 Summary of instrumentation used for test specimen #1

INSTRUMENTATION TYPE	QUANTITY USED	APPROXIMATE LOCATIONS
Load cells	6	Supporting the test specimen, in line with stems and near both ends of the specimen
Linear potentiometers	37	35 vertically mounted above and below the deck slab 2 mounted horizontally to the outer two stems
Inclinometers	3	On one end of specimen, at the intersection between the mid-plane of deck and the centerlines of the three stems
Strain gages	115	Throughout deck and stems- attached to steel reinforcement and attached to either the top or the bottom of the FRP panels

5.4.1 Linear Potentiometers and Inclinometers

Linear potentiometers were used to measure the deflections of the test specimen and determine the shape of the structure under the applied load. The locations of the linear potentiometers placed on the underside and top side of the deck are shown in Figure 5.10 and Figure 5.11 respectively. Selected pairs of linear potentiometers were placed in pairs with one linear potentiometer on the top side of the deck and the other located on the underside of the deck in order to evaluate any separation between the concrete and the FRP panels that may occur during loading.

Horizontal linear potentiometers and the inclinometers were used to measure changes in slope within the deck and determine more information regarding the end conditions of the deck slab. The layout of the horizontal linear potentiometers and the inclinometers, which was the same as for test specimen #1, is shown in Figure 3.22.

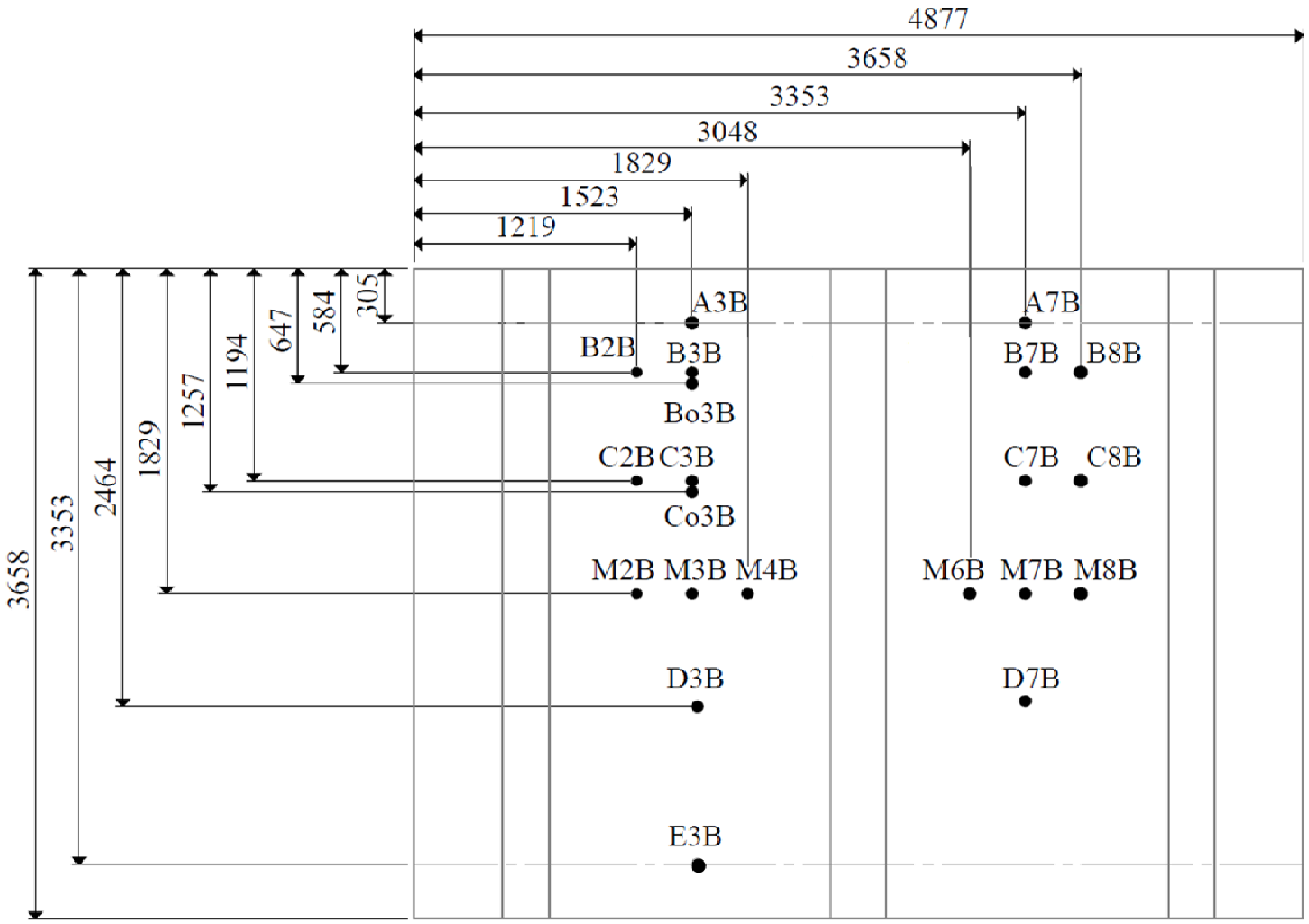

Figure 5.10 Layout of linear potentiometers located on the underside of the composite deck

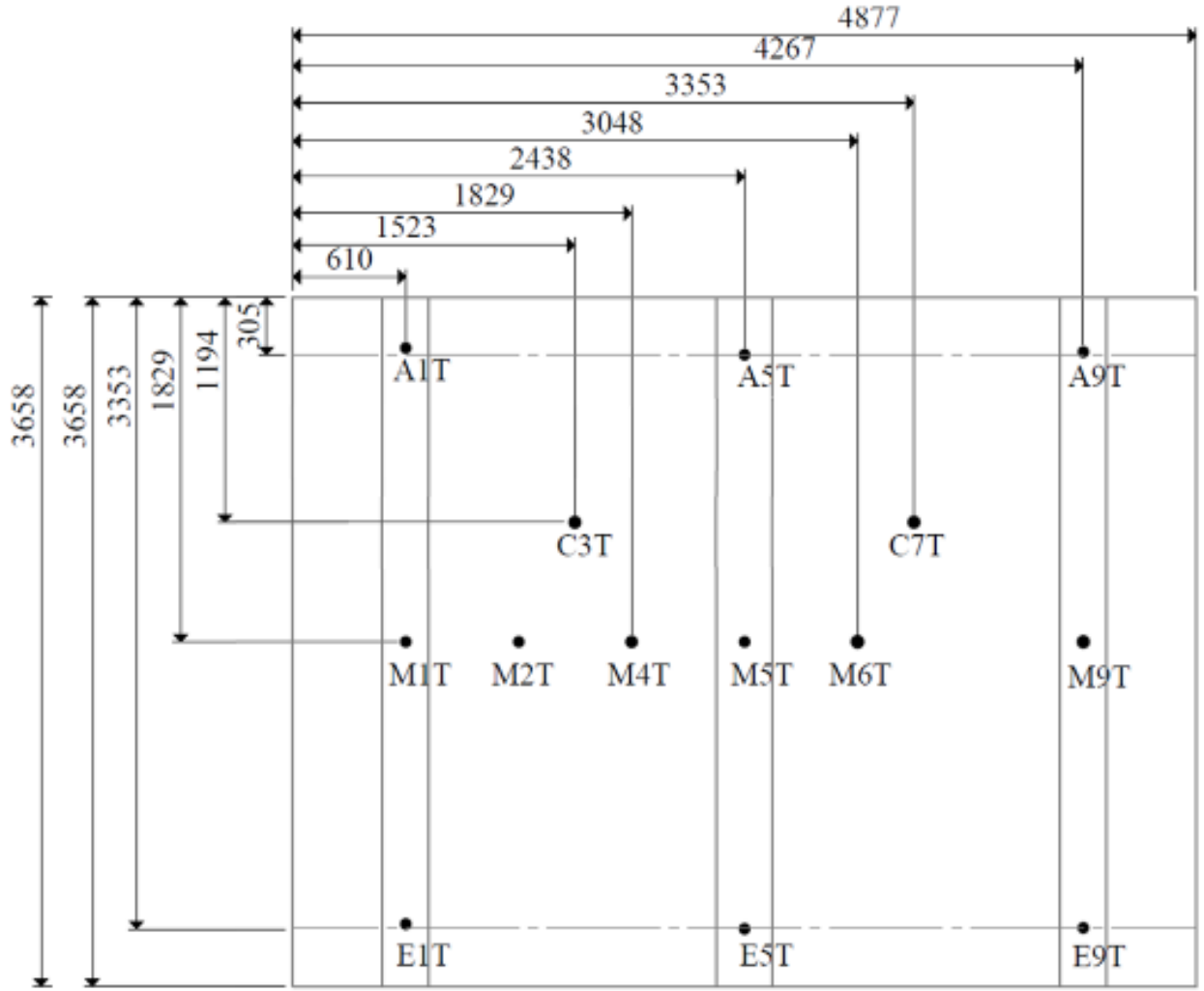

Figure 5.11 Layout of linear potentiometers located on the top of the composite deck

5.4.2 Strain Gages

A total of 121 strain gages were attached to the steel reinforcement throughout the test specimen as well as to the top and bottom side of the FRP panel. The precise layouts of the strain gages are shown in Figure 5.12 through Figure 5.19. A brief summary of the distribution of strain gages throughout the specimen is provided in Table 5.4.

Table 5.4 Strain gages used in test specimen #2

GENERAL LOCATION	ORIENTATION	NO. OF STRAIN GAGES USED	LAYOUT DETAILS
Bottom side of FRP deck panels	Longitudinal	15	Figure 5.12
Bottom side of FRP deck panels	Transverse	8	Figure 5.13
Top side of FRP deck panels	Longitudinal	2	Figure 5.14
Top side of FRP deck panels	Transverse	8	Figure 5.15
Bottom layer of deck rebar	Longitudinal	2	Same as Figure 5.16
Bottom layer of deck rebar	Transverse	9	Figure 5.18
Top layer of deck rebar	Longitudinal	2	Figure 5.16
Top layer of deck rebar	Transverse	27	Figure 5.17
Rebar in stems	Vertical	48	Figure 5.19

The positions of the strain gages attached to the bottom side of the FRP panel side deck are shown in Figure 5.12 and Figure 5.13 , oriented in the longitudinal and transverse directions, respectively. The strain gages attached the bottom of the FRP

deck were spaced 305 mm (1 ft) apart from each other in the transverse direction and approximately 610 mm (2 ft) apart from each other in the longitudinal direction.

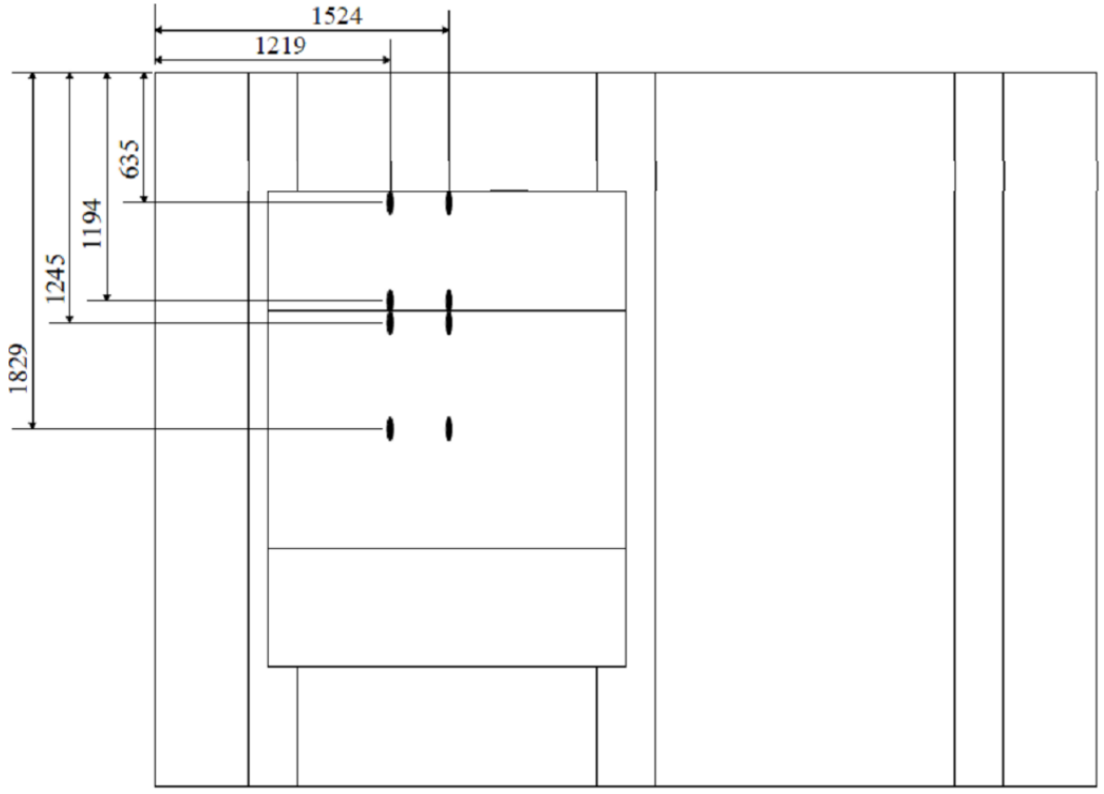

Figure 5.12 Layout of longitudinal strain gages attached to bottom of FRP side deck

The longitudinally oriented strain gages shown in Figure 5.12 were positioned in two rows along the FRP deck slab, with one longitudinal row at the midspan of the slab and the other offset from the slab centerline by 305 mm (12 in) in the direction of the outer stem. These longitudinal lines of strain gages serve to assess the progression of strains at different distances away from the applied load. Strain gages were located directly on either side of the intersection between FRP panels in order to evaluate the effectiveness of stress transfer between adjacent panels. The transversely oriented strain gages attached to the bottom of the FRP side deck consisted of two long rows of

gages as shown in Figure 5.13, with one row along the test specimen centerline and another row located 610 mm (2 ft) away from the specimen centerline.

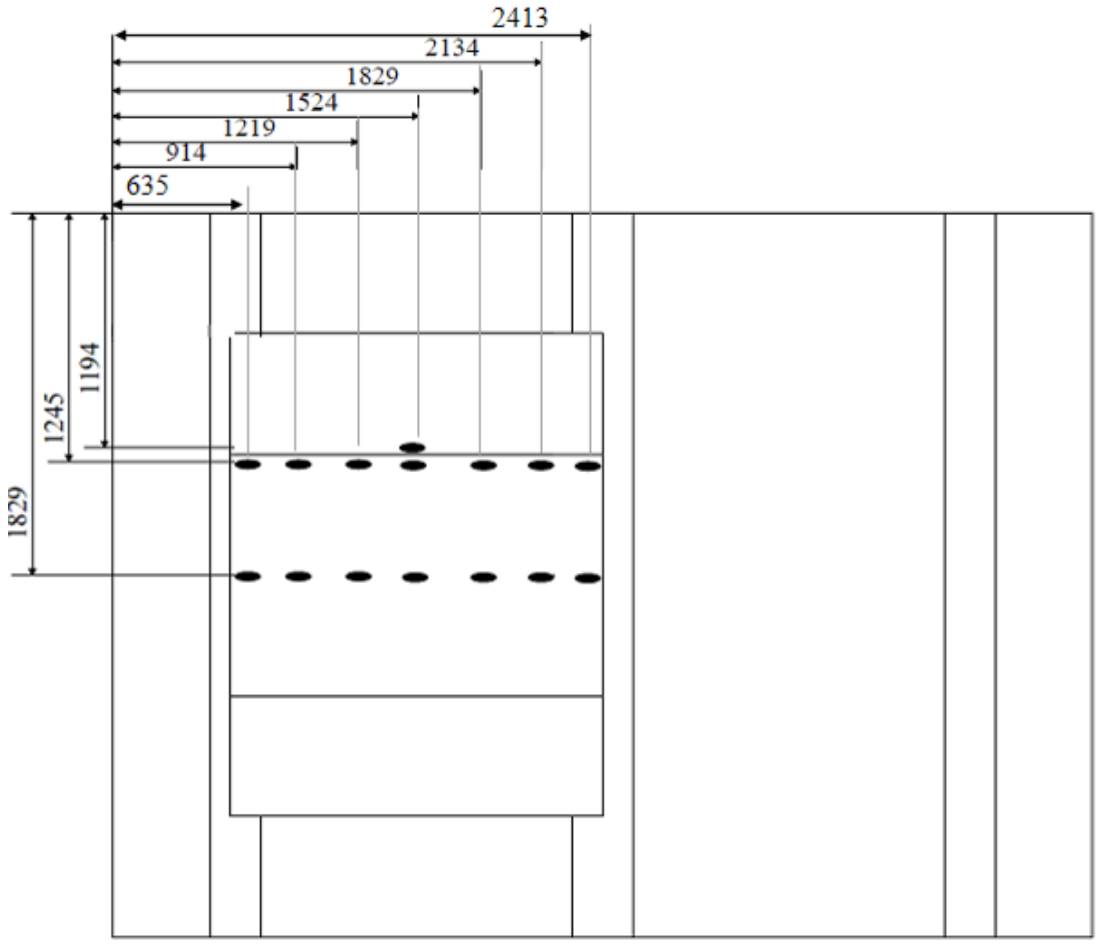

Figure 5.13 Layout of transverse strain gages attached to bottom of FRP side deck

In order to further investigate the structural response of the FRP panels, strain gages were attached in different locations throughout the top side of the central FRP panel. The two longitudinal strain gages shown in Figure 5.14 were positioned along the midspan of the FRP side deck at the same location as gages that were applied to the bottom of the FRP panel, therefore allowing for direct comparison of strain values between the top and bottom side of the FRP panel. The transversely oriented strain

gages shown in Figure 5.15 were attached along the midspan of the FRP deck, both in the middle of the flat panel sections as well as on top of the FRP panel stiffeners, and near the edges of the FRP panel.

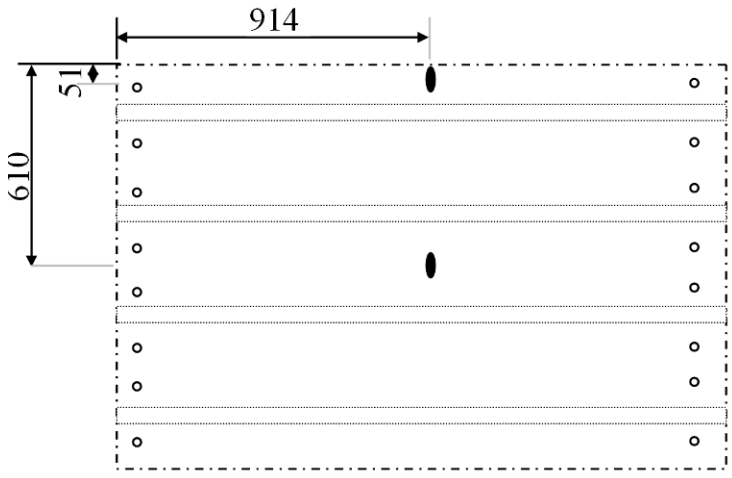

Figure 5.14 Layout of longitudinal strain gages attached to top of central FRP panel

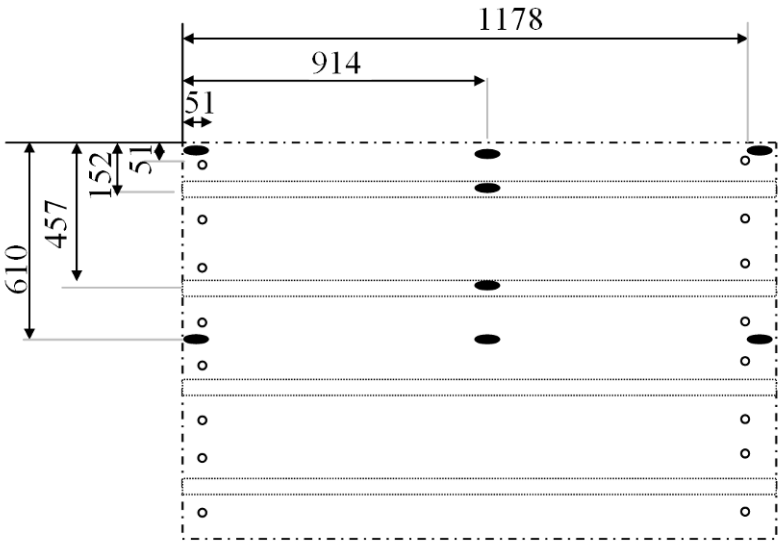

Figure 5.15 Layout of transverse strain gages attached to top of central FRP panel

Strain gages were also attached to the top and bottom layer of steel reinforcement in the deck slab and were attached to both longitudinally and transversely oriented rebar. Two strain gages were attached to the top longitudinal rebar in a row that was as close as possible to the centerline of the two deck slabs. The middle strain gage in each row was placed at the centerline of the test specimen and the second strain gage was spaced a distance of 610 mm (2 ft) increments along the bar as shown in Figure 5.16. The top transverse steel rebar that ran along the specimen centerline was instrumented with nine strain gages as shown in Figure 5.17.

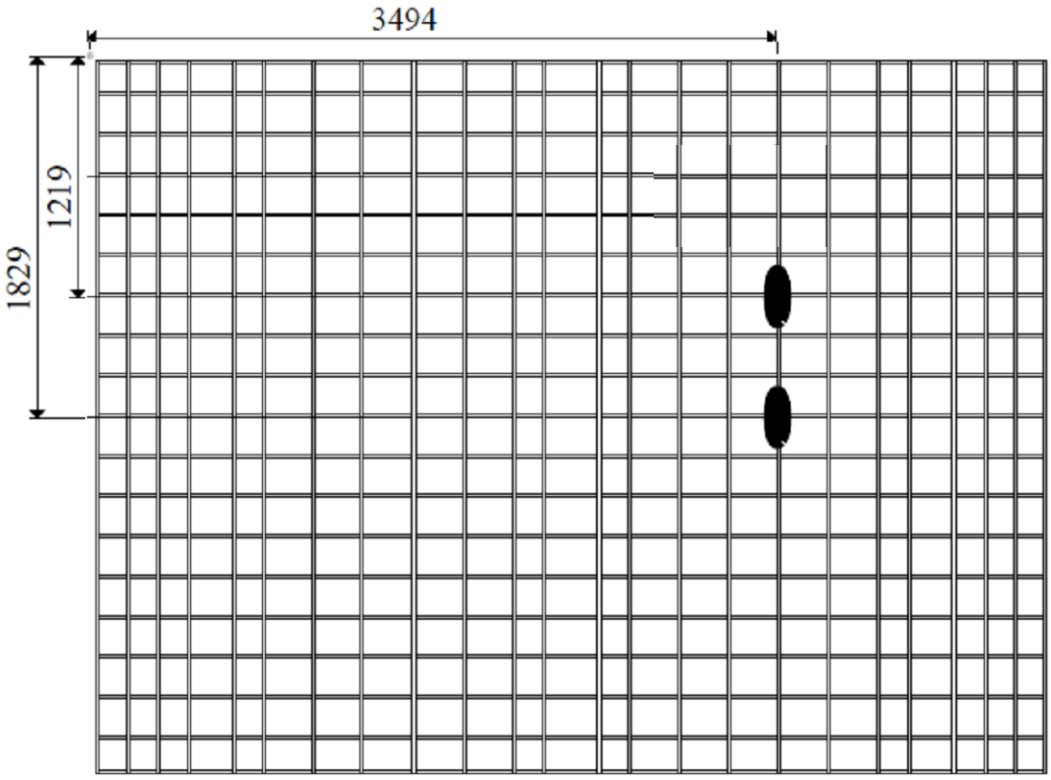

Figure 5.16 Layout of strain gages attached to top longitudinal steel reinforcement (same layout of strain gages attached to the bottom longitudinal reinforcement)

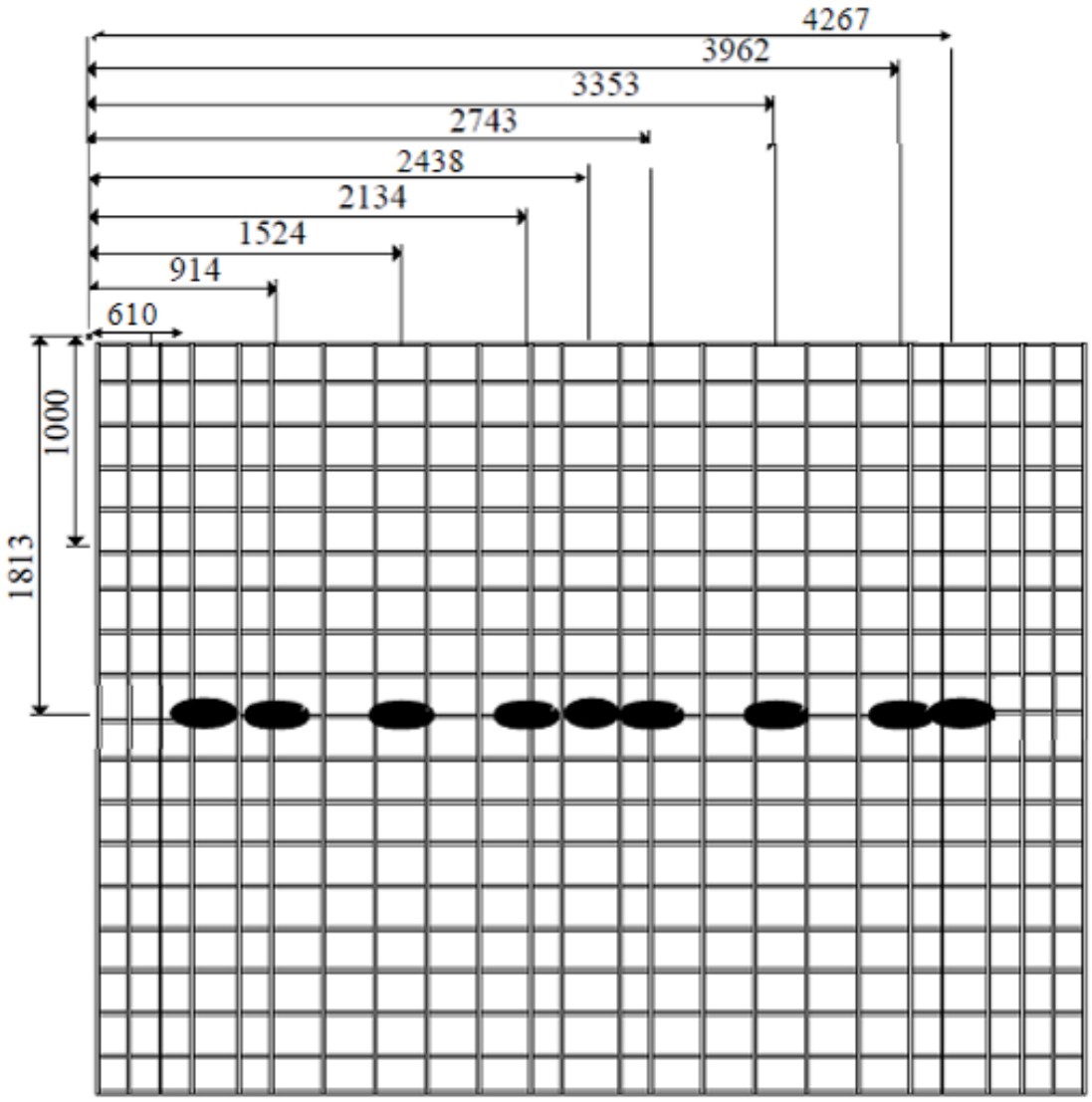

Figure 5.17 Layout of strain gages attached to top transverse steel reinforcement

The 27 strain gages attached to the bottom layer of transverse rebar were primarily located on three lines of strain gages, which each contained eight strain gages as shown in Figure 5.18. Three additional bars with one strain gage each added further instrumentation to the reinforced concrete side. The bottom longitudinal rebar in the deck were instrumented with a total of two strain gages, located in the same

position as the strain gages on the top longitudinal steel reinforcement, as shown in Figure 5.16.

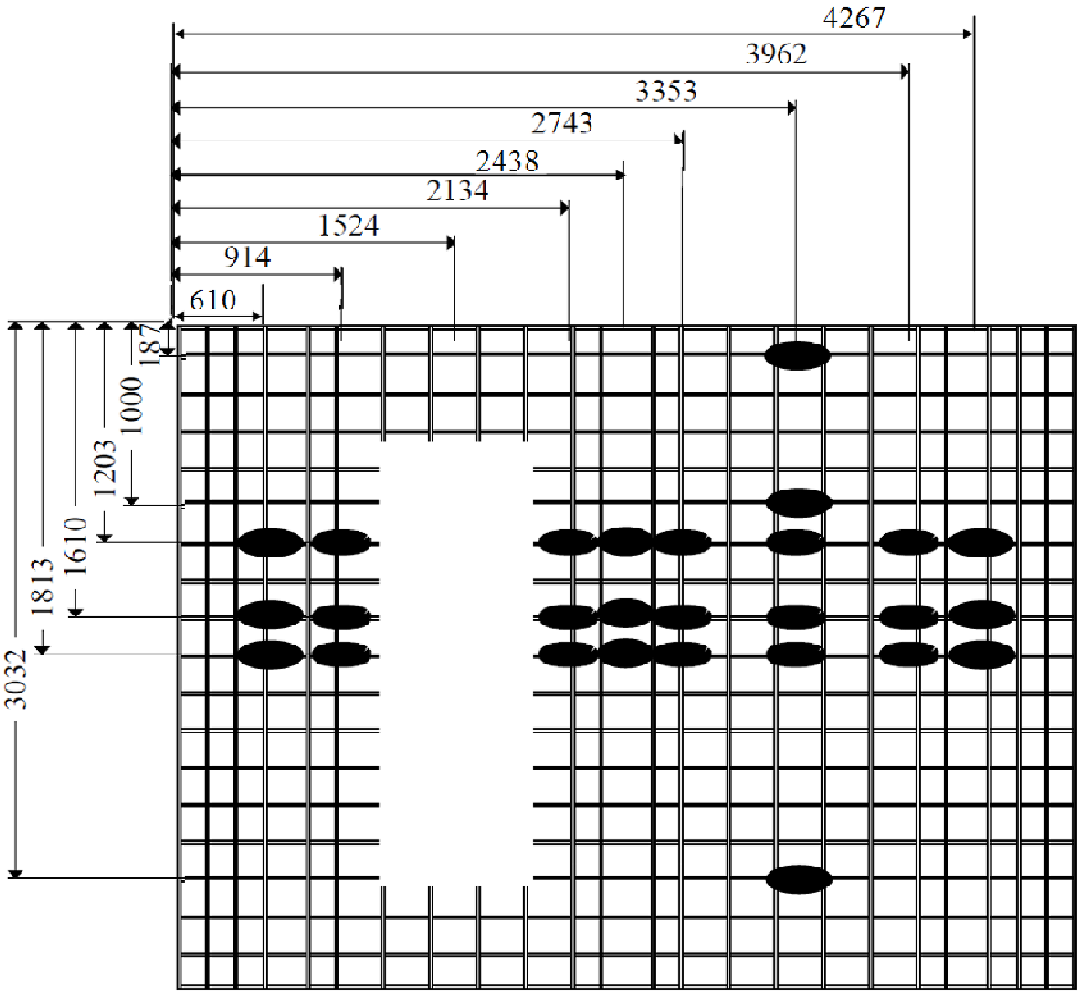

Figure 5.18 Layout of strain gages attached to bottom transverse steel reinforcement

The strain gages attached to the vertical steel reinforcement in the stems are arranged in one of two patterns, termed “A” and “B”, and are located at different positions within the test specimen cross section as shown in Figure 5.19. Strain gage pattern A contains eight gages, with six attached to the outer stem of the FRP side and

two attached to the center stem as shown in Figure 5.20. Strain gage pattern B contains three strain gages total, with one strain gage attached to the outer FRP side stem and two gages attached the center stem as shown in Figure 5.21. There are a total of 48 strain gages attached to the vertical stem rebar.

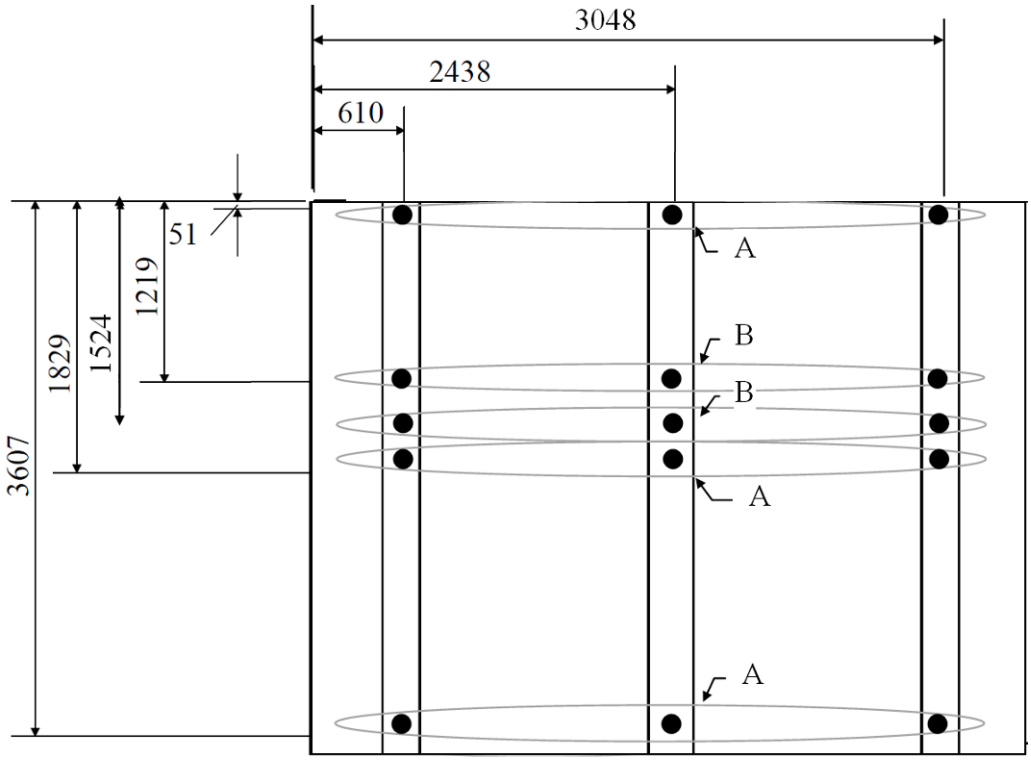

Figure 5.19 Strain gage pattern locations for gages attached to vertical stem rebar

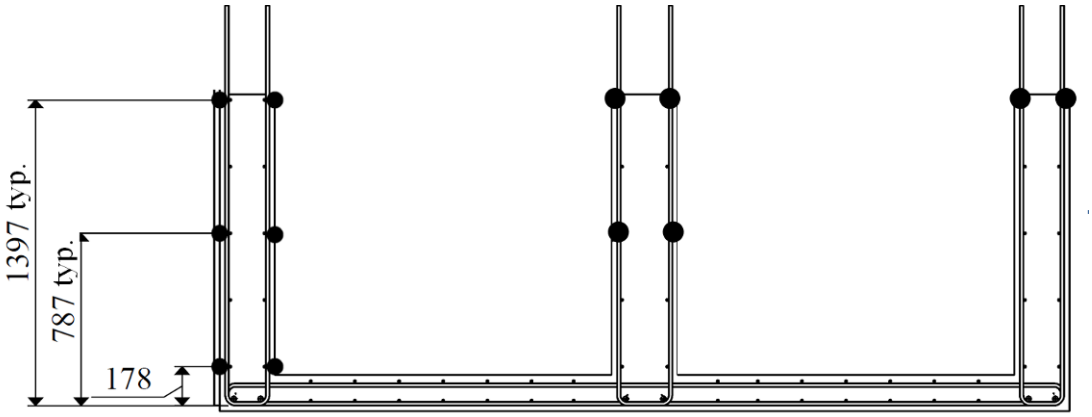

Figure 5.20 Strain gage pattern “A”
(Consists of six strain gages attached to the vertical stem rebar of the FRP side outer stem and two strain gages attached to the vertical stem rebar of the center stem)

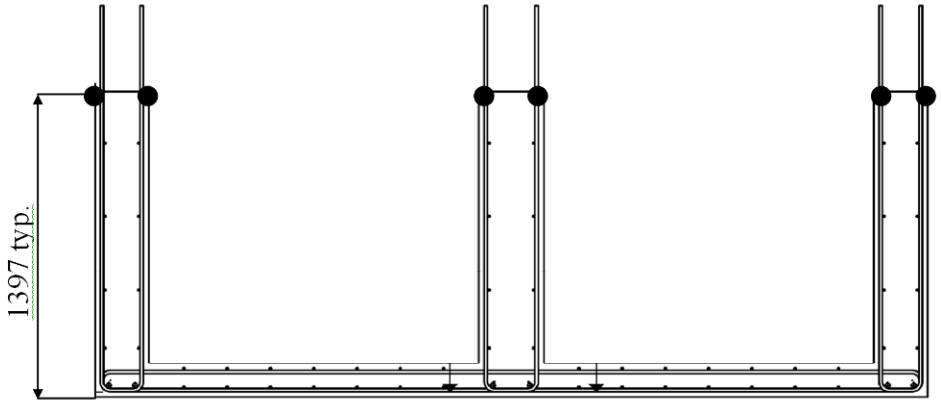

Figure 5.21 Strain gage pattern “B”
(Consists of one strain gage attached to the vertical stem rebar of the FRP side outer stem and two strain gages attached to the vertical stem rebar of the center stem)

5.5 DATA FROM CASTING OF DECK CONCRETE

Following the same process as the first test specimen, concrete was cast to create a 178 mm (7 in) thick deck slab, which applied a load per unit area of 4.21 N/mm^2 (88 psf). During the pouring of the concrete, the composite deck panel had peak deflections of less than half that of the wooden shored formwork used for the

reinforced concrete side, 2.2 mm (0.087 in) versus 5.9 mm (0.232 in), respectively as shown in Figure 5.22. Forty-eight hours after the completion of the concrete pour, the deflections for the composite side versus reinforced concrete side were 1.4 mm (0.055 in) versus 5.1 mm (0.201 in) respectively.

The deflection of the composite formwork during construction was 78.4% less than the AASHTO specified deflection limit of 10.2 mm (0.4 mm), which was determined from the span length divided by 180. These deflection results indicate that the FRP panels function well as formwork, exhibiting minimal deflections under construction loading.

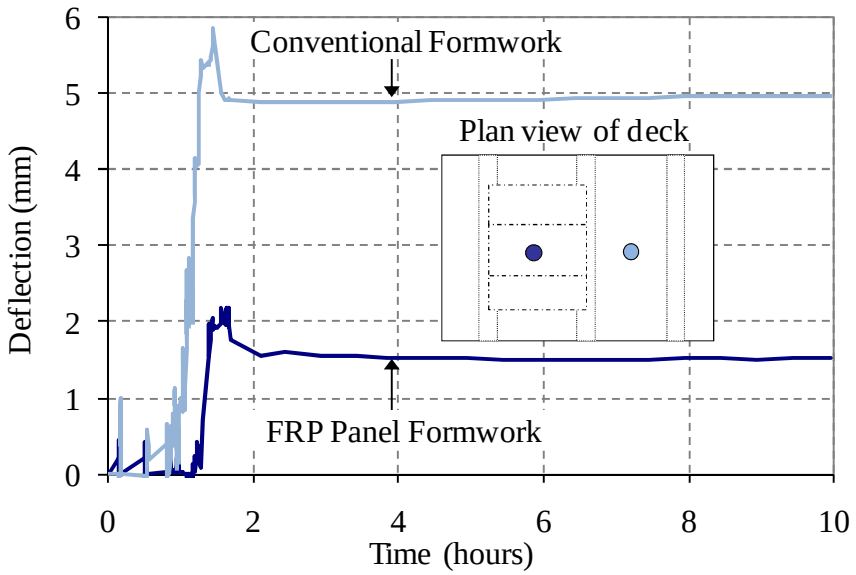

Figure 5.22 Comparison of formwork center deflections under construction loading

Temperature and strain data were also taken during the construction pour to determine the temperature of the concrete during cure and the strains imposed on the

deck due to construction loading and shrinkage. To measure the temperature of the deck, three thermocouples were used with one thermocouple embedded in the center of the composite side deck concrete, another embedded in the center of the RC side deck concrete and the final thermocouple placed adjacent to the test specimen, to measure ambient temperatures. Figure 5.23 shows the temperatures measured by the three thermocouples over a 72 hour period.

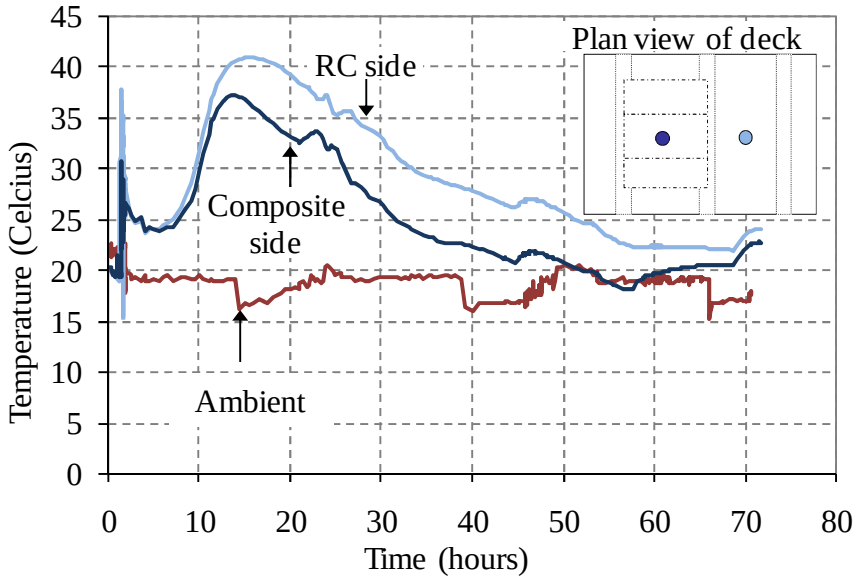

Figure 5.23 Temperature progression over three days for freshly poured deck concrete (Deck pour completed within first two hours from start of data acquisition)

Note that the sudden shifts in the ambient temperature directly correspond with the operating hours of the testing facility, in which large bay doors are opened and closed at the start and close of business hours respectively. The peak temperature in the composite side deck slab was 37.2 degrees Celsius and was achieved approximately 11.5 hours after- the completion of the concrete deck pour, whereas the RC side deck

slab achieved a peak temperature of 40.9 degrees Celsius approximately 13.5 hours after completion of the concrete deck pour.

Strain values from the strain gages located throughout the specimen changed by less than 100 microstrains during the twenty-four hours after the deck concrete pour. The results from temperature and strain data measured within the deck indicate that the change in temperature due to the exothermic reaction from the concrete deck pour has a negligible effect on the performance of the FRP panel system.

5.6 STATIC LOADING OF TEST SPECIMEN

5.6.1 Loading Protocol

Load was applied to the specimen using the same testing setup as the first test specimen, with two 890 kN (200 kip) capacity actuators spaced 1830 mm (6 ft) apart from each other and at the center of each deck slab. The current test specimen was subjected to quasi static up to 70% of the load at which punching shear occurred for the first test specimen followed by extensive cyclic loading. This section describes the static portion of loading, whereas the details and test results from cyclic loading are described in Section 5.7.

The quasi static portion of testing was applied via single cycles at 98 kN (22 kip), 169 kN (38 kip), 338 kN (76 kip), 489 kN (110 kip) and 578 kN (130 kip). The high loading levels applied to the specimen during the static phase were applied in order to establish a performance comparison between systems and ensure the system

exhibits a stable response even when exposed to large overloads. A summary of the static loading protocol is shown in Table 5.5.

In addition to the loading described in Table 5.5, two additional loading steps were applied. After the 489 kN (110 kip) load level, the unloaded specimen was loaded to 98 kN (22 kip) then unloaded prior to continuing on to the 578 kN (130 kip) load level. An additional static loading of the test specimen in a single cycle up to 578 kN (130 kN) was also performed after the completion of the quasi static loading phase and immediately prior to the start of the cyclic phases.

Table 5.5 Static loading protocol for test specimen #2

TARGET LOAD		SINGLE LOAD-UNLOAD CYCLE (Yes/ No)	MULTIPLE OF SERVICE I LOAD 98 kN (22 kip)	MULTIPLE OF STRENGTH I LOAD 169 kN (38 kip)	MULTIPLE OF PERMIT LOAD 180 kN (41 kip)
kN	kip				
73	16	No	0.7	0.4	0.4
98	22	Yes	1.0	0.6	0.5
169	38	Yes	1.7	1.0	0.9
254	57	No	2.6	1.5	1.4
338	76	Yes	3.4	2.0	1.9
400	90	No	4.1	2.4	2.2
489	110	Yes	5.0	2.9	2.7
578	130	Yes	5.9	3.4	3.2

5.6.2 Overall Behavior

At each load level in which a single cycle was performed, the target load was held briefly to allow inspection of the test specimen in the loaded state prior to unloading the specimen. This allowed for easier observation of any cracking or

damage which had occurred to the test specimen during a given load level. The first minor cracks due to loading were observed at the 489 kN (110 kip) load level, which was equivalent to 5.0 times the AASHTO service load. These small discontinuous cracks were less than 0.1mm (0.004 in) width and were located on the top surface of the deck near the center stem. Linear potentiometer and strain gage data described in Section 5.6.8 indicate that the FRP panel and adjacent concrete remained bonded to each other throughout the static loading phase.

The maximum midspan deflections of the deck slabs under the applied load of 578 kN (130 kip) were 3.99 mm (0.157 in) for the FRP panel reinforced slab and 3.62 mm (0.143 in) for the reinforced concrete slab. The overall load versus midspan displacement response curves for the two slabs are shown in Figure 5.24. In order to better compare the structural response of the two reinforcing schemes, the unloading portion of each curve was removed and the envelope plot of load versus center deflections is shown in Figure 5.25.

At the 98 kN (22 kip) load level, equivalent to the AASHTO HS20 wheel load of 73 kN (16.4 kip) with an additional 33% impact factor, the vertical midspan deflection for the FRP side slab was 0.36 mm (0.014 in) whereas the midspan deflection for the RC side slab was 0.29 mm (0.011 in). Throughout the loading of the test specimen, the composite side deflected slightly more at the midspan than the reinforced concrete side, with a maximum difference between the two slabs of 0.36 mm (0.014 in), equivalent to a 9.9% greater composite side deflection, which occurred at a the maximum applied load level of 578 kN (130 kip).

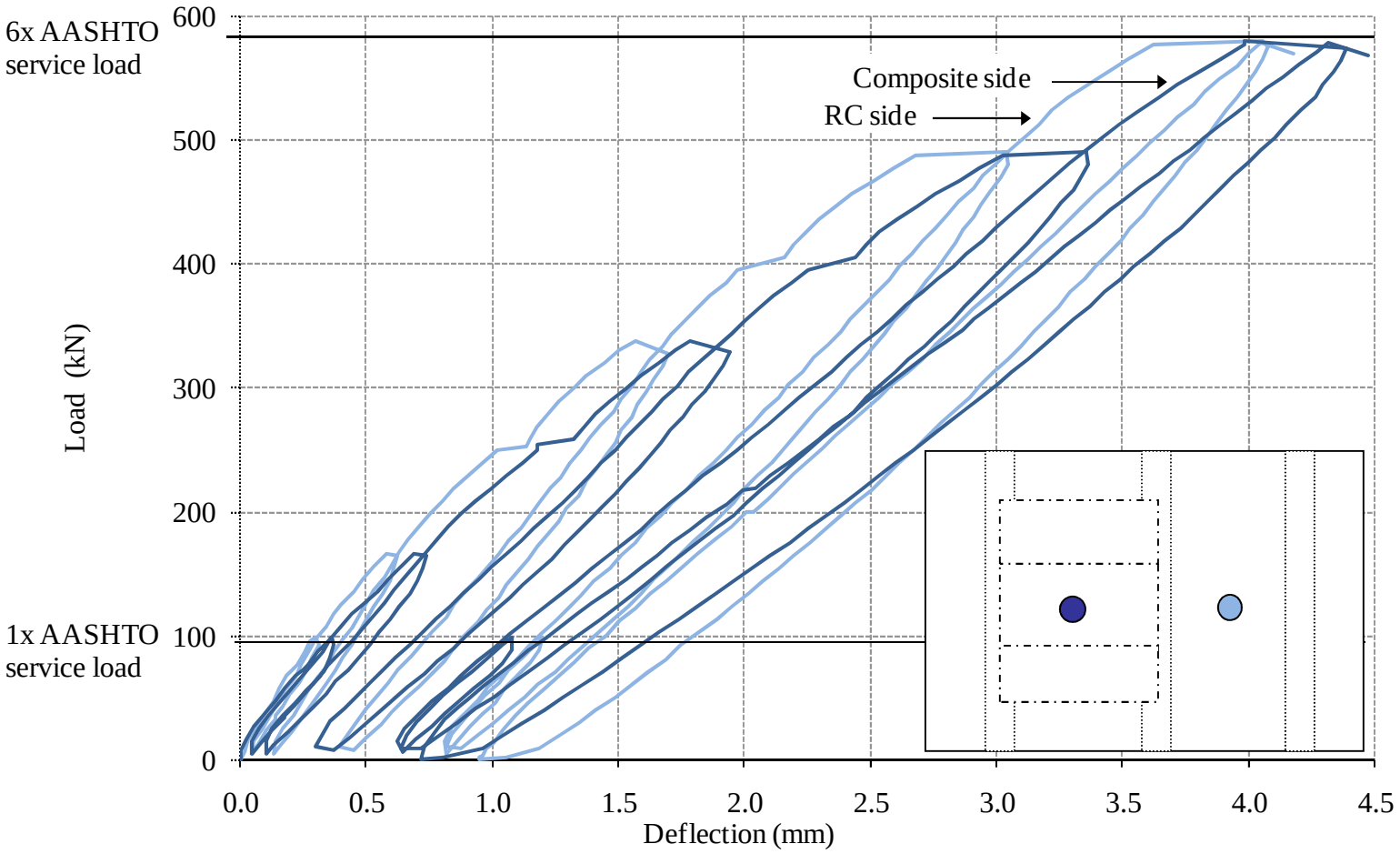

Figure 5.24 Load versus center deflections

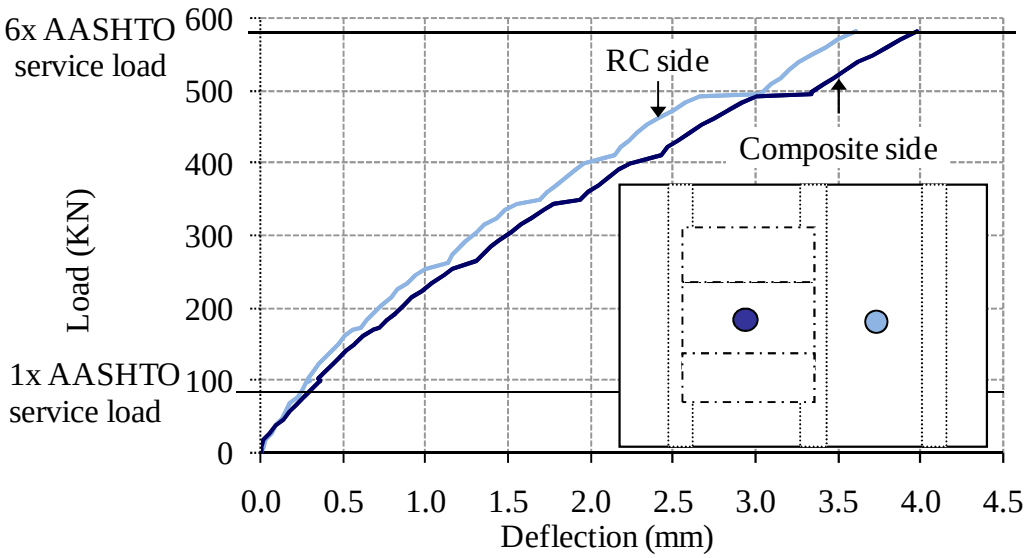

Figure 5.25. Envelope plot of load versus center deflections

5.6.3 Stiffness change per increment

Progression of damage within the deck slabs as observed through degradation of the slope of the load-deflection response is compared using effective stiffness ratios. The effective stiffness ratio, which is defined and discussed in greater detail in Section 3.8.3, calculates an adaptive secant stiffness using the center deflection for each slab and normalizes this value using the adaptive secant stiffness calculated at a baseline load. Use of effective stiffness ratio values rather than center deflection values provides a more reliable metric for performance comparisons the two deck slabs. The effective stiffness ratios shown in Table 5.6 and Table 5.7 highlight the difference in the degradation trends of the load deflection slopes for the two reinforcing systems.

Table 5.6 Effective stiffness ratio of FRP side slab from linear potentiometer data

Target actuator load		Actual target actuator load, P_f		Actual min. threshold actuator load, P_i		Deflection at target load, δ_f		Deflection at min. threshold load, δ_i		Effective stiffness ratio
kN	kip	kN	kip	kN	kip	mm	in	mm	in	---
98	22	98.0	22.0	7.7	1.7	0.36	0.014	0.00	0.000	1.00
169	38	165.2	37.1	5.0	1.1	0.69	0.027	0.04	0.002	0.98
254	57	253.4	57.0	5.0	1.1	1.18	0.046	0.10	0.004	0.91
338	76	338.1	76.0	5.0	1.1	1.79	0.070	0.10	0.004	0.78
400	90	395.1	88.8	7.5	1.7	2.26	0.089	0.37	0.014	0.81
489	110	487.4	109.6	7.5	1.7	3.02	0.119	0.37	0.014	0.71
578	130	575.9	129.5	5.2	1.2	3.99	0.157	0.64	0.025	0.67

Table 5.7 Effective stiffness ratio of RC side slab from linear potentiometer data

Target actuator load		Actual target actuator load, P_f		Actual min. threshold actuator load, P_i		Deflection at target load, δ_f		Deflection at min. threshold load, δ_i		Effective stiffness ratio
kN	kip	kN	kip	kN	kip	mm	in	mm	in	---
98	22	98.0	22.0	6.5	1.5	0.30	0.012	0.01	0.000	1.00
169	38	165.2	37.1	5.0	1.1	0.58	0.023	0.04	0.002	0.93
254	57	252.8	56.8	5.1	1.1	1.14	0.045	0.13	0.005	0.76
338	76	338.0	76.0	5.1	1.1	1.56	0.062	0.13	0.005	0.72
400	90	405.1	91.1	7.3	1.6	2.16	0.085	0.45	0.018	0.72
489	110	487.4	109.6	7.3	1.6	2.68	0.105	0.45	0.018	0.67
578	130	575.9	129.5	5.0	1.1	3.63	0.143	0.82	0.032	0.63

The degradation trends for the two slabs are most easily observed in Figure 5.26, which plots the effective stiffness values of both slabs for each load level. The reinforced concrete side slab displayed the most significant effective stiffness degradation at the 254 kN (57 kip) load level, where the effective stiffness ratio for the reinforced concrete side had decreased by 24% since the start of the current loading phase as compared to FRP panel side, which only experienced a 9% decrease in its effective stiffness ratio.

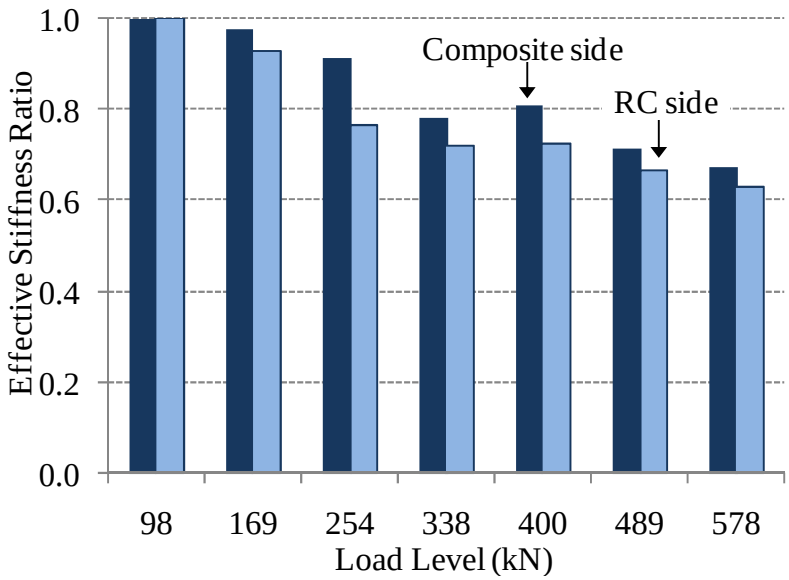

Figure 5.26 Effective stiffness ratios of the two slabs

The FRP panel side slab maintained higher effective stiffness ratios than the reinforced concrete side slab. Both sides showed minor decreases in the effective stiffness ratio, with a decrease of 33% for the FRP side slab and 37% for the

reinforced concrete slab effective stiffness ratio at the 578 kN (130 kip) load level, which is 5.9 times the AASHTO factored service load.

5.6.4 Deflection Profiles

In this section, deflection profiles throughout the test specimen for key load levels up to maximum applied load are presented. The primary purposes for obtaining the displacement profiles was to determine the extent to which the two reinforcement systems were able to distribute the wheel load over a larger area in both the longitudinal and the transverse directions, thus helping to avoid localized punching shear failure. Unless otherwise noted, the deflection profile figures in this section all maintain the same deflection scale, which accommodates the maximum values observed in the specimen at the maximum load applied during this loading phase of 578 kN (130 kip) in order provide context for each deflection value in relation to the overall deformation of the structure.

The deflection profile along the length of the deck above the central stems is presented in Figure 5.27. This figure indicates that the deck above the center stem deflected evenly along its length. Comparable profiles are also observed for the deflections above the two outer stems. The small and uniform deflections observed in the deck above the stems indicate that the structure is loaded evenly and that the vertical deformations of the stems do not significantly affect the overall structural response of the test specimen. The maximum deflection in the deck above the stems at the 578 kN (130 kip) load level was 0.64 mm (0.252 in), which was approximately

6.2 times smaller than the corresponding midpoint deflection of the reinforced concrete side slab.

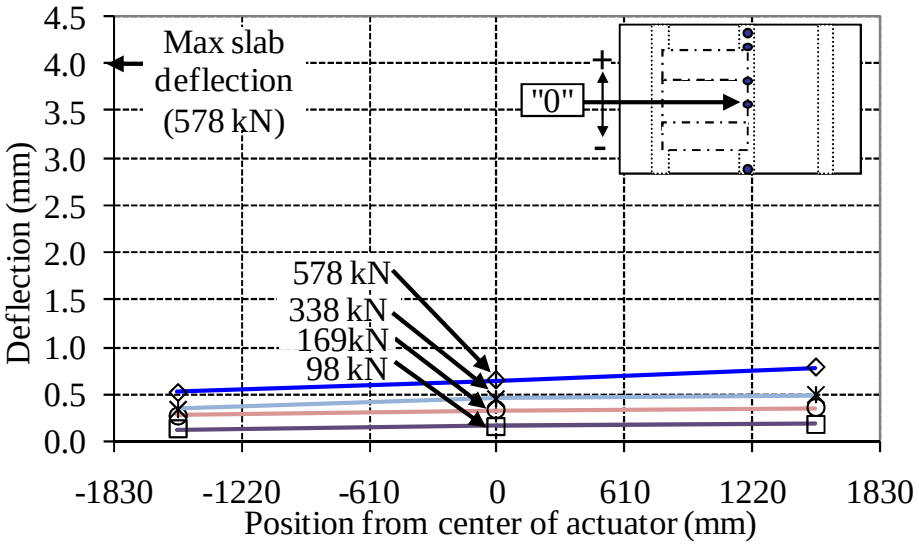

Figure 5.27 Deflection profile along length of deck above central stem

The deflection profiles along the centerline of the two slabs are shown in Figure 5.28 and Figure 5.29. Both slabs maintained comparably shaped deflection profiles throughout the loading range. As expected, the highest deflection values for both slabs were observed for the linear potentiometers below the two hydraulic actuators, with progressively smaller deflections at distances away from these locations. Similarly, because the centerline deflection profiles shown in Figure 5.28 and Figure 5.29 were directly below the actuators, these deflection profiles contain higher deflection values as compared to deflection profiles offset from the centerlines, shown in Figure 5.31 and Figure 5.32.

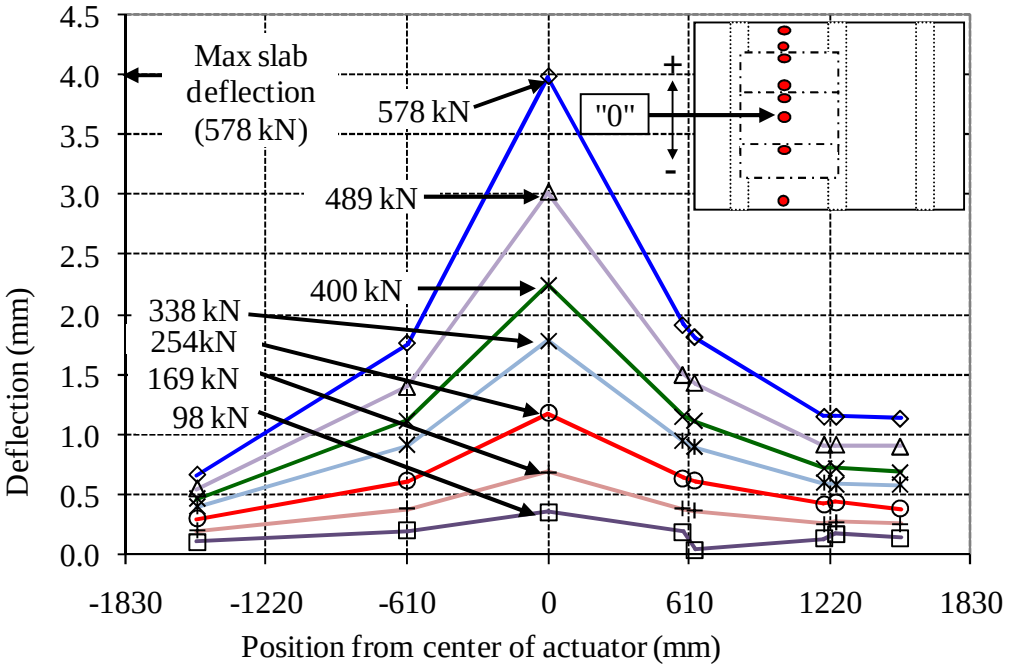

Figure 5.28 Deflection profile along centerline of the composite side deck

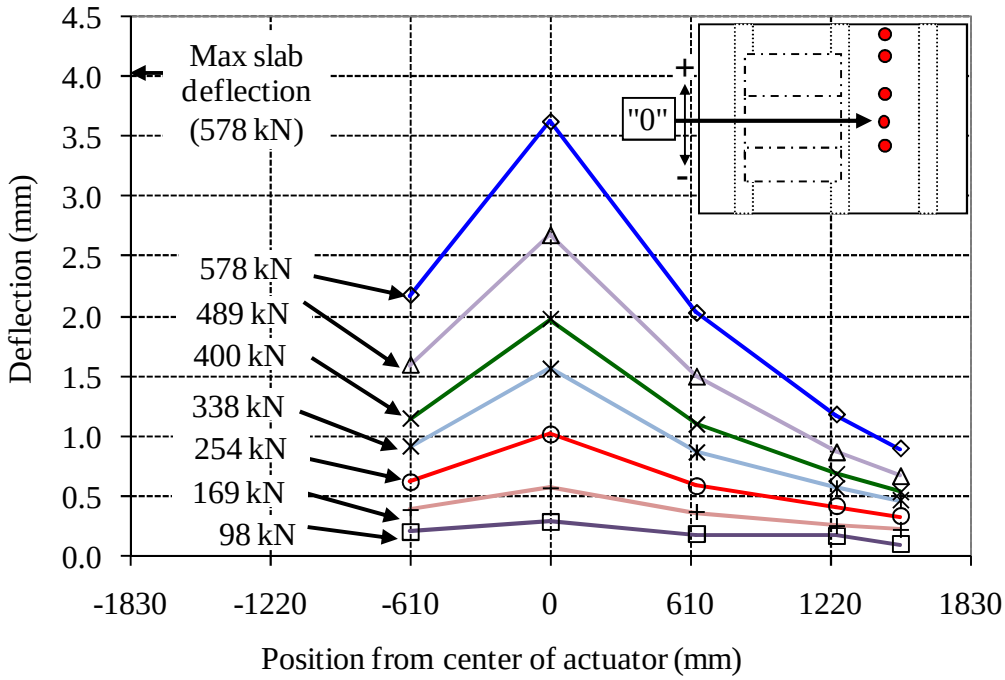

Figure 5.29 Deflection profile along centerline of the RC side deck

In order to more thoroughly compare the level of localized deformations in the slabs, the superimposed deflection profiles along the centerline of the decks are shown at different load levels. The deflection profiles shown in Figure 5.30 at the load level of 578 kN (130 kip), equivalent to 5.9 times the AASHTO service load, are comparably shaped for the two sides, with each of the deflection values for the two sides similar to within 0.5 mm (0.02 in) of each other.

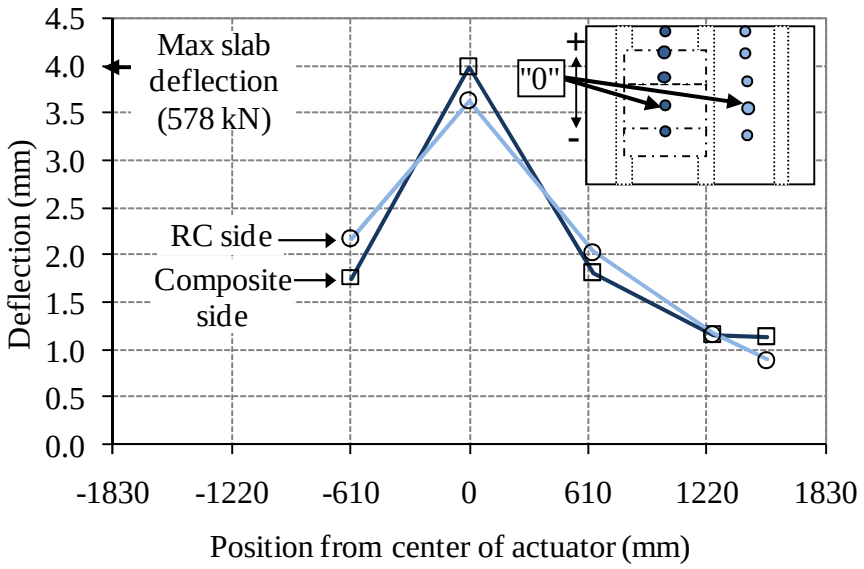

Figure 5.30 Comparison of deflection profiles at a load level of 578 kN

The deflection profiles along the length of the deck, which are offset from the centerlines of the slabs by 305 mm (12 in) towards the outer stems, are shown in Figure 5.31 and Figure 5.32. These figures give information regarding the effectiveness of the reinforcement systems to distribute the actuator load to the surrounding regions.

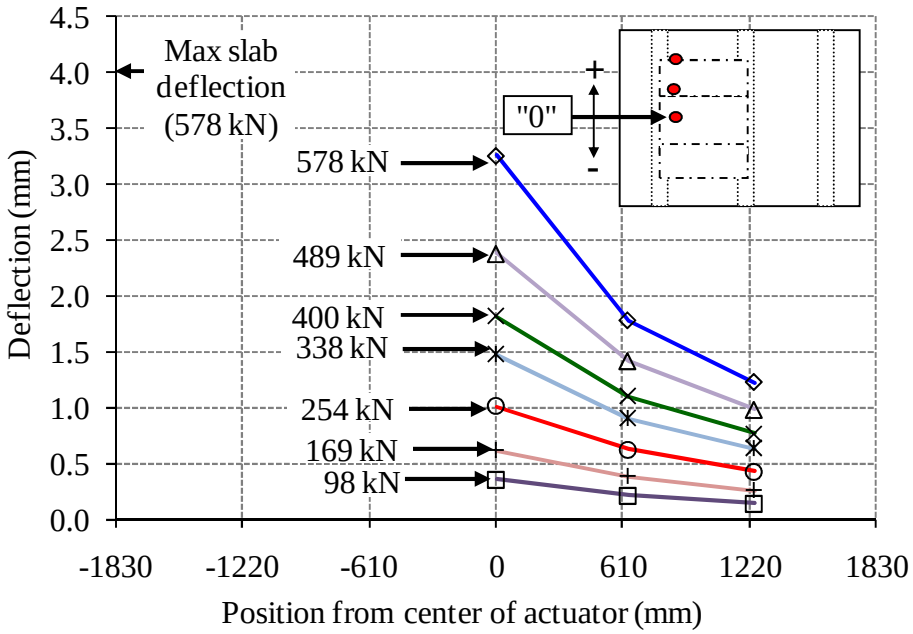

Figure 5.31 Deflection profile along row 2 of linear potentiometers (offset from the composite side centerline by 305 mm)

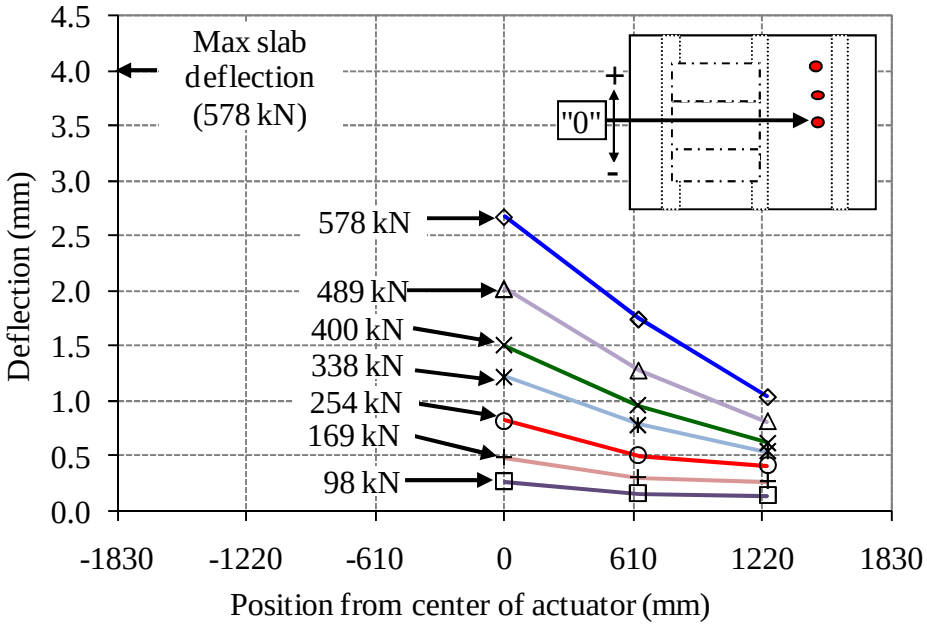

Figure 5.32 Deflection profile along row 8 of linear potentiometers (offset from the RC side centerline by 305 mm)

Throughout the loading range, the deflection profiles in the longitudinal direction near the outer stems shown in Figure 5.31 and Figure 5.32 illustrate comparable deflections in both slabs, with slightly larger values observed on the FRP panel side.

The deflection profile along the transverse centerline of the test specimen is presented in Figure 5.33. As expected, the highest deflection values were observed near the actuator locations and the lowest deflection values were observed above each of the three stems. At the 578 kN (130 kip) load level, equivalent to nearly six times AASHTO service load, the composite side displayed a 3.99 mm (0.157 in) center deflection, while the reinforced concrete side displayed a 3.63 mm (0.143 in) center deflection. A detailed discussion of the progression of the center deflections, as they pertain to the effective stiffness of the slabs, is provided in Section 5.6.3, for the FRP panel reinforced slab and for the reinforced concrete slab. Both sides maintained deflection profiles that were to each other throughout the loading range.

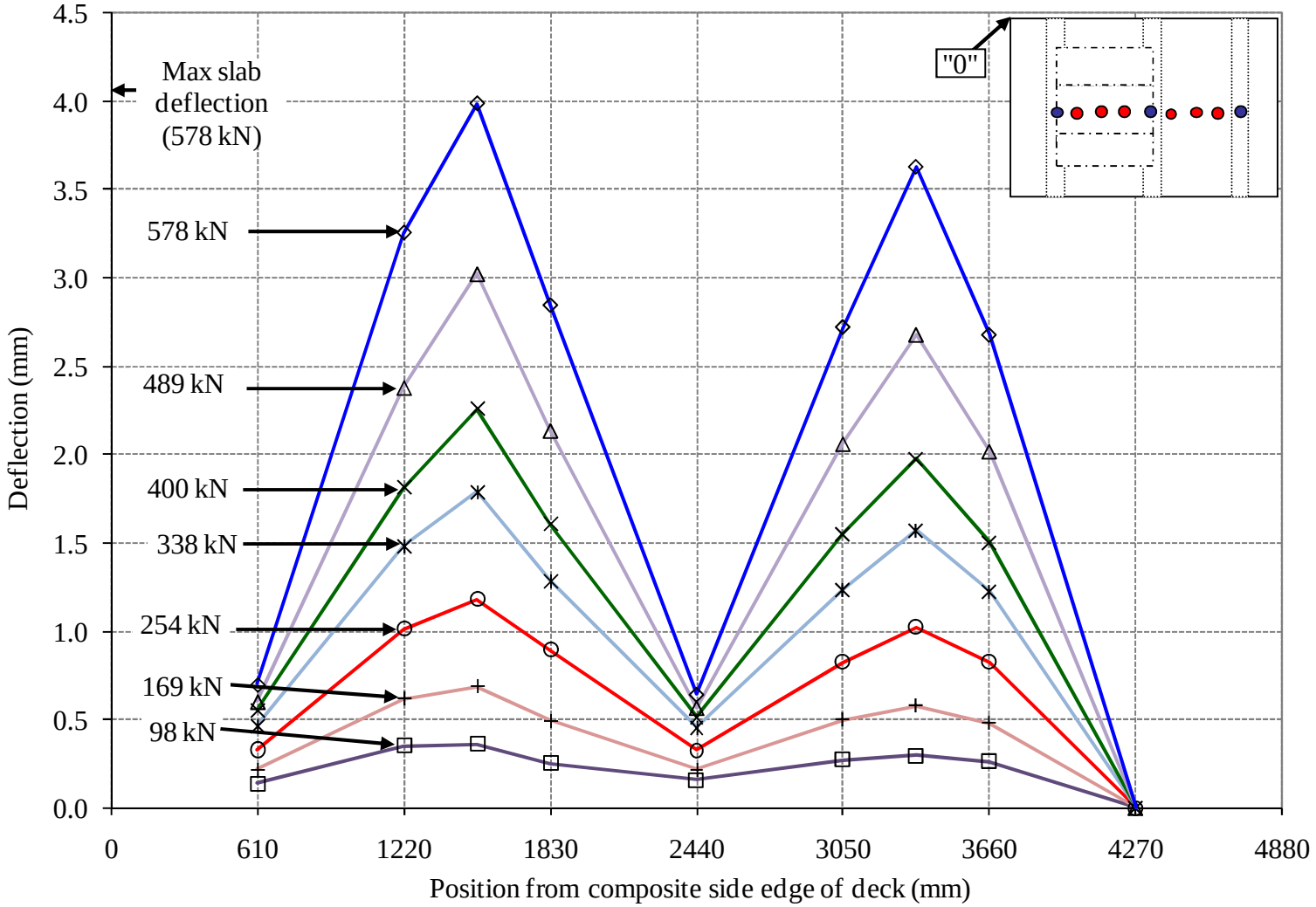

Figure 5.33 Deflection profile along centerline of specimen

5.6.5 Strain Development

The strain development within the test specimen was observed though the examination of measurements from strain gages applied to the steel reinforcement and FRP panels within the test specimen. The precise location of all strain gages is given in Section 5.4.2. Note that strain values reported as negative indicate compressive strains whereas positive values indicate tensile strains.

5.6.5.1 Comparison of Strains in FRP Panel Deck and RC Deck

The load versus strain envelope plot of the bottom longitudinal strain gages located directly below the RC side and composite side actuators is shown in Figure 5.34. The RC side strain values have been adjusted using the method described in Section 3.8.5, which assumes a linear strain distribution within the section, in order to determine the apparent strains at the depth within the reinforced concrete side slab that are in line with the FRP panel strain gage as shown in Figure 3.63.

As observed in Figure 5.34, the reinforced concrete side displays higher strain values than the strains on the FRP panel side throughout the loading range. The adjusted strain in the reinforced concrete side bottom longitudinal strain gage at the maximum applied load of 578 kN (130 kip) was 1505.8 microstrains, which was 960 microstrains greater than the corresponding strain on the FRP panel longitudinal gage of 545.8 microstrains.

The load versus strain envelope plots for the bottom transverse strain gages indicate that the strain for the reinforced concrete side gage initially increases at a

slower rate than the strain for the FRP panel side gage, as shown in Figure 5.35. For loading above approximately 250kN (56 kip), the two strain values from the two sides increase at comparable rates.

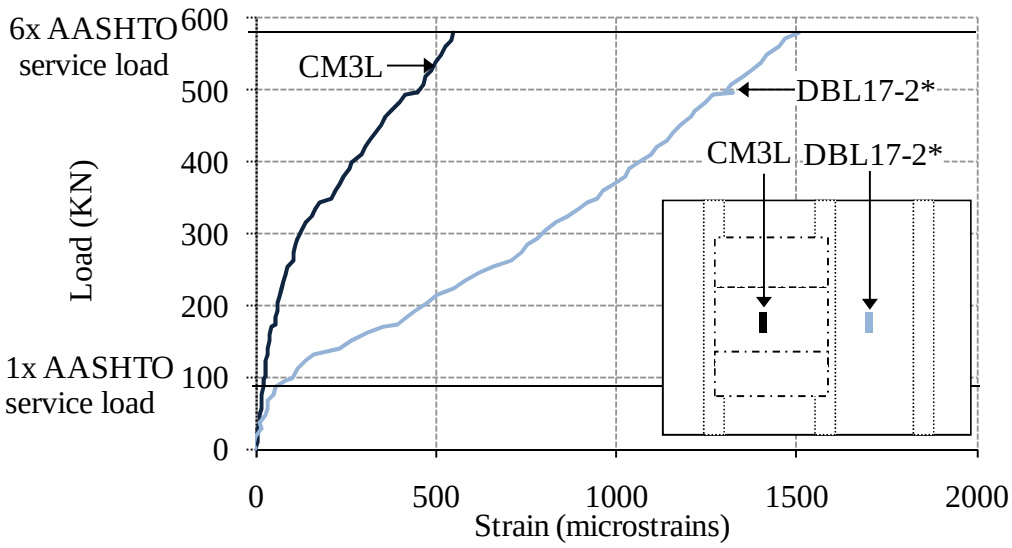

Figure 5.34 Load versus strain for bottom longitudinal strain gages
(Gages are located directly below the two actuators. CM3L is on the composite side on the underside of the FRP panel; DBL17-2 is on the RC side bottom longitudinal steel reinforcement and therefore is adjusted using Equations 3.7 and 3.8)

The strain profile for the top transverse steel reinforcement along the centerline of the specimen is shown in Figure 5.36. As expected for a top rebar under the given loading conditions, the strain gages located at the middle of each deck display the highest compression strains while the gage at the center of the two stems displays the highest levels of tensile strain. For each of the displayed load levels, the reinforced concrete side strain gages exhibit comparable or higher values as compared to the corresponding strain gages on the composite side of the test specimen.

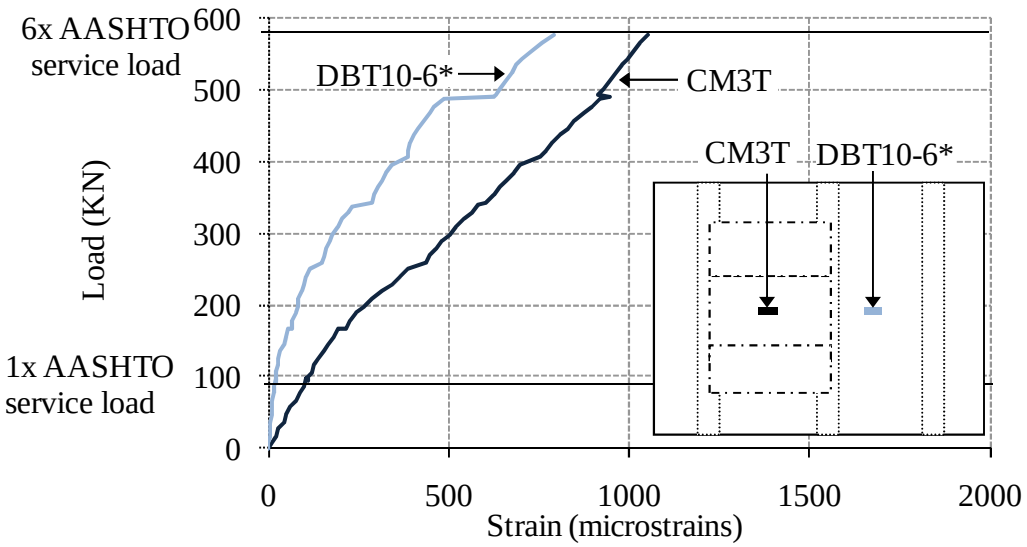

Figure 5.35 Load versus strain for bottom transverse strain gages (Gages are located directly below the two actuators. DBT10-6 is on the RC side bottom transverse steel reinforcement; CM3T is on the composite side underside of the FRP panel and therefore is adjusted using Equations 3.7 and 3.8)

In order to better quantify the difference in response between the two sides individual comparisons of load versus strain plots for pairs of strain gages examined. The load versus strain responses for the top transverse strain gages located directly below the two actuators, shown in Figure 5.37, illustrate equivalent strain values for the two sides during initial loading. For loads above 230 kN (52 kip) until the maximum applied load, the RC side strain gage exhibits strain values that are between 19% and 21% larger than the FRP panel side strains.

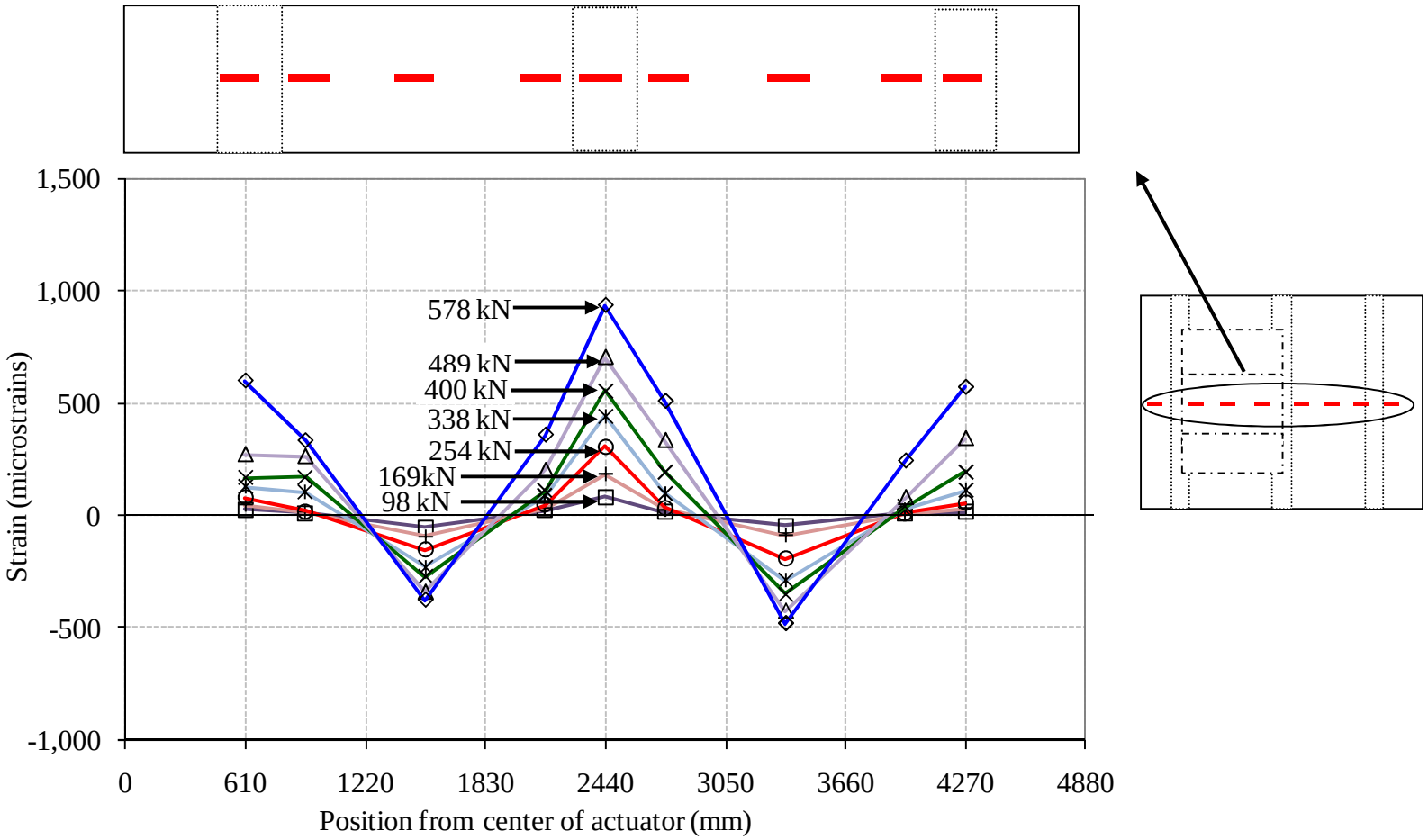

Figure 5.36 Strain profile for top transverse rebar along centerline

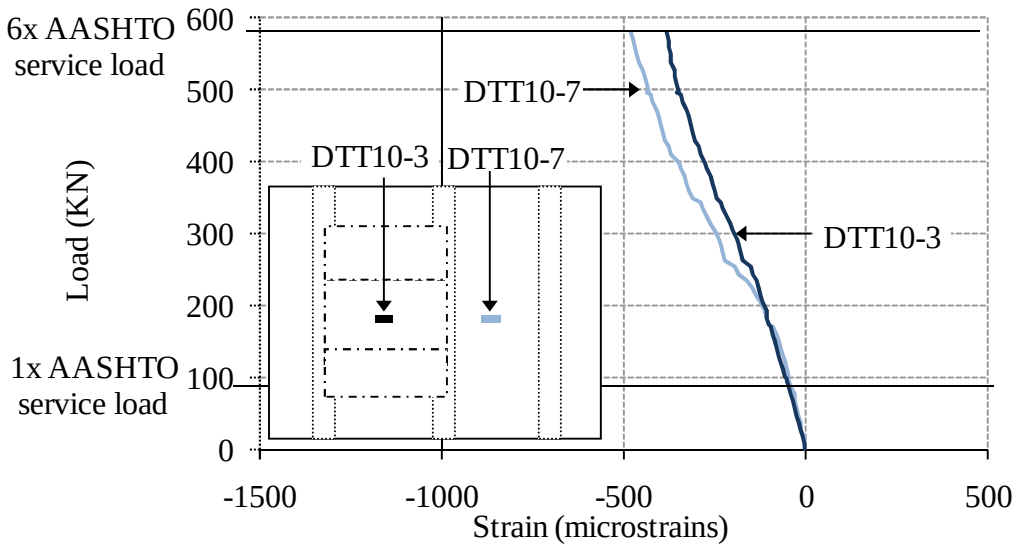

Figure 5.37 Load versus strain for top transverse strain gages
(Both gages are located on the top transverse steel reinforcement directly below the two actuators. DTT10-7 is on the RC side and DTT10-3 is on the composite side)

The load versus strain envelope plots for the top transverse strain gages located 152 mm (6 in) away from either side of the central stem and 610 mm (2 ft) away from the centerline of the two deck slabs are shown in Figure 5.38. The two strain gages showed equivalent strain values up to a load of approximately 338 kN (76 kip)), which is 3.4 times the AASHTO service load. For the remainder of the loading phase, the reinforced concrete side strain gage increased in strain values more quickly than the FPP panels side gage such that the maximum strain in the RC side gage during this loading phase was 150 microstrains or 42.2% greater than the equivalent strain from the FRP panel side strain gage. The envelope plots for load versus strain of the top transverse strain gages located directly above the outer stems, as shown in Figure 5.39, maintain comparable strain values throughout the loading range, with less than 50 microstrains separating the two sides at any load level.

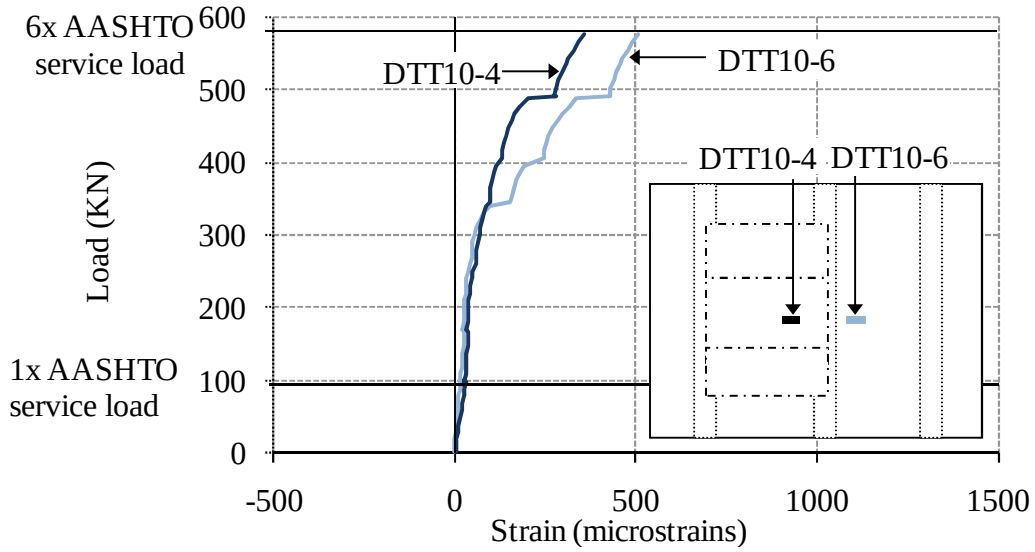

Figure 5.38 Load versus strain for top transverse strain gages near central stem (Both gages are located on the top transverse rebar directly along the test specimen centerline, each a distance of 610 mm away from the midspan of the decks, towards the central stem. DTT10-6 is on the RC side and DTT10-4 is on the composite side)

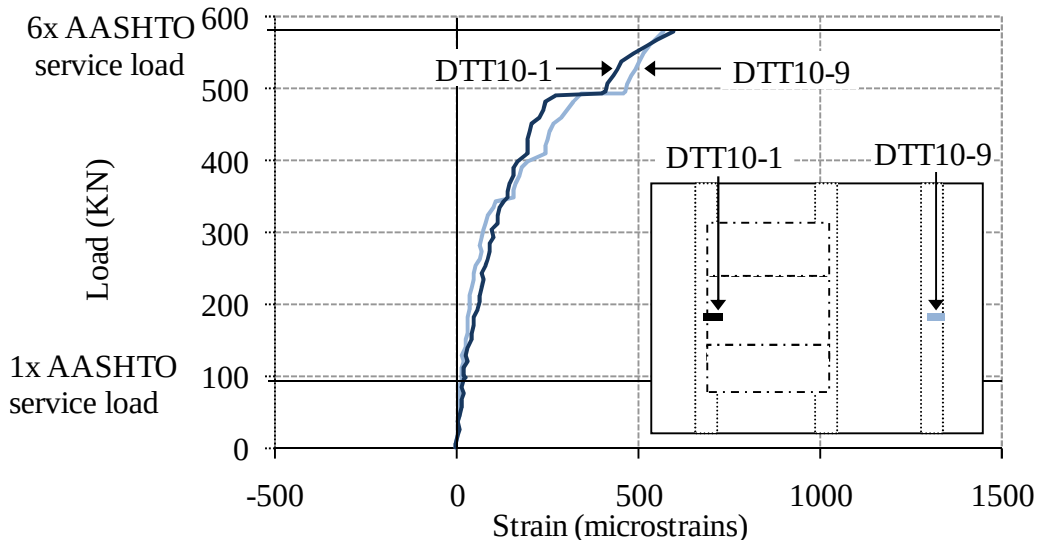

Figure 5.39 Load versus strain for top transverse strain gages above outer stems (Both gages are located on the top transverse rebar directly along the test specimen centerline. DTT10-9 is on the RC side and DTT10-2 is on the composite side)

5.6.5.2 Strain Profiles along the Longitudinal Direction of the Decks

The strain profiles along the longitudinal directions for the centerlines of the composite side and reinforced concrete side deck slabs are shown in Figure 5.40 and Figure 5.41 respectively. These strain profiles can be used to determine the level of stress distribution within the bridge deck due to live loading applied to the deck surface. Note that as discussed in Section 3.8.5, the position of the strain gages within the composite side and RC side deck of the test specimen with respect to the depth of the slab will have an effect on the direct comparability of the absolute magnitude of the strains. Since the FRP side does not have a bottom layer of rebar, the strain gages for the bottom layer on the composite side are attached the underside of the FRP panels, which is located a distance of approximately 57 mm (2.25 in) lower within the deck slab than the gages attached to the bottom longitudinal rebar on the reinforced concrete side.

Regardless of the magnitude of the strain values, the strain profiles of two deck slabs can be compared in terms of profile geometry and loads at which major changes occur. As described previously in Section 5.6.5.1, which examines the load versus strain plots for the center strain gages, the RC side center strain values are significantly higher than the FRP panel side center strain values throughout all loading levels. The composite side and reinforced concrete side deck slabs shown in Figure 5.40 and Figure 5.41 both maintain large tensile values in the strain gage directly below the actuator and compressive strains in the strain gages located greater than 610 mm (2 ft) away from the actuator.

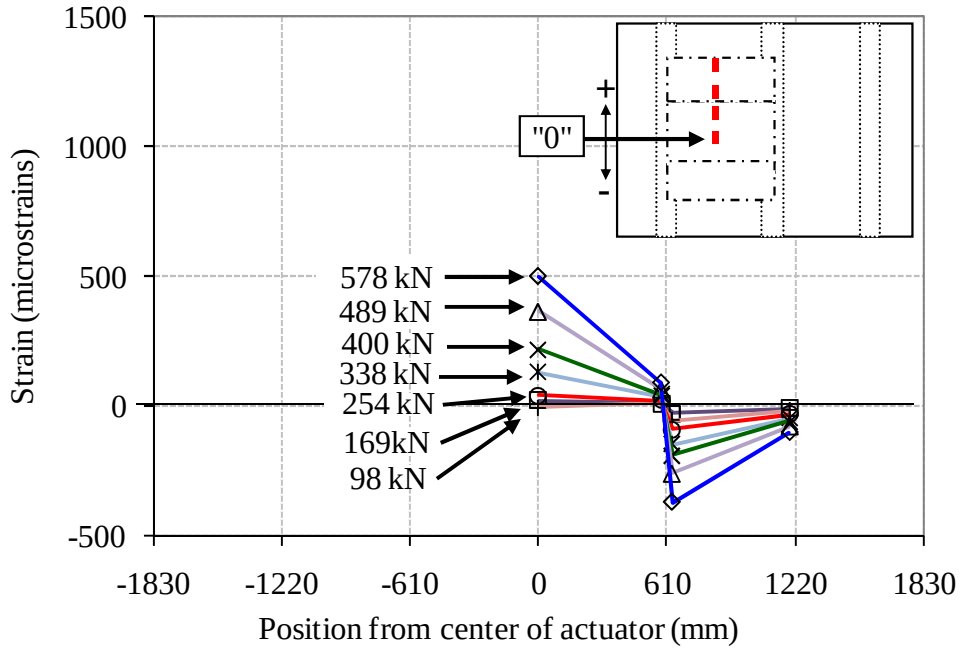

Figure 5.40 Strain profile for gages attached to bottom of FRP panel along line 3
(Line of gages is located directly along the composite side centerline)

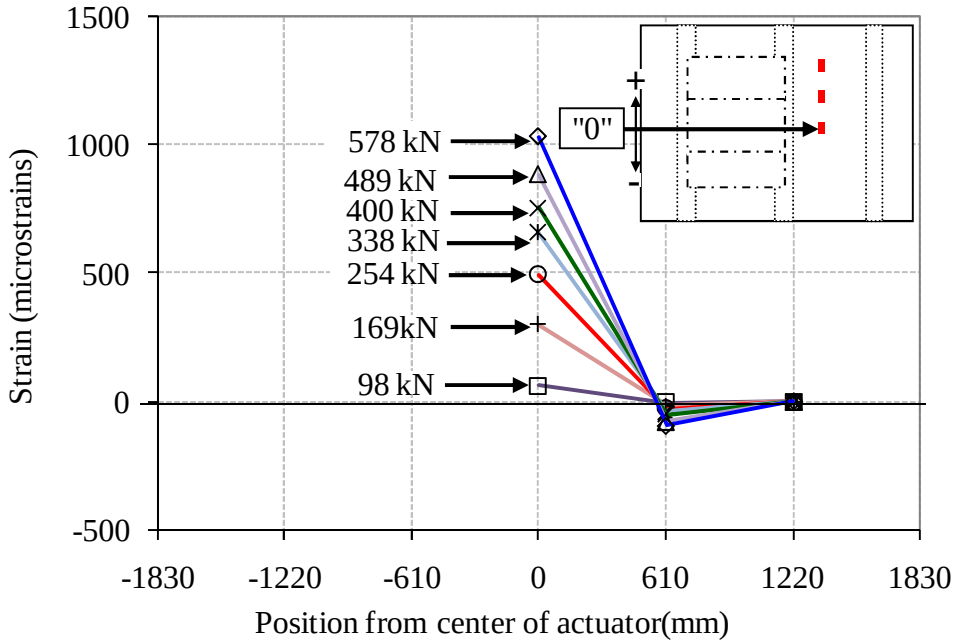

Figure 5.41 Strain profile for bottom longitudinal rebar along line 17
(Rebar is offset from RC side centerline by 140 mm towards the center stem)

The switch in strain values from tension to compression along the RC side strain profile indicates that the point of inflection for the RC side slab in the longitudinal direction is less than 610 mm (2 ft) longitudinally away from the centroid of the actuators. The FRP panel side strains switch from tension to compression at the intersection between the FRP panels. Since the point of inflection for both decks occurs approximately 610 mm (2 ft) away from the centroid of the actuators and this location is near the intersection between panels on the FRP panel side deck, further experimental work is needed that specifically addresses the transfer of stresses between panels.

5.6.6 Strain Progression and Maximum Strain Levels

At the 1x AASHTO service load level of 98 kN (22 kip) per actuator, all strains in the test specimen were less than 100 microstrains, with the exception of the FRP panel side transverse gages on the top and bottom side of the center FRP panel, directly below the actuator, which displayed values of 106 microstrains and 110 microstrains respectively. The strain profiles of nearly all strain gages within the specimen exhibited linear increases under increasing load up until the 489 kN (110 kip) load level. The specimen is unloaded then reloaded at this load level and the strain values before and after the unloading exhibit minor strain discontinuities throughout the specimen. While this was the load level at which initial damage to the concrete composite interface was observed on the first specimen, a thorough examination of the data indicated that full composite action between the FRP panels and the concrete was maintained for the current specimen at this load level and

throughout the entire static loading phase. Details regarding detection of separation between the FRP panel and the concrete are described in Section 5.6.8.

Prior to unloading the test specimen at the 489 kN (110 kip) load level, which is equivalent to approximately five times the AASHTO service load, the highest strain value of 1549 microstrains was recorded from the FRP side longitudinal strain gage on top of the center panel, directly below the FRP side actuator. The strains in the FRP side transverse strain gage, directly below the FRP side actuator, on the top and bottom of the center panel, were 864 microstrains and 924 microstrains respectively. The highest strain values observed on the RC side deck at this load level were located adjacent to the RC side actuator in the bottom layer of transverse and longitudinal rebar read values of 812 microstrains and 805 microstrains respectively.

At the maximum applied load of 578 kN (130 kip), equivalent to nearly six times the AASHTO service load, the maximum strain in the deck slab was 2104 microstrains for the FRP side longitudinal strain gage on top of the center panel, directly below the FRP side actuator. The highest strain observed for the RC side was 1145 microstrains for the bottom transverse RC side strain gage at midspan located 203 mm (8 in) longitudinally away from the centerline of the RC side actuator. The strains for the bottom transverse RC side and composite side center gages at this load level were 559 microstrains and 1054 microstrains respectively whereas the bottom longitudinal strains on the RC side and composite side were 950 microstrains and 546 microstrains respectively. The strains measured in the vertical stem rebar ranged from -243 microstrains to 262 microstrains, with the largest strain values measured in gages located closer to the actuators and at the tops of the stem rebar.

5.6.7 Residual Deflections and Strains

The presence of residual deflections and residual strains observed in the test specimen deck slab throughout the loading protocol are an indication of damage which has occurred. Throughout the loading steps, the residual deflection accumulated for each load level at the midspan of each slab was determined and the results are displayed in Table 5.8. Note that the reinforced concrete side exhibited slightly higher residual deflection values for each load level as compared the composite side values. The total residual deflection accumulated with loading up to the 578 kN (130 kip) load level was 1.15 mm (0.045 in) for the composite side as compared to 1.45 mm (0.057 in) for the reinforced concrete side.

Table 5.8 Residual deflections of deck slabs (from central linear potentiometers)

LOAD LEVEL		COMPOSITE SIDE				RC SIDE			
		Individual residual deflections for the given load level		Accumulated residual deflections up to the given load level		Individual residual deflections for the given load level		Accumulated residual deflections up to the given load level	
kN	kip	mm	in	mm	in	mm	in	mm	in
169	38	0.04	0.002	0.04	0.002	0.04	0.002	0.04	0.002
254	57	0.10	0.004	0.14	0.006	0.13	0.005	0.18	0.007
400	90	0.37	0.014	0.51	0.020	0.45	0.018	0.63	0.025
578	130	0.64	0.025	**1.15**	**0.045**	0.82	0.032	**1.45**	**0.057**
TOTAL RESIDUAL DEFLECTIONS		**1.15**	**0.045**	---	---	**1.45**	**0.057**	---	---

5.6.8 Separation between FRP Panels and Concrete

During the static loading of the test specimen, examination of specific strain and deflection data was used in order to detect the presence of a separation between the FRP panels and the concrete. A select number of linear potentiometers were placed above and below the composite deck in the same location such that their deflections could be compared. The difference in deflection values obtained from pairs of these linear potentiometers was used to obtain information regarding the level of separation that had occurred. A differential between the top and bottom pot readings indicates that the concrete and composite are no longer acting together as a connected unit and are now deflecting independent of each other.

The load versus deflection envelope plots from a pair of linear potentiometers located on the FRP panel side deck along the transverse centerline of the test specimen on the side of the actuator closest to the central stem are shown in Figure 5.42. Throughout the static loading phase, the largest difference between the deflections measured from the top and bottom side of the FRP panel side deck was 0.09 mm (0.004 in). This difference in deflection values was 44% below the threshold value established in Section 3.8.8 for measuring a separation between the FRP panel and the concrete.

The values from strain gauges which were attached to the composite panel, the bottom rebar which protrudes onto the composite panel in order to satisfy the development length required by code, and the top rebar layer which is continuous throughout the specimen were also examined as a means of detection of the separation between the concrete and the FRP panels.

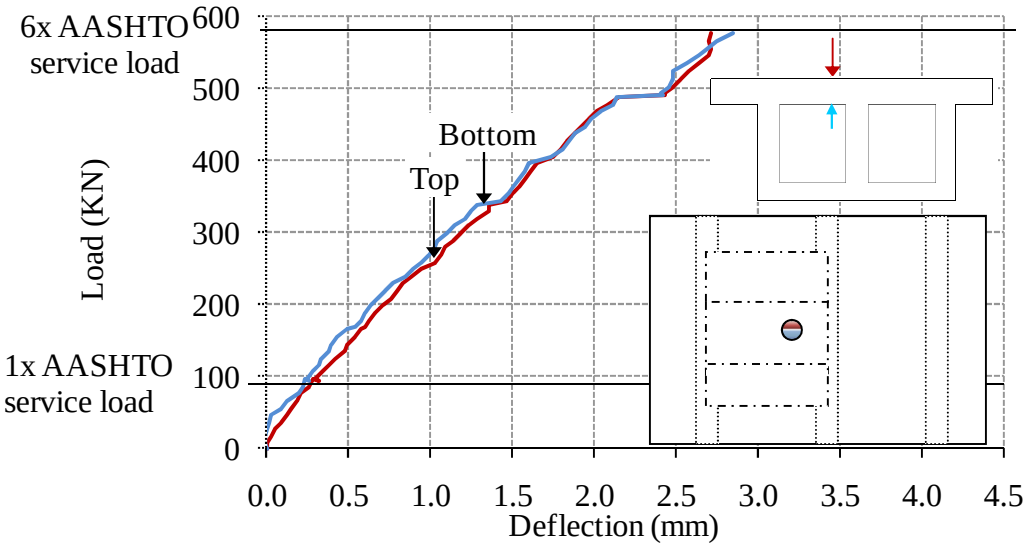

Figure 5.42 Load versus deflection plots for linear potentiometers on top and bottom of deck- located along test specimen centerline and 610 mm away from the composite side centerline, 178 mm from the composite side edge of the center stem

The vertical difference between the strain gauge on the bottom of the FRP plate and the strain gauge on the bottom rebar is approximately 50mm and so similar strain values are expected, with the strain gage on the bottom of the FRP plate reading slightly higher strains than the strain gage on the bottom rebar. Note that regions observed are outside the point of contraflexure for the FRP panel side deck slab in the transverse direction, therefore compressive strains are expected for the gages attached to the FRP panel, whereas tensile strains are expected for the gages attached to the top transverse rebar. The lack of significant discontinuities within the strain profiles shown in Figure 5.43 and Figure 5.44 indicate that the system maintains strain compatibility throughout the section depth. The smooth load verses strain profiles with the top rebar in tension, the FRP panel in compression and the bottom rebar with

negligible strain values also indicate that the neutral axis for the deck slab is located adjacent to the bottom rebar.

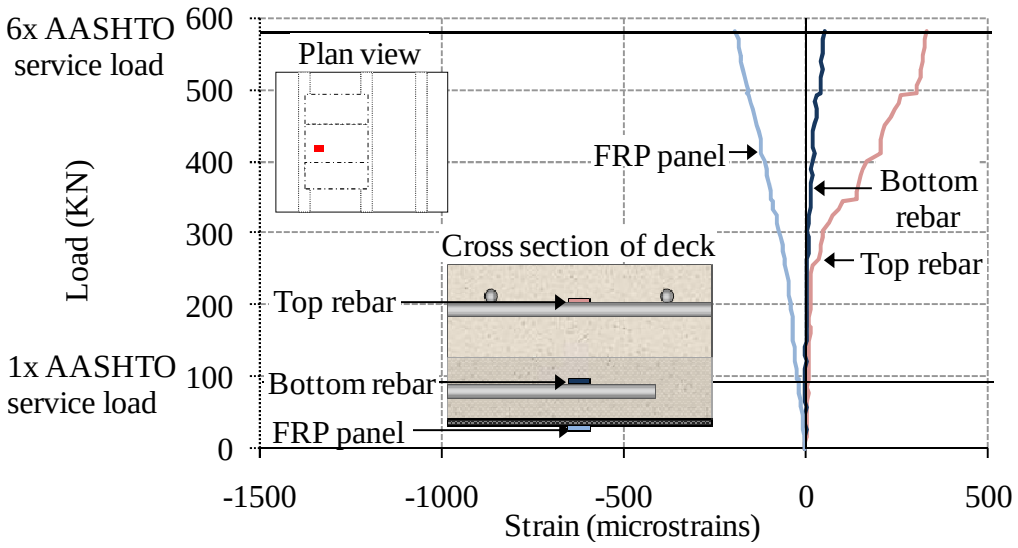

Figure 5.43 Load versus strain comparison of three transverse gages along test specimen centerline at the same location and at different depths within the deck (located 610 mm (2 ft) away from the FRP side actuator towards the outer stem)

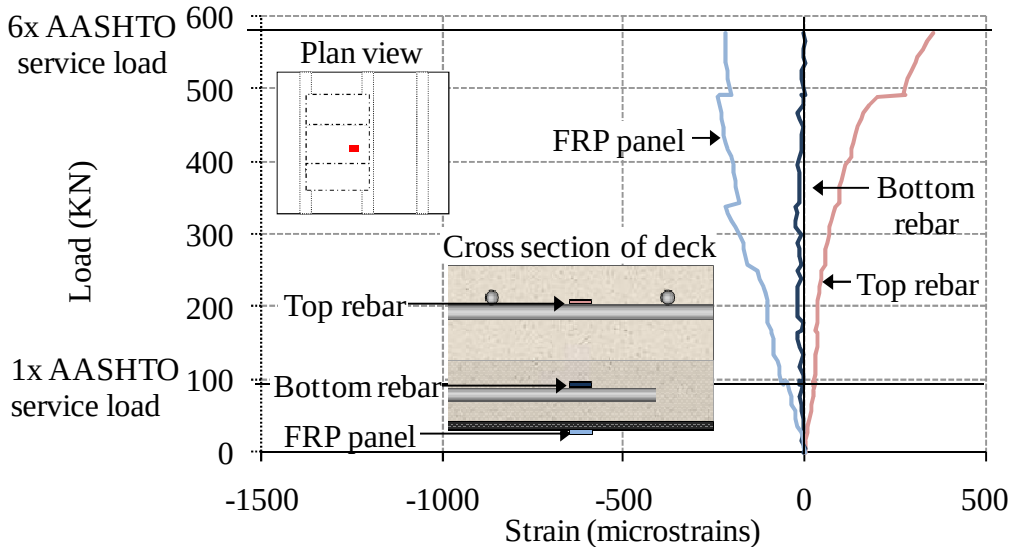

Figure 5.44 Load versus strain comparison of three transverse gages along test specimen centerline at the same location and at different depths within the deck (located 610 mm (2 ft) away from the FRP side actuator towards the central stem)

Based on the two detection methods described above, the bond between the FRP panels and the concrete was determined to remain fully intact throughout the static loading phase.

5.7 CYCLIC LOADING OF TEST SPECIMEN

5.7.1 Loading Protocol

After the static loading phase was completed, cyclic loading was performed at increasing load levels up to 5x service load for a cumulative total of 32,000 cycles. During each cycle, the test specimen was loaded to the designated load level, then unloaded to a nominal zero load of 4 kN (0.9 kip). The purpose of the cyclic loading phases was to examine the extent to which the bridge deck system exhibited a stable structural response under repeated overloads. The different loading levels applied per actuator for the cyclic phases are multiples of the AASHTO HS20 wheel load of 73 kN (16.4 kip) with an additional fatigue factor of 15% per wheel for the fatigue limit state [91]. The loading protocol used is shown in Table 5.9 with a graphical representation of the loading sequence shown in Figure 5.45.

In addition to the loading described in Table 5.9, a single static load-unload cycle up to a load of 168 kN (37.8 kip) was performed at the start of each 5,000 cycles such that the test specimen could be checked for cracks in the loaded and unloaded state. At each load level in which a single cycle was performed, the target load was held briefly to allow inspection of the test specimen in the loaded state prior to unloading the specimen.

Table 5.9 Cyclic loading protocol for test specimen #2

PHASE AND CORRESPONDING LOADING LEVEL PER ACTUATOR	LOAD LEVEL PER ACTUATOR		NUMBER OF CYCLES	CUMULATIVE NUMBER OF CYCLES
	(kN)	(kip)		
Phase I: Static loading (single cycles up to 568kN)	568	130	4	4
Phase II: Cyclic at 2P	168	37.8	10,000	10,000
Phase III: Cyclic at 2.5P	210	47.4	7,000	17,000
Phase IV: Cyclic at 3P	252	56.7	5,000	22,000
Phase V: Cyclic at 5P	420	94.8	10,000	32,000
Note: P = 1.15 x AASHTO unfactored service load, where AASHTO unfactored service load is 73kN (16.4 kip)				

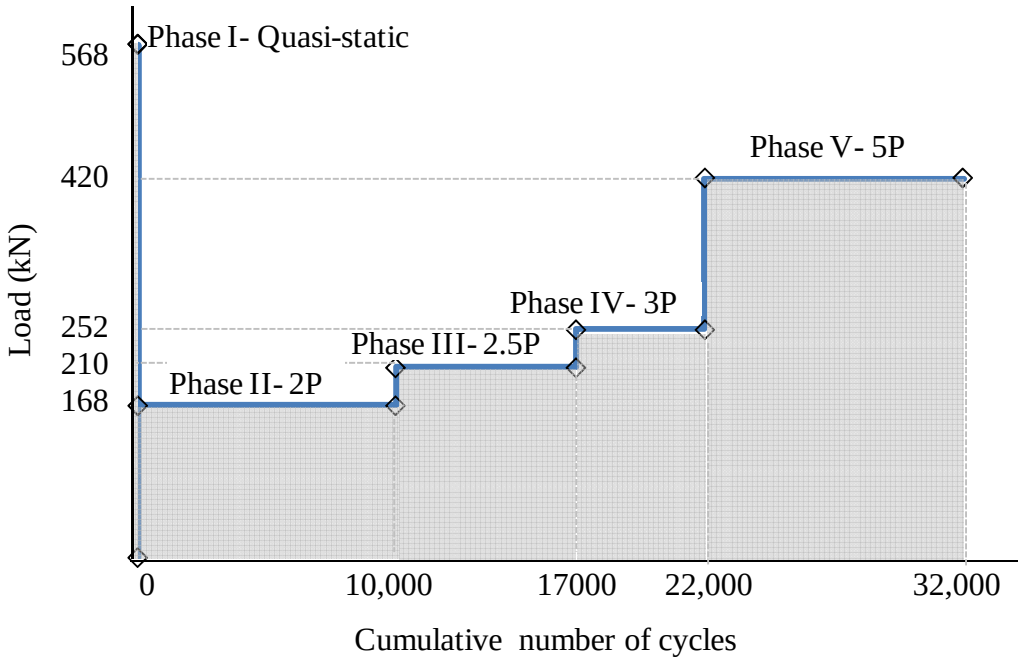

Figure 5.45 Loading phases for test specimen #2

5.7.2 Crack Patterns

Prior to the start of the cyclic loading, the test specimen was carefully inspected and any cracks from concrete shrinkage and from the static loading phase of testing were marked on the specimen. The discontinuous hairline cracks observed on the top surface of the deck prior to the cyclic loading phase had crack widths less than 0.1 mm (0.004 in) and ran primarily in the longitudinal direction near the center stem.

At the end of 10,000 cycles at 168 kN (37.8 kip), which is twice the AASHTO service load, approximately ten 51 mm (2 in) long cracks located above the center stem, running in the longitudinal direction, were observed to have crack widths of approximately 0.4 mm (0.016 in). The remainder of cracks within the specimen varied in width from 0.1 mm (0.004 in) to 0.3 mm (0.012 in) and length from 51 mm (2 in) to 127 mm (5 in). Throughout the remainder of the cyclic phases, only minor discontinuous crack progression was observed, with the largest crack at the end of all cyclic phases only 0.7 mm (0.028 in) wide.

5.7.3 Progression of Center Deflections

Center deflections were chosen as the primary indicator by which to compare the two deck slabs in terms of structural response and progression of damage. Since the stability of the system during the cyclic loading was the focus of this loading phase, changes in deflection and strain values over the course of the cyclic loading rather than their absolute magnitudes are of primary concern. The plots of load versus center deflections during the course of the cyclic loading phases are shown for the

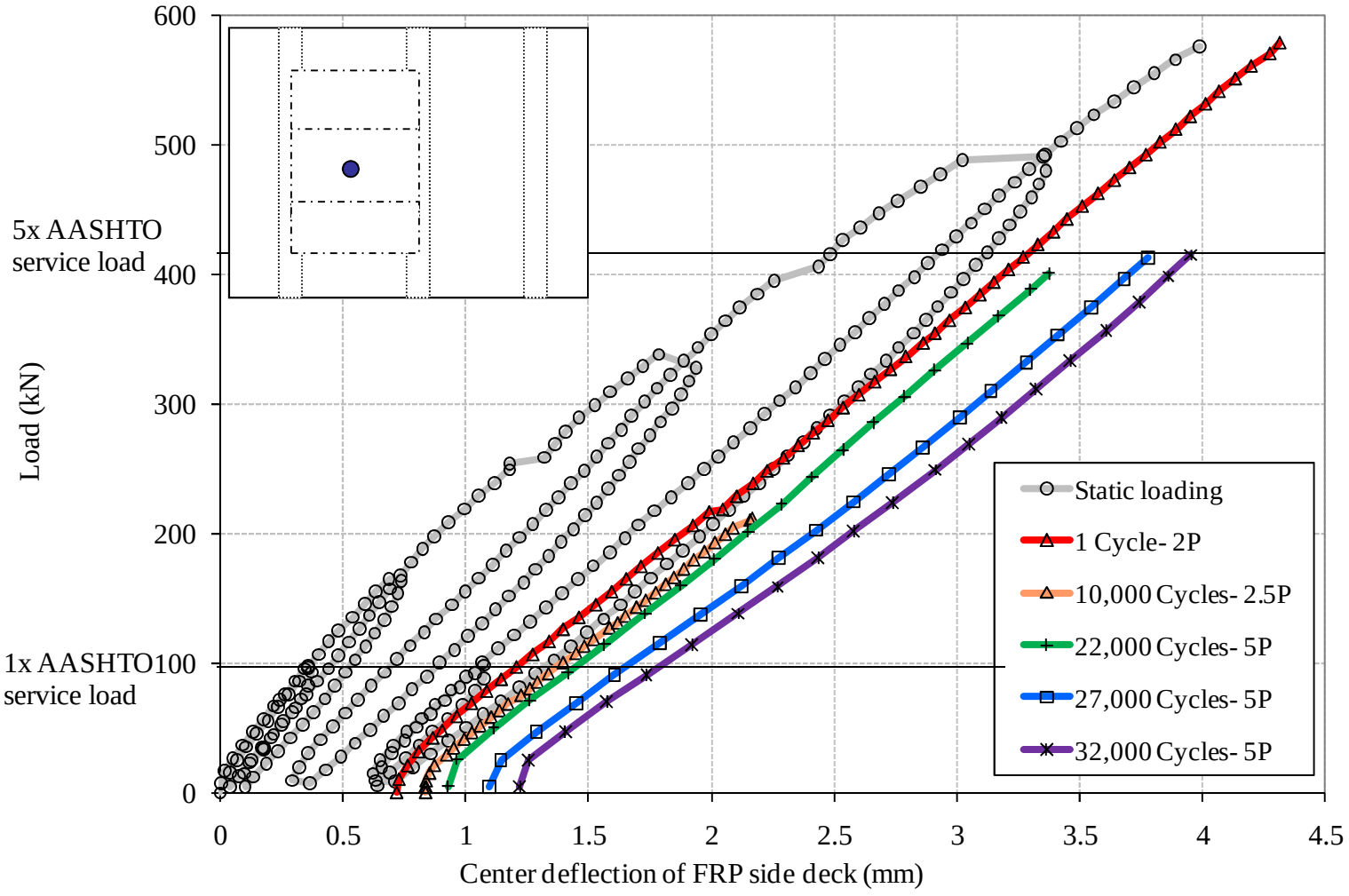

Figure 5.46 FRP side center deflections throughout cyclic loading phases

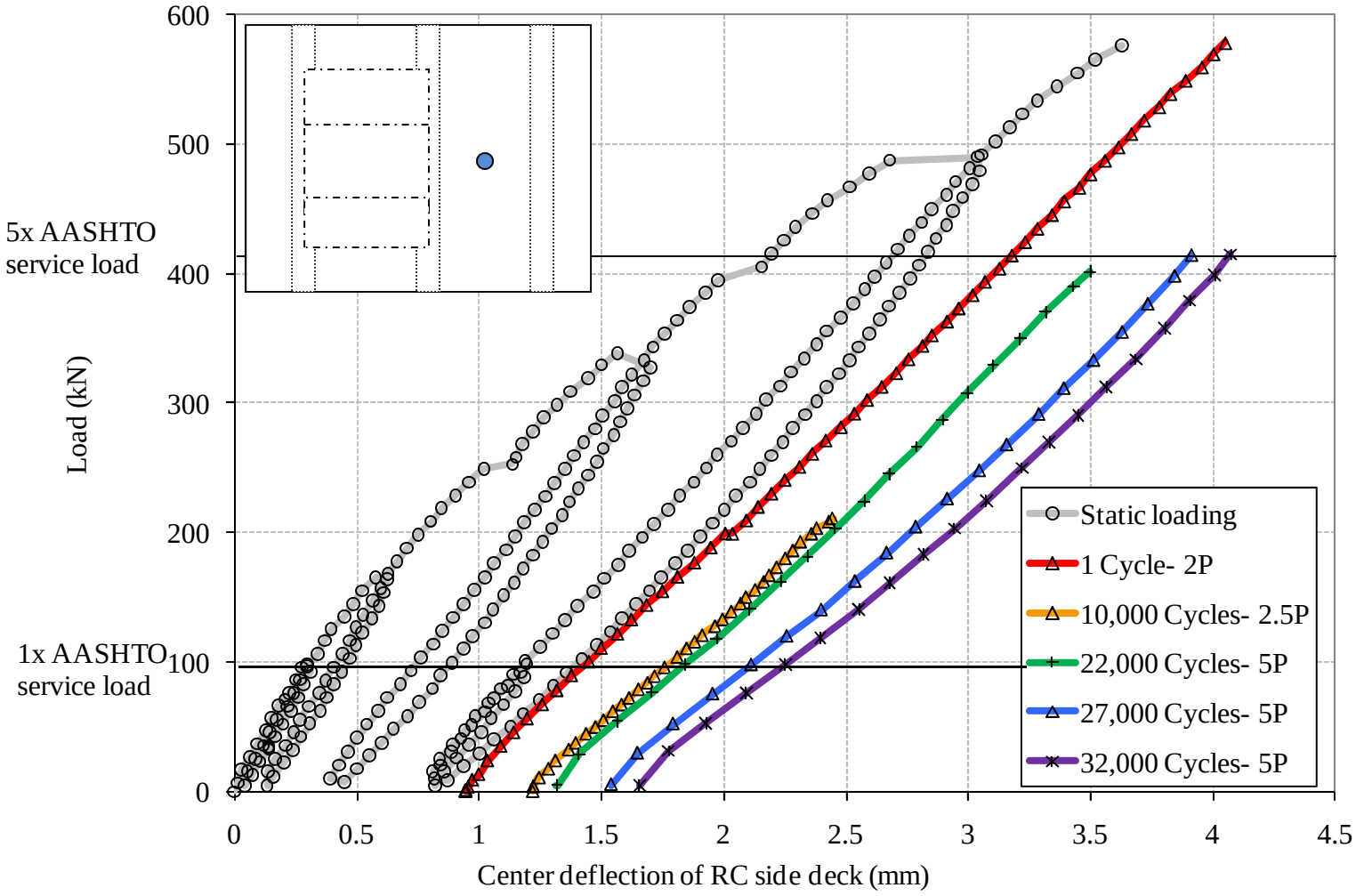

Figure 5.47 FRP panel side center deflections throughout cyclic loading phases

FRP panel side and RC side in Figure 5.47 and Table 5.10 respectively. As observed in both figures, the slopes of the load deflection curves remain relatively constant throughout the loading phases, whereas the residual deflections gradually increase for both sides.

Changes in the slope of the load-deflection response as measured using effective stiffness ratios are shown in Table 5.10 and illustrated in Figure 5.48. The effective stiffness ratio, which is defined and discussed in detail in Section 3.8.3 calculates an adaptive secant stiffness using the center deflection for each slab and normalizes this value using the adaptive secant stiffness calculated at a baseline load. Use of effective stiffness ratio values rather than center deflection values provides a more reliable metric for performance comparisons of the two decks.

Table 5.10 Effective stiffness ratios of the two slabs throughout cyclic loading

PHASE	CYCLE #	CUMULATIVE NUMBER OF CYCLES	EFFECTIVE STIFFNESS RATIO	
			FRP SIDE	RC SIDE
Phase II: Cyclic at 2P	1	1	1.00	1.00
Phase II: Cyclic at 2P	5,000	5,000	0.98	0.99
Phase II: Cyclic at 2P	10,000	10,000	0.99	0.89
Phase III: Cyclic at 2.5P	1	10,001	1.00	0.93
Phase III: Cyclic at 2.5P	5,000	15,000	0.95	0.90
Phase III: Cyclic at 2.5P	7,000	17,000	0.97	0.89
Phase IV: Cyclic at 3P	1	17,001	0.98	0.89
Phase IV: Cyclic at 3P	2,500	19,500	1.00	0.90
Phase IV: Cyclic at 3P	5,000	22,000	1.00	0.88
Phase V: Cyclic at 5P	1	22,001	1.00	0.89
Phase V: Cyclic at 5P	5,000	27,000	0.94	0.83
Phase V: Cyclic at 5P	10,000	32,000	0.87	0.79

During the first 22,000 cycles in which the test specimen was loaded up to 252 kN (56.7 kip) per actuator, equivalent to 3 times the AASHTO fatigue service load, Table 5.10 shows the FRP panel side exhibited negligible degradation in stiffness whereas the RC side decreased in stiffness by approximately 10%. The decrease in stiffness for the RC side occurred primarily during the first cyclic loading phase of 10,000 cycles at twice the AASHTO fatigue service load, with a minimal change in stiffness during the next 12,000 cycles. Throughout the course of the final cyclic phase in which the test specimen was loaded up 420 kN (94.8 kip), equivalent to 5 times the AASHTO fatigue service load, the FRP panel side decreased in stiffness by 13% whereas the RC side decreased by 11%. After all cyclic loading phases were completed, the final effective stiffness ratio for the FRP panel side was 0.87, which was 10% higher than the final RC side effective stiffness ratio value of 0.79.

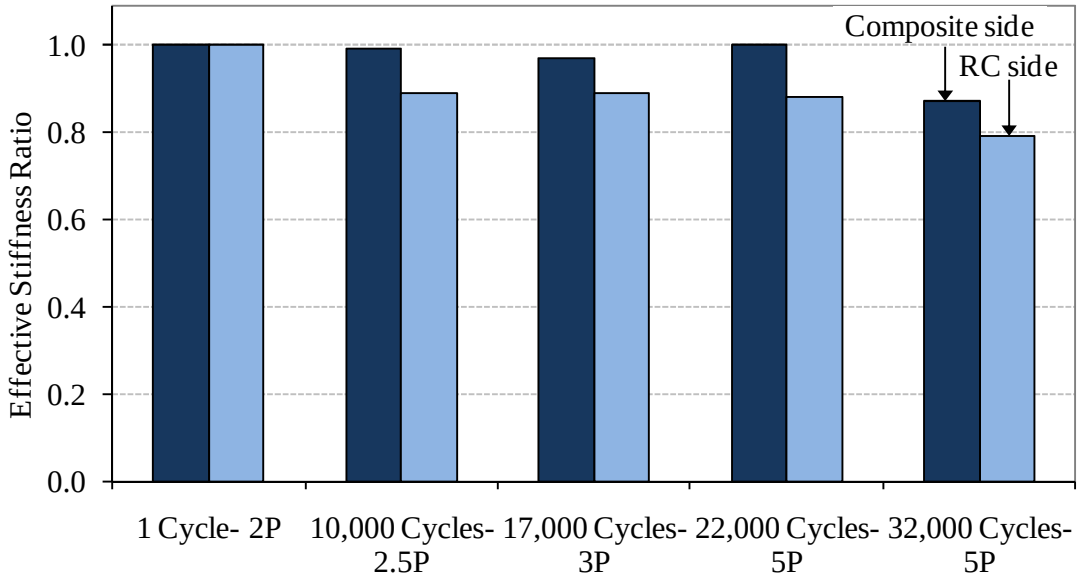

Figure 5.48 Effective stiffness ratios of the two slabs throughout cyclic loading

Figure 5.48 illustrates the trend of the effective stiffness ratios for the two slabs in which the FRP panel side maintains higher effective stiffness ratios throughout the course of the cyclic loading phases.

The center deflections of the two slabs under 1x AASHTO fatigue service load, or 84 kN (18.9 kip), are shown in Figure 5.49. While both deck slabs meet the AASHTO defined serviceability limitation for the deflection-to-span ratio of a deck under service loads, defined as L/800 2.29 mm (0.090 in) [91], the reinforced concrete side deck deflected over 20% greater than the FRP panel side deck.

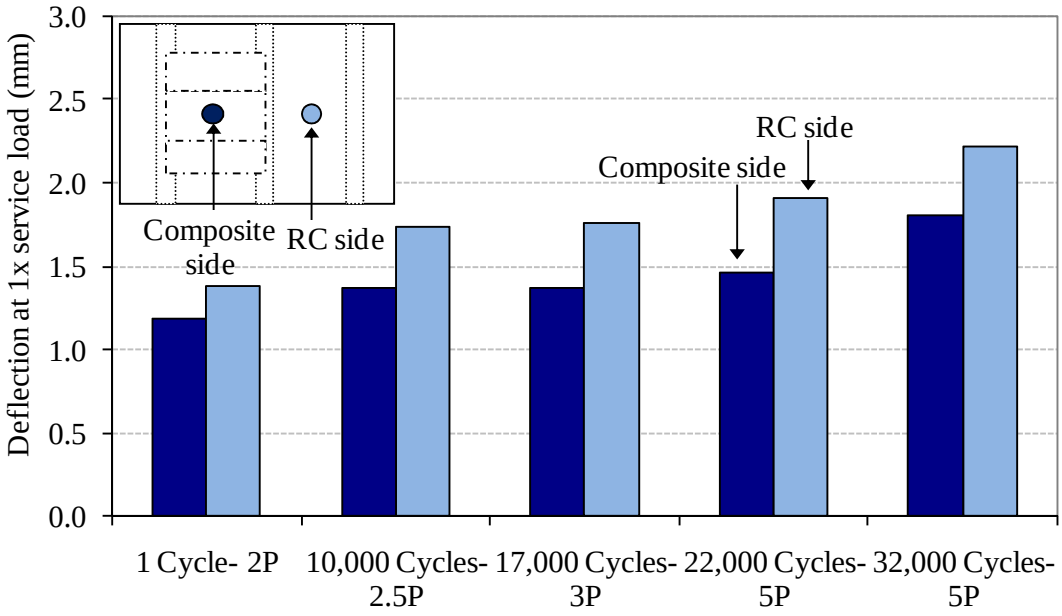

Figure 5.49 Center deflections at 1x service load throughout cyclic loading

At the start of the cyclic loading phases, the FRP panel side deflects 1.38 mm (0.054 in) as compared to 1.18 mm (0.047 in) for the FRP panel side. By the end of the cyclic loading phases, the difference between the RC side and the FRP panel side

deflections increased from 0.20 mm (0.054 in) to 0.41 mm (0.087 in), with deflections of 2.22 mm (0.87 in) for the RC side versus 1.80 (0.071 in) for the FRP panel side.

Differences in the residual deformations between the two systems are also significant because residual deflections accounted for 30% to 40% of the observed service load deflections. For the current experiment, residual deflection is defined as the center deflection of the slabs measured while the test specimen was unloaded to the nominal zero load of 4 kN (0.9 kip). The progressions of residual deflections for both decks throughout the static and cyclic loading phases are shown in Figure 5.50.

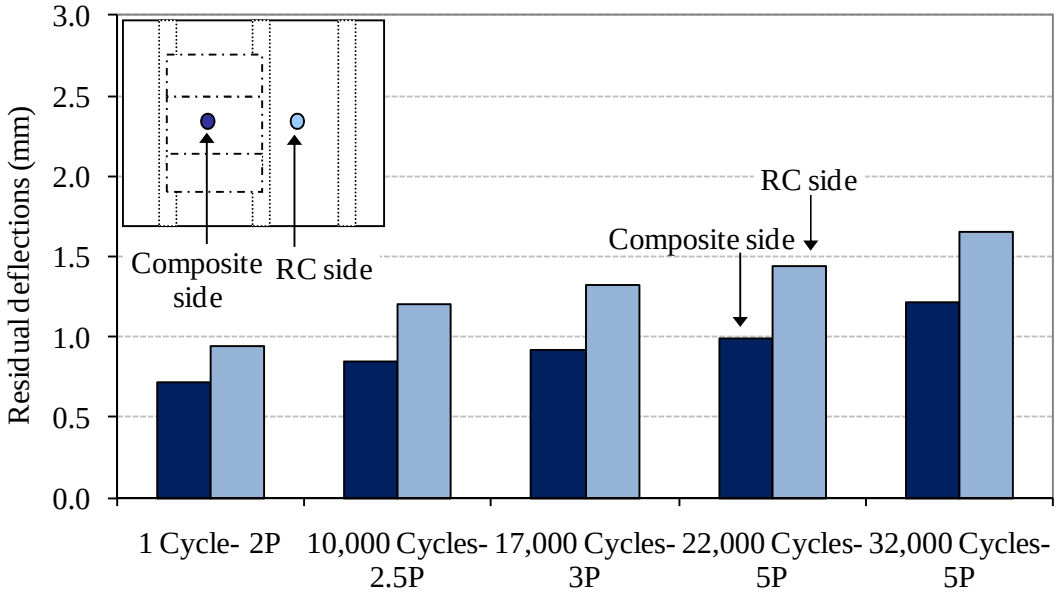

Figure 5.50 Residual deflection comparisons throughout cyclic loading

At the start of cyclic loading, the reinforced concrete side exhibited 32% larger residual deflections than the FRP panel side, 0.95 mm (0.037 in) versus 0.72 mm (0.028 in) for the RC side and FRP panel side respectively. This disparity in residual

deflections increased to 45% after 17,000 cycles. At the end of the cyclic loading phases, the RC side exhibited a residual deflection of 1.66 mm (0.065 in) as compared to 1.21 mm (0.048 in). The higher residual deflections for the reinforced concrete side provide an explanation for the larger overall deflections observed on the reinforced concrete side at peak loads as compared to the composite side, even though the reinforced concrete side exhibits a slightly higher stiffness.

5.7.4 Deflection Profiles

The deflection distributions for the deck slab throughout the cyclic loading phases are shown in Figure 5.51 - Figure 5.52. These figures are shown with an applied load of twice the AASHTO fatigue service load and contain compiled data from each of the different important loading phases. As observed in Figure 5.51, the center deflection for the composite side at 2x service load is initially greater than the deflection for the reinforced concrete side. However, over the course of the cyclic loading phases the midspan deflection of the reinforced concrete side increases beyond the FRP panel side deflection.

Unlike the response during the static phase, the load distribution along the transverse direction during the cyclic loading phases is more localized for the reinforced concrete side as compared to the FRP panel side. Throughout the cyclic phases, the composite side maintains the same dispersed deflection profile as observed in Figure 5.28 when low level static loads were applied. It should be noted that the composite side only exhibited the more localized deformation during the static loading levels greater than 4x factored service load.

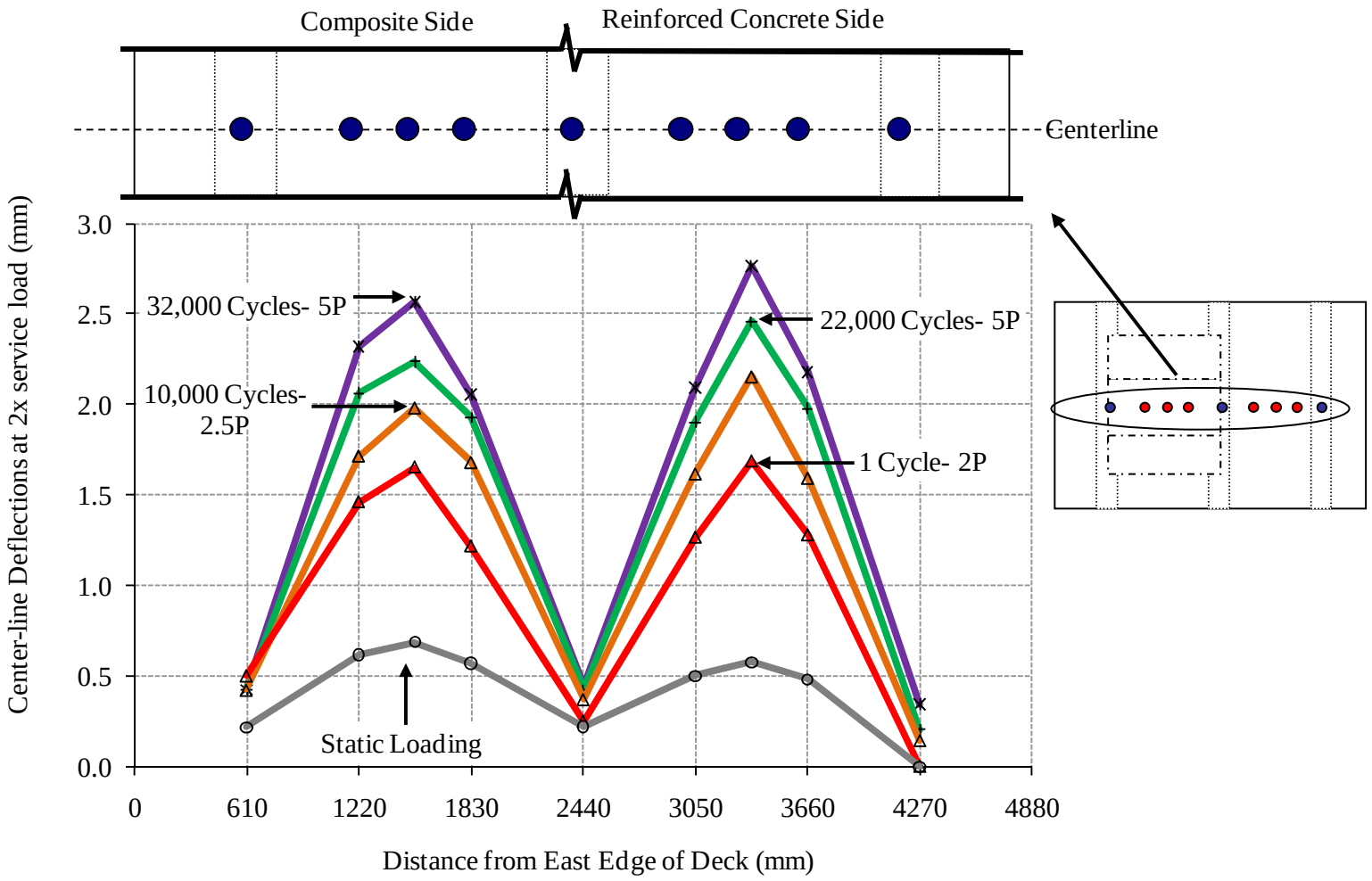

Figure 5.51 Deflection response at 2x service load along centerline during cyclic loading

However, the reinforced concrete side deflection response changes during the loading phases from a dispersed profile at the start of the static phase to a localized deformation at the end of the cyclic phase as seen in Figure 5.51. This difference in the deflection profiles serves as an additional indicator showing the superior structural integrity of the composite system in response to cyclic loading.

The vertical deflection response along the longitudinal direction exhibits a very similar profile for both the FRP panel side and the reinforced concrete side as shown in Figure 5.52 and Figure 5.53 respectively. Since the two sides responded with very comparable profiles, a sectional analysis was necessary to get a more quantitative side by side comparison of the change in deflection values for a given linear potentiometer. Four different sets of linear potentiometers placed at the midpoint between stems were used to compare the deflection profiles in the longitudinal direction for the composite and reinforced concrete sides. Figure 5.58 (a) shows a schematic of the linear potentiometers used for sectioned deflection comparisons, which are shown in Figure 5.58 (b)-(e). Section M is located directly below the actuator centerline and sections C, B, and A were located 610 mm (2 ft), 1220 mm (4 ft) and 1525 mm (5 ft) away from the actuator centerline respectively.

From Figure 5.55 to Figure 5.58, a similar load distribution phenomenon is observed as described for the transverse deflection profile. The more dispersed deflection profile observed for the composite side under low applied loads is maintained throughout the cyclic loading phases.

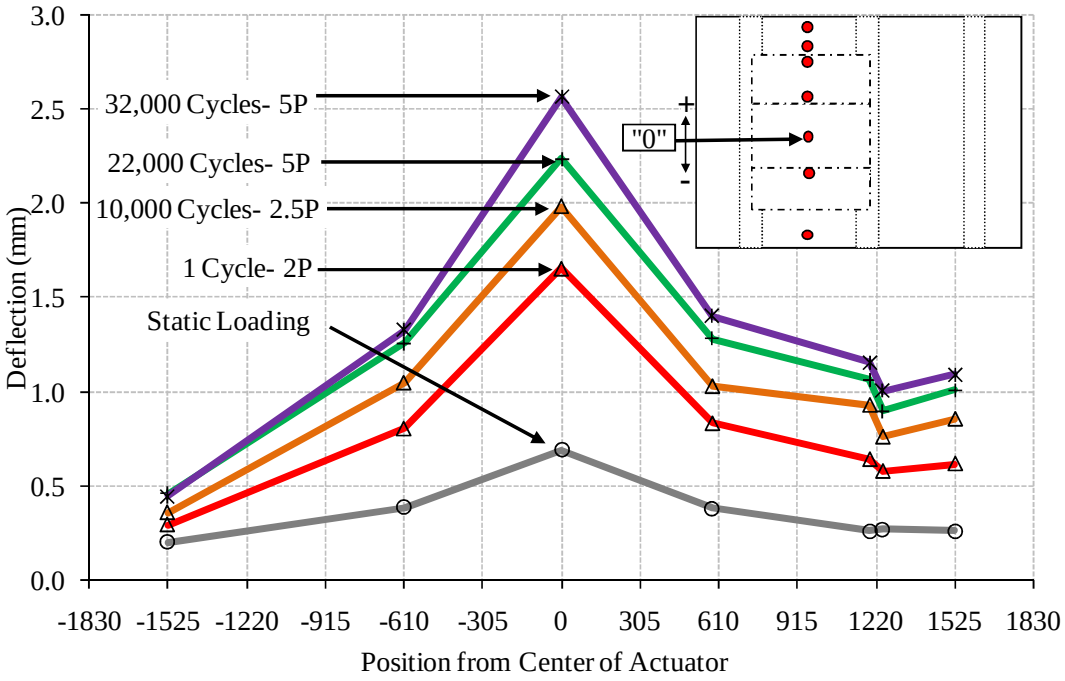

Figure 5.52 Deflection response of FRP side at 2x service load during cyclic loading

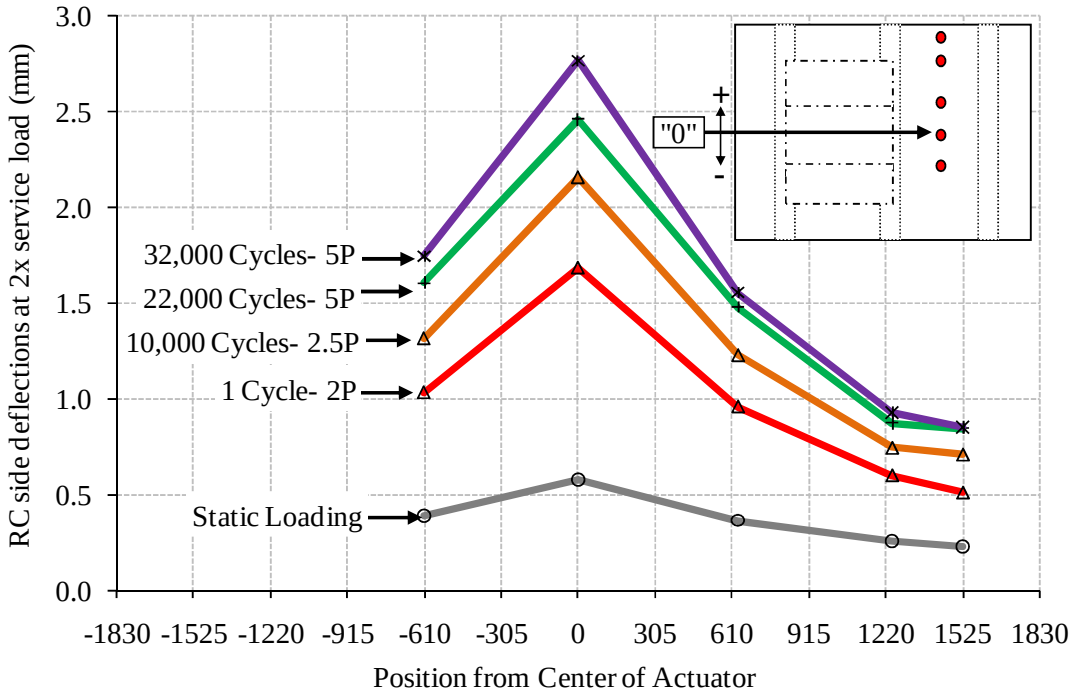

Figure 5.53 Deflection response of RC side at 2x service load during cyclic loading

The reinforced concrete side begins with a similar dispersed deflection profile but as the cyclic loading progresses, the deflections on the reinforced concrete side become more localized. This is indicative of greater, more localized damage experienced by the reinforced concrete side as compared to the FRP formwork system.

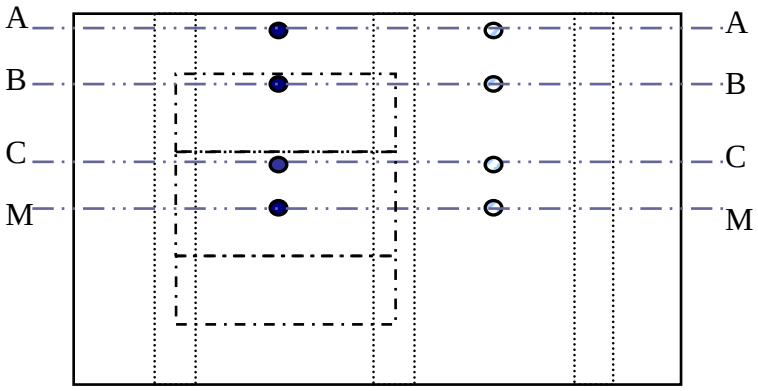

Figure 5.54 Positioning of linear potentiometers used for deflection comparisons

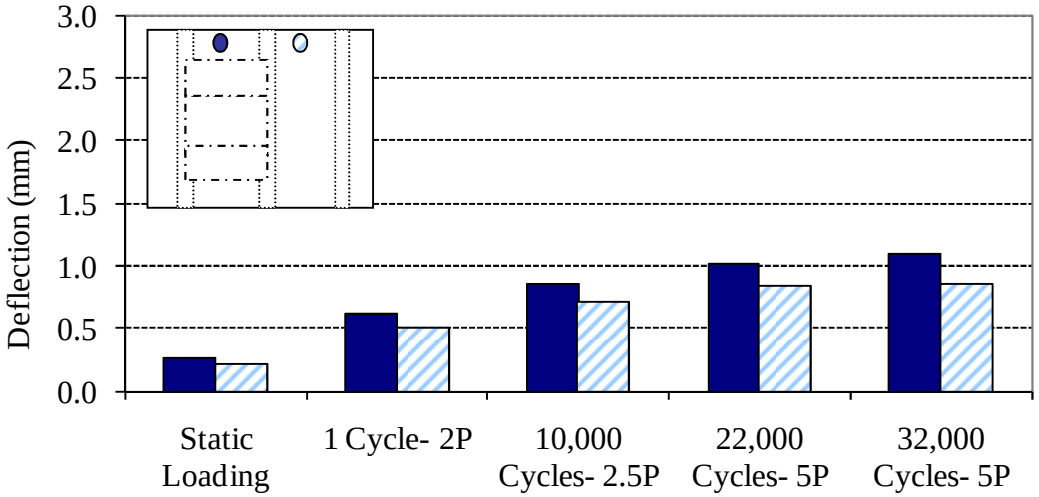

Figure 5.55 Composite side and RC side deflections at different cyclic loading stages (Section A-A: 1525 mm from actuator centerline)

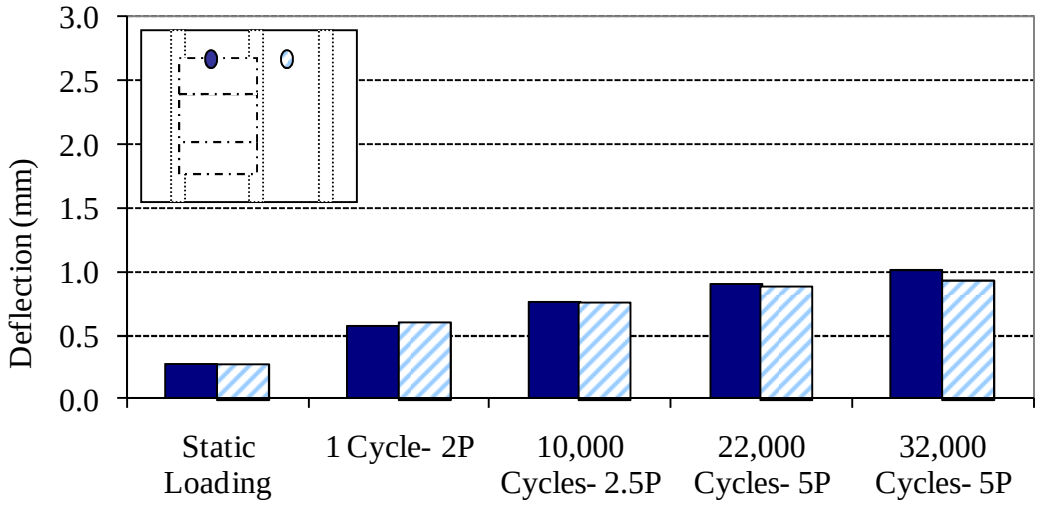

Figure 5.56 Composite side and RC side deflections at different cyclic loading stages (Section B-B: 1220 mm from actuator centerline)

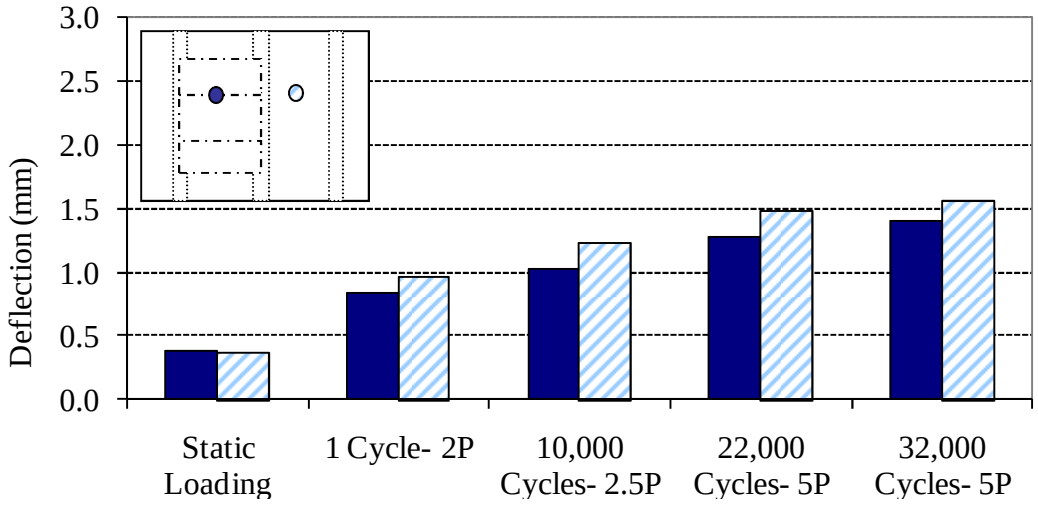

Figure 5.57 Composite side and RC side deflections at different cyclic loading stages (Section C-C: 610 mm away from actuator centerline)

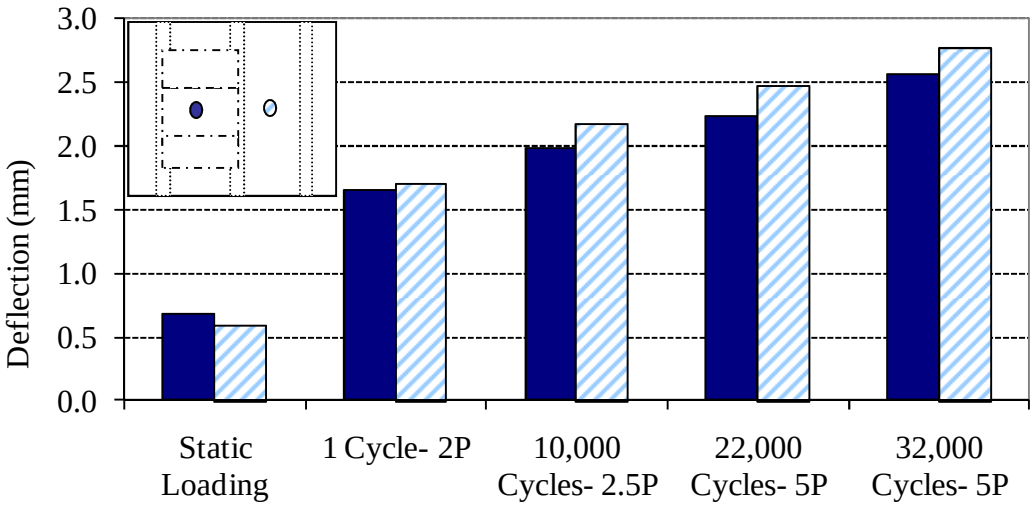

Figure 5.58 Composite side and RC side deflections at different cyclic loading stages (Section M-M: Directly below actuator actuators)

5.7.5 Summary

During the static loading phase, two deck slabs showed comparable performance with linear responses and negligible deterioration due to loading. Examination of the additional single cycle to 578 kN (130 kip) immediately prior to the start of cyclic loading also corroborated that insignificant damage had accumulated during the static loading phase. The bond between the FRP panels and the adjacent concrete remained intact such that full composite action for the slab was maintained throughout the static loading phase. The FRP panel side exhibited slightly higher center deflections, however maintained a higher effective stiffness ratio at each load level and displayed smaller residual deflections throughout the static loading. Strain profiles in the longitudinal direction indicated that the point of inflection for both deck slabs occurred approximately 610 mm (2 ft) away from the center of the actuators.

Results from the cyclic loading phases indicate that FRP panel system exhibited better structural response to sustained cyclic loading as compared to the reinforced concrete deck system. The FRP panel side deck showed smaller residual deflections, maintained higher effective stiffness ratios, and deflected 19% less than the RC side deck under 1x service loads. Overall, the FRP panel system exhibited a more stable structural response under cyclic loading.

6 USE OF NEAR SURFACE MOUNTED FRP REINFORCEMENT AS A MEANS OF RAPID BRIDGE DECK REHABILITATION

6.1 PROJECT SPECIFIC NEED FOR FRP REHABILITATION

CALTRANS is installing sound barriers along freeways to minimize the impact of freeway noise on local residents. These sound barriers are installed on the barrier rail located on the edge of the bridge deck as shown in Figure 6.1. These sound barrier walls are typically of masonry construction and their addition to bridge deck overhangs can sometimes increase the dead load of the bridge in excess of the original design loads. Currently the entire edge region of the box girder is removed and rebuilt using additional reinforcement. This process is labor intensive and can significantly impact traffic.

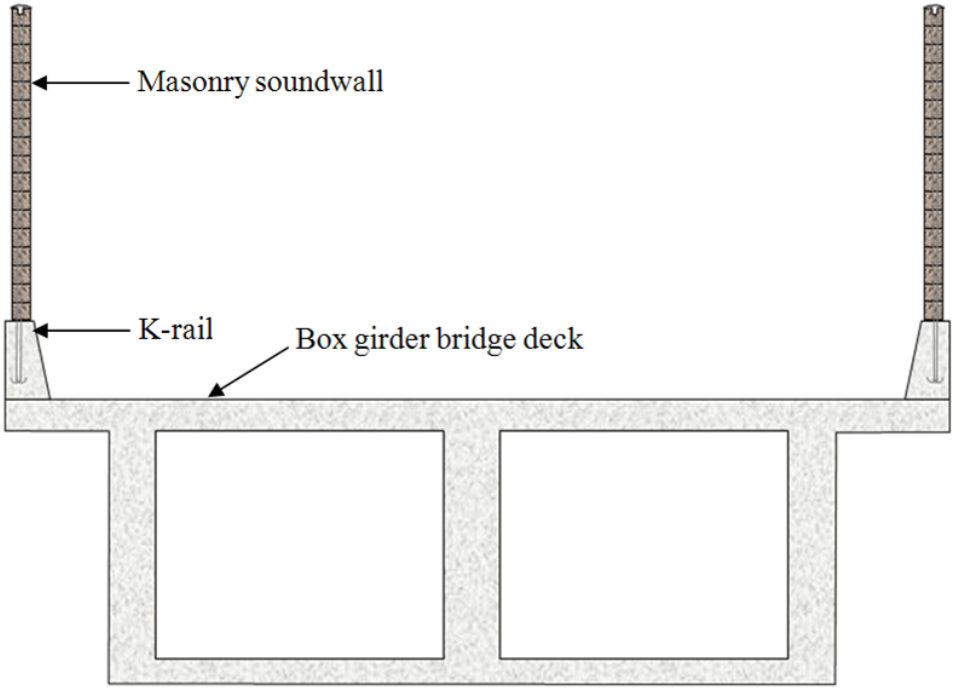

Figure 6.1 Sound wall placed onto the overhang of a box girder bridge deck

An alternative to partial replacement of the bridge deck is the rapid rehabilitation of the overhang using fiber reinforced polymers (FRPs). The use of near-surface-mounted (NSM) FRP reinforcement for rehabilitation has a number of advantages over the more common externally bonded FRP reinforcement, including the potential for reduced surface preparation, which in turn reduces the impact to traffic. This reduces the likelihood of debonding failures from the concrete surface due to significantly improved anchoring ability and improved protection from mechanical damage provided by recessing the NSM reinforcement into the concrete surface. A discussion of different types of near surface mounted composites, previous applications, and observed failure modes can be found in Section 2.4.

The goal of the current investigation is to provide preliminary validation of the use of near surface mounted composites for increasing the load carrying capacity of the overhang region for historic concrete box girder bridges. In order to achieve this goal, the following research tasks were accomplished:

1. evaluate the load carrying capacity and structural response for an as-built reinforced concrete bridge deck overhang without FRP strengthening through analytical predictions and experimental studies;
2. examine different near surface mounted rehabilitation schemes that would provide additional strength to the bridge deck overhang so that the overhang can to safely accommodate the increased dead load from the addition of the sound walls;
3. implement the selected NSM strengthening design into a 1.68 m (5ft 6in) long section of reinforced concrete bridge deck overhang and provide

analytical predictions of performance as well as a discussion of results from experimental testing;

4. compare the rehabilitated specimen's experimental results to theoretical predictions and to the experimental results from the testing of the as-built reinforced concrete specimen without FRP; and
5. provide conclusions for design and use.

6.2 SPECIMEN GEOMETRY AND CONSTRUCTION

The overall test configuration used for this experimental work consists of a reinforced concrete two-cell box girder, with a center-to-center span of 1830 mm (6 ft) between each of the girders and a length of 3660 mm (12 ft) as shown in Figure 3.1 and Figure 3.2. The specimen deck is 178 mm (7 in) thick and the distance from the stem wall to the edge of the overhang is 483 mm (19 in). Information relating to the detailing and construction of the test specimen can be found in Section 3.2.

Following construction of the test specimen, the specimen was used for a separate test series described in Chapter 4 after completion of which two 203 mm (8 in) deep cuts located 305 mm (12 in) apart from each other were created that ran longitudinally along the entire width of the specimen (Figure 6.2). It is noted that previous testing was restricted to loading applied at the central section of each cell and did not involve any load application or distress to the overhang regions. The two edge segments of the deck bounded by the longitudinal cuts were also removed as shown in Figure 6.2. The purpose of the cuts was to allow for multiple independent tests on sections of edge slab 1.68 m (5ft 6in) long.

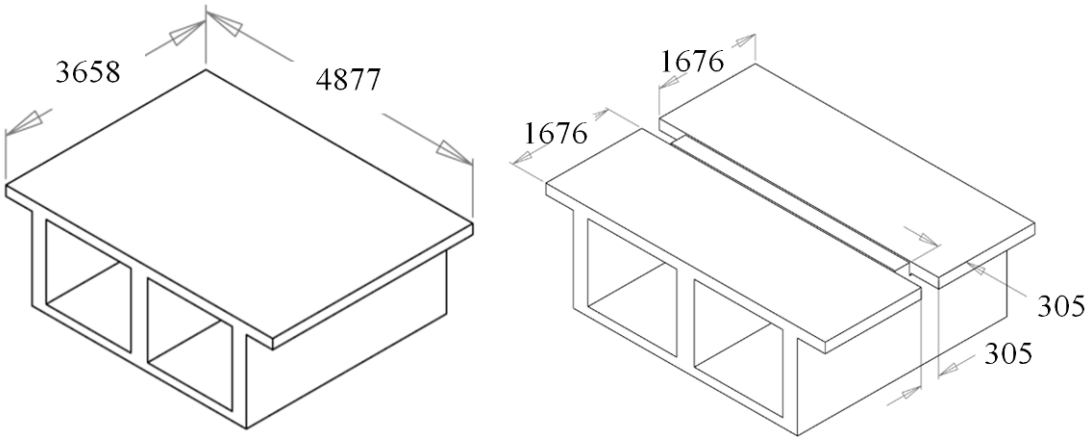

a) Original specimen b) Sectioned specimen, as tested

Figure 6.2 Overall dimensions of specimen

6.3 LOADING SETUP

Vertical loads were applied to the edge region of the deck slab using two hydraulic jacks spaced 1.83 m (6 feet) apart and mounted below the strong floor of the testing facility. The load was transferred through two 44.5 mm (1 ¾ in) diameter threaded rods to a steel loading beam positioned 76 mm (3 in) on-center back from the end of the overhang section of the deck. A 51 mm (2 in) thick and 152 mm (6 in) wide elastomeric bearing pad was placed between the steel beam and the deck slab in order to reduce stress concentrations and provide more even loading of the test specimen as shown in Figure 6.3. The overall test setup is shown in Figure 6.4.

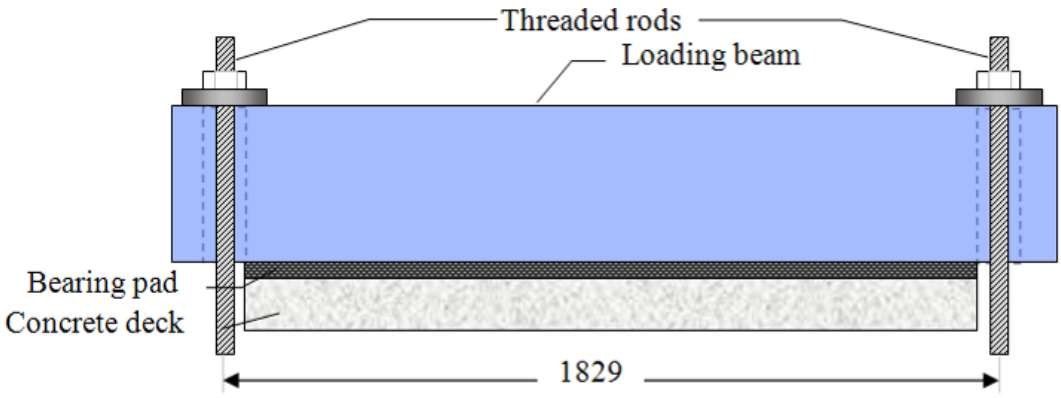

Figure 6.3 Plan view of test fixture used to load overhang

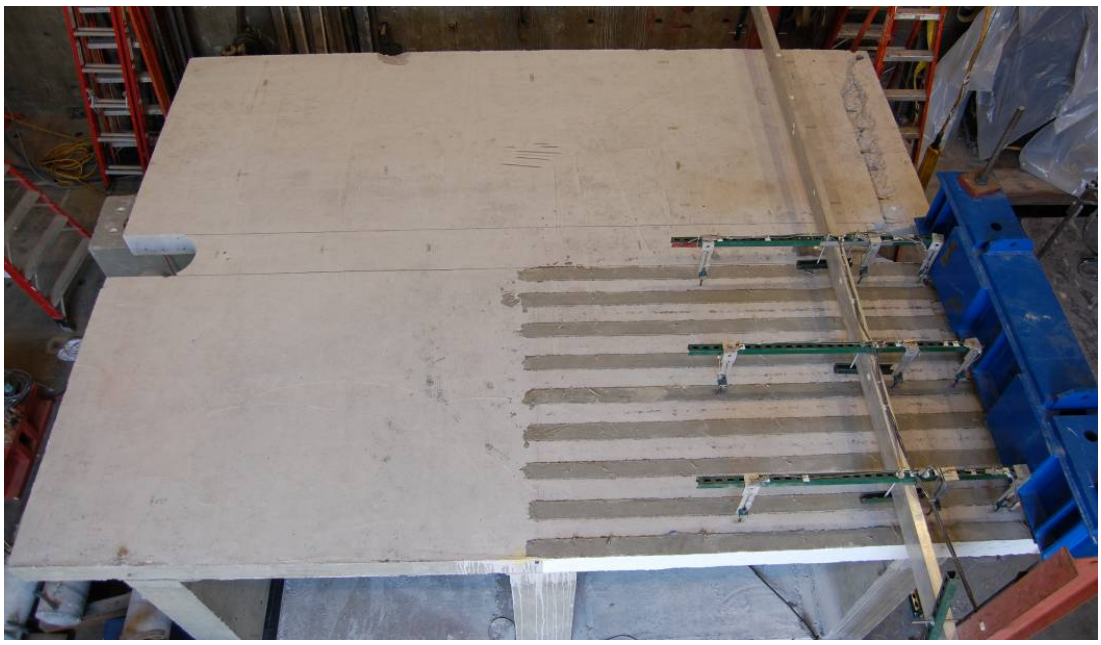

Figure 6.4 Overall test setup

6.4 AS-BUILT TEST

In order to establish a baseline for the effectiveness of the FRP repair, the test specimen used was isolated into separate sections as described in Section 6.2 and a portion of the concrete box girder specimen was tested as-built, without FRP

rehabilitation. The following section discusses the calculations, experimental setup, loading, test observations and results from the testing of this section of as-built reinforced concrete bridge deck.

6.4.1 Demand Calculations

The combined dead weight of a typical sound wall and traffic barrier used for bridges in California was calculated from the CALTRANS' concrete masonry sound wall design on bridges as shown in Figure 6.5 [159]. Using this design with normal weight grout and concrete, the gravity load per unit length for the sound wall and traffic barrier were determined to be 13.5 kN/m (0.92 kip/ft) and 8.1 kN/m (0.56 kip/ft) respectively, for a combined weight per unit length of 21.6 kN/m (1.5 kip/ft). The tested section of overhang was 1600 mm (5 ft 6 in) long therefore the total load applied to the specimen from the sound wall and traffic barrier is 36.2 kN (8.1 kip). The load was applied to the structure by two hydraulic jacks such that each jack applied half the total loading to the overhang. In equation form, this can be expressed as

$$weight_{wall\_per\_jack} = \frac{weight_{wall}}{2} \tag{6.1}$$

where

$weight_{wall}$ = The total load applied to the overhang due to the combined weight of the sound wall and the traffic barrier.

This yields a load per hydraulic jack of approximately 18 kN (4 kip) to represent the equivalent sound wall load, which is corresponds to a distributed load of 10.7 kN/m (0.74 kip/ft).

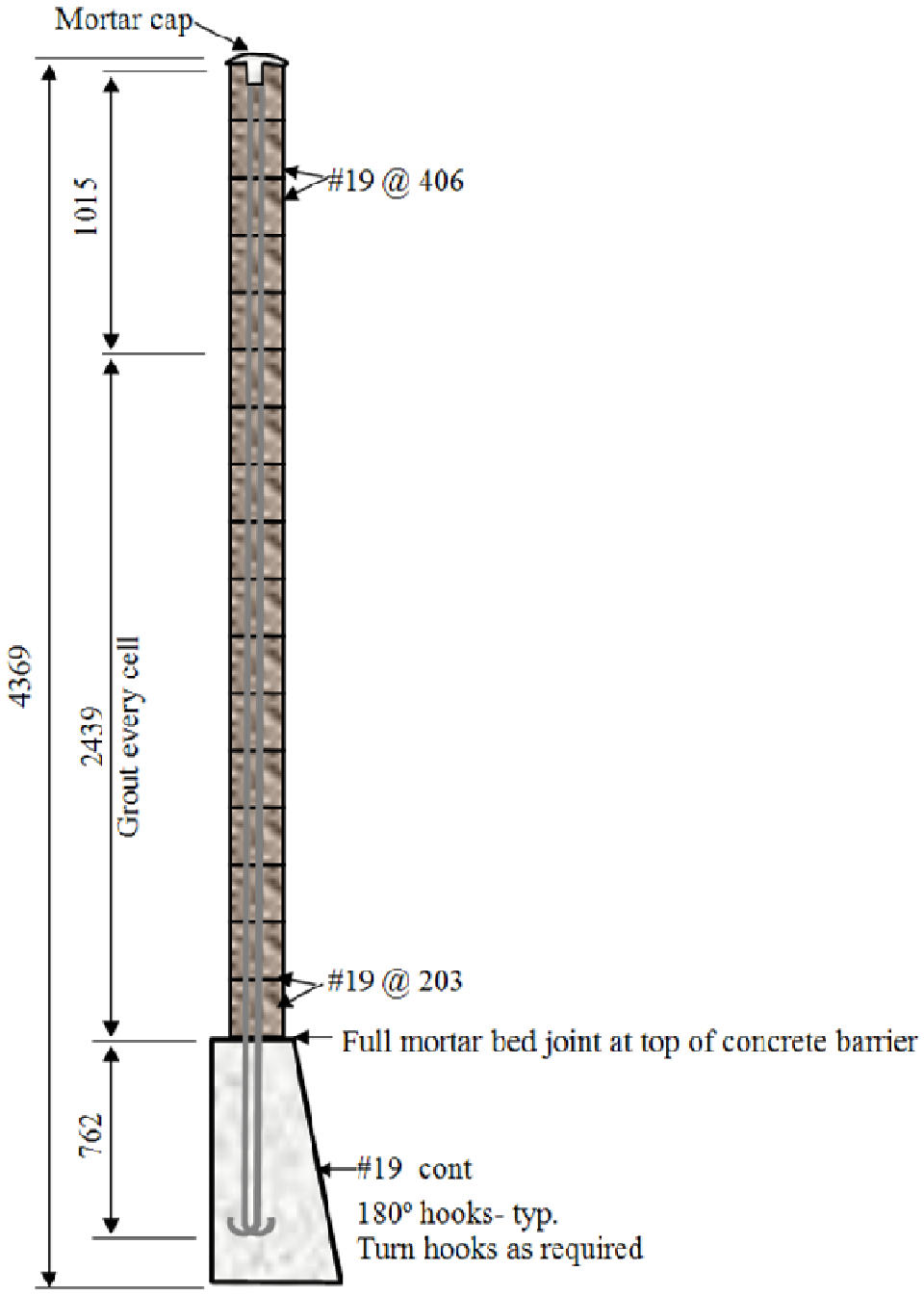

Figure 6.5 Standard CALTRANS masonry sound wall design [159]

6.4.2 Capacity Calculations

The testing method of the deck slab overhang through a loading beam across the entire slab width can be assumed to apply a uniformly distributed load across the width of the deck slab. This loading condition allowed the system to be treated as a one-way slab rather than a two way slab, thereby allowing the analysis for the problem to be simplified from a three dimensional system to two dimensional system with the properties of the deck slab cross-section assigned to the 2D structural element. In this section, the shear capacity of the deck slab overhang is calculated using code provided equations, whereas the moment capacity of for the deck slab overhang is calculated using code provided equations and a moment curvature analysis.

The shear capacity of the slab was computed according to ACI 318-08 Section 11.3 using both the general and the more detailed calculations [118]. Note that the California Bridge Design Specifications for reinforced concrete structures used by CALTRANS were patterned after and are in conformity with ACI Standard 318 [152]. The general calculation for shear capacity of the slab was given by the ACI 318-08 Equation 11-3 as

$$V_c = 2\sqrt{f_c^{'}}\, b_w d \tag{6.2}$$

where

$f_c^{'}$ = Concrete compressive strength (psi)

b_w = Width of the concrete slab (in)

d = Distance from the extreme compression fiber to the centroid of the tensile reinforcement (in)

This equation yields a total shear capacity of 236 kN (53 kip) for the slab, which translates to an applied force of 118 kN (26.5 kip) per hydraulic jack. The more detailed shear capacity equation is given by ACI 318-08 equation 11-5 as

$$V_c = \left(1.9\sqrt{f_c^{'}} + 2500\rho_w \frac{V_u d}{M_u}\right) b_w d \qquad 6.3$$

where

$f_c^{'}$ = Concrete compressive strength (psi)

ρ_w = Steel reinforcement ratio of the slab in the direction perpendicular to traffic

V_u = Factored shear in the slab at the edge of the outer vertical stem

M_u = Factored moment in the slab at the edge of the outer vertical stem

b_w = Width of the concrete slab (in)

d = Distance from the extreme compression fiber to the centroid of the tensile reinforcement (in)

Equation 6.3 yields a slightly more conservative total shear capacity of 233 kN (52.4 kip) for the slab, which translates to an applied force of 116 kN (26.2 kip) per hydraulic jack.

The moment capacity of the slab was calculated as

$$M_n = A_s f_y \left(d - \frac{a}{2}\right) \qquad 6.4$$

where

A_s = Area of steel reinforcement in the direction perpendicular to traffic flow

f_y = Yield stress of the slab steel

d = Distance from the compression fiber to the centroid of the tensile reinforcement

a = Depth of the equivalent rectangular compression stress block

Using Equation 6.4, the total moment capacity was calculated to be 97.0 kN-m (71.6 kip-ft). The equivalent force applied through the loading beam can be obtained by dividing the moment by the distance between the applied load and the edge of the stem, also known as the moment arm. The equivalent applied force per hydraulic jack was 101 kN (23 kip). Since this capacity value is the lower than the computed shear capacity, it is predicted that flexural damage will be govern the performance of the slab.

The moment capacity of the specimen was also found from the moment-curvature response obtained by a computer program used conventionally for structural analysis (RESPONSE 2000) to be 117.2 kN-m (85.6 kip-ft) [160]. This corresponds to a maximum load per hydraulic jack of 122 kN (27.5 kip). The moment curvature response of the as-built reinforced concrete deck slab is shown in Figure 6.6 below.

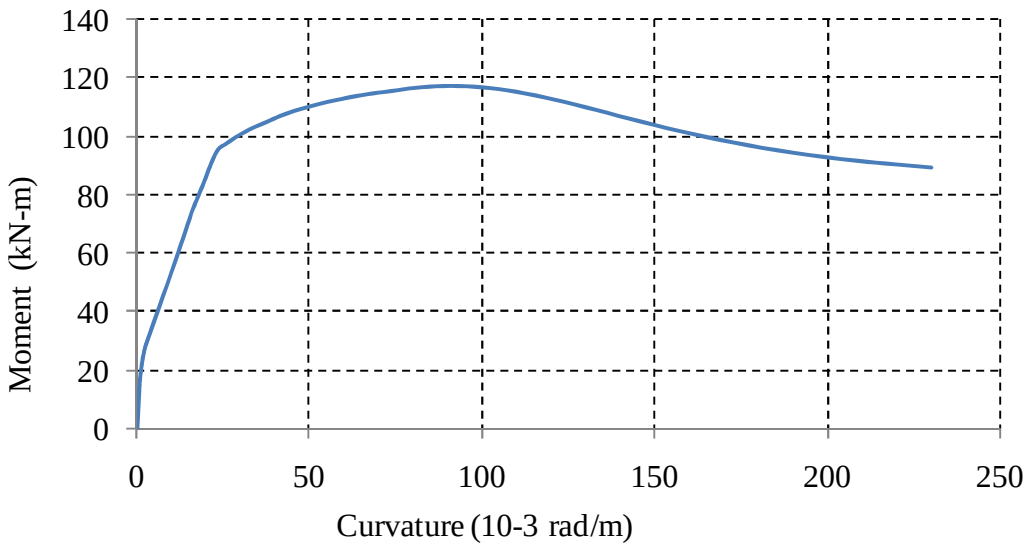

Figure 6.6 Moment-curvature response for as-built specimen

6.4.3 Analytical Predictions

The vertical deflections of the deck slab overhang were predicted using a piecewise linear structural analysis that employs varying sectional properties throughout the system. The analytical method developed for deflection predictions relies on the fundamental equation that relates the moments and the curvatures within a section:

$$\varphi = \frac{M}{E \cdot I} \tag{6.5}$$

where
φ = Curvature of a section
M = Moment applied a section
E = Young's modulus of a section
I = Moment of inertia of a section

The moment of inertia for a reinforced concrete section reduces significantly as the concrete cracks under applied loads. The adjusted moment of inertia for a section at any point along a moment-curvature profile can be obtained by rearranging Equation 6.5 as shown in Equation 6.6.

$$I = \frac{M}{E \cdot \varphi} \tag{6.6}$$

where
φ = Curvature of a section
M = Moment applied a section
E = Young's modulus of a section
I = Moment of inertia of a section

Moment-curvature data from Response 2000, which is a computer program conventionally used for structural analysis, is used in order to obtain values for M and

φ as shown in Figure 6.7. The moment of inertia values were calculated for each point along the moment-curvature profile.

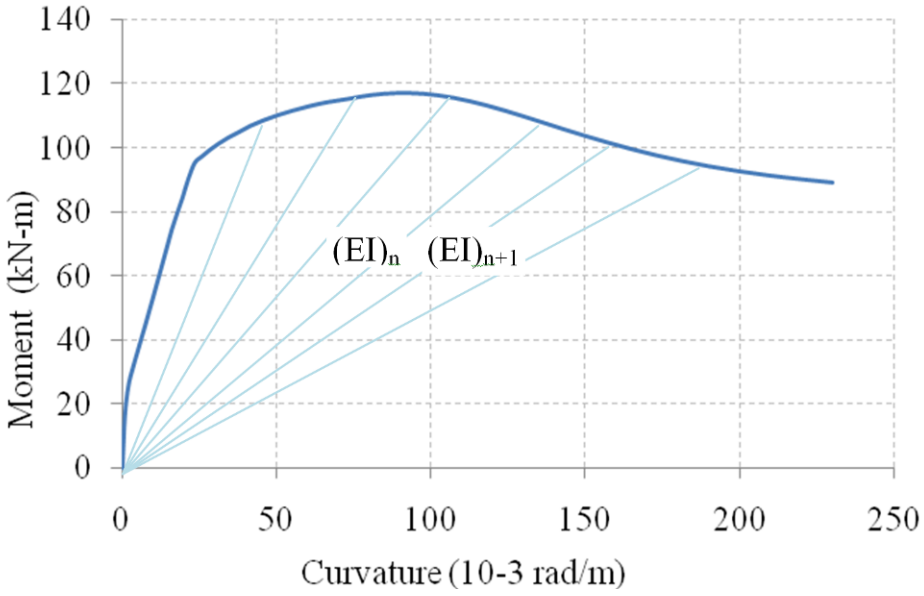

Figure 6.7 Adjustment of moment of inertia along moment curvature profile

Next, the moment profile for the deck slab was determined by using another computer program conventionally used for structural analysis, RISA-2D [161]. The deck slab was modeled as a beam which was placed on three pinned supports located at the center of each vertical stem. The deck slab was sectioned into multiple pieces that maintain continuity throughout the member in order to allow different properties to be assigned to each piece. Moment values at different points along the deck slab were determined from the moment profile due to a downward vertical load applied to the end of the overhang region of the deck slab, as shown in Figure 6.8.

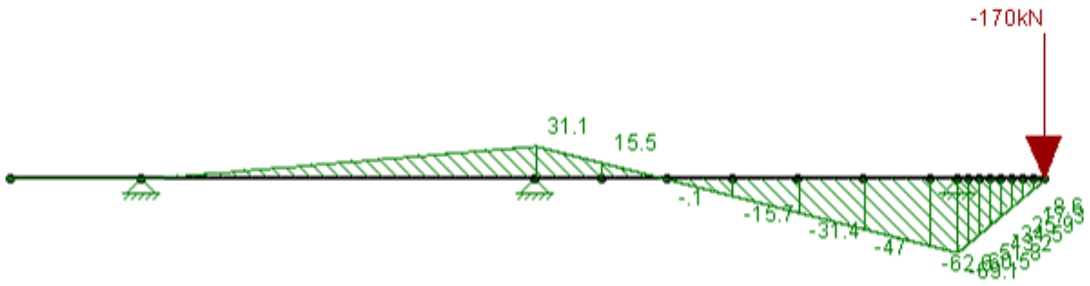

Figure 6.8 Moment profile on deck due to a point load at the edge of the overhang

The average moment acting within each section was determined and the moment of inertia value for each section was changed based on the moment of inertia values from Equation 6.6 that were obtained from moment-curvature data. The moment of inertia value that corresponds to the same moment applied to a given section was used as the input property for that section. After the moment of inertia properties were adjusted for each section, the deflections of the deck slab overhang were calculated. This procedure was repeated at different loading levels up to loads which correspond to the ultimate moment capacity of the system. Note that this procedure assumes zero vertical deflection for the vertical stems, therefore this deflection prediction method provides deflection values for the overhang relative to the adjacent vertical stem. A discussion of the deflection predictions and comparisons with experimental results is included in Section 6.4.7.

6.4.4 Instrumentation

The total instrumentation for this experiment consisted of 16 linear potentiometers and 2 load cells. One central row and two outer rows, each with four

linear potentiometers were used to measure the vertical deflection of the deck slab. The four linear potentiometers within each row were positioned at the midspan of the adjacent cell, above the adjacent stem, in between the stem and the loading beam, and directly below the loading beam, as shown in Figure 6.10 (a) and (b). The deflection of the elastomeric bearing pad was measured using four linear potentiometers, with one linear potentiometer at each corner of the loading beam as shown in Figure 6.9.

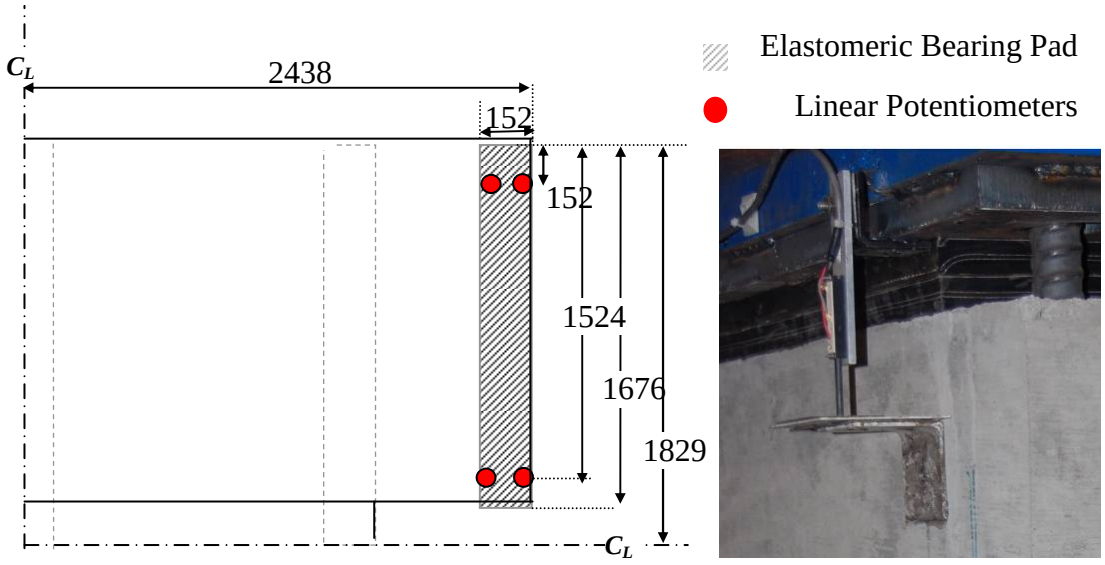

(a) Instrumentation detailing for bearing pad (b) Representative linear potentiometer

Figure 6.9 Instrumentation locations used for measuring compression of bearing pad

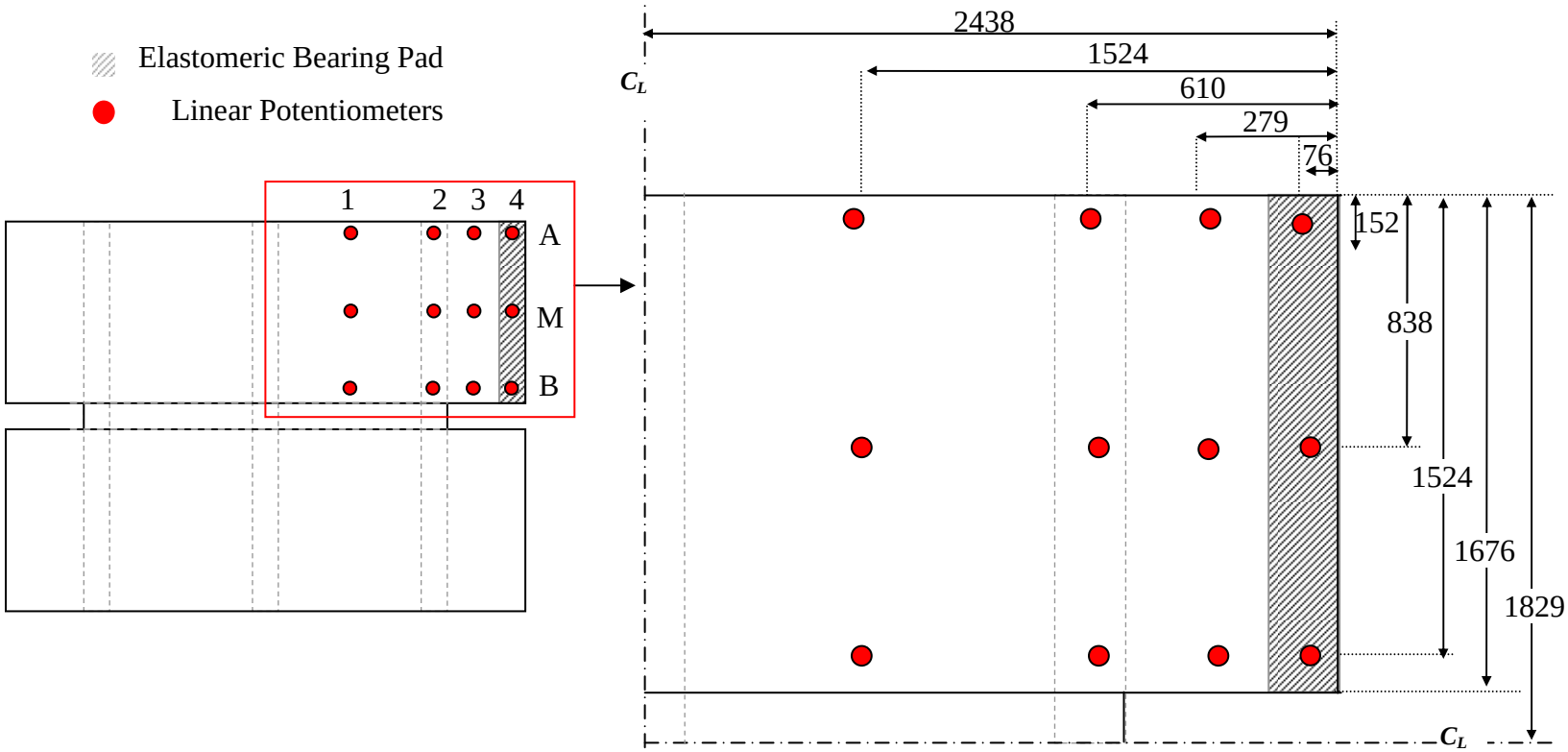

(a) Plan view of specimen

(b) Section of deck slab with linear potentiometer details

Figure 6.10 Position of linear potentiometers for measuring deflections of deck slab (Note: not to scale)

6.4.5 Loading Protocol

In addition to the test setup described in Section 3.1, a 64 mm (2½ in) diameter hole was drilled through the deck of the specimen at a distance 76 mm (3 in) by 76 mm (3 in) on center away from the corner of the deck as shown in Figure 6.11 in order to accommodate the spacing constraints imposed by the testing setup.

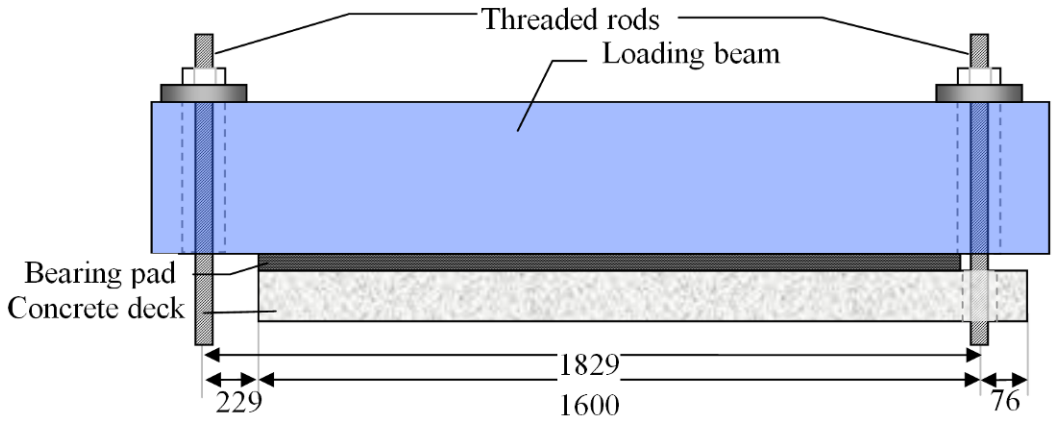

Figure 6.11 Specific test setup schematic for as-built specimen

The overhang of the deck slab was tested by incrementally increasing the hydraulic pressure supplied to the two hydraulic jacks, which loaded the overhang through the test setup shown in Figure 6.11. Adequate time was taken between loading levels to ensure that the hydraulic pressure had stabilized and the pressure had equalized as much as possible between the two jacks. The load applied to the deck slab was monotonically increased following the loading sequence shown in Table 6.1. The load was held briefly at each load level so that observations could be made at each stage.

Table 6.1 Loading protocol for as-built test specimen

Loading step	Load per hydraulic jack		Equivalent uniform distributed load		Load level	Notes
	(kN)	(kip)	(kN/m)	(kip/ft)		
1	24	5	30.0	2.1		Initial load
2	36	8	45.0	3.1	2x wall load	
3	48	11	60.0	4.1		
4	60	13	75.0	5.1		
5	72	16	90.0	6.2	4x wall load	
6	84	19	105.0	7.2		1st set of cracks observed
7	90	20	112.5	7.7	5x wall load	
8	96	22	120.0	8.2		
9	102	23	126.3	8.7	Calculated moment capacity	2nd set of cracks observed
10	114	26	142.5	9.8	6.33x wall load	Ultimate Capacity

6.4.6 Experimental Results

The ultimate capacity of the slab was reached at an applied load of 114 kN (26 kips) per hydraulic jack, equivalent to a uniform distributed load of 142.5 kN/m (9.8 kip/ft), which is 6.33x the nominal wall load. Note that the additional load carrying capacity of the deck slab overhang beyond the dead load of a single sound barrier is necessary to resist lateral loading. As the loading of the edge of the slab was

increased, the top layer of transverse reinforcement above the outer edge of the stem yielded, followed by loss of aggregate interlock resulting in failure. The deflection of the middle of the slab directly under the loading beam when the system was loaded to ultimate capacity was 6.36 mm (0.25 in).

As a baseline, Figure 6.12 shows the specimen prior to testing. The markings on the top of the deck in this figure show preexisting hairline cracks in the deck. Cracking was first observed on the top side of the deck at the 84 kN (19 kip) load per jack and were marked on the specimen in dark blue ink. The thin cracking on the top of the deck surface was discontinuous and approximately followed the two top longitudinal steel reinforcement bars adjacent to the edge of the stem wall as shown in Figure 6.13. Minor diagonal cracks along both the central and the exterior edge of the deck slab were also observed at this load level as seen in Figure 6.14. Small diagonal cracks initiating on the top surface of the deck observed at each end of the specimen are shown in Figure 6.14 (a) and (b).

Figure 6.12 Deck slab prior to experimental testing

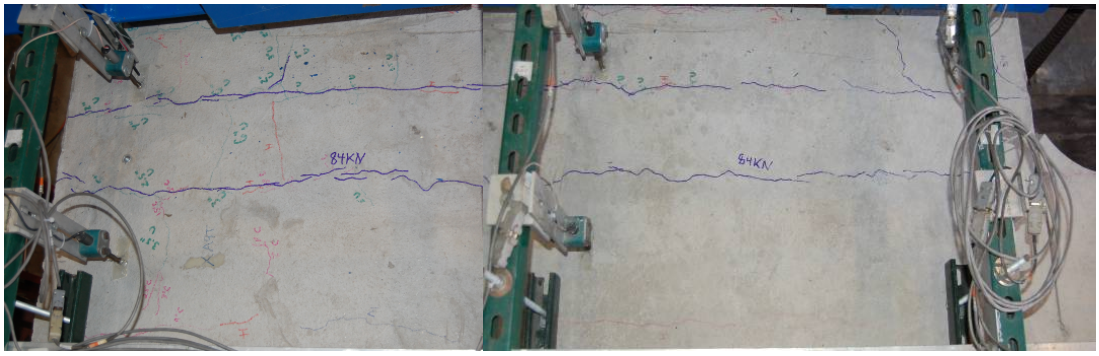

Figure 6.13 Initial cracking of deck slab at 84kN (19 kip) per jack- top view of deck

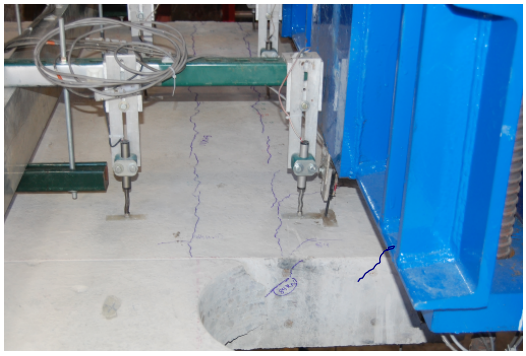

(a) Detail of central edge of slab

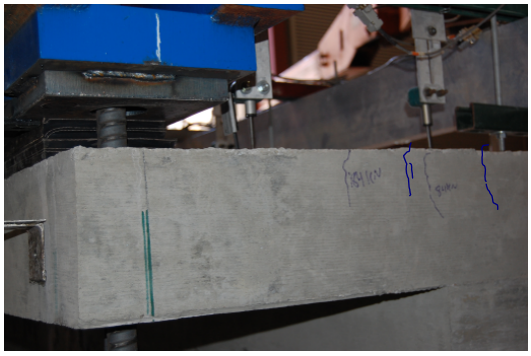

(b) Detail of exterior edge of slab

Figure 6.14 Initial cracking of deck slab at 84kN (19 kip) per jack - side view of deck

Additional opening of small cracks was observed at the load level of 102 kN (23 kip) per jack and these cracks were marked with red ink as shown in Figure 6.15. The cracks that followed the two top longitudinal bars opened further and became continuous over the majority of the specimen. Cracks oriented across the width of the specimen also formed on the top of the slab at this load level, as seen in Figure 6.15.

When the load level of 114 kN (26 kip) per jack was reached, a large diagonal crack opened and quickly propagated, which was clearly visible on the central edge of the slab as shown in Figure 6.16 (a). This load level was determined to be the ultimate

capacity of the overhang for resisting vertical loads. The cracking progressed rapidly along the top surface of the deck as shown in Figure 6.17 and the concrete adjacent to the loading beam settled several millimeters as seen in Figure 6.18. After the loading of the specimen was completed, all testing equipment and instrumentation was fully removed and the observed cracks were marked in orange ink. The orange diagonal cracks on the top surface of the deck face toward the hole in the deck as shown in the upper left-hand corner of Figure 6.19.

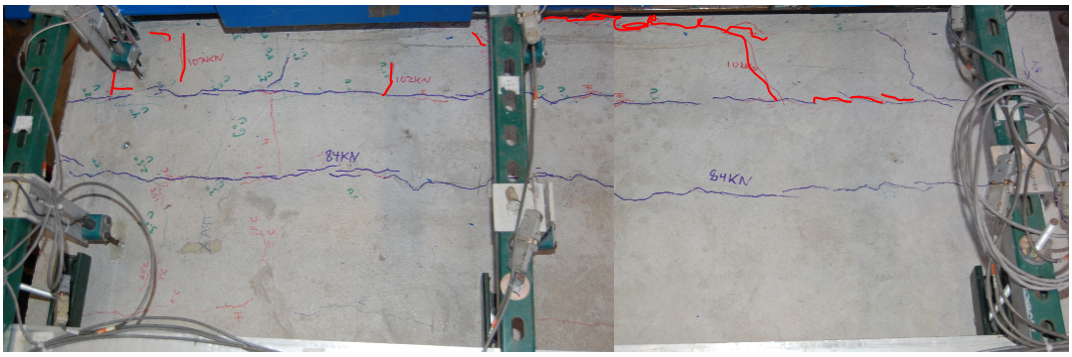

Figure 6.15 Crack marking of deck slab at 102 kN (23 kip) per jack- top view of deck

(a) Central side of slab

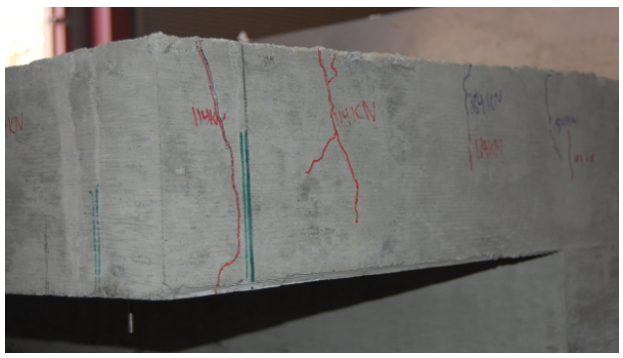

(b) Exterior side of slab

Figure 6.16 Cracking observed at ultimate capacity- side view of deck

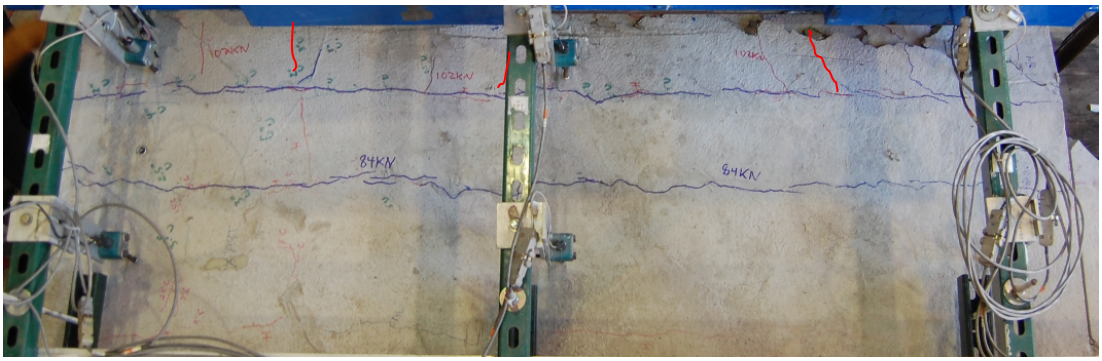

Figure 6.17 Cracking observed at ultimate capacity- top view of deck

Figure 6.18 Detail of cracking at ultimate capacity in central section of deck near loading beam

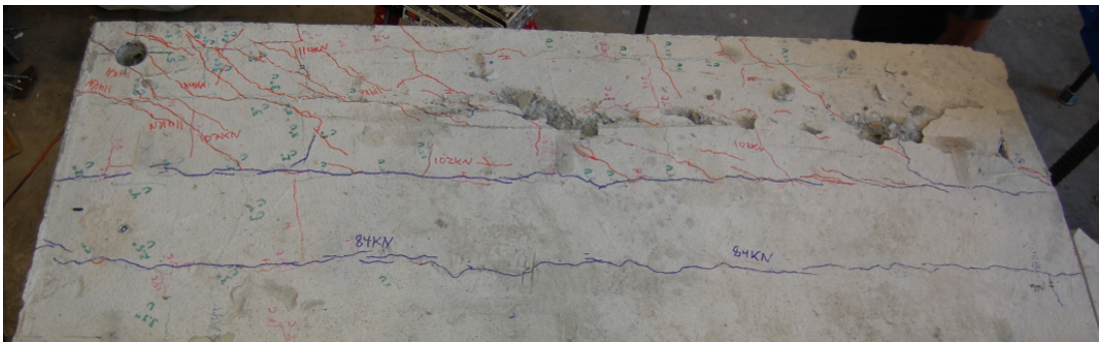

Figure 6.19 Cracks observed on top of slab tested to ultimate capacity

The loose concrete was then removed in order to better observe the failure surfaces as shown in Figure 6.20 and Figure 6.21. Increased damage was present on the central side of the deck as compared to the exterior side. In Figure 6.21 (b), the

slight deformation in the rebar due to the yielding of the steel is observed. It is also noted that the concrete remained firmly attached beyond the longitudinal rebar.

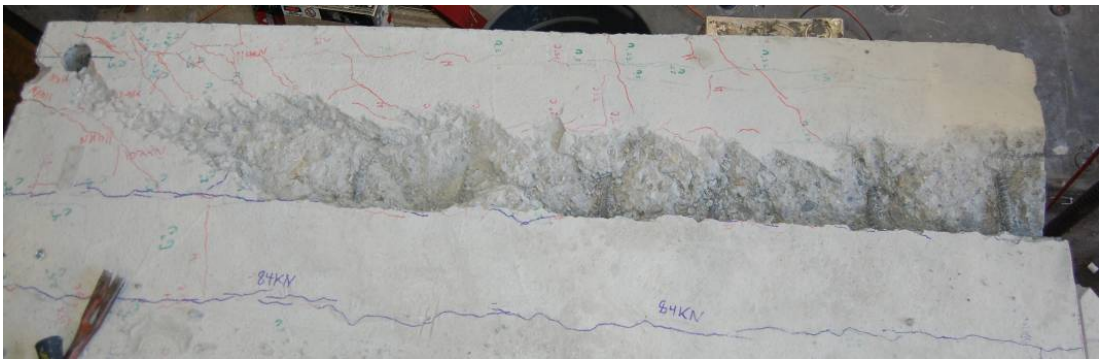

Figure 6.20 Deck slab tested to ultimate capacity after removal of loose concrete

(a) Edge of deck prior to loose concrete removal

(b) After removal

Figure 6.21 Detail of most severely damaged section

The primary variables in defining the overall structural response of the bridge deck slab are the load per hydraulic jack at which significant damage or failure occurred and the corresponding center deflection of the slab, directly below the actuator. Additional instrumentation serves to add supplementary data regarding the deformation of the specimen during testing. As observed in Figure 6.22, the

deflection of the three linear potentiometers directly below the loading beam indicate comparable deflections for lower loading levels and higher deflections with increasing load at the central edge of the overhang, which contains linear potentiometer B4.

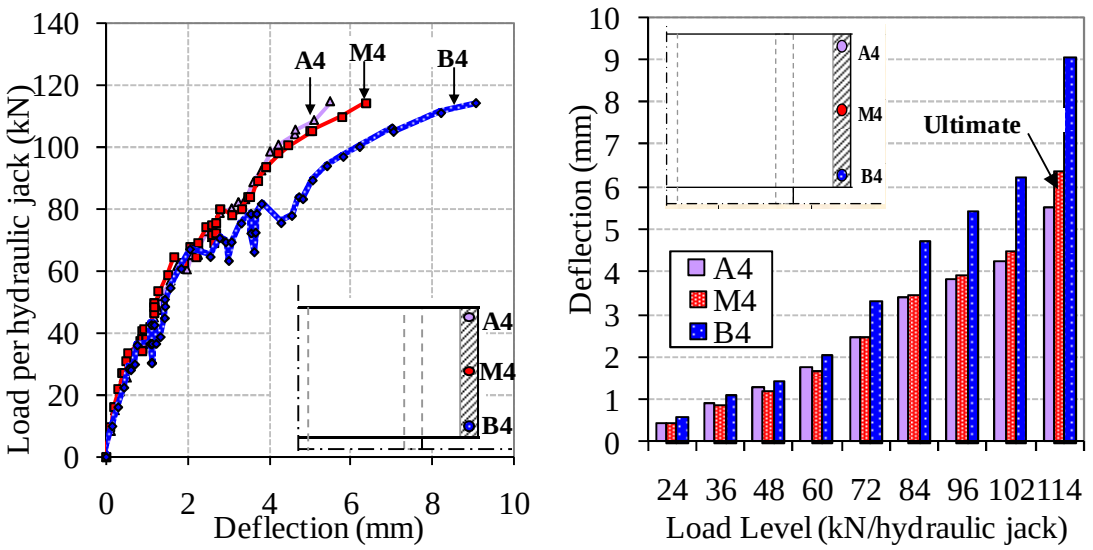

(a) Load versus deflection profiles

(b) Comparison of linear potentiometers below loading beam

Figure 6.22 Comparisons of deflections at the edge of the deck slab overhang

At the load level of 84 kN (19 kips) per hydraulic jack where cracking in the deck was first observed, equivalent to a uniform distributed dead load of 105 kN/m (7.2 kip/ft) or approximately 5x the nominal wall load, linear potentiometers A4 and M4 deflected similarly while the linear potentiometer B4 exhibited a 1.3 mm (0.051 in) or 37% greater deflection value. At the load level of 102 kN (23 kip) per hydraulic jack where the 2nd set of crack marking took place, equivalent to a uniform distributed dead load of 126 kN/m (8.7 kip/ft) or nearly 6x the nominal wall load, the deflection at B4 was 2.0 mm (0.078 in) or 39% greater than the other two linear potentiometers.

The profiles along the center of the specimen (Figure 6.24) and at both edges (Figure 6.23 and Figure 6.25) shown below exhibit similar deflection profiles and indicate that negligible vertical deformations occur in the deck beyond the adjacent stem wall due to edge loading of the deck slab overhang.

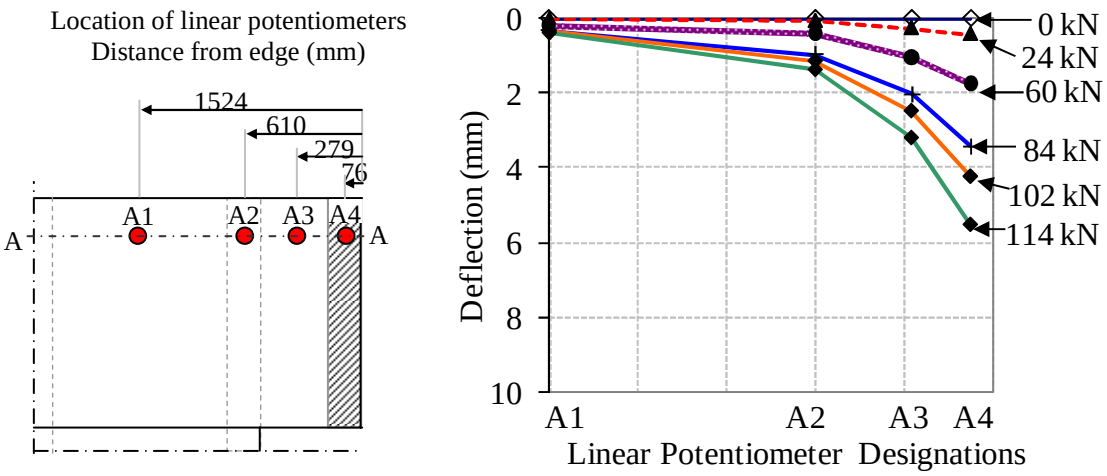

Figure 6.23 Deflection profile along the outer edge of specimen (Line A)

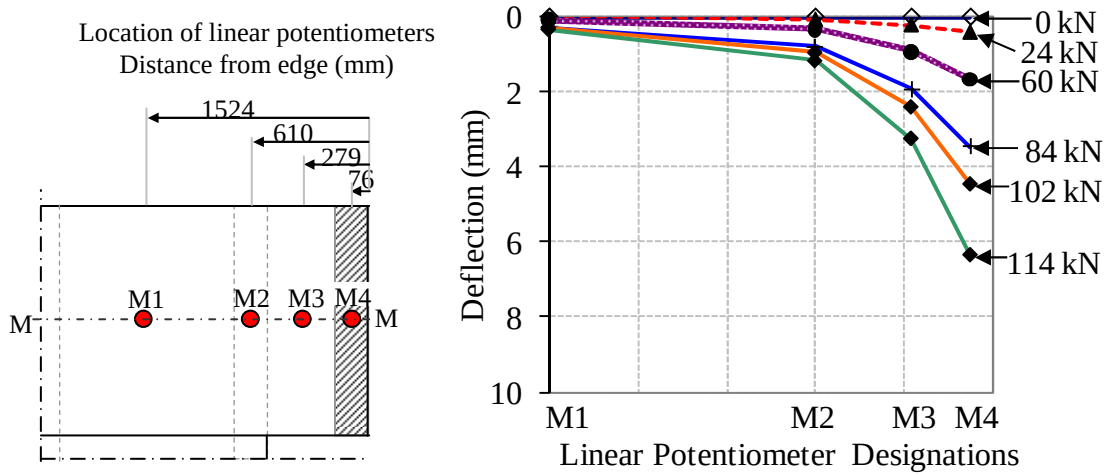

Figure 6.24 Deflection profile along center of specimen (Line M)

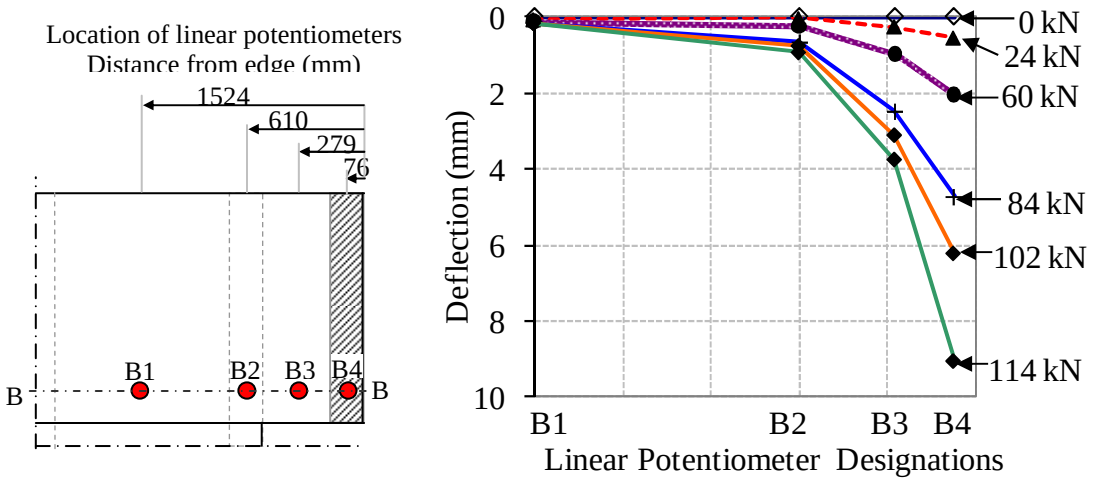

Figure 6.25 Deflection profile along the central edge of specimen (Line B)

The deflection profile shown in Figure 6.26 shows comparable deflections along the overhang at a distance midway to the adjacent stem wall. Figure 6.27 illustrates comparable deflections directly below the point of load application along the overhang for lower load levels with less symmetric deformations observed for higher load levels after cracking was observed throughout the specimen.

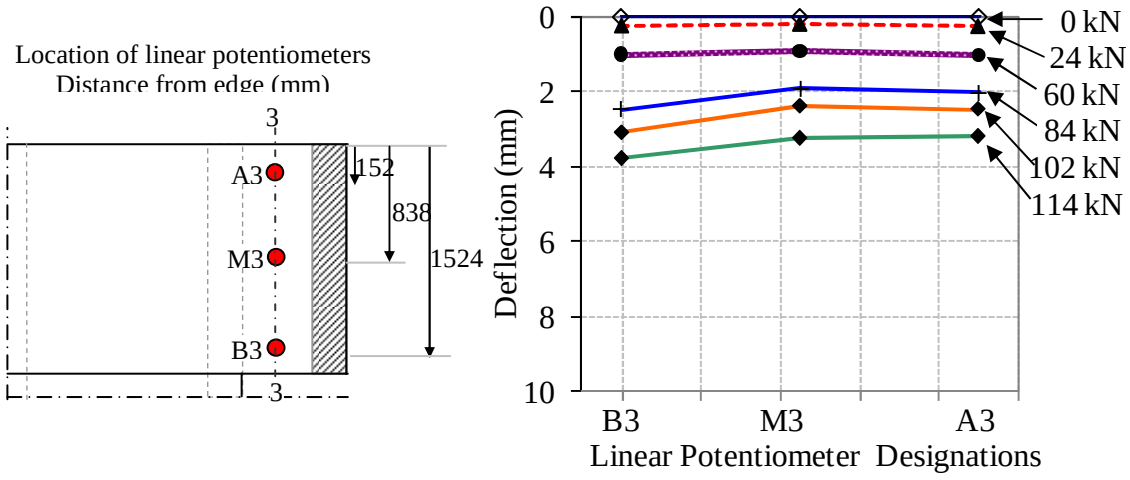

Figure 6.26 Deflections midway along overhang (Line 3)

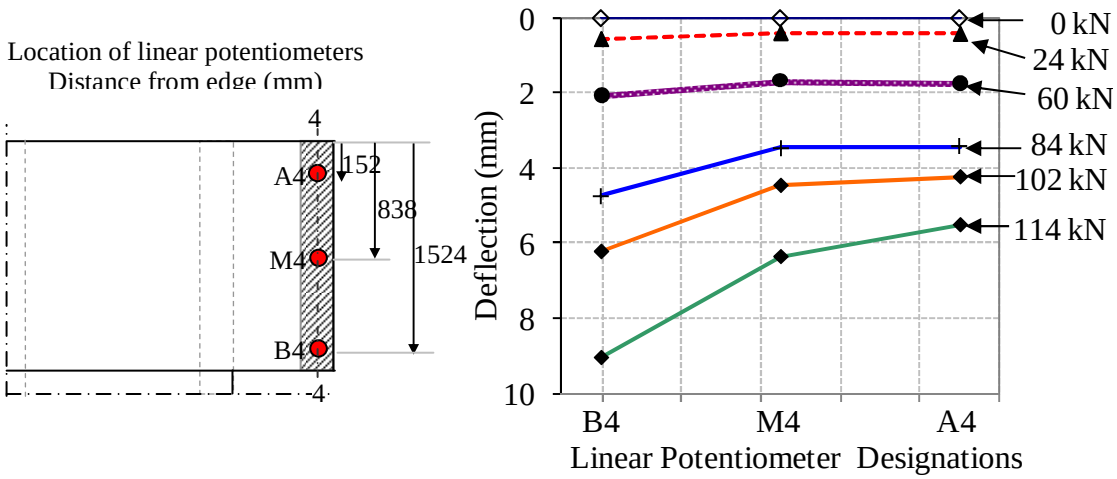

Figure 6.27 Deflections directly below loading beam (Line 4)

Through a comparison of these figures, the results indicate a symmetric structural response for load levels prior to the initial observation of cracking in the specimen and greater deflections on one side at higher loading levels.

6.4.7 Comparison with Theory

The max moment found via moment curvature analysis of 117.2 kN-m (85.6 kip-ft) was within 6.5 % of the actual moment applied to the structure at the max loading of 114 kN (26 kip) per hydraulic jack, which corresponds to an applied moment of 110.0 kN-m (81.0 kip-ft). The moment capacity estimate of 97.0 kN-m (71.6 kip-ft), determined using the ACI 318-08 prescribed equation, was off from the experimentally determined moment capacity by 11.8%.

Figure 6.28 compares the experimentally determined deflection of the overhang with predicted deflection values, which were adjusted to accommodate for the deflection of the adjacent vertical stem. The analytical prediction of deflection

values offers close correlation with experimental results throughout the loading range. At 114 kN (26 kip) per jack, the experimentally determined ultimate capacity of the deck slab, the predicted deflection was 5.3 % less than the experimentally determined deflection, with predicted and experimental deflections of 6.03 mm (0.237 in) and 6.36 mm (0.250 in) respectively.

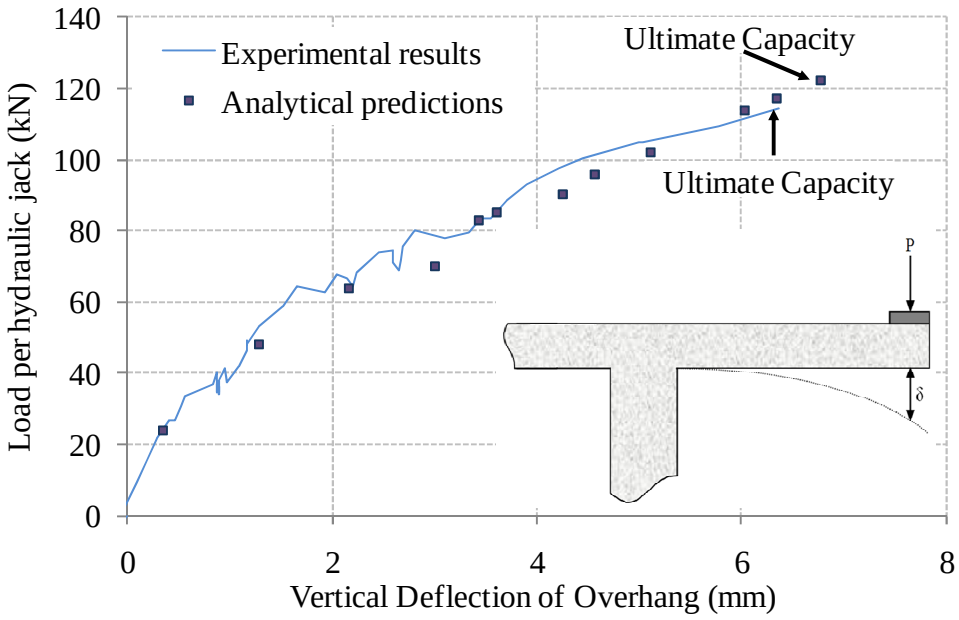

Figure 6.28 Deflection values from experimental results with analytical predictions

6.5 REHABILITATED TEST

The following section presents NSM FRP strengthening design options for achieving the desired capacity increase and describes the implementation, testing and analysis of the chosen rehabilitation design.

6.5.1 Calculations for Potential CFRP NSM Strengthening Schemes

The increased moment demand on the test specimen's deck slab due to the addition of the sound wall is calculated and this value is used as the basis for determining the desired capacity increase. The corresponding total area of NSM CFRP needed to achieve the desired moment capacity increase is calculated and design options for five different available CFRP reinforcement products are presented.

The dead weight of a typical sound wall used for bridges in California was calculated from the CALTRANS' concrete masonry sound wall design on bridges [159]. Using this design with normal weight concrete, the gravity load per unit length for the sound wall was determined to be 13.5 kN/m (0.92 kip/ft). Note that the weight of the traffic barrier is not included as part of the increased moment demand calculation because it is assumed that the weight of the traffic barrier was already accounted for in the original design of the deck slab overhang. The tested section of overhang was 1600 mm (5 ft 6 in) long therefore the total load applied to the specimen from the sound wall is 22.6 kN (5.08 kip). The equivalent moment applied to the structure due to this dead load can be obtained by multiplying the total load applied by the distance between the applied load and the edge of the stem, also known as the moment arm. The equivalent additional moment demand due to the sound wall was found to be 10.91 kN-m (8.05 kip-ft).

A successful repair would strengthen the overhang to accommodate this increased moment demand with a reasonable safety margin. For initial calculation purposes, a safety margin of 3 was deemed appropriate.

$$M_{demand\_increase} = M_{wall} \cdot 3 \quad 6.7$$

where
M_{wall} = Moment demand due to the addition of a sound wall onto the overhang

This translates to an increase in moment demand of 32.7 kN-m (24.1 kip·ft). Therefore, the NSM flexural strengthening will be designed to increase the capacity of the overhang by at least this value. The experimentally determined moment capacity of the as-built reinforced concrete deck slab overhang without FRP was found to be 110 kN-m (81 kip-ft). Therefore, the new moment capacity after strengthening should be at least 142.7 kN-m (105.1 kip-ft), which corresponds to a minimum required moment capacity increase of 29.7 percent over the capacity of the as-built specimen without FRP.

6.5.2 Analytical Strength

The increased moment capacity due to FRP strengthening is equal to the sum of the contribution from the tension steel (compression steel is ignored for this calculation) and the contribution from the FRP reinforcement:

$$M_{n\_strengthened} = A_s f_y \left(d - \frac{a}{2} \right) + \psi_f \cdot A_f f_{fe} \cdot \left(d_f - \frac{a}{2} \right) \quad 6.8$$

where
A_s = Total area of tension steel in slab overhang test specimen
f_y = Experimentally determined yield strength of steel reinforcement
d = Distance from extreme compression fiber to tensile reinforcement
a = Depth of concrete compression block, assuming rectangular stress distribution

Ψ_f = Additional reduction factor from ACI 440.06R (Section 9.6.1) [148]
d_f = Distance from the compression fiber to the centroid of the FRP
f_{fe} = $E_f \cdot \varepsilon_{fe}$ Effective stress in the FRP assuming elastic behavior
E_f = Experimentally determined modulus of /elasticity of FRP
ε_{fe} = Effective strain in FRP reinforcement

By rearranging Equation 6.8, an expression for the area of FRP reinforcement required in order to achieve a specified moment capacity increased can be obtained:

$$A_{f\_required} = \frac{M_{n\_strengthened} - A_s f_y \left(d - \frac{a}{2}\right)}{\psi_f \cdot f_{fe} \cdot \left(d_f - \frac{a}{2}\right)} \qquad 6.9$$

The required area of FRP obtained from this expression can be used to evaluate the feasibility of different FRP strengthening options. Note that the area of FRP required is the total area needed for the specimen overhang and thus must be distributed along the width of the slab overhang.

6.5.3 Options for Rehabilitation

The seven product options evaluated for this rehabilitation design were different sizes of SIKA's pultruded carbon fiber CarboDur rods and strips as well as Hughes Brothers' pultruded carbon fiber Aslan 500 rectangular bars [162-164]. The physical properties of each option are provided in Table 6.2 for reference.

The number of strips required to attain the desired moment capacity increase was calculated for each of the seven potential options using calculations described in the previous section (Equation 6.9) and the results are shown in Figure 6.29. For

calculation of the effective stress in the FRP, f_{fe}, a strain of ε_{fe} =0.65% was assumed based on design recommendations for FRP post-strengthening of reinforced concrete slabs [165, 166]. The tensile modulus for each of the different FRP reinforcement options was obtained from manufacturer reported data. Since the FRP reinforcement type had not been selected yet, the distance from the compression fiber to the centroid of the FRP, d_f, was assumed to be the full depth of the slab. Note that this assumption will slightly overestimate the moment capacity contribution from the FRP because for NSMR applications, the reinforcement is located slightly below the surface of the structure. Assuming that the centroid of the FRP reinforcement is below the surface of the structure by a distance of between 2 mm (0.079 in) and 10 mm (0.393 in) the calculations would have overestimated the moment capacity increase due to the FRP reinforcement by between 1% and 6%.

Spacing requirements were also considered in the calculations performed for each FRP strengthening option. The maximum spacing recommendations provided by the manufacturer state that on center spacing should be limited to no more than the lesser of 0.2 times the span length (L) or five times the slab thickness (h):

$$s_{\max} = \min\left(0.2L,\ 5h\right) \tag{6.10}$$

Note that the span for cantilever is taken as twice the distance to the support. This spacing limit yields a maximum recommended spacing of 203 mm (8 in). Table 6.3 below shows the number of units needed as well as the theoretical moment capacity increase for each type of CFRP reinforcement. As observed in Table 6.3, spacing limitations govern rather than actual strength requirement limitations. Since

all seven of the design options are able to achieve the increased capacity requirements, other aspects such as cost and constructability are now used to select the FRP reinforcement system.

One notable difference between the installation of CFRP strips as opposed to rods is the required depth of grooves cut into the deck. The 6.4 mm (1/4 in) diameter rods require 12.7 mm (1/2 in) deep slots and the 9.5 mm (3/8 in) rods require 15.9 mm (5/8 in) deep rods, while the strips only require a 4 mm (0.16 in) deep groove. From a construction viewpoint, strips as opposed to rods are far easier to implement due to required groove depth.

Table 6.2 Physical properties of pultruded CFRP strengthening product options [162-164]

Product type	Source	Product designation	Diameter		Thickness		Width		Area		Tensile Modulus	
			mm	in	mm	in	mm	in	mm^2	in^2	GPa	Msi
Rod	SIKA	¼ in. dia.	6.35	0.250					1.27	0.050	155	22.5
Rod	SIKA	⅜ in. dia.	9.53	0.375					2.79	0.110	155	22.5
Strip	SIKA	S 512			1.2	0.047	50	1.97	60	0.093	165	23.9
Strip	SIKA	S 812			1.2	0.047	80	3.15	96	0.149	165	23.9
Strip	SIKA	S 1012			1.2	0.047	100	3.94	120	0.186	165	23.9
Bar	Hughes Brothers	#2			2	0.079	16	0.63	31.2	0.049	124	18
Bar	Hughes Brothers	#3			4.5	0.177	16	0.63	71.3	0.110	124	18

The lower modulus of the CFRP tape of 124 GPa (18.0 Msi) versus that of the CFRP strips, 165 GPa (23.9 Msi), resulted in appreciably greater material usage for comparable strengthening schemes. As a comparison, the S512 CFRP strip has an estimated moment capacity increase of 81%, whereas the #3 size CFRP tape has an estimated moment capacity increase of only 71 % and requires an additional 19% of material above that used for the strip to achieve this increase.

Based on guidelines, material cost considerations, and the insight that in field determination of concrete cover would be a concern because nondestructive determination of cover depth over large areas is considered time consuming [167], the CarboDur strips were chosen. Because the smallest size strip far exceeded the required moment capacity, the CarboDur S512 strips were selected, which have a 50 mm (2 in) width. The spacing was set at 203 mm (8 in) on center for the width of the test specimen such that nine total CFRP strips were used as shown in Figure 6.29. The bars were extended past the point of inflection to achieve a necessary development length of 300 mm (11.8 in).

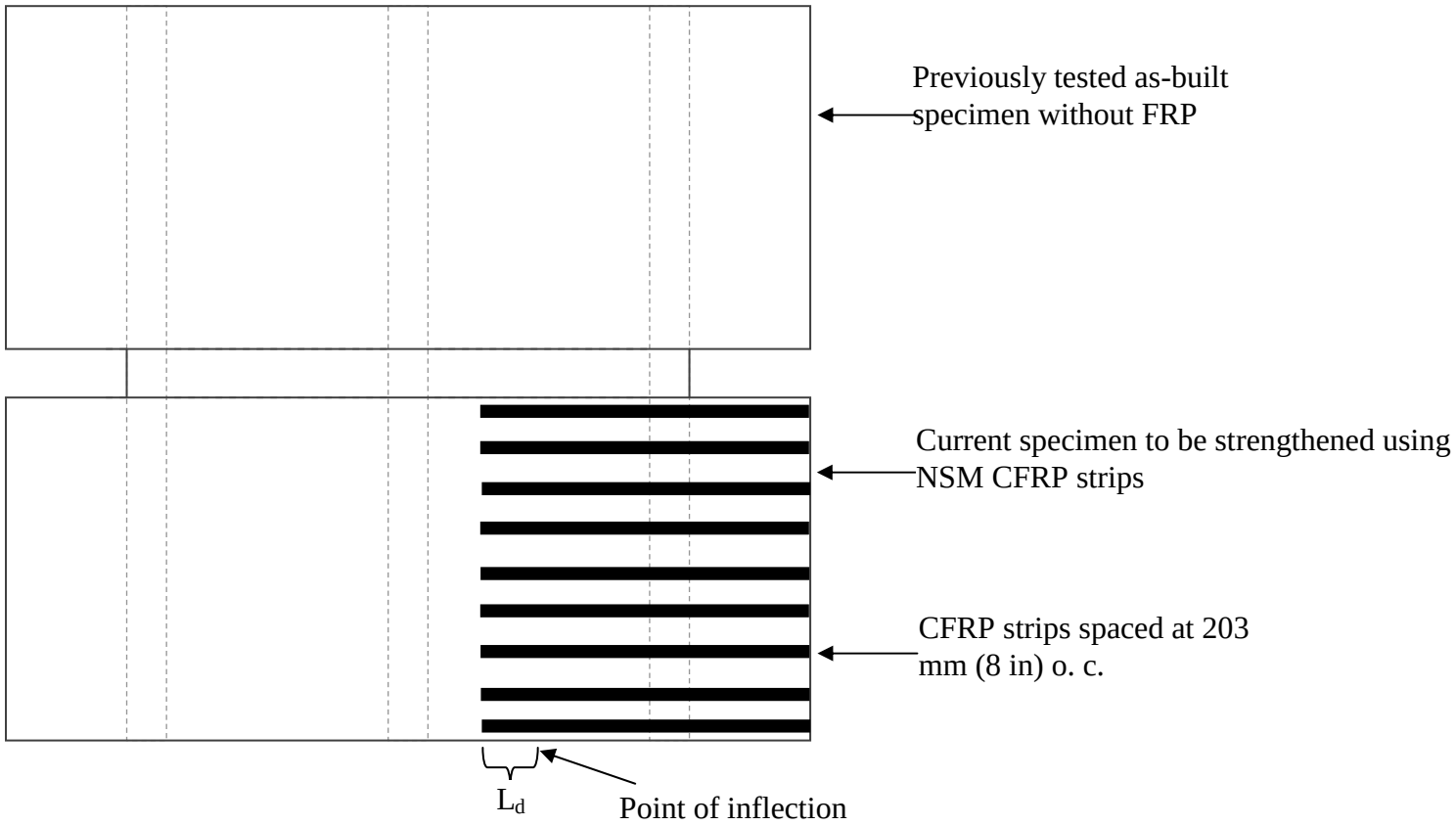

Figure 6.29 Plan view of deck illustrating chosen CFRP strengthening scheme

Table 6.3 Different NSM FRP strengthening options

Reinforcement type	Cross-sectional Area		# of units needed	O.C. Spacing		O.C. Spacing used		Actual # of units	Total area of FRP used		Theoretical moment capacity		Moment capacity increase	Normalized structural efficiency
	mm^2	in^2	rounded up	w/o considering spacing limits		considering spacing limits		rounded up	mm^2	in^2	kN-m	kip-ft	%	(Relative to desired capacity increase)
				mm	in	mm	(in)							
Rod: 1/4" diameter	32	0.050	7	254	10	203	8	9	226	0.45	140.7	103.7	28%	Doesn't meet requirements
Rod: 3/8" diameter	71	0.110	4	432	17	203	8	9	639	0.99	191.8	141.5	74%	1.00
Strip: S512-50mm width	60	0.093	4	432	17	203	8	9	540	0.84	182.4	134.5	66%	1.18
Strip: S812-80mm width	96	0.149	3	559	22	203	8	9	865	1.34	233.2	172.0	112%	0.74
Strip: S1012-100mm width	120	0.186	2	838	33	203	8	9	1080	1.67	256.6	189.2	133%	0.59
Bar: #2	31	0.049	9	203	8	203	8	9	281	0.44	131.5	96.9	20%	Doesn't meet requirements
Bar: #3	71	0.110	4	432	17	203	8	9	642	0.99	173.1	127.6	57%	1.00

6.5.4 Rehabilitation Construction

The following section details the implementation of the NSMR strengthening scheme chosen in Section 5.2. Nine (9) rectangular groves spaced at 203 mm (8 in) o.c. were cut in the top deck of the test specimen with dimensional tolerances of 70 mm - 76 mm (2 ¾ in - 3 in) for the width and 6 mm - 13 mm (¼ in to ½ in) for depth. The grooves were each 2.74 m (8 ft) long and the cut grooves are shown in Figure 6.30. After the grooves were cut to the proper dimensions, the surface was roughened to achieve the minimum required concrete surface profile (CSP) of 3 as defined by the ICRI surface profile guidelines [168].

Figure 6.30 Grooves cut in deck for NSM strengthening

The CarboDur S 512 carbon fiber laminate strips were cut to length and the top and bottom surfaces were wiped clean using methyl ethyl ketone (MEK) to remove all residual carbon dust from the surface prior to the installation of strain gages on the top surface of the strips. An additional cleaning with MEK was performed immediately prior to installation of the strips into the test specimen to remove any remaining

contaminates and surface oxidization. A high-modulus, high-strength, structural epoxy paste known as SikaDur 30 was used for bonding the CFRP strips to the concrete. The structural properties of the CarboDur S 512 strips and SikaDur 30 resin system were experimentally determined through material characterizations performed at the University of California, San Diego within the authors' research group and these properties are shown in Table 6.4 and Table 6.5 [169].

Table 6.4 Tensile properties of SikaDur 30 resin system [169]

SikaDur 30 Tensile Properties (ASTM D-638)		
	Mean	Standard Deviation
7 day Tensile Strength	25.29 MPa (3.671 ksi)	2.54 MPa (0.369 ksi)
Modulus of Elasticity	6.93 GPa (1.006 Msi)	0.48 GPa (0.0697 Msi)

Table 6.5 Tensile properties of SIKA CarboDur S512 CFRP strips [169]

CarboDur S 512 Tensile Properties (ASTM D-3039)		
	Mean	Standard Deviation
Ultimate Tensile Strength	2,505 MPa (363.6 ksi)	82.85 MPa (12.0 ksi)
Ultimate Tensile Modulus	138.1 GPa (20.05 Msi)	5.22 GPa (0.76 Msi)
Ultimate Tensile Strain	1.580 %	0.084 %

After the SikaDur 30 resin system was thoroughly mixed, the neat resin was applied to each groove as a primer using a spatula to form a uniform thickness of 1.6

mm (1/16 in) as shown in Figure 6.31. A specialized applicator was also used to apply a precisely controlled thickness of resin onto each of the carbon fiber strips and the strips were carefully placed in the grooves.

Figure 6.31 Application of resin system used in grooves to bond CFRP strips to concrete

A rubber roller was then used to properly seat each strip, using adequate pressure to force SikaDur 30 gel out on both sides of the laminate so that the bond line between the concrete and FRP strip does not exceed 3 mm (1/8 in) [170]. Excess gel was carefully removed and the installed strips are shown in Figure 6.32. After the resin system had cured for 24 hours, a low viscosity resin system, which was used for the wear surface applied to the top of the FRP strips, was poured over the top of the strips up to the level of the original concrete deck. The top layer of resin was mixed with sand to allow for improved thermal compatibility with the surrounding concrete

and to provide a non-skid wear surface for the top of the deck. After the installation of the NSM CFRP strengthening scheme was completed, the instrumentation was installed and the specimen was ready for testing to determine the effectiveness of the repair.

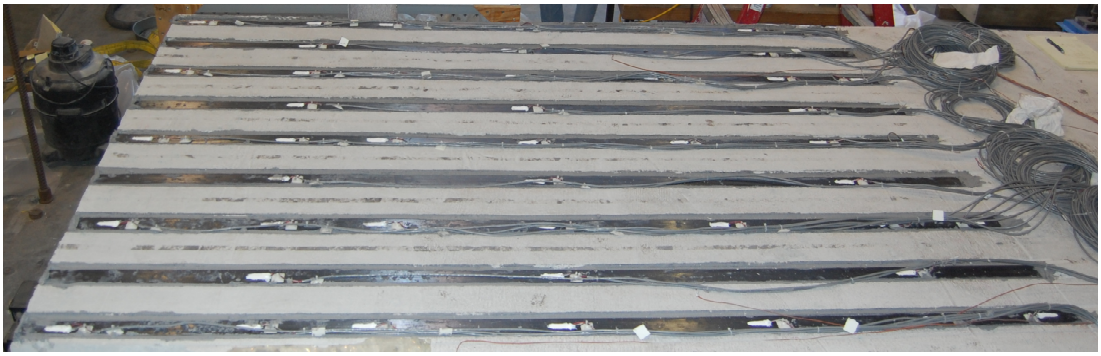

Figure 6.32 CFRP strips installed

In order to monitor the curing of the CarboDur 30 resin system used to attach the CFRP strips to the deck slab, small test samples were made using resin mixed for installation of the strips and the samples were placed adjacent to the test specimen to ensure comparable curing conditions. These resin samples were tested daily for a period of seven days using both dynamic mechanical thermal analysis (DMTA) and differential scanning calorimetry (DSC) techniques. The results obtained from these experiments regarding the glass transition temperature, T_g, of the resin system are shown in Table 6.6 as well as Figure 6.33 and Figure 6.34. The trends from the glass transition temperature data over time shown below indicate that the SikaDur 30 resin system achieved nearly full cure after approximately 4-5 days.

Table 6.6 T_g progression of CarboDur 30 resin used in NSMR installation

Time	DMTA T_g results	DSC T_g results
	°C	°C
Day 1	57.1	37.5
Day 2	59.2	38.5
Day 4	64.4	41.5
Day 5	62.3	42.3
Day 6	64.3	43.0
Day 7	63.6	43.0

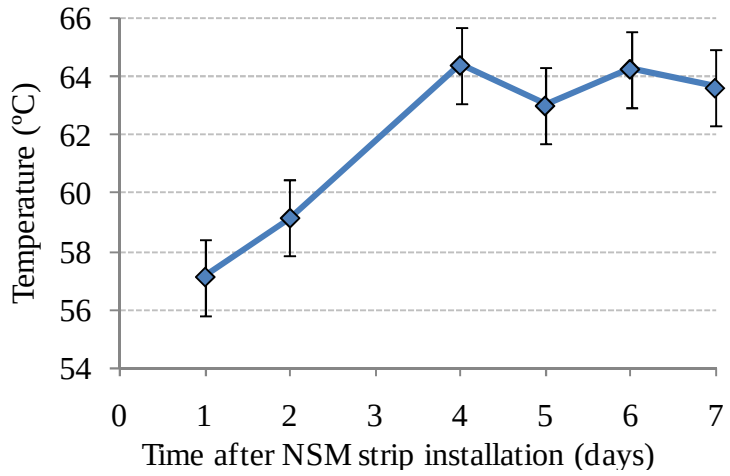

Figure 6.33 Progression of T_g determined from DMTA tests

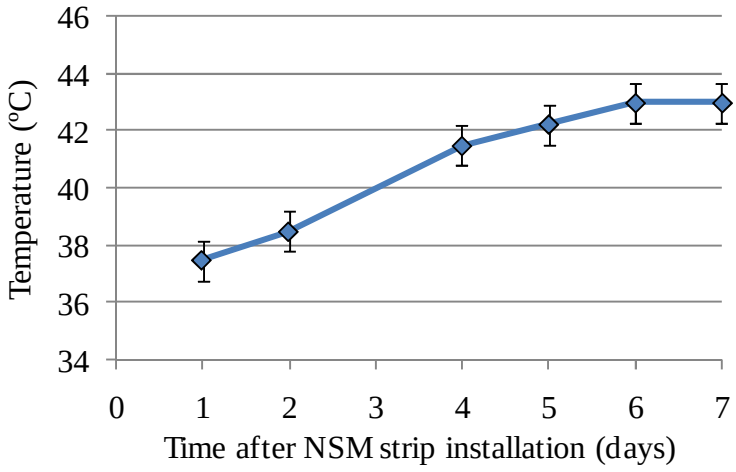

Figure 6.34 Progression of T_g determined from DSC tests

6.5.5 Capacity Calculations

Following the implementation of the chosen NSM CFRP strip rehabilitation scheme, theoretical predictions for capacity were recalculated using the experimentally determined material properties given in Table 6.5 along with an assumed CFRP strip embedment depth of 3 mm (1/8 in) and reduced FRP strain capacity of 0.65% as described in Section 6.5.3. The increased moment capacity calculation due to FRP strengthening described in Section 5.1 yields a theoretical moment capacity of 167.3 kN-m (123.4 kip-ft), which corresponds to a 52% increase in moment capacity over the experimentally determined value for the as-built specimen. The moment curvature analysis performed on the FRP rehabilitated specimen yielded a moment capacity of 185.5 kN-m (136.4 kip-ft), which corresponds to a 69 % increase in load carrying capacity over the as-built specimen.

Predictions of deflection at the end of the deck slab overhang were performed using the analytical method described in Section 6.4.3. The results from these analytical predictions are discussed in Section 6.5.9.

6.5.6 Instrumentation

The total instrumentation for this experiment consisted of 16 linear potentiometers, 47 strain gages and 2 load cells. One central row and two outer rows, each with four linear potentiometers were used to measure the vertical deflection of the deck slab. The four linear potentiometers within each row were positioned at the midspan of the adjacent cell, above the adjacent stem, in between the stem and the loading beam, and directly below measuring compression of bearing pad. The

deflection of the elastomeric bearing pad was measured using four linear potentiometers, with one linear potentiometer at each corner of the loading beam using the same layout as the as-built specimen shown in Figure 6.9.

All 47 strain gages were applied to the top side of the nine pultruded CFRP strips, parallel to the direction of the fibers as shown in Figure 6.32. The two strain gage layout patterns used on this specimen, illustrated in Figure 6.36, were applied to alternating CFRP strips throughout the width of the specimen as shown in Figure 6.37.

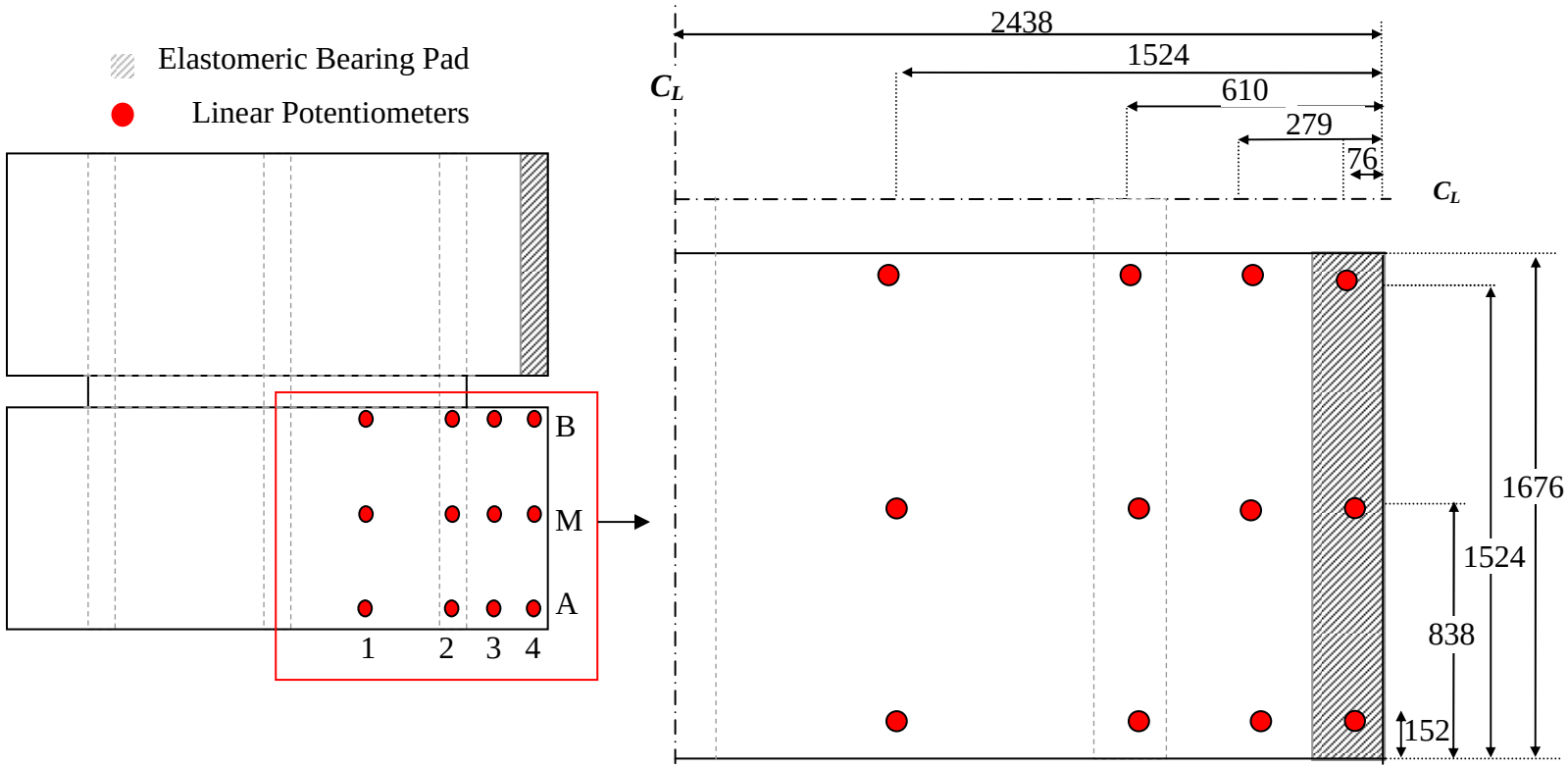

(a) Plan view of specimen

(b) Section of deck slab with linear potentiometer details

Figure 6.35 Position of linear potentiometers for measuring deflections of deck slab
(Note: not to scale)

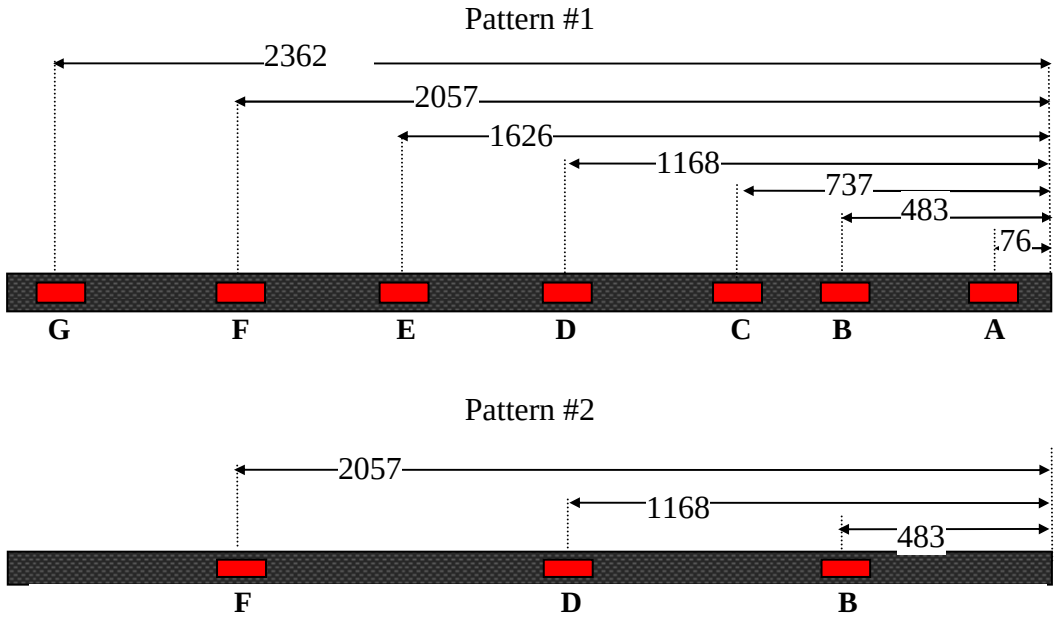

Figure 6.36 Strain gage patterns and designations

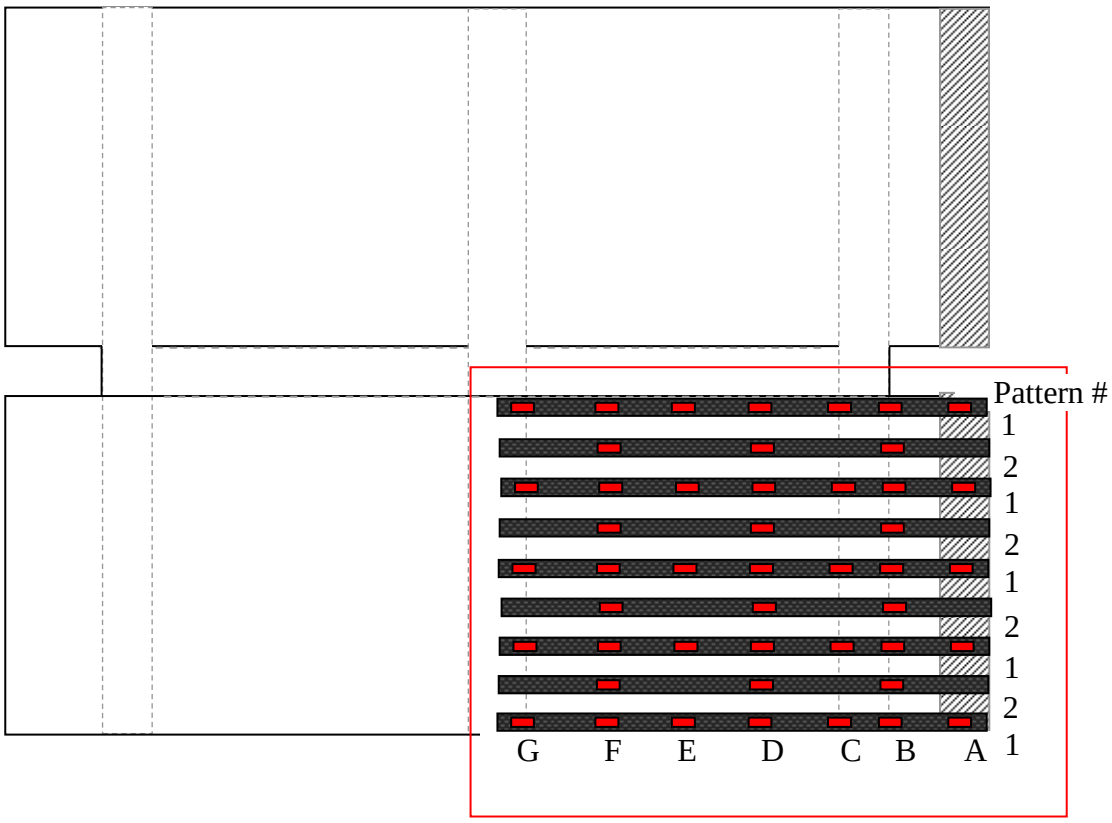

Figure 6.37 Position of strain gages attached to CFRP strips

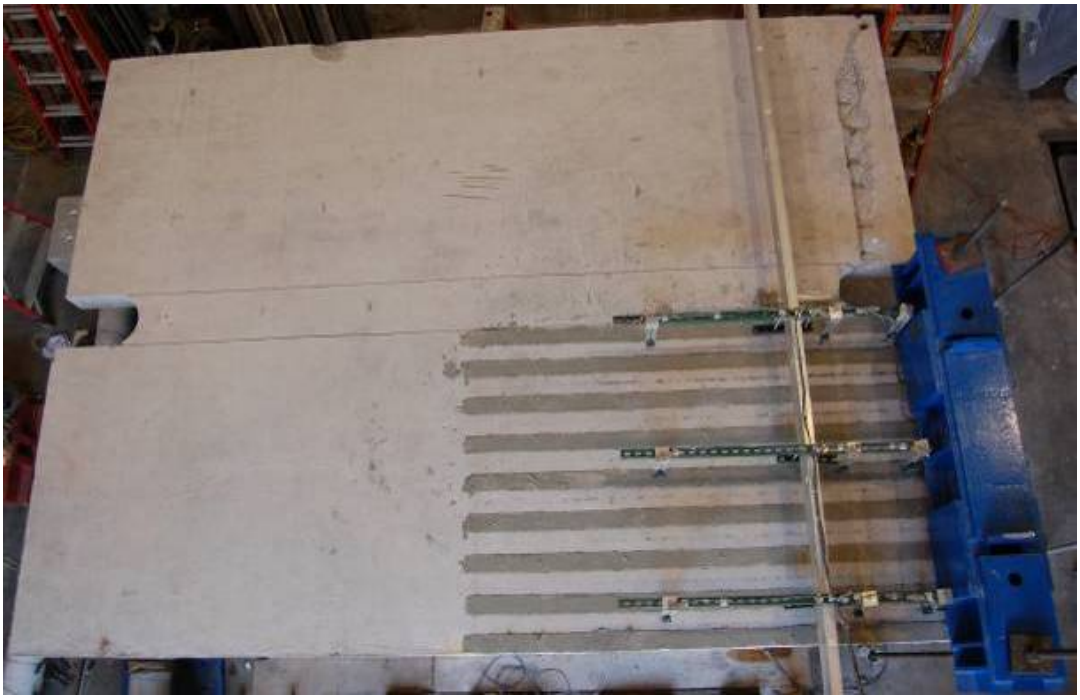

Figure 6.38 Completed installation of CFRP strips with full instrumentation setup

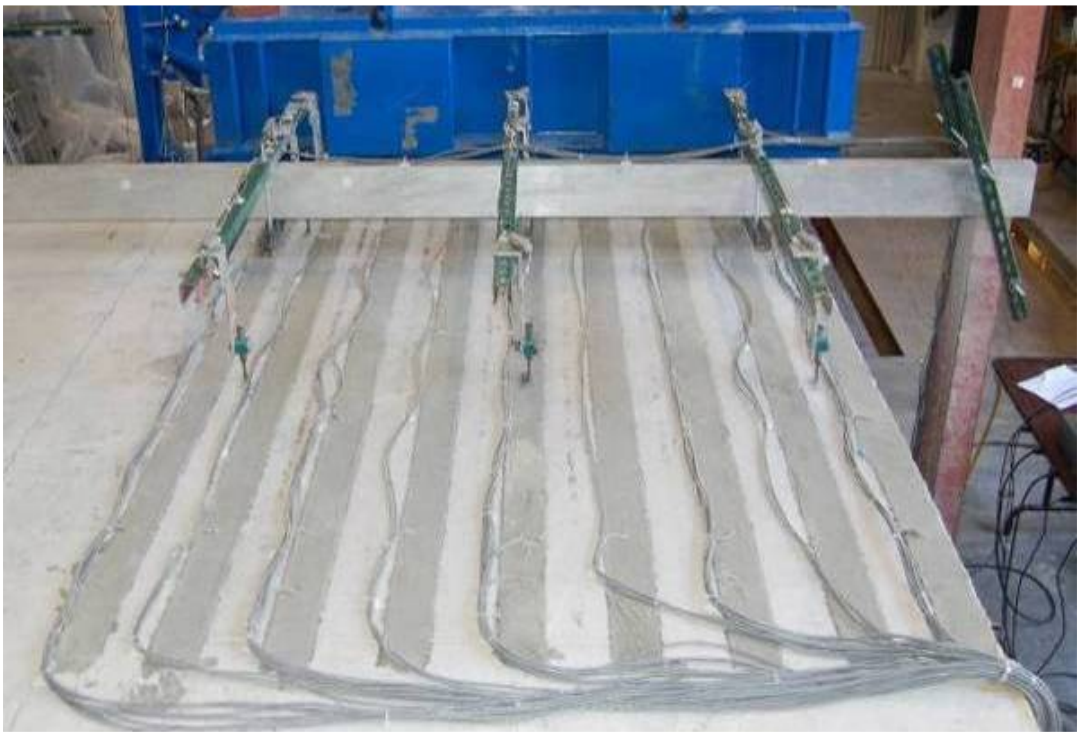

Figure 6.39 Side view of completed installation of CFRP strips with full instrumentation setup

6.5.7 Loading Protocol

The overhang of the deck slab was loaded using the test setup shown in Figure 6.3 and described in Section 3.1 by incrementally increasing the hydraulic pressure supplied to the two hydraulic jacks. Adequate time was taken between loading levels to ensure that the hydraulic pressure had stabilized and the pressure had equalized as much as possible between the two jacks. The load applied to the deck slab was monotonically increased following the loading sequence shown in Table 6.7. The load was held briefly at each load level so that observations could be made.

Table 6.7 Loading protocol used for FRP rehabilitated specimen

Loading step	Load per hydraulic jack		Equivalent uniform distributed load		Load Level	Notes
	(kN)	(kip)	(kN/m)	(kip/ft)		
1	24	5	30.0	2.1	---	Initial load
2	36	8	45.0	3.1	2x wall load	---
3	48	11	60.0	4.1	---	---
4	60	13	75.0	5.1	---	---
5	72	16	90.0	6.2	4x wall load	---
6	84	19	105.0	7.2	1st set of cracks observed for as-built specimen	---
7	90	20	112.5	7.7	5x wall load	---
9	101	23	126.3	8.7	Calc'd moment capacity as-built specimen	---
10	114	26	142.5	9.8	Ultimate capacity as-built specimen	---
11	116	26	145.0	9.9	Calc'd shear capacity as-built specimen	1st set of cracks observed
12	130	29	162.5	11.1	---	
13	136	31	170.0	11.6	---	2nd set of cracks observed
14	142	32	177.5	12.2	~8x wall load	---
15	148	33	185.0	12.7	---	---
16	160	36	200.0	13.7	~9x wall load	3rd set of cracks observed
17	166	37	207.5	14.2	---	---
18	172	39	215.0	14.7	---	---
19	178	40	222.5	15.2	~10x wall load	---
20	184	41	230.0	15.8	---	4th set of cracks observed
21	190	43	237.5	16.3	---	---
22	196	44	245.0	16.8	~11x wall load	Ultimate Capacity

6.5.8 Experimental Results

The ultimate capacity of the FRP rehabilitated deck slab was reached at an applied load of 196 kN (44 kips) per hydraulic jack, equivalent to a uniform distributed load of 245 kN/m (16.8 kip/ft), which is 11 x the nominal sound wall load. At this load level, the deflection of the middle of the slab under the loading beam was 8.73 mm (0.34 in). The maximum strain value achieved in the CFRP strips at ultimate capacity was 3846 microstrains. At the ultimate capacity of the specimen, debonding of the FRP from the concrete occurred due to a tensile failure of the concrete cover layer located between the FRP and the top layer of rebar. This loss of compatibility within the section was quickly followed by the opening and propagation of a large diagonal crack along the compression strut formed with the adjacent stem wall.

Cracking was observed and marked on the specimen at the four load levels of 116 kN (26 kip), 136 kN (31 kip), 160 kN (36 kip) and 184 kN (41 kip) per hydraulic jack. The extent of visible cracking on the top and sides of the deck of the FRP rehabilitated specimen shown in Figure 6.40 and Figure 6.41 occurred at the load level of 184 kN (41 kip) per hydraulic jack, which was over twice the load at which comparable cracking was observed on the as-built specimen. The comparable initial cracking observed on the as-built specimen occurred at a load level of 84 kN (19 kip) per hydraulic jack and is shown in Figure 6.13 and Figure 6.14. The thin cracking on the top of the deck surface that occurred in the FRP rehabilitated specimen observed at the load level of 184 kN (41 kip) per hydraulic jack was discontinuous and approximately followed the top longitudinal steel reinforcement bars adjacent to the edge of the stem wall as shown in Figure 6.40. Minor diagonal cracks along both the

edges of the slab, which initiated from the top surface of the deck, are shown in Figure 6.41.

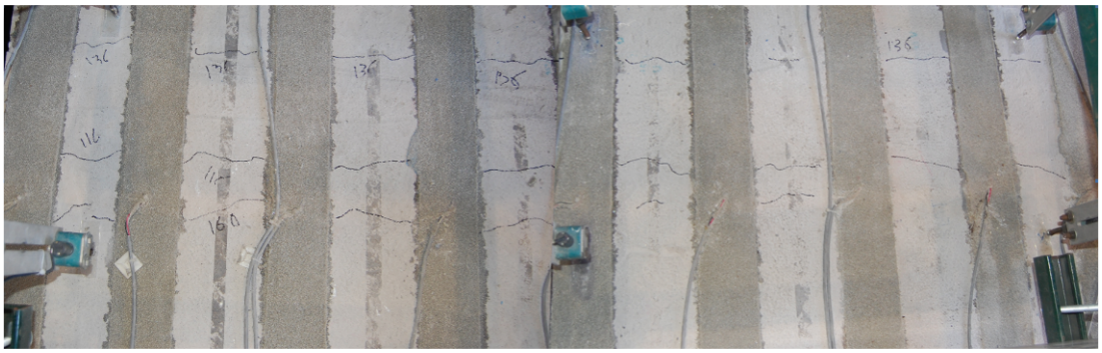

Figure 6.40 Cracking of deck slab at 184 kN (41 kip) per jack- top view of deck

(a) Detail of central edge of slab

(b) Detail of exterior edge of slab

Figure 6.41 Cracking of deck slab at 184 kN (41kip) per jack - side view of deck

When the load level of 196 kN (44 kips) per hydraulic jack was reached, the ultimate tensile strength of the top concrete cover layer was exceeded and the bond between the FRP and the concrete was lost. This damage was quickly followed by the opening and propagation of a large diagonal crack along the compression strut formed

with the adjacent stem wall shown in Figure 6.42. This load level was determined to be the ultimate capacity of the overhang for resisting vertical loads.

(a) Central side of slab (b) Exterior side of slab

Figure 6.42 Cracking observed at ultimate capacity- side view of deck

The top surface of the deck slab after failure of the specimen can be observed in Figure 6.43 and the cracking due to the interfacial failure between the FRP strips and the concrete can be observed in the in the upper left hand corner of Figure 6.43, adjacent to the loading beam.

Figure 6.43 Cracking of deck slab at ultimate capacity- top view of deck

After the loading of the specimen was completed, all testing equipment and instrumentation was fully removed to allow for easier observation of the damage present on the specimen. Figure 6.66 shows the top view of the deck at ultimate capacity. Any loose concrete was removed in order to better observe the failure surfaces, however unlike the as-built specimen in which significant loose concrete was removed after it was tested, nearly all of the concrete remained attached to the tested FRP rehabilitated specimen, despite the interfacial failure that occurred between the FRP and the concrete. Note that the debonding of the CFRP strips from the concrete occurred adjacent to where the tensile stresses on the top of the deck are maximum while the CFRP strips remained attached for the majority of the of the slab overhang.

Figure 6.44 Side view of tested FRP rehabilitated specimen after removal of loose concrete

As observed in Figure 6.45, the three linear potentiometers directly below the loading beam maintained comparable deflections throughout the loading range applied to the test specimen. At the failure load for the specimen, the deflections of these three linear potentiometers were within 10% of each other which corresponds to less than 1 mm (0.04 in) difference in deflection values.

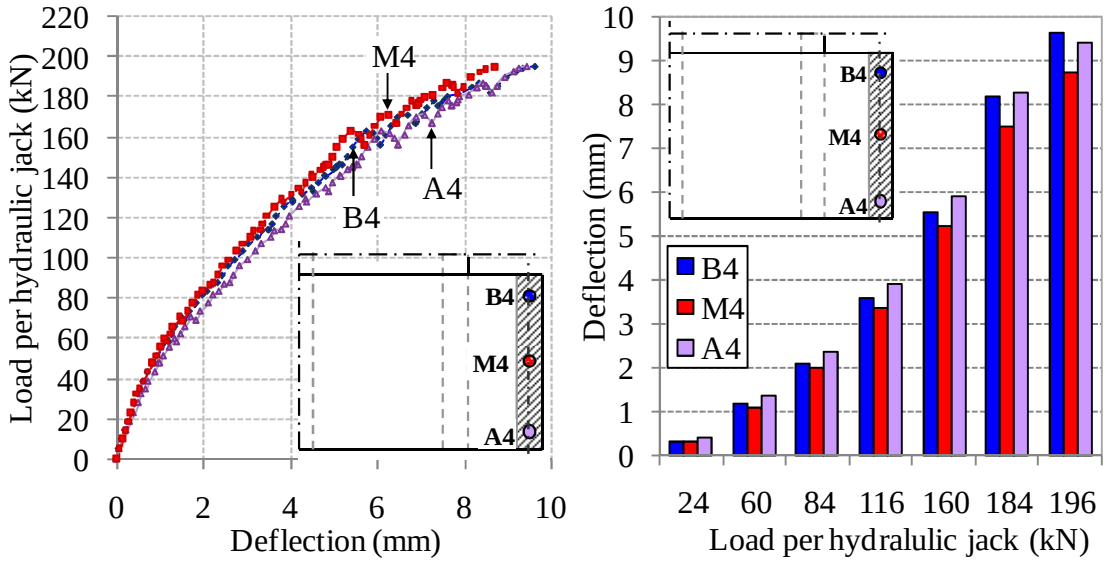

(a) Load versus deflection profiles

(b) Comparison of linear potentiometers below loading beam

Figure 6.45 Comparisons of deflections at the edge of the deck slab overhang

The profiles along the center of the specimen (Figure 6.47) and at both edges (Figure 6.46 and Figure 6.48) shown below exhibit similar deflection profiles throughout the loading range.

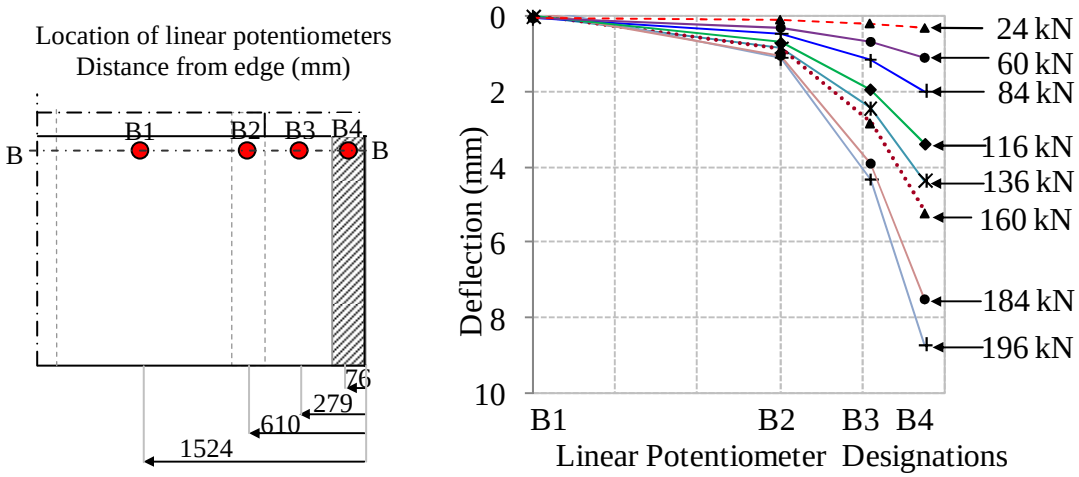

Figure 6.46 Deflection profile along the central edge of specimen (Line B)

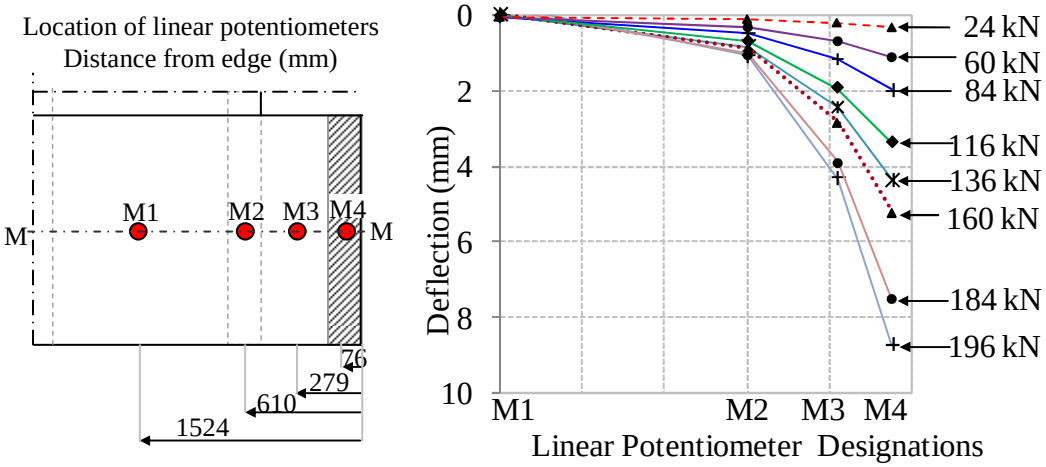

Figure 6.47 Deflection profile along center of specimen (Line M)

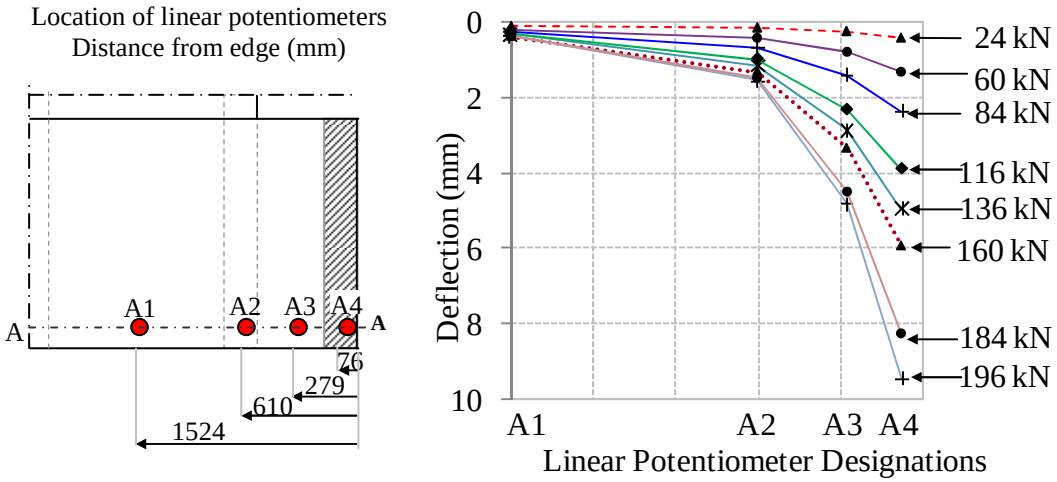

Figure 6.48 Deflection profile along the outer edge of specimen (Line A)

The deflection profiles shown in Figure 6.49 and Figure 6.50 also indicate comparable deflections along the overhang at a distance midway to the adjacent stem wall and directly below the point of load application respectively.

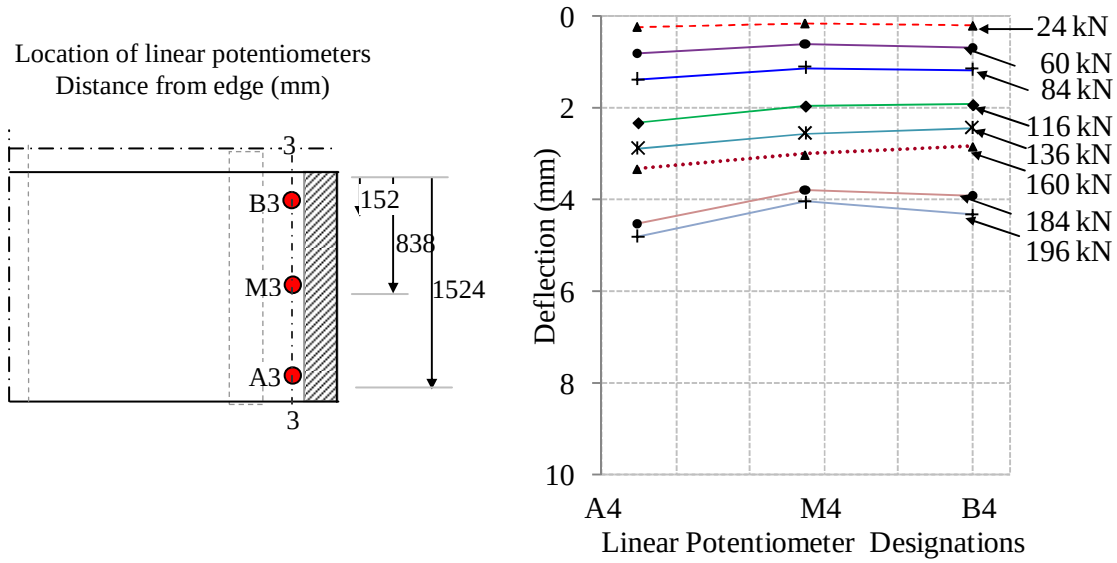

Figure 6.49 Deflections midway along overhang (Line 3)

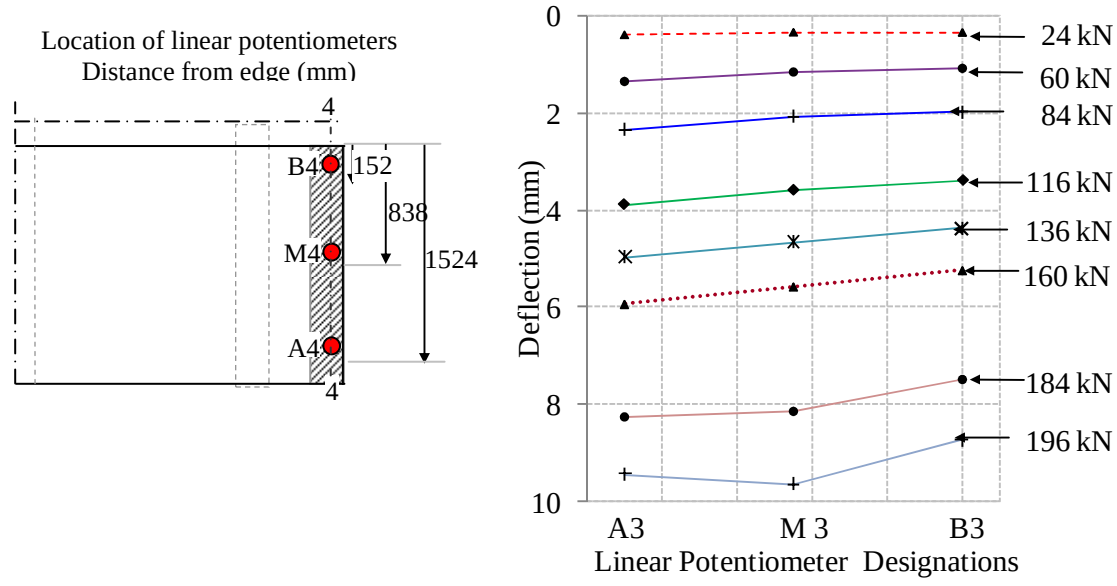

Figure 6.50 Deflections directly below loading beam (Line 4)

The strains in the FRP strips are also examined throughout the NSM CFRP rehabilitated specimen. The strain profiles along the edges and the middle of the specimen are shown in Figure 6.51, Figure 6.53, and Figure 6.52 respectively. These strain profiles indicate that the maximum strain in the CFRP strips occurs directly above the edge of the stem wall adjacent to the deck slab overhang, referred to with the designation, “line B”. At ultimate capacity, the maximum strain in the specimen of 3846 microstrains occurs in strain gage 4B, which is located in line B near the middle of the specimen overhang.

The strains drop off sharply for distances further away from the end of the overhang, with the majority of the strain gages on the opposite side of the stem wall (line C) exhibiting less than a third of the strain values shown in line B.

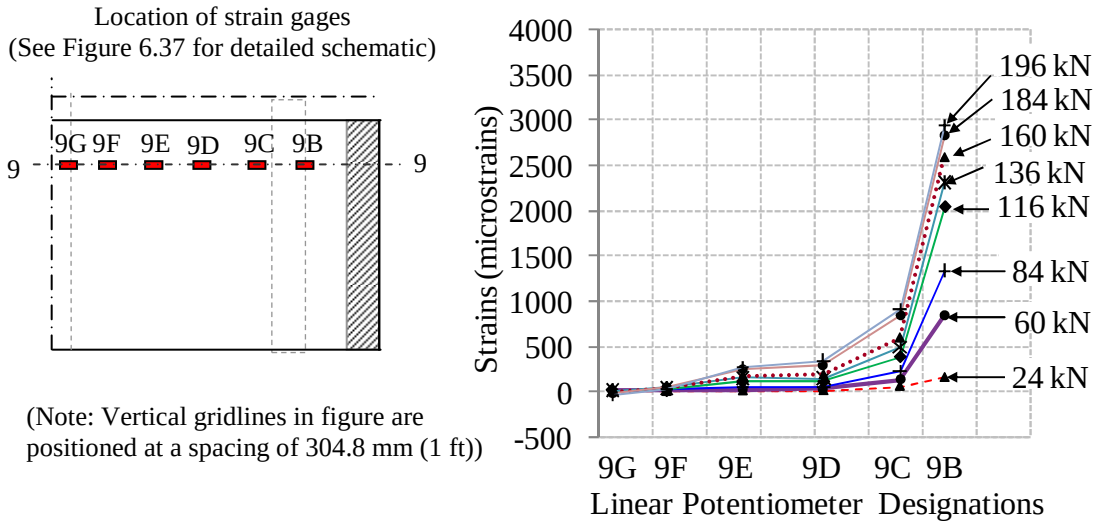

Figure 6.51 Strain profile along the central edge of specimen (Line 9)

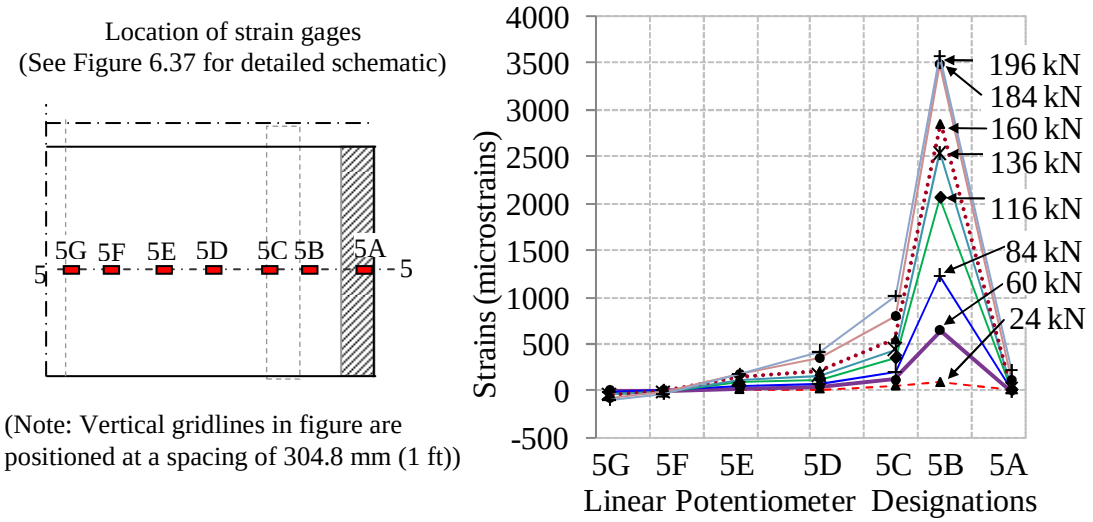

Figure 6.52 Strain profile along the middle of specimen (Line 5)

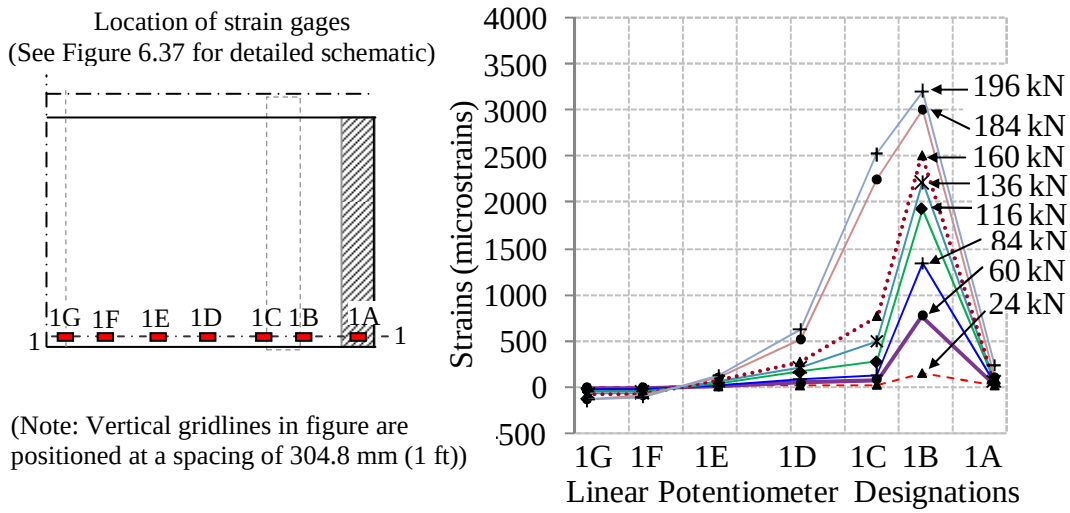

Figure 6.53 Strain profile along the outer edge of specimen (Line 1)

The sharp drop in strain values at distances away from the adjacent stem wall and the insignificant strains within these regions indicate that the significantly shorter lengths of CFRP strips could be used to optimize material usage and improve constructability without affecting load transfer and the overall system response. The strains along line

B, the location where the maximum strains occur in the specimen is shown in Figure 6.54. This figure indicates that the distribution of strains was even along the specimen until the load level of 116 kN (26 kip) per jack was reached. At this level, cracking was first observed on the specimen and higher loading levels showed comparable but slightly less uniform strains along the specimen. The average strain along line B in the specimen at ultimate capacity was 3423 microstrains, whereas the minimum and maximum strains along line B were 2943 microstrains and 3846 microstrains respectively.

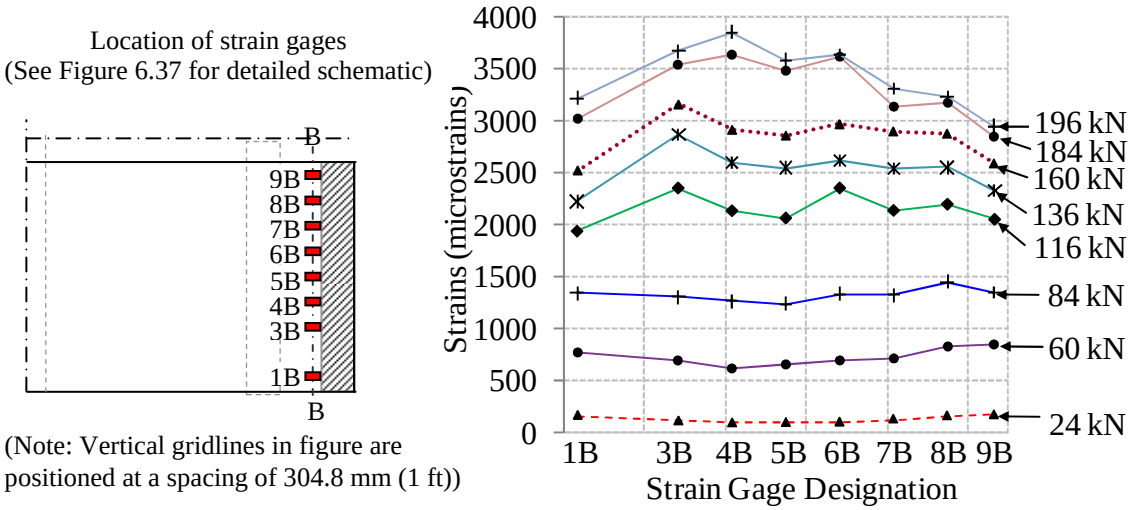

Figure 6.54 Strains along the edge of the stem adjacent to the deck overhang (Line B)

Using the strain data throughout the specimen and following a procedure described by Siem *et al*. [166], the shear stress between the concrete and the CFRP strips were calculated using the following equation:

$$\bar{\tau}_{n,n+1} = \left| \frac{(\varepsilon_{n+1} - \varepsilon_n) \cdot E_L \cdot t_L}{(x_{n+1} - x_n)} \right| \qquad 6.11$$

where

$(x_{n+1} - x_n)$ = Distance between two strain gages

E_L = Tensile elastic modulus of the CFRP strip

t_L = Thickness of the CFRP strips

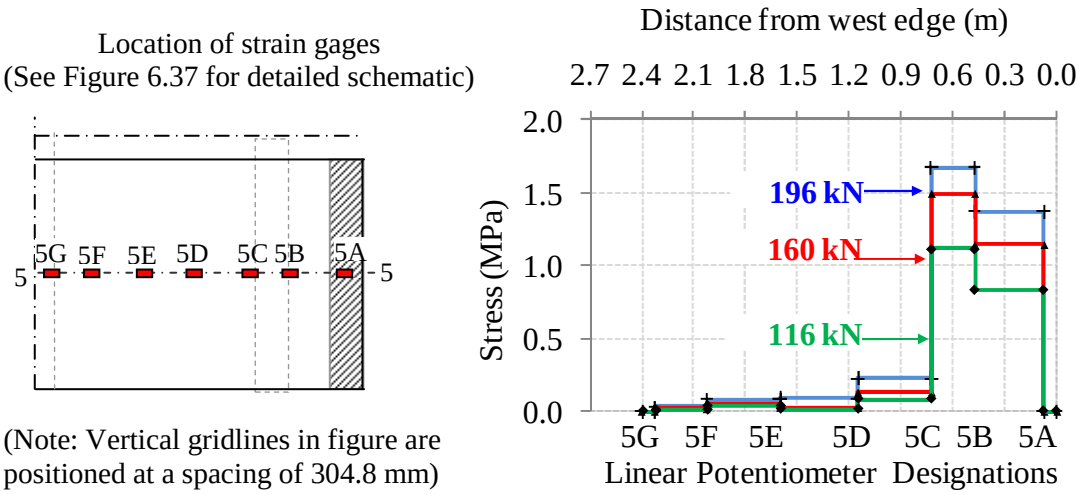

Figure 6.55 Shear stress distribution within adhesive along the middle of specimen (Line 5)

The calculated shear stress values within the adhesive are simply the mean value between two strain gages, which ignore localized stress peaks and gradients.

After the testing of the NSM CFRP rehabilitated specimen was completed, the overhang of the specimen was cut off and carefully removed from the rest of the test specimen as shown in Figure 6.56 to allow for further examination of this critical region. One point of interest to examine on the removed overhang was the actual location of the CFRP strip reinforcement within the section. Figure 6.57 shows that the actual embedment depth of the near surface mounted CFRP strips was

approximately 6 mm (0.25 in) and the actual thickness of the SikaDur 30 resin layer used to bond the CFRP strips to the concrete was also approximately 6 mm (0.25 mm). An embedment depth of 6 mm (0.25 in) is reasonable for NSM applications because it allows enough space for an adequate top surface of resin, which will serve as environmental protection and the wear surface for the deck. However, the 6 mm (0.25 mm) thickness of the SikaDur 30 bottom resin layer was exceeded the maximum manufacturer recommended value of 3 mm (1/8 inch).

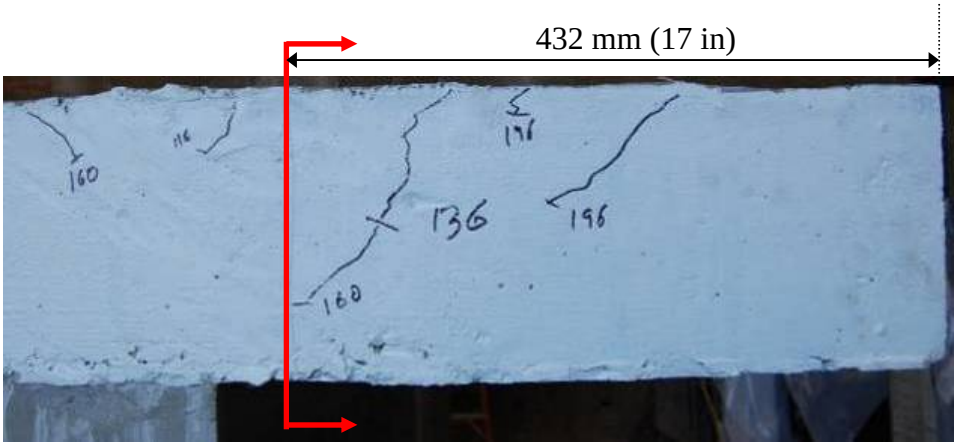

Figure 6.56 Location of cut for removal of FRP strengthened overhang

Figure 6.57 Detail showing actual location of reinforcement

While the current system performed very well, the use of an overly thick resin layer could have had a negative effect on the overall structural response of the system. Figure 6.58 shows the failure surface of an FRP strip, which has been detached from the top surface of the deck. The center portion of the strip with the firmly attached concrete was the region in which the interfacial failure in the concrete occurred, while the outer sections of the strip were neatly detached from the resin system, due to the method of removal of the strip.

Figure 6.58 Detail of failure surface of FRP strip

6.5.9 Comparison with Theory

The NSM CFRP rehabilitated specimen reached ultimate capacity under an applied load of 196 kN (44 kip) per hydraulic jack which is equivalent to an applied moment of 189.2 kN-m (139.2 kip-ft). This improved performance corresponds to a 72% increase in ultimate capacity over the as-built specimen, which failed under an

applied load of 114 kN (26 kip) corresponding to an applied moment of 110.0 kN-m (81.0 kip-ft). The ACI 440-02 calculation for externally bonded FRP reinforcement predicted a maximum moment capacity of 166.0 kN-m (122.4 kip-ft), which corresponds to a 51% increase in load carrying capacity over the experimentally determined capacity of the as-built specimen. The moment curvature analysis predicted a maximum moment capacity of 185.5 kN-m (136.4 kip-ft), which corresponds to a 69% increase in load carrying capacity over the as-built specimen. The theoretical predictions and experimental results were within 12% using the ACI 440 approach and were in close agreement with only a 2% error using the moment curvature analysis. The larger disagreement with experimental data found from the ACI 440 moment capacity increase equation likely exists because this calculation is a more simplified approach that does not take into account the over strength of the steel reinforcement.

The predicted deflections for the overhang provide good correlation up until a load of approximately 160 kN/jack and under predict deflections for higher loads. This under-prediction is likely caused by the analytical model assumption that full composite action is maintained for the section throughout the loading range, because failure in the concrete directly adjacent to the CFRP strips was observed.

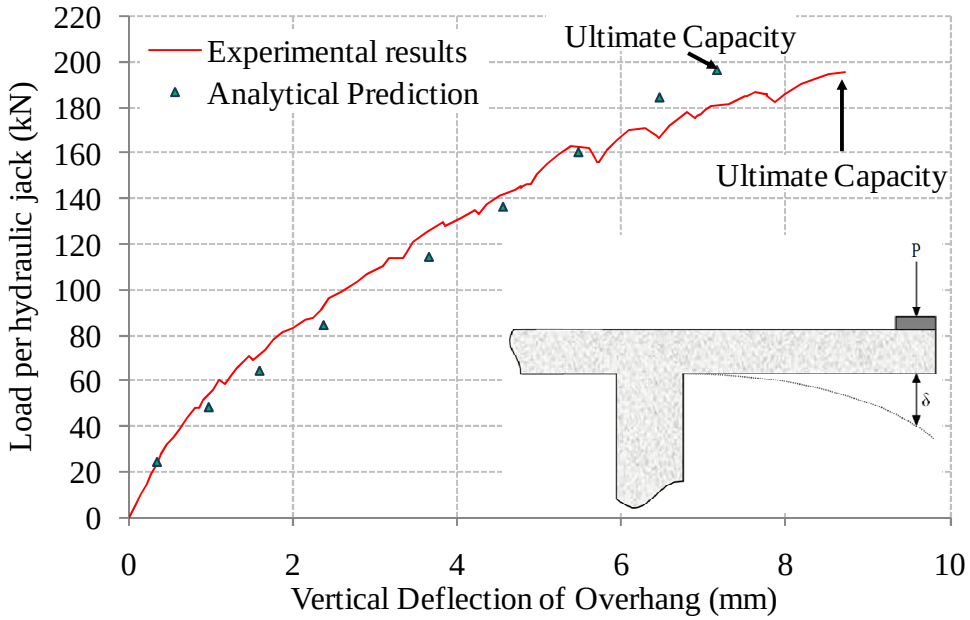

Figure 6.59 Experimental and analytical load versus deflection plots for FRP strengthened deck overhang

6.6 COMPARISON OF FRP STRENGTHENED AND AS-BUILT OVERHANGS

The ultimate capacity of the near surface mounted CFRP strip rehabilitated slab was reached at an applied load of 196 kN (44 kips), equivalent to a uniform distributed load of 245 kN/m (16.8 kip/ft), which is 11 x the nominal sound wall load. This ultimate capacity is 78% greater than that obtained by the as-built specimen, which occurred at 114 kN (26 kips) per hydraulic jack, equivalent to a uniform distributed load of 142.5 kN/m (9.8 kip/ft), which is 6.33x the nominal wall load. The center deflections under the loading beam for both specimens over the complete loading ranges applied are compared in Figure 6.60 and Figure 6.61.

At the failure load level of the as-built specimen, the as-built specimen had a center deflection under the loading beam of 6.36 mm (0.25 in) whereas the FRP rehabilitated specimen deflected approximately half that of the as-built specimen, or 3.33 mm (0.13 in). At ultimate capacity of the FRP rehabilitated specimen, the center deflection under the loading beam was 8.73 mm (0.34 in), which indicates the rehabilitated specimen exhibited a 31.8% increase in deformation capacity over the as-built specimen.

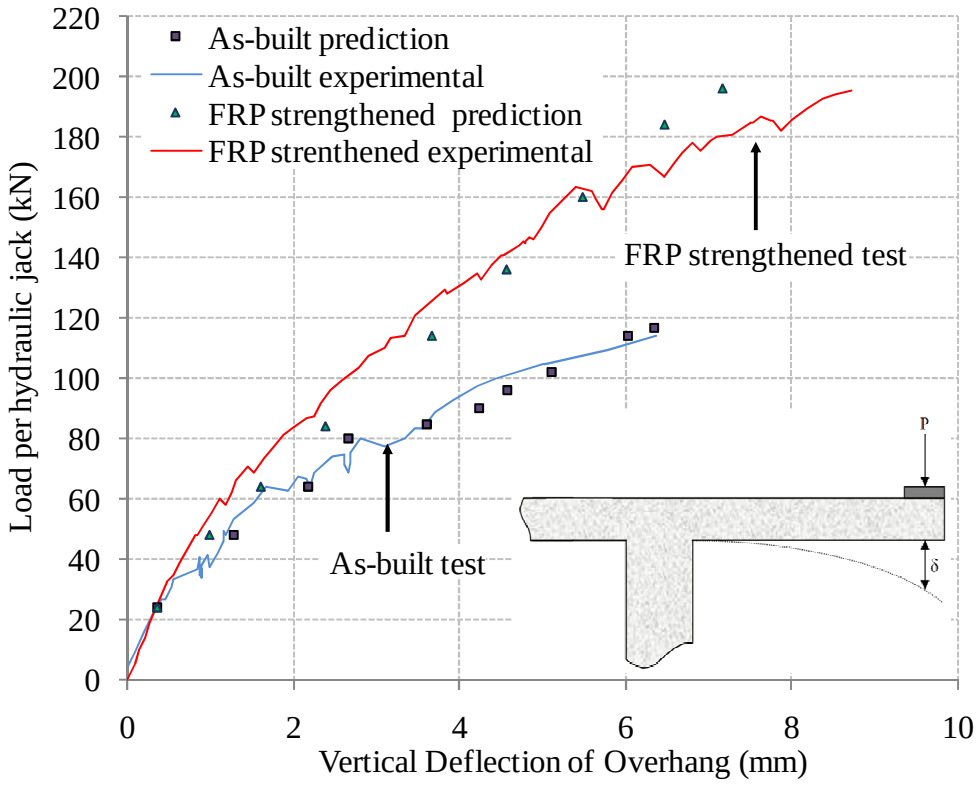

Figure 6.60 Comparison of load versus deflection profiles for deck overhang (Deflections are measured from the location below the center of the loading beam)

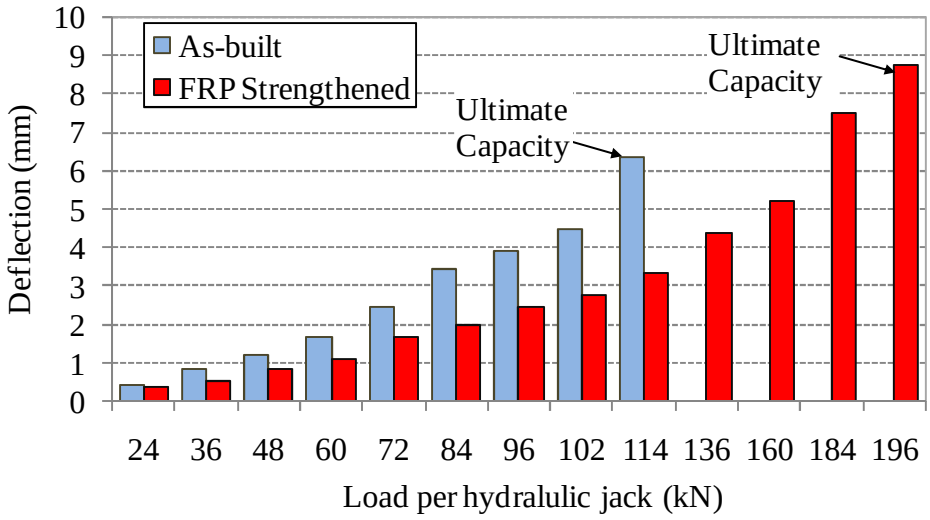

Figure 6.61 Comparisons of deflections of the deck overhang at different load levels (Deflections are measured from the location below the center of the loading beam)

In addition to increasing the overall load and deformation capacity of the system, the near surface mounted CFRP strips act to increase the stiffness and improve the stability of the system. The load versus deflection profile shown in Figure 6.60 shows the significantly increased stiffness and more linear profile for the FRP rehabilitated specimen over the as-built specimen.

The deflection profile comparison at the 114 kN (26 kip) per jack load level along the middle of the two slabs is shown in Figure 6.62. This figure illustrates that for the same load level, the deflections within the FRP rehabilitated specimen are lower than the deflections of the as-built specimen throughout the deck slab and not just at the point of load application. The first set cracking observed on the as-built specimen occurred at the load level of 84 kN (19 kip), whereas the first set cracking observed on the FRP rehabilitated specimen occurred at 116 kN (26 kip), which is

corresponds to a 38% greater load. A comparison of the deflection profiles along the center of the specimens at these loading levels shown in Figure 6.63 reveals nearly identical deformations for the two specimens.

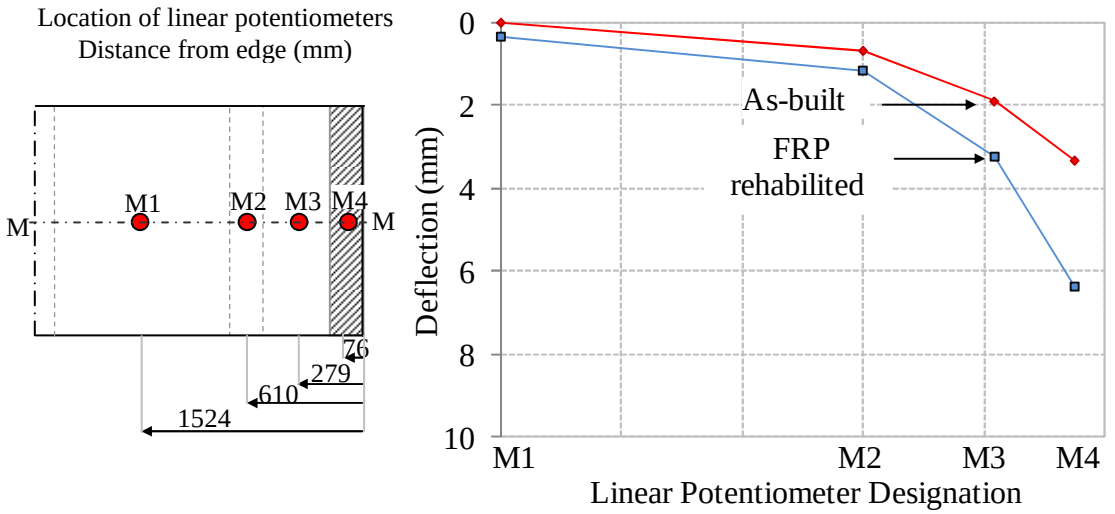

Figure 6.62 Comparison of center deflection profiles (Line M) at a load level of 114 kN (26 kip) per jack

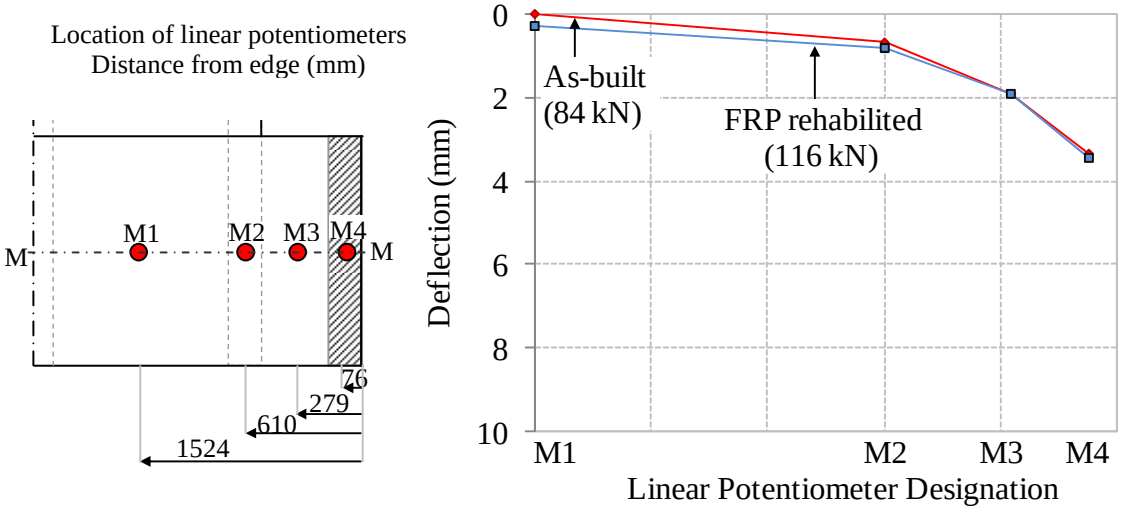

Figure 6.63 Comparison of center deflection profiles (Line M) at 1st observed cracking loads

The second set of cracking observed on the as-built specimen occurred at the load level of 101 kN (23 kip), whereas the second set of cracking observed on the FRP rehabilitated specimen occurred at 136 kN (31 kip), which is corresponds to a 35% greater load. The deflection profile comparison at the load levels where the second set of cracking was observed in Figure 6.67 also exhibits nearly identical deformations for the two specimens. This indicates that while the FRP reinforcement acts to stiffen the system and increase the load carrying capacity of the overhang region, the shape of the deflection response profile of the system is not modified significantly with the addition of the CFRP strips.

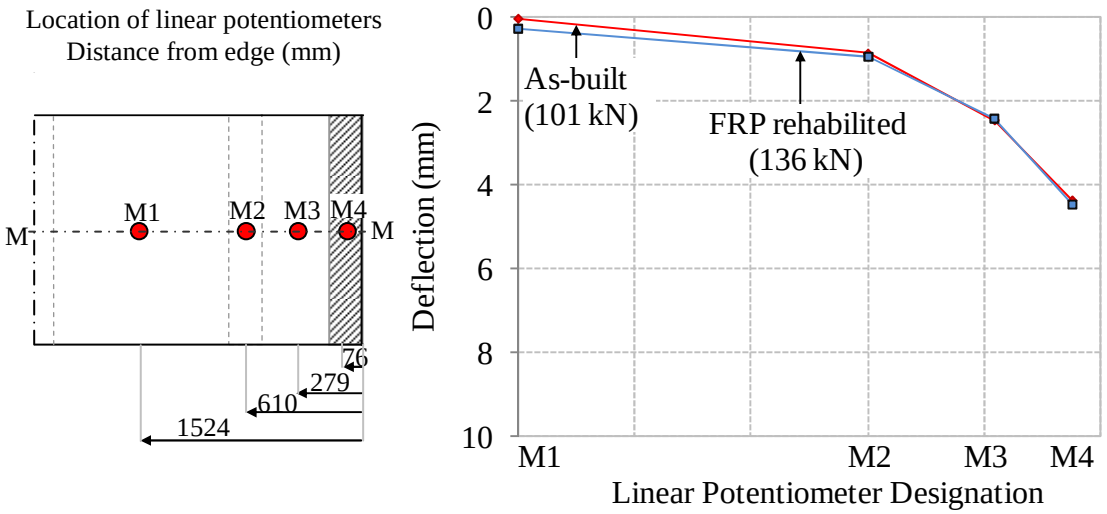

Figure 6.64 Comparison of center deflection profiles at 2nd observed cracking loads (Line M)

Figure 6.67 shows the side by side top decks of the two specimens after testing has been completed and all loose concrete on the top deck removed. Details of the critical region of the as-built and FRP rehabilitated top deck are shown in Figure 6.65

and Figure 6.66 respectively. For the as-built specimen, extensive damage and spalling of the concrete on the top of the deck slab was seen. Yielding in the transverse steel reinforcement followed by loss of aggregate interlock, resulting in failure was observed. For the FRP rehabilitated specimen, negligible spalled concrete and loose concrete rubble was detected. A concrete splitting failure mode was observed in the FRP rehabilitated specimen.

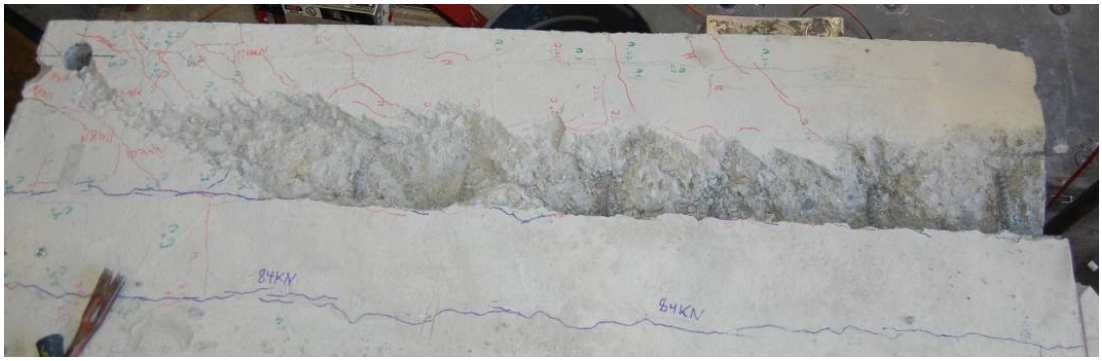

Figure 6.65 Detail of cracking observed at ultimate capacity- top view of as-built deck

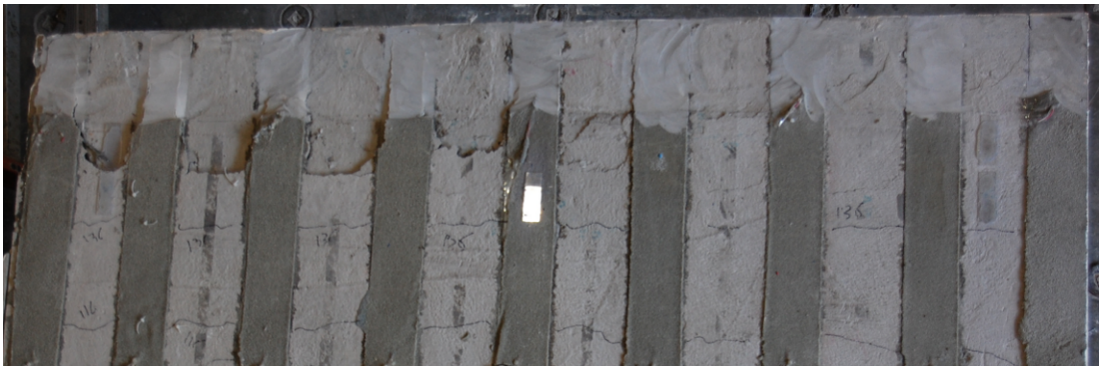

Figure 6.66 Detail of cracking observed at ultimate capacity- top view of FRP rehabilitated deck

Figure 6.67 Top view of deck slab tested to ultimate capacity after removal of loose concrete

6.7 SUMMARY OF RESULTS

Experimental results from the testing of the rehabilitated specimen indicate that the NSMR strengthening scheme was successful at achieving the desired load carrying capacity increase. The ultimate load carrying capacity of the FRP rehabilitated specimen was 196 kN (44 kips) per hydraulic jack, which was 78% higher that the ultimate load of the as-built specimen of 114 kN (26 kips) per hydraulic jack. This value well exceeded the desired load capacity increase of 29.7% above the experimentally determined capacity of the as-built specimen, exhibited a very stable structural response and increased the deformation capacity of the system. The theoretical moment capacity predictions for the as-built specimen were within 11% and 6.5% of the experimentally determined value using ACI 318 and moment curvature analysis respectively. The theoretical moment capacity predictions for the FRP rehabilitated specimen were within 12% of the experimental value using the modified ACI 440-02 approach and were within 2 % using moment curvature analysis.

The NSM FRP rehabilitated specimen exhibits a variety of structural performance improvements over the as-built specimen including increased ultimate load carrying capacity, enhanced deformation capacity and more stable overall structural performance. Design options for the near surface mounted CFRP strengthening schemes allow for great flexibility in terms of tailoring the reinforcement parameters for specific applications. With consideration of the minimal disruption to traffic flow and ease of installation, this system is a viable and very attractive rehabilitation option for bridge deck slab overhangs.

7 CONCLUSIONS AND RECOMMENDATIONS FOR FUTURE WORK

7.1 SUMMARY AND CONCLUSIONS

As the nation's inventory of concrete box girder bridges deteriorate over time and more bridges are in need of repair or replacement, the development of improved rehabilitation techniques becomes increasingly important. Rapid rehabilitation techniques that use FRP materials can provide significant advantages over use of conventional materials in terms of potential for enhanced durability, increased construction schedules and optimized material usage.

The current research has focused primarily on two aspects related to the use of FRP composites for rapid rehabilitation of reinforced concrete box girder bridges. The development, assessment and validation of a FRP stay-in-place combined formwork and reinforcement system as part of a structural system for the deck of a reinforced concrete box girder bridge were addressed in this research. The examination of rapid rehabilitation technique of minimally invasive flexural strengthening of box girder bridge overhangs using NSM FRP reinforcement placed into shallow groves on the top of the bridge deck, was also addressed. The primary findings of these research endeavors as well as recommendations for future research are presented in this section.

7.1.1 FRP Panel SIP Structural Formwork System for Box Girder Bridges

The developed hybrid FRP-concrete bridge deck system provides an alternative rehabilitation and replacement option for deteriorated bridge decks. The stiffened FRP structural formwork panels serve as positive moment reinforcement in

place of corrosion prone steel as well as stay-in-place formwork for the bridge deck of a concrete box girder bridge. By combining the installation of formwork and the lower level of reinforcement into a single construction step, this system improves construction efficiency and speed, resulting in significant labor savings and accelerated construction schedules.

The experimental investigation of two full scale two-cell box girder bridge specimens provided the current research with enhanced relevance for addressing rehabilitation needs facing current the nation's aging box girder bridges. Data from the casting of the concrete deck showed that the change in temperature due to the casting of the concrete had minimal impact on the performance of the system and the deflection of the FRP panels was within allowable limits. The FRP panel bridge deck system has significant reserve strengths, with experimentally determined safety limit state for the system occurring at approximately nine times AASHTO factored service load. The observed failure mode of the system was crushing of the concrete in compression, which is the preferred failure mode for this type of hybrid FRP-concrete system, rather than the catastrophic failure that accompanies FRP rupture. The system exhibited a stable post-failure structural response under cyclic loading of over twice the AASHTO factored service load.

Fundamental comparisons between a conventional steel reinforced concrete system and the composite SIP structural formwork panel system, showed comparable performance in terms of numerous metrics including deflection distributions, distribution widths and strain profiles. The FRP panel system exhibited superior performance in comparison with the RC system in terms of reduced damage

accumulation throughout the application of 32,000 cycles at loads up to 5x the AASHTO cyclic load. Table 7.1 provides a brief summary of the relative performance of the FRP panel bridge deck system and the reinforced concrete bridge deck system.

Table 7.1 Performance comparison between FRP panel system and RC system

PERFORMANCE CHARACTERISTIC ASSESSED	DECK SYSTEM WITH SUPERIOR PERFORMANCE	
	FRP panel system	Conventional RC system
Labor required for construction of deck system	✓	
Deflection of formwork during casting of deck concrete	✓	
Cracks observed on top of bridge deck	✓	
Center deflection at 1x the AASHTO service load	Comparable performance	
Center deflection at maximum applied load	✓	
Secant stiffness changes throughout loading range	✓	
Deflection profiles	Comparable performance	
Residual deflections	✓	
Strain profiles	Comparable performance	
Structural response under extensive cyclic loading	✓	

The resin injection repair technique, utilized on the post-failure test specimen to reinstate load transfer between the concrete and the composite, was successful at improving the structural response of the system and the repaired system was able to perform comparably to the undamaged test specimen, with superior integrity of the concrete-FRP panel and response to cyclic loading.

7.1.2 Rehabilitation of Bridge Decks Using Near Surface Mounted FRP

Near surface mounted FRP composites have significant advantages over surface mounted composites for numerous reasons including improved structural efficiency, reduction in necessary surface preparation, better protection for the FRP reinforcement from the surrounding environment, and decreased likelihood of exhibiting debonding failure modes as discussed in the literature review conducted, which is summarized in Section 2.4. Rectangular FRP strips were also shown to be superior as compared to square or round FRP bars in terms of improved material efficiency, smaller groove dimension needed, better three-dimensional distribution of bond stresses, and larger perimeter to cross-sectional area ratios.

Different NSM FRP designs were evaluated as options for flexural strengthening of a reinforced concrete bridge deck overhang. The strengthening scheme which most efficiently satisfied necessary strength requirements and design guidelines while taking construction considerations into account was used to strengthen a 1.68 m (5 ft 6 in) long section of bridge deck overhang. summarizes the different FRP reinforcement systems evaluated as potential strengthening options and illustrates that the chosen system, 50 mm (2 in) wide strips, easily satisfies the desired capacity increase requirement of 29% greater moment capacity as compared to the as-built overhang. The chosen strengthening scheme also has 18% greater structural efficiency than comparable strengthening schemes which use bars or rods.

A full cure of the resin system used to attach the FRP reinforcement was determined through monitoring the progression of the resin system’s glass transition temp temperature to be achieved after approximately 4-5 days. Results from the NSM

FRP strengthened overhang showed a 78% increase in ultimate load carrying capacity as well as a 32% increase in deformation capacity as compared to the as-built specimen without FRP.

7.2 CONCLUSIONS

7.2.1 FRP Panel SIP Structural Formwork System for Box Girder Bridges

Based on this research, the following primary conclusions are summarized:

1) The assessed FRP panel bridge deck system validates the efficacy of hybridization with optimized material usage;
2) The modular prefabricated panels and their role as stay-in-place structural formwork enable rapid placement and significant labor savings, with a straightforward construction process similar to a conventional reinforced concrete bridge deck;
3) The FRP panel system has applicability for repair or replacement of bridge decks between girders, either for small sections of a bridge deck or for the entire bridge. The FRP panel system also indicates potential for new construction of decks for box girder bridges or other slab-on-girder bridge systems;
4) Concrete shear damage in the bridge deck system can be mitigated by the presence of the FRP panels such that the punching shear failure mode, which normally results in a catastrophic failure for a conventional reinforced concrete deck, is avoided;

5) The service load the distribution width of the FRP panel system is comparable to the reinforced concrete bridge deck system;
6) The resin injection system employed was shown be a simple and very effective repair method for reinstating load transfer between the FRP panel and the concrete; and
7) The results from this research indicate that the developed FRP structural formwork system is a viable alternative to a conventional steel reinforced concrete bridge deck;

7.2.2 Rehabilitation of Bridge Decks Using Near Surface Mounted FRP

Based on this research, the following primary conclusions are summarized:

1) The use of near surface mounted FRP reinforcement offers an effective and minimally invasive rapid rehabilitation technique for strengthening the negative moment regions of a bridge deck;
2) The addition of NSM strengthening can significantly increase both the load carrying capacity and the deformation capacity of a concrete bridge deck overhang;
3) The developed analytical methods provided an effective means for predicting load carrying capacity of the NSM strengthened overhang region as well as the deflections and strains in the system at different loading levels. The analytical methods can be used as part of the design process for future NSM strengthening projects;

4) Strengthening of a bridge deck overhang using NSM strips can be feasibly achieved with partial closure of the bridge for only a few days, as compared to a bridge closure for well over a month that would be necessary for a partial rebuild of the deck using conventional reinforced concrete construction.
5) Strains in the FRP strips are significantly reduced in regions beyond the girder stems, which indicate that further curtailment of the FRP reinforcement is possible in order to improve the cost effectiveness of the system; and

7.3 RECOMMENDATIONS FOR FUTURE RESEARCH

7.3.1 FRP Panel SIP Structural Formwork System for Box Girder Bridges

There are several topics which should be addressed further through future research. Based on the observations regarding loads at which changes to the composite action between the FRP panels and the concrete occurred, further examination of the interface between the concrete and the FRP panels is recommended. This would provide useful information on design modifications that would ensure composite action is maintained between the two materials. Although the analysis of the structural response of the system in terms of load transfer between panels and from panels to surrounding concrete deck and stems was addressed in a very preliminary form in this research, further experimental and analytical investigations which apply loading at different positions in relation to the FRP deck

panels would be extremely useful. The development of detailed design guidelines which address aspects specifically relevant to the design of this type of bridge deck structure is also recommended.

7.3.2 Rehabilitation of Bridge Decks Using Near Surface Mounted FRP

Since the field of near surface mounted FRP reinforcement is still relatively new, with the most significant research activity occurring during the past ten years, there are a variety of aspects which can benefit from further research. There has been significant experimental work on bond tests, however work is still needed to provide improved correlations between bond testing experiments performance of flexural tests of NSM FRP systems. Since the efficacy of NSM FRP strengthening is intrinsically related to the ability of the adhesive to not only bond to the reinforcement to the concrete substrate but also to enable efficient stress transfer, study also needs to be conducted on adhesive rheology, performance characteristics, durability, and cure. Also, since it is likely that the NSM will be covered by asphalt, the effect of heat due to asphalt on the adhesive and bond should be studied.

The optimization of groove dimensions and spacing for NSM use through both analytical and experimental study is recommended. A study of adhesive rheology and bond quality as well as durability would also provide useful information for further progression of this research. The examination of the minimum required development length and the effect of the girder stems on the necessary development length are also recommended. It is emphasized that the studies recommended should be conducted on specimens of sufficient size since small scale tests would likely provide erroneous

results due to effects of scale and configuration. Finally, the development of design guidelines and development of examples comparing NSM use to surface bonding would provide significant benefit to this research field.

REFERENCES

1. American Society of Civil Engineers., *Report card for America's infrastructure,* 2009 Report card for America's infrastructure advisory council., Editor. 2009, American Society of Civil Engineers. pp. 160.

2. American Association of State Highway and Transportation Officials., *Bridging the gap: restoring and rebuilding the nation's bridges*. 2008, American Association of State and Highway Transportation Officials. pp. 68.

3. National Surface Tranportation Policy and Revenue Study Commission., *Transportation for tomorrow,* in *Report of the National Surface Transportation Policy and Revenue Study Commission*. 2007.

4. Bettigole, N.H., *Replacing bridge decks.* Civil Engineering, 1990. **60**(9): pp. 76-77.

5. Karbhari, V.M. and L. Zhao, *Use of composites for 21st century civil infrastructure.* Computer Methods in Applied Mechanics and Engineering, 2000. **185**(2-4): pp. 433-454.

6. Bettigole, N.H. and R. Robinson, *Bridge decks: design, construction, rehabilitation, replacement*. 1997, New York, New York: American Society of Civil Engineers (ASCE) Press. pp.

7. Kay, T., *Assessment and rennovation of concrete structures*. 1992, Harlow, Essex, England: Longman Scientific & Technical. 224. pp.

8. Menzies, T.R., *Corrosion forms and control for infrastructure, ASTM STP 1137,* ed. V. Chaker. 1991. pp.

9. Danish Standards Association., *Repair of concrete structures to EN 1504*. 2004, Jordon Hill, Oxford., Burlington, Massachusetts Elsevier Butterworth-Heinemann. pp.

10. Xanthakos, P.P., *Bridge strengthening and rehabilitation.* Transportation structures series. 1996, Upper Saddle River, New Jersey: Prentice Hall. 966. pp.

11. Keller, T., *Use of fiber reinforced polymers in bridge construction*. Structural engineering document 7. 2003, Zurich, Switzerland: International Association for Bridge and Structural Engineering. 131. pp.

12. Nanni, A., *Composites: coming on strong.* Concrete Construction, 1999. **44**(1): pp. 120-124.

13. Zureick, A.H., B. Shih, and E. Munley, *Fiber-Reinforced Polymeric Bridge Decks.* Structural Engineering Review, 1995. **7**(3): pp. 257-266.

14. Zhou, A.X., J.T. Coleman, A.B. Temeles, J.J. Lesko, and T.E. Cousins, *Laboratory and field performance of cellular fiber-reinforced polymer composite bridge deck systems.* Journal of Composites for Construction, 2005. **9**(5): pp. 458-467.

15. Wu, H.C., G. Fu, R.F. Gibson, A. Yan, K. Warnemuende, and V. Anumandla, *Durability of FRP composite bridge deck materials under freeze-thaw and low temperature conditions.* ASCE Journal of Bridge Engineering, 2006. **11**(4): pp. 443-451.

16. Salim, H.A., J.F. Davalos, P.Z. Qiao, and S.A. Kiger, *Analysis and design of fiber reinforced plastic composite deck-and-stringer bridges.* Composite Structures, 1997. **38**(1-4): pp. 295-307.

17. Salim, H.A. and J.F. Davalos, *FRP composite short-span bridges: Analysis, design and testing.* Journal of Advanced Materials, 1999. **31**(1): pp. 18-26.

18. Prachasaree, W., H.V.S. Gangarao, and V. Shekar, *Performance Evaluation of FRP Bridge Deck Under Shear Loads.* Journal of Composite Materials, 2009. **43**(4): pp. 377-395.

19. Park, K.T., S.H. Kim, Y.H. Lee, and Y.K. Hwang, *Pilot test on a developed GFRP bridge deck.* Composite Structures, 2005. **70**(1): pp. 48-59.

20. Liu, Z.H., P.K. Majumdar, T.E. Cousins, and J.J. Lesko, *Development and evaluation of an adhesively bonded panel-to-panel joint for a FRP bridge deck system.* Journal of Composites for Construction, 2008. **12**(2): pp. 224-233.

21. Kumar, P., K. Chandrashekhara, and A. Nanni, *Structural performance of a FRP bridge deck.* Construction and Building Materials, 2004. **18**(1): pp. 35-47.

22. Keller, T. and H. Gurtler, *Quasi-static and fatigue performance of a cellular FRP bridge deck adhesively bonded to steel girders.* Composite Structures, 2005. **70**(4): pp. 484-496.

23. Karbhari, V.M., *Fiber reinforced composite bridge systems - transition from the laboratory to the field.* Composite Structures, 2004. **66**(1-4): pp. 5-16.

24. Jeong, J., Y.H. Lee, K.T. Park, and Y.K. Hwang, *Field and laboratory performance of a rectangular shaped glass fiber reinforced polymer deck.* Composite Structures, 2007. **81**(4): pp. 622-628.

25. Harries, K., *FRP bridge decks - A maturing technology.* ASCE Journal of Bridge Engineering, 2006. **11**(4): pp. 382-382.

26. Busel, J.P., *Engineered FRP bridge decks - Solutions for the future.* SAMPE Journal, 2002. **38**(5): pp. 46-48.

27. Aref, A.J., S. Alampalli, and Y.H. He, *Performance of a fiber reinforced polymer web core skew bridge superstructure. Part 1: field testing and finite element simulations.* Composite Structures, 2005. **69**(4): pp. 491-499.

28. Alampalli, S. and J. Kunin, *Load testing of an FRP bridge deck on a truss bridge.* Applied Composite Materials, 2003. **10**(2): pp. 85-102.

29. Alnahhal, W. and A. Aref, *Structural performance of hybrid fiber reinforced polymer-concrete bridge superstructure systems.* Composite Structures, 2008. **84**(4): pp. 319-336.

30. Aref, A.J., Y. Kitane, and G.C. Lee, *Analysis of hybrid FRP-concrete multi-cell bridge superstructure.* Composite Structures, 2005. **69**(3): pp. 346-359.

31. Bradberry, T.E. *Concrete bridge decks reinforced with fiber-reinforced polymer bars*. in *Design of Structures 2001*. 2001: Trasportation Research Board.

32. Burgueno, R., A. Davol, L. Zhao, F. Seible, and V.M. Karbhari, *Flexural behavior of hybrid fiber-reinforced polymer/concrete beam/slab bridge component.* ACI Structural Journal, 2004. **101**(2): pp. 228-236.

33. Hejll, A., B. Taljsten, and M. Motavalli, *Large scale hybrid FRP composite girders for use in bridge structures - theory, test and field application.* Composites Part B-Engineering, 2005. **36**(8): pp. 573-585.

34. Keller, T., E. Schaumann, and T. Vallee, *Flexural behavior of a hybrid FRP and lightweight concrete sandwich bridge deck.* Composites Part A-Applied Science and Manufacturing, 2007. **38**(3): pp. 879-889.

35. Schaumann, E., T. Vallee, and T. Keller, *Direct load transmission in hybrid FRP and lightweight concrete sandwich bridge deck.* Composites Part A-Applied Science and Manufacturing, 2008. **39**(3): pp. 478-487.

36. Cheng, L.J. and V.M. Karbhari, *New bridge systems using FRP composites and concrete: A state-of-the-art review.* Progress in Structural Engineering and Materials, 2006. **8**(4): pp. 143-154.

37. Bank, L.C. *Application of FRP Composites to Bridges in the USA*. in *Proceedings of the International Colloquium on Application of FRP to Bridges*. 2006. Tokyo, Japan: Japan Society of Civil Engineers (JSCE).

38. Bakis, C.E., L.C. Bank, V.L. Brown, E. Cosenza, J.F. Davalos, J.J. Lesko, A. Machida, S.H. Rizkalla, and T.C. Triantafillou, *Fiber-reinforced polymer*

composites for construction-state-of-the-art review. Journal of Composites for Construction, 2002. **6**(2): pp. 73-87.

39. Keller, T., *Recent all-composite and hybrid fibre-reinforced polymer bridges and buildings.* Progress in Structural Engineering and Materials, 2001. **3**(1): pp. 132-140.

40. Berg, A.C., *Analysis of a bridge deck built on U.S. highway 151 with FRP stay-in-place forms, FRP grids, and FRP rebars.* Thesis submitted to the Department of Civil Engineering in partial fulfillment of the requirements for the degree of Masters of Science, 2004: pp. 289.

41. Nystrom, H.E., S.E. Watkins, A. Nanni, and S. Murray, *Financial viability of fiber-reinforced polymer (FRP) bridges.* ASCE Journal of Management in Engineering, 2003. **19**(1): pp. 2-8.

42. Benmokrane, B., E. El-Salakawy, S. El-Gamal, and S. Goulet, *Construction and testing of an innovative concrete bridge deck totally reinforced with glass FRP bars: Val-Alain Bridge on Highway 20 East.* ASCE Journal of Bridge Engineering, 2007. **12**(5): pp. 632-645.

43. Benmokrane, B., E. El-Salakawy, A. El-Ragaby, and T. Lackey, *Designing and testing of concrete bridge decks reinforced with glass FRP bars.* ASCE Journal of Bridge Engineering, 2006. **11**(2): pp. 217-229.

44. Capozucca, R., *Analysis of the experimental flexural behaviour of a concrete beam grid reinforced with C-FRP bars.* Composite Structures, 2007. **79**(4): pp. 517-526.

45. Cosenza, E., G. Manfredi, and R. Realfonzo, *Development length of FRP straight rebars.* Composites Part B-Engineering, 2002. **33**(7): pp. 493-504.

46. DeLorenzis, L.A., Nanni, A., and A. L. Tegola. *Flexural and shear strengthening of reinforced concrete structures with near-surface-mounted FRP bars*. in *Proceedings of the 3rd international conference on advanced composite materials in bridges and structures*. 2000. Ottawa, Canada.

47. El-Gamal, S., E. El-Salakawy, and B. Benmokrane, *Behavior of concrete bridge deck slabs reinforced with fiber-reinforced polymer bars under concentrated loads.* ACI Structural Journal, 2005. **102**(5): pp. 727-735.

48. El-Gamal, S., E. El-Salakawy, and B. Benmokrane, *Influence of reinforcement on the behavior of concrete bridge deck slabs reinforced with FRP bars.* Journal of Composites for Construction, 2007. **11**(5): pp. 449-458.

49. El-Ragaby, A., E. El-Salakawy, and B. Benmokrane, *Fatigue analysis of concrete bridge deck slabs reinforced with E-glass/vinyl ester FRP reinforcing bars.* Composites Part B-Engineering, 2007. **38**(5-6): pp. 703-711.

50. El-Ragaby, A., E. El-Salakawy, and B. Benmokrane, *Fatigue life evaluation of concrete bridge deck slabs reinforced with glass FRP composite bars.* Journal of Composites for Construction, 2007. **11**(3): pp. 258-268.

51. El-Salakawy, E., B. Benmokrane, and G. Desgagne, *Fibre-reinforced polymer composite bars for the concrete deck slab of Wotton Bridge.* Canadian Journal of Civil Engineering, 2003. **30**(5): pp. 861-870.

52. El-Salakawy, E., B. Benmokrane, A. El-Ragaby, and D. Nadeau, *Field investigation on the first bridge deck slab reinforced with glass FRP bars constructed in Canada.* Journal of Composites for Construction, 2005. **9**(6): pp. 470-479.

53. El-Salakawy, E., R. Masmoudi, B. Benmokrane, F. Briere, and G. Desgagne, *Pendulum impacts into concrete bridge barriers reinforced with glass fibre reinforced polymer composite bars.* Canadian Journal of Civil Engineering, 2004. **31**(4): pp. 539-552.

54. Theodorakopoulos, D.D. and N. Swamy, *Analytical model to predict punching shear strength of FRP-reinforced concrete flat slabs.* ACI Structural Journal, 2007. **104**(3): pp. 257-266.

55. Bank, L.C., M.G. Oliva, J.S. Russell, D.A. Jacobson, M. Conachen, B. Nelson, and D. McMonigal, *Double-layer prefabricated FRP grids for rapid bridge deck construction: case study.* Journal of Composites for Construction, 2006. **10**(3): pp. 204-212.

56. Banthia, N., M. Alasaly, and S. Ma, *Behavior of Concrete Slabs Reinforced with Fiber-Reinforced Plastic Grid.* Journal of Materials in Civil Engineering, 1995. **7**(4): pp. 252-257.

57. Banthia, N., C. Yan, and K. Sakai, *Impact resistance of concrete plates reinforced with a fiber reinforced plastic grid.* ACI Materials Journal, 1998. **95**(1): pp. 11-18.

58. Dieter, D.A., *Experimental and analytical study of concrete bridge decks constructed with FRP stay-in-place forms and FRP grid reinforcing*, in *Thesis submitted to the Department of Civil Engineering in partial fulfillment of the requirements for the degree of Masters of Science*. 2002, University of Wisconsin-Madison: Madison, Wisconsin. pp. 226.

59. Dieter, D.A., J.S. Dietsche, L.C. Bank, M.G. Oliva, and J.S. Russell. *Concrete bridge decks constructed with fiber-reinforced polymer stay-in-place forms and grid reinforcing*. in *Design of Structures. Transportation Research Record*. 2002.

60. Jeong, S.K., S. Lee, C.H. Kim, D.M. Ok, and S.J. Yoon, *Flexural behavior of GFRP reinforced concrete members with CFRP grid shear reinforcements.* Fracture and Strength of Solids Vi, Pts 1 and 2, 2006. **306-308**: pp. 1361-1366.

61. Saafi, M., *Design and fabrication of FRP grids for aerospace and civil engineering applications*. Journal of Aerospace Engineering, 2000. **13**(4): pp. 144-149.

62. Schmeckpeper, E.R. and C.H. Goodspeed, *Fiber-Reinforced Plastic Grid for Reinforced-Concrete Construction.* Journal of Composite Materials, 1994. **28**(14): pp. 1288-1304.

63. Yost, J.R., C.H. Goodspeed, and E.R. Schmeckpeper, *Flexural performance of concrete beams reinforced with FRP grids.* Journal of Composites for Construction, 2001. **5**(1): pp. 18-25.

64. Zhang, B.R., R. Masmoudi, and B. Benmokrane, *Behaviour of one-way concrete slabs reinforced with CFRP grid reinforcements.* Construction and Building Materials, 2004. **18**(8): pp. 625-635.

65. Bae, H.U., *Design of reinforcement-free bridge decks with wide flange prestressed precast girders*, in *Dissertation submitted to the Department of Civil Engineering in partial fulfillment of the requirements for the degree of Doctor of Philosophy*. 2008, University of Wisconsin-Madison: Madison, Wisconsin.

66. Bank, L.C., A.P. Malla, M.G. Oliva, J.S. Russell, A. Bentur, and A. Shapira, *A model specification for fiber reinforced non-participating permanent formwork panels for concrete bridge deck construction.* Construction and Building Materials, 2009. **23**(7): pp. 2264-2677.

67. Berg, A.C., L.C. Bank, M.G. Oliva, and J.S. Russell, *Construction and cost analysis of an FRP reinforced concrete bridge deck.* Construction and Building Materials, 2006. **20**(8): pp. 515-526.

68. Frost, S.L., *Effect of stay-in-place metal forms on performance of concrete bridge decks, M.S. Thesis*. 2006, Department of Civil and Environmental Engineering, Brigham Young University, Provo UT. 66. pp.

69. Hanus, J.P., L.C. Bank, and M.G. Oliva, *Combined loading of a bridge deck reinforced with a structural FRP stay-in-place form.* Construction and Building Materials, 2009. **23**(4): pp. 1605-1619.

70. Lopez-Anido, R., P.K. Dutta, J. Bouzon, S. Morton, B. Shahrooz, and I.E. Harik, *Fatigue evaluation of FRP-concrete bridge deck on steel girders at high temperature*. Society for the Advancement of Material and Processs Engineering, Evolving and revolutionary technologies for the new millenium. Vol. 44. 1999: SAMPE. pp.

71. Bank, L.C., M.G. Oliva, H.U. Bae, J.W. Barker, and S.W. Yoo, *Pultruded FRP plank as formwork and reinforcement for concrete members.* Advances in Structural Engineering, 2007. **10**(5): pp. 525-535.

72. Cheng, L.J. and V.M. Karbhari, *Design approach for a FRP structural formwork based steel-free modular bridge system.* Structural Engineering and Mechanics, 2006. **24**(5): pp. 561-584.

73. Hall, J.E. and J.T. Mottram, *Combined FRP Reinforcement and Permanent Formwork for Concrete Members.* Journal of Composites for Construction, 1998. **2**(2): pp. 78.

74. National Cooperative Highway Resarch Program., *Development of design specifications and commentary for horizontally curved concrete box-girder bridges, NCHRP Report 620, Project 12-71*. 2008: Washington, D.C.

75. Hurd, M.K., *Formwork for concrete*. 7th ed. Prepared under the direction of ACI committee 347, formwork for concrete. 2005, Farmington Hills, Michigan: American Concrete Institute. pp.

76. Johnston, D.W., *Design and construction of concrete formwork.* 2nd ed. Concrete construction engineering handbook, ed. E.G. Nawy. 2008, Boca Raton :: CRC Press. pp.

77. ACI Committee 622., *Formwork for concrete.* American Concrete Institute Journal Proceedings, 1961. **32**: pp. 993-1040.

78. Hanna, A.S., *Concrete formwork systems*. Civil and environmental engineering series ;. Vol. 2. 1999, New York :: Marcel Dekker. pp.

79. Harding, M.A., *Deck forms for girder bridges*, in *The Aberdeen Group*. 1994, Publication #C940771.

80. McClelland, R., *Current practice sheet No. 12- Permanent formwork for composite bridge decks*, Concrete Bridge Development Group., Editor. 2005, CBDG.

81. American Concrete Institute., *Guide to formwork for concrete*, ed. ACI Committee 347. 2004, Detroit, Mich.: American Concrete Institute. pp.

82. Bakht, B. and A. Mufti, *Stay-in-place concrete formwork for deck slabs of girder bridges.* Journal of the Institution of Engineers, 1997. **78**(November): pp. 129-135.

83. Bakht, B. and C. Lam, *Behaviour of transverse confining systems for steel-free deck slabs.* ASCE Journal of Bridge Engineering, 2000. **5**(2): pp. 139-147.

84. Mufti, A.A. and J.P. Newhook, *On the use of steel-free concrete bridge decks in continuous span bridges.* Canadian Journal of Civil Engineering, 1999. **26**(5): pp. 667-672.

85. Mufti, A.A., L.G. Jaeger, B. Bakht, and L.D. Wegner, *Experimental Investigation of Fiber-Reinforced Concrete Deck Slabs without Internal Steel Reinforcement.* Canadian Journal of Civil Engineering, 1993. **20**(3): pp. 398-406.

86. Newhook, J. and A. Mufti, *A reinforcing steel-free concrete deck slab for the Salmon River bridge.* Concrete International, 1996. **18**(6): pp. 30-34.

87. Canadian Standards Association., *FRC in Deck Slabs*. Canadian highway bridge design code, Section 16.7. 2000, Rexdale, Ontario, Canada: Canadian Standards Association (CSA). pp.

88. Mufti, A.A., B. Bakht, and J.P. Newhook, *Precast concrete decks for slab-on-girder systems: A new approach.* ACI Structural Journal, 2004. **101**(3): pp. 395-402.

89. Bakht, B., A. Mufti, and G. Tadros. *Transverse confinement of deck slabs by metallic stay-in-place forms*. in *Proc., 4th Structural specialty conference of the Canadian Society of Civil Engineers*. 2002. Montreal: Canadian Society for Civil Engineering.

90. Grace, N.F., J. Hanson, and T. R.D., *Inspection and deterioration of bridge decks constructed using stay-in-place metal forms and epoxy-coated reinforcement*. 2004, Southfield, Michigan: Department of Civil Engineering, Lawrence Technological University. pp.

91. American Association of State Highway and Transportation Officials., *AASHTO LRFD bridge construction specifications*. 2nd ed. 2004, Washington, D.C.: American Association of State Highway and Transportation Officials. 1 v. (various pagings). pp.

92. Kim, G.B., K. Pilakoutas, and P. Waldron, *Thin FRP/GFRC structural elements.* Cement & Concrete Composites, 2008. **30**(2): pp. 122-137.

93. Kim, G.B., K. Pilakoutas, and P. Waldron, *Development of thin FRP reinforced GFRC permanent formwork systems.* Construction and Building Materials, 2008. **22**(11): pp. 2250-2259.

94. Bank, L.C., A.P. Malla, M.G. Oliva, J.S. Russell, A. Bentur, and A. Shapira, *Specification and design of fiber reinforced bridge deck forms for use on wide flange T-girders*, in *Report No WHRP 07-10*. 2007, University of Wisconsin-Madison: Madison, Wisconsin.

95. Bakeri, P.A., *Analysis and deisgn of polymer composite bridge decks*. Thesis submitted to the Department of Civil Engineering in partial fulfillment of the requirements for the degree of Master of Science. Vol. Master of Science. 1989, Cambridge, Massachusetts: Massachusetts Institute of Technology. 85. pp.

96. Hillman, J.R. and T.M. Murray. *Innovative lightweight floor systems for steel framed structures*. in *IASBE Symposium on mixed structures , including new materials*. 1990. Brussels, Belgium: International Association for Bridge and Structural Engineering.

97. Schaumann, E., T. Vallée, and T. Keller, *Direct load transmission in hybrid FRP and lightweight concrete sandwich bridge deck.* Composites Part A-Applied Science and Manufacturing, 2008. **39**(3): pp. 478-487.

98. Keller, T., E. Schaumann, and T. Vallée, *Flexural behavior of a hybrid FRP and lightweight concrete sandwich bridge deck* Composites Part A: Applied Science and Manufacturing, 2006. **38**(3): pp. 879.

99. Schaumann, E., T. Vallée, and T. Keller, *Shear resistance of lighweight concrete core of fiber-reinforced polymer concrete sandwich structure.* ACI Materials Journal, 2009. **106**(1): pp. 33-41.

100. Deskovic, N., T.C. Triantafillou, and U. Meier, *Innovative Design of FRP Combined with Concrete: Short-Term Behavior*. Journal of Structural Engineering, 1995. **121**(7): pp. 1069-1078.

101. Deskovic, N., U. Meier, and T.C. Triantafillou, *Innovative Design of FRP Combined with Concrete: Long-Term Behavior*. Journal of Structural Engineering, 1995. **121**(7): pp. 1079-1089.

102. Deskovic, N., *Innovative design of FRP composite members combined with concrete*, in *Civil Engineering*. 1993, Massachusetts Institute of Technology: Massachusetts. pp. 317.

103. Banks, W.M. and J. Rhodes. *Instability of composite channel sections*. 1983. Paisley, Scotl: Applied Science Publ.

104. Holmes, M. and D.J. Just, *GRP in structural engineering*. 1983, London ; New York :: Applied Science Publishers. pp.

105. Canning, L., L. Hollaway, and A.M. Thorne, *An investigation of the composite action of an FRP/concrete prismatic beam.* Construction and Building Materials, 1999. **13**(8): pp. 417-426.

106. Hulatt, J., L. Hollaway, and A. Thorne, *The use of advanced polymer composites to form an economic structural unit.* Construction and Building Materials, 2003. **17**(1): pp. 55-68.

107. Kitane, Y., A.J. Aref, and G.C. Lee, *Static and fatigue testing of hybrid fiber-reinforced polymer-concrete bridge superstructure.* Journal of Composites for Construction, 2004. **8**(2): pp. 182-190.

108. Aref, A.J., S. Alampalli, and Y.H. He, *Performance of a fiber reinforced polymer web core skew bridge superstructure. Part II: failure modes and parametric study.* Composite Structures, 2005. **69**(4): pp. 500-509.

109. Alnahhal, W., A. Aref, and S. Alampalli, *Composite behavior of hybrid FRP-concrete bridge decks on steel girders.* Composite Structures, 2008. **84**(1): pp. 29-43.

110. Reising, R.M.W., B.M. Shahrooz, V.J. Hunt, A.R. Neumann, A.J. Helmicki, and M. Hastak, *Close look at construction issues and performance of four fiber-reinforced polymer composite bridge decks.* Journal of Composites for Construction, 2004. **8**(1): pp. 33-42.

111. Reising, R.M.W., B.M. Shahrooz, V.J. Hunt, A.R. Neumann, and A.J. Helmicki, *Performance comparison of four fiber-reinforced polymer deck panels.* Journal of Composites for Construction, 2004. **8**(3): pp. 265-274.

112. Reising, R.M.W., B.M. Shahrooz, V.J. Hunt, M.S. Lenett, S. Christopher, A.R. Neumann, A.J. Helmicki, R.A. Miller, S. Kondury, and S. Morton, *Performance of five-span steel bridge with fiber-reinforced polymer composite deck panels.* Design of Structures 2001, 2001(1770): pp. 113-123.

113. Reising, R.M.W., *Testing and long-term monitoring of a five-span bridge with multiple FRP decks- performance and design issues*. *Dissertation submitted to the Department of Civil and Environmental Engineering in partial fulfillment of the requirements for the degree of Doctorate of Philosophy*. 2003, Cincinnati, Ohio: University of Cincinnati. 350. pp.

114. Harik, I.E., P. Alagusundaramoorthy, R. Siddiqui, R. Lopez-Anido, S. Morton, and P.K. Dutta. *Testing of concrete/fiber-reinforced polymer composite deck*

panels. in *Proceedings of the fifth ASCE materials engineering conference*. 1999. Cincinnati, Ohio: American Society of Civil Engineers.

115. Alagusundaramoorthy, P., I.E. Harik, and C.C. Choo, *Structural behavior of FRP composite bridge deck panels.* ASCE Journal of Bridge Engineering, 2006. **11**(4): pp. 384-393.

116. Dutta, P.K., R. Lopez-Anido, and S.C. Kwon, *Fatigue durability of FRP composite bridge decks at extreme temperatures.* International Journal of Materials & Product Technology, 2007. **28**(1-2): pp. 198-216.

117. Bank, L.C., Z. Xi, and E. Munley. *Tests of full-sized pultruded FRP grating reinforced concrete bridge decks*. in *ASCE materials engineering congress*. 1992. Atlanta, Georgia: American Society of Civil Engineers.

118. American Concrete Institute., *Building Code Requirements for Structural Concrete*. 2008, Detroit, Mich: ACI 318-08. 430. pp.

119. Cheng, L.J., L. Zhao, V.M. Karbhari, G.A. Hegemier, and F. Seible, *Assessment of a steel-free fiber reinforced polymer-composite modular bridge system.* Journal of Structural Engineering-ASCE, 2005. **131**(3): pp. 498-506.

120. Cheng, L., *Development of a steel-free FRP-concrete slab-on-grider modular bridge system*, in *Structural Engineering*. 2005, University of California: La Jolla, California. pp. 388.

121. Cheng, L.J. and V.M. Karbhari, *Fatigue behavior of a steel-free FRP-concrete modular bridge deck system.* ASCE Journal of Bridge Engineering, 2006. **11**(4): pp. 474-488.

122. Brinckerhoff, P., *Bridge inspection and rehabilitation : a practical guide*, ed. L.G. Silano. 1993, New York, N.Y.: Wiley. xiii, 288 p. pp.

123. Allen, R.T.L., S.C. Edwards, and J.D.N. Shaw, *The Repair of concrete structures*. 2nd ed. 1993, London ; New York: Blackie Academic & Professional. xii, 212 p. pp.

124. Tonias, D.E., *Bridge engineering : design, rehabilitation, and maintenance of modern highway bridges*. 1995, New York: McGraw-Hill. 470 p. pp.

125. Mailvaganam, N.P., *Repair and protection of concrete structures*. 1992, Boca Raton, Fla.: CRC Press. 473 p. pp.

126. American Concrete Institute., *Guide for the design and construction of externally bonded FRP systems for strengthening concrete structures*. ACI manual of concrete practice, ed. A. 440.2R-08. 2008, Detroit, Mich.: American Concrete Institute. 75. pp.

127. Rizkalla, S., T. Hassan, and N. Hassan, *Design recommendations for the use of FRP for reinforcement and strengthening of concrete structures.* Progress in Structural Engineering and Materials, 2003. **5**(1): pp. 16-28.

128. Ghosh, K.K., *Assessment of FRP composite strengthened reinforced concrete bridge structures at the component and systems level through progressive damage and Non-Destructive Evaluation (NDE).* Dissertation submitted to the Department of Structural Engineering in partial fulfillment of the requirements for the degree of Doctorate of Philosophy. 2006, La Jolla, California: Universit of California, San Diego. 481. pp.

129. De Lorenzis, L. and J.G. Teng, *Near-surface mounted FRP reinforcement: An emerging technique for strengthening structures.* Composites Part B-Engineering, 2007. **38**(2): pp. 119-143.

130. Asplund, S.O., *Strengthening bridge slabs with grouted reinforcement.* Journal of the American Concrete Institute, 1949. **45**(1): pp. 397-406.

131. Parretti, R. and A. Nanni, *Strengthening of RC members using near-surface mounted FRP composites: Design overview*. Advances in Structural Engineering, 2004. **7**(6): pp. 469-483.

132. Nanni, A., T. Alkhrdaji, M. Barker, G. Chen, R. Mayo, and X.B. Yang. *Overview of testing to failure program of a highway bridge strengthened with FRP composites*. in *FRPRCS-4*. 1999. Baltimore, Maryland.

133. Nordin, H. and B. Taljsten, *Concrete beams strengthened with prestressed near surface mounted CFRP*. Journal of Composites for Construction, 2006. **10**(1): pp. 60-68.

134. Szabo, Z.K. and G.L. Balazs, *Near surface mounted FRP reinforcement for strengthening of concrete structures.* Periodica Polytechnica-Civil Engineering, 2007. **51**(1): pp. 33-38.

135. Hollaway, L.C. and P.R. Head, *Advanced polymer composites and polymers in the civil infrastructure*. 1 ed. 1991: Elsevier. 316. pp.

136. Blaschko, M., *Bond behaviour of CFRP strips glued into slits*, in *Fibre-reinforced polymer reinforcement for concrete structures, FRPRCS-6*, H.K. Tan, Editor. 2003: Singapore. pp. 205-214.

137. Teng, J.G., L. De Lorenzis, B. Wang, R. Li, T.N. Wong, and L. Lam, *Debonding failures of RIC beams strengthened with near surface mounted CFRP strips.* Journal of Composites for Construction, 2006. **10**(2): pp. 92-105.

138. Burke, P.J., *Low and high temperature performance of near surface mounted FRP strengthened concrete slabs*, in *Thesis submitted to the Department of*

Civil Engineering in conformity with requirements for the degree of Master of Science. 2008, Queen's University: Kingston, Ontario, Canada.

139. Concrete Society., *Design guidance for strengthening concrete structures using fibre composite materials*. 2nd ed. Concrete Society technical report No. 55. 2004, Camberley, Surrey, UK: Cromwell Press. 102. pp.

140. De Lorenzis, L., A. Rizzo, and A. La Tegola, *A modified pull-out test for bond of near-surface mounted FRP rods in concrete.* Composites Part B-Engineering, 2002. **33**(8): pp. 589-603.

141. El-Hacha, R. and S.H. Rizkalla, *Near-surface-mounted fiber-reinforced polymer reinforcements for flexural strengthening of concrete structures.* Aci Structural Journal, 2004. **101**(5): pp. 717-726.

142. Yost, J.R., S.P. Gross, D.W. Dinehart, and J.J. Mildenberg, *Flexural behavior of concrete becams strengthened with near-surface-mounted CFRP strips.* ACI Structural Journal, 2007. **104**(4): pp. 430-437.

143. Tang, W.C., R.V. Balendran, A. Nadeem, and H.Y. Leung, *Flexural strengthening of reinforced lightweight polystyrene aggregate concrete beams with near-surface mounted GFRP bars.* Building and Environment, 2006. **41**(10): pp. 1381-1393.

144. Barros, J.A.O., S.J.E. Dias, and J.L.T. Lima, *Efficacy of CFRP-based techniques for the flexural and shear strengthening of concrete beams.* Cement & Concrete Composites, 2007. **29**(3): pp. 203-217.

145. Warren, G., *Waterfront repair and upgrade, advanced technology demonstration site No. 2: Pier 12, NAVSTA, San Diego*

in *Site specific report SSR-2419-SHR*. 1998, Naval facilities engineering service center, Port Hueneme, CA: San Diego, CA.

146. Farmer, N., *Near-surface-mounted reinforcement preserves car park for Merseyside police.* Concrete, 2003. **37**(9): pp. 36-38.

147. Alkhradaji, T., A. Nanni, G. Chen, and M. Barker, *Upgrading the transportation infrastructure: solid RC decks strengthened with FRP.* Concrete International, 1999. **21**(10): pp. 37-41.

148. American Concrete Institute., *Guide for the design and construction of externally bonded FRP systems for strengthening concrete structures*, ed. A. 440.06R. 2006, Detroit, Mich.: American Concrete Institute. pp.

149. Canadian Standards Association., *Canadian highway bridge design code-Section 15: Fibre-reinforced structures*. 2006. 1 v. (various pagings). pp.

150. Mufti, A.A., B. Bakht, N. Banthia, B. Benmokrane, G. Desgagne, R. Eden, M.A. Erki, V. Karbhari, J. Kroman, D. Lai, A. Machida, K. Neale, G. Thadros, and B. Taljsten, *New Canadian highway bridge Design code design provisions for fibre-reinforced structures.* Canadian Journal of Civil Engineering, 2007. **34**(3): pp. 267-283.

151. American Society for Testing and Materials., *Annual book of ASTM standards*. 2000, Philadelphia, PA: American Society for Testing and Materials (ASTM). pp.

152. California Department of Transportation., *Bridge Design Specifications, Section 8- Reinforced concrete*. Vol. Revision Number 32. 2004, Sacramento, CA: California Department of Transportation. pp.

153. MacGregor, J.G. and J.K. Wight, *Reinforced concrete : mechanics and design*. 4th ed. 2005, Upper Saddle River, N.J.: Prentice Hall. xx, 1132 p. pp.

154. Nawy, E.G., A. Scanlon, and American Concrete Institute., *Designing concrete structures for serviceability and safety*. 1992, Detroit: American Concrete Institute. vi, 346 p. pp.

155. American Concrete Institute., *Building Code Requirements for Structural Concrete*. 2005, Detroit, Mich: ACI 318-05. pp.

156. Sika Corporation., *Product data sheet for SikaDur 55 SLV*, in www.sikaconstruction.com. 2008: Lyndhurst, NJ.

157. Loyola Construction Products., *Simposon Epoxy-Tie Technical Data*. 2008.

158. American Concrete Institute., *Anchorage to Concrete- Designing structural connections to concrete, SCM-31 (06)*. 2006, Detroit, Mich.: American Concrete Institute. pp.

159. California Department of Transportation., *Memo to designers: 22-1. Soundwall design criteria*. 2004, Sacramento, California: California Department of Transportation. pp.

160. Bentz, E. and M.P. Collins, *RESPONSE 2000- Reinforced concrete sectional analysis using the modified compression field theory*. 2000: Toronto, Canada.

161. Bates, B.R., *RISA-2D Educational Version 1.0*. 2002, Risa Technologies.

162. Sika Corporation., *Product data sheet for Sika CarboDur- carbon fiber laminate for structural strengthening*, in www.sikaconstruction.com. 2005: Lyndhurst, NJ.

163. Sika Corporation., *Product data sheet for Sika CarboDur rods- carbon fiber rods for structural strengthening*, in *www.sikaconstruction.com*. 2003: Lyndhurst, NJ.

164. Hughes Brothers Incorporated., *Product data sheet forAslan 500- CFRP tape*, in *www.hughesbros.com*. 2002: Lyndhurst, NJ.

165. Seim, W., M. Horman, V. Karbhari, and F. Seible, *External FRP poststrengthening of scaled concrete slabs.* Journal of Composites for Construction, 2001. **5**(2): pp. 67-75.

166. Seim, W., A. Vasquez, V. Karbhari, and F. Seible, *Poststrengthening of concrete slabs: Full-scale testing and design recommendations.* Journal of Structural Engineering-ASCE, 2003. **129**(6): pp. 743-752.

167. Sohanghpurwala, A.A., *Manual on service life prediction of corrosion-damaged reinforced concrete bridge superstructure elements*, in *National Cooperative Highway Resarch Program.,* . 2006: Washington, D.C. pp. 59.

168. International Concete Repair Institute., *ICRI Guideling No. 037324, Selecting and specifying concrete surfacte preparation for sealers, coatings and polymer overlays*. 1997. pp.

169. Jin, S.-J., *Reliability-based characterization of prefabricated FRP composites for rehabilitation of concrete structures*, in *Thesis submitted to the Department of Structural Engineering in partial fulfillment of the requirements for the degree of Master of Science*. 2008, University of California, San Diego: La Jolla, California.

170. Sika Corporation., *CarboDur installation guide, Sika construction documents*, in *www.sikaconstruction.com*: Lyndhurst, NJ.